Atmospheric and Climate Effects of Biomass Burning using different Injection Heights

Mónica Adriana Lozano Juárez

geb. in Mexiko-Stadt

Mainz, den 30. Mai 2015

Abstract

Inspired by the need for a representation of the biomass burning emissions injection height in the ECHAM/MESSy Atmospheric Chemistry model (EMAC) , four schemes and a vertical distribution function have been developed and implemented in this thesis. The most realistic scheme accounts for fire intensity and local weather conditions in the plume height estimation, and it reproduces more than half (52%) of the plumes observed by MISR globally and up to 75% regionally. The changes associated with the modified biomass burning (BB) injection height (e.g., aerosol lifetime, global burden and transport) and several important atmospheric impacts associated with fires (e.g., gas emissions as aerosol precursors, changes in ozone concentrations, influence on atmospheric oxidation capacity, aerosol emissions as efficient cloud condensation nuclei and influence on the atmospheric radiation transfer) have been evaluated to asses the impact of the injection height and vertical distribution on the chemical composition of the atmosphere and climate. The BB aerosol deposition efficiency has been affected by their injection at higher altitudes. The annual mean dry deposition of BB aerosol has been reduced (35%–47%). Sedimentation has also been reduced slightly, whereas annual wet deposition has been enhanced globally (6%–10%). Overall, the global mean lifetime of the BB aerosols has increased (1.5%–3%): regionally and seasonally, these changes are larger (8%–20%). The lifetime increase causes a global burden increment of the aerosol species from BB sources (6%–13% annual mean). The BB aerosol surface concentrations have been reduced (54%–73%) close to source regions, whereas downwind increases are found (33%–108%). The BB aerosol column burden show regional enhancements (15%–66%). The release of the aerosol precursors NO_x at higher altitudes enhances the regional annual mean concentration of the associated species NO_3^- (13%–24%). The release

of SO_2 and the local variations in the oxidation capacity results in regional increments of the SO_4^{2-} annual mean concentration (6%–9%). The influence on the oxidation capacity result in a reduction of the CO column density (1%–6%) and of the CH_4 lifetime (2.5%). The interplay of all these processes results in enhancements of regional annual mean surface O_3 concentrations (3%–5%). The aerosol optical density (AOD) has been enhanced (8%–23%), which results in an improvement (10%) compared to satellite observations. Enhancement in the absorption (compared to releasing the BB aerosols at the surface) is found in the troposphere. The efficiency of BB in the CCN activation is evident as a regional CCN enhancement (25%–42%) at the top of the planetary boundary layer. The effects on the radiation budget of the atmosphere result in a positive enhancement of the net "all-sky" radiative forcing (compared to the reference simulation) in the range of 0.1 to 0.25 Wm^{-2}. Most of this forcing emerges from changes of the cloud properties.

Zusammenfassung

Da für die Emissionen von Biomasseverbrennung (BB) die vertikale Verteilung bestimmt werden soll, in der eine Injektion von Spurenstoffen erfolgen soll, sind in dieser Arbeit sind 4 Schemata inklusive einer vertikalen Verteilungsfunktion für das atmosphärische Chemie-Klimamodell ECHAM5/MESSy Atmospheric Chemistry (EMAC) entwickelt worden. Das realitätsnächste Schema, das sowohl die Feuerintensität und lokale Wetterbedingungen zur Bestimmung der "Plume"-Höhe beinhaltet, reproduziert mehr als die Hälfte (52%) der von MSIR beobachteten "Plumes" global und bis zu 75% in bestimmten Regionen. Die Änderungen, die aus einer modifizierten Emissionshöhe der Biomassenverbrennung stammen (wie z.B. Aerosollebensdauer, globale Gesamtmenge und Transport), und wichtige Auswirkungen von Feuern auf die Atmosphäre (z.B. Emissionen von Gasen (die als Aerosolvorläuferspezies dienen), Änderungen in Ozonkonzentrationen, Auswirkungen auf die Oxidationskapazität der Atmosphäre, und direkte Aerosolemissionen (die als Wolkennukleationskeime agieren können und den atmosphärischen Strahlungstransport beeinflussen) sind evaluiert worden, um die Einflüsse der Emissionshöhe und der vertikalen Verteilung der Emissionen auf die chemische Zusammensetzung der Atmosphäre und das Klima zu untersuchen. Die Effizienz von Aerosoldeposition aus BB Quellen wird direkt durch die Injektion in größerer Höhe modifiziert. Die jährliche trockene Deposition ist gesunken (35%–47%). Ebenso hat die Sedimentation auch leicht abgenommen. Auf der anderen Seite wird dies teilweise durch erhöhte Feuchtdeposition (6%–10%) kompensiert. Dies hat Auswirkungen auf die global mittlere Lebensdauer von BB Aerosolspezies (1.5%–3%). Auf einer regionalen Skala sind diese Effekte deutlich größer (8%–20%). Die längere Verweilzeit in der Atmosphäre bewirkt eine Erhöhung der Gesamtaerosolmasse aus BB Quellen (6%–13% im Jahresmittel). Nahe der Er-

doberfläche sind die Konzentration deutlich niedriger in den Quellregionen (54%–73%), jedoch lassen sich stromabwärts deutliche Erhöhungen finden (33%–108%). Auch die vertikale Gesamtsäulendichte zeigt Erhöhungen von 15%–66%. Die Emission von NO_x, was als Aerosolvorläufersubstanz agieren kann, in größerer Höhe bewirkt regional Erhöhungen der mittleren Konzentration von Nitrat (NO_3^-) von 13%–24%. Emissionen von SO_2 und die lokalen Veränderungen in der Oxidationskapazität der Atmosphäre resultieren in mittleren Erhöhungen der SO_4^{2-} Konzentration von 6%–9%. Der Einfluss auf die Oxidationskapazität der Atmosphäre reduziert die Kohlenstoffmonoxidsäulendichten (1%–6%) und senkt regional die CH_4 Lebensdauer um 2.5%. Die Kombination all dieser Effekte bewirkt auch eine Erhöhung der bodennahen O_3 Konzentrationen um 3%–5%. Die "Aerosol-Optische-Dicke" (AOD) weist eine Erhhung um 8%–23% auf, was einer Verbesserung der simulierten Werte gegenüber Satellitenbeobachtungen um 10% entspricht. Auch wird eine Erhöhung der Absorption von Strahlung in der Troposphäre im Vergleich zu einer Emission von BB Aerosolen am Boden gefunden. Für die CCN-Effizienz, also der Effizienz der Aktivierung von Aerosolteilchen in Wolkentropfen, wird eine deutliche Erhöhung der CCN Konzentrationen (25%–42%) in Höhe der Grenzschichtoberkante sichtbar. Die Auswirkungen auf die Strahlungsbilanz zeigen, dass sich ein Netto-Forcing von 0.1 bis 0.25 Wm^{-2} für unbewölkte und bewölkte Bedingungen ergibt, wobei der Großteil dieses Effekte durch Änderungen der Wolkeneigenschaften bewirkt wird.

Contents

CONTENTS

1

Introduction

Figure 1.1: Schematic of Biomass Burning.

Biomass burning (BB) refers to the combustion of living and dead vegetation. Fires have been occurring since the beginning of time and have influenced tropospheric chemistry as well as the radiative balance of the planet. Fires release important trace gasses and aerosols in a magnitude comparable to other anthropogenic sources. The effect associated with BB must be properly represented as a background in order to evaluate the role of other anthropogenic emissions. Unlike other sources of pollutants, fires can inject tracers at higher altitudes because of plume dynamics and local air circulation originating from the plume as well as the sensible heat fluxes of the fire. This can enhance the effect of the BB emissions.

1.1   Biomass Burning Emissions

Biomass burning is an important source of trace gases and aerosols (comparable to other anthropogenic sources) and contributes to the composition of the atmosphere at both regional and global level. This source has a seasonal cycle determined by the natural conditions for fires to occur and by agricultural practices. The emissions vary strongly according to the properties of the fuel (type, amount, and dryness) as well as the stages of the fires, which are characterized by the chemical and physical processes that occur during combustion (Lobert and Wamatz, 1993; Yokelson et al., 1996, 1997). The information of each individual tracer is estimated by emission factors or emissions ratios (Andreae and Merlet, 2001), which relate the emission of a particular species to a reference species such as CO_2 or CO (emission ratio) or to the amount of fuel consumed (emission factor). In this thesis, emission factors (based on Andreae and Merlet (2001) and Christian et al. (2003)) are used to estimate the emission field provided by the Global Fire Emission Database (GFED3), as described in Section 2.2.1. Several species (summarized in Andreae and Merlet (2001)) are emitted during biomass combustion. These include greenhouse gases (carbon monoxide, methane, and nitrous oxide). The annual contribution of the BB emissions is comparable to other anthropogenic sources (Table 1.1). Furthermore, considering the seasonal cycle of BB, for certain species, the global monthly contribution of this source can reach more than half of the monthly emissions (Figure 1.2).

1.2   The Influence of Biomass Burning on the Climate System

Biomass burning influences the climate system in many ways. Fires play an important role in the carbon and nitrogen cycles (Crutzen and Andreae, 1990). Emissions adversely affect human health in adjacent urban areas (e.g., Lei et al., 2013). Emissions from BB influence the hydrological cycles (Ramanathan et al., 2001a) by modifying cloud properties (e.g., Andreae et al., 2004) resulting from the ability of BB aerosols to act as cloud condensation nuclei (CCN) as well as the influence of BB on radiative transfer and hence temperature profiles (e.g., Hobbs et al., 1997). Biomass burning emissions both directly (by the emission of radiative species) and indirectly (by the modification of cloud properties) influence the radiative balance of the planet. Fires
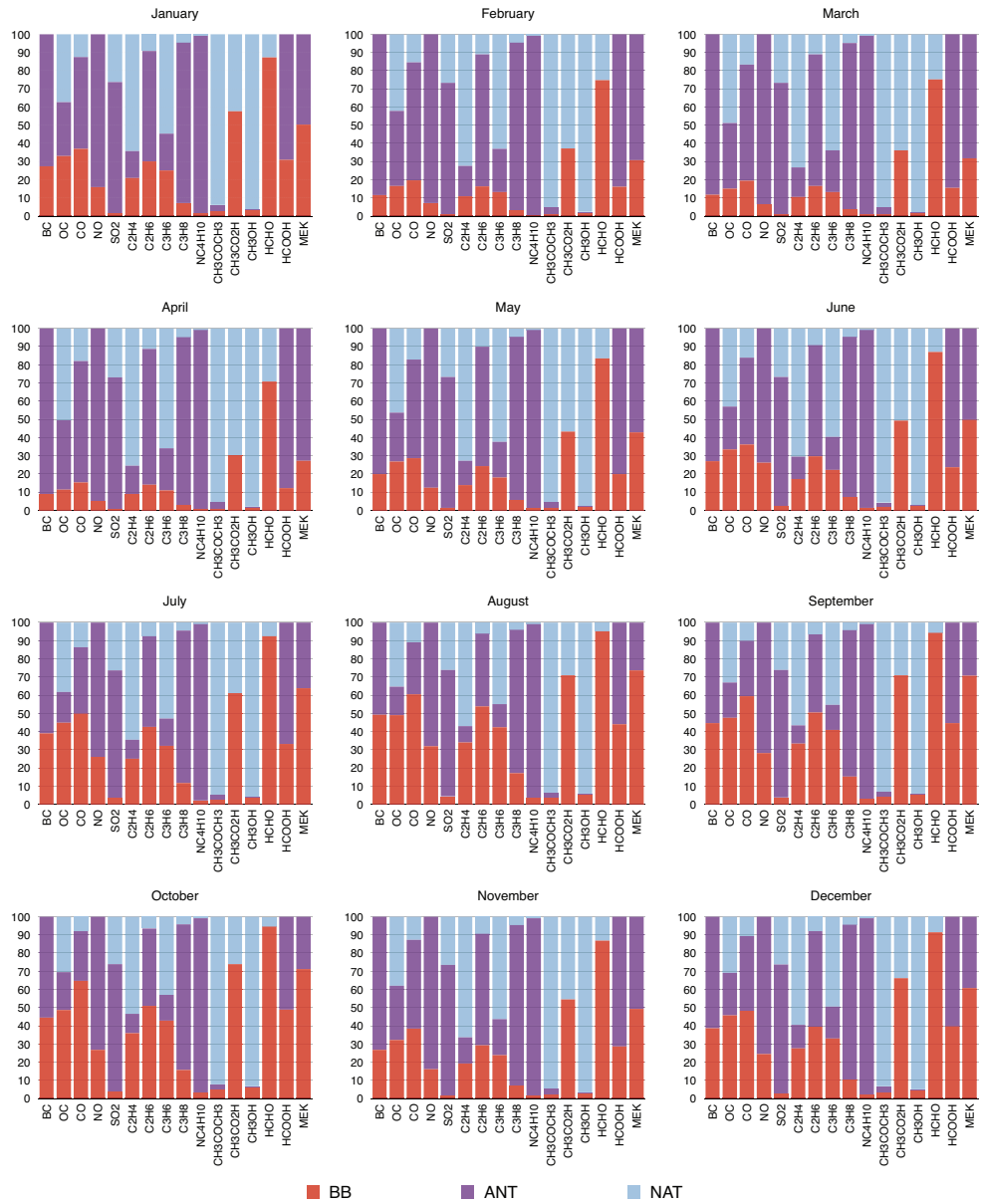
Figure 1.2: Species emitted by BB in this thesis

Monthly contribution (in percentage) of the biomass burning (BB), anthropogenic (ANT) and natural (NAT) sources to the species emitted by BB in 2006.

1. INTRODUCTION

Table 1.1: Global BB emissions for 2006

	BB [%]	ANT [%]	NAT [%]	TOTAL [Tg]
BC	31.7	68.3		6.83
OC	37.3	24.5	38.2	50.02
CO	45.0	42.5	12.6	894.05
NO_x	19.3	80.7		53.00
SO_2	2.2	71.4	26.4	115.88
C_2H_4	23.3	12.5	64.2	17.67
C_2H_6	36.3	55.4	8.4	6.43
C_3H_6	28.9	17.6	53.6	6.36
C_3H_8	9.2	86.4	4.4	7.90
NC_4H_{10}	1.8	97.5	0.8	52.85
CH_3CHO	100.0			1.59
CH_3COCH_3	2.5	3.1	94.9	58.98
CH_3CO_2H	59.9		40.1	8.43
CH_3OH	3.2	0.8	96.0	156.68
HCHO	90.2	9.8		2.99
HCOOH	32.8		67.2	8.30
MEK	57.4	42.7		6.09

Biomass Burning (BB); Anthropogenic (ANT); Natural (NAT).

can also modify the albedo of the surfaces e.g., the deposition of black carbon on snow. Trace gases emitted by BB regionally (e.g., Andrés-Hernández et al., 2009; Crutzen et al., 1985; Greenberg et al., 1984) and globally (e.g., Andreae and Merlet, 2001; Crutzen and Andreae, 1990; Crutzen et al., 1979) influence the tropospheric chemistry. The release of NO_x influences the oxidation capacity of the atmosphere through its role in recycling hydroxyl radicals (OH), which are primarily formed via the photo-dissociation of ozone (Lelieveld et al., 2008; Taraborrelli et al., 2012).

The production of ozone is limited by the supply of HO_x (OH + HO_2) and NO_x (NO + NO_2) (Levy, 1971; Logan et al., 1981). In the troposphere, ozone is mainly lost as a result of photolysis (to $O(^1D)$, followed by reaction with water vapor) and the reaction with OH and HO_2 (Seinfeld and Pandis, 2006), as well as surface deposition.

Therefore, the release of NO_x together with volatile organic compounds (VOC) affects the production of ozone via the photochemical oxidation of the released NO_2, which is usually observed in BB regions (e.g., Anderson et al., 1996; Delany et al., 1985; Honrath et al., 2004; Jonquières et al., 1998; Jost et al., 2004; Pickering et al., 1996).

In remote areas, NO_x and acetaldehyde (CH_3CHO) emissions also contribute to the production of ozone through the formation of peroxyacetil nitrate (PAN), which is observed in BB smoke plumes (e.g., Chatfield et al., 1996; Wofsy et al., 1992). Acetaldehyde reacts with OH (as well as O_2) to create the peroxyacetyl radical ($CH_3C(O)O_2$), which reacts with NO_2 to form PAN ($CH_3C(O)O_2NO_2$). Peroxyacetil nitrate is stable at lower temperatures, which makes it an effective reservoir of NO_x in the upper troposphere and facilitates its transport and subsequent role in the production of ozone in remote areas (Seinfeld and Pandis, 2006).

All of these processes can be enhanced by injecting BB emissions at higher altitudes. The changes in the vertical distribution of BB emissions allow them to be transported to remote areas and higher altitudes, which implies different background concentrations and temperature regimes. This affects the production of tropospheric ozone, the recycling of OH (e.g., Cantrell et al., 2003; Lelieveld and Crutzen, 1994) and the production of PAN.

Enhanced concentrations of VOC associated with BB have been identified downwind of production regions (e.g., Blake et al., 1994; Chatfield et al., 1996; Christian et al., 2003; Reid et al., 1998; Thompson et al., 1996; Yokelson et al., 1997). Of these emissions, acetone ($CH_3C(O)CH_3$) contributes to the concentration of HO_x in the upper troposphere and can thereby influence the production of ozone. Moreover, the radiative forcing of tropospheric ozone strongly depends on height and latitude distribution through the influence of ozone on temperature, water vapor, and clouds (Berntsen et al., 1997; Bowman et al., 2013; Lacis et al., 1990; Worden et al., 2008, 2011). Consequently, an appropriate spatiotemporal ozone distribution is required to accurately assess the climate effects.

Gaseous species (nitrogen oxides and sulfur dioxide) emitted by BB act as aerosol precursors that influence the transfer of atmospheric radiation. This process may be enhanced by releasing the aerosol precursors at higher altitudes.

Biomass burning is an important source of aerosols, which directly and indirectly (i.e. interactions with clouds) affect the climate system. The direct effect of the aerosols is

determined by the optical properties of the particles. The emissions of BB aerosol can scatter and absorb both short and long-wave radiation, which modifies the radiative balance of the planet by changing the incoming solar radiation and the outgoing long-wave radiation. The trend of scattering and absorption are determined by three optical parameters: the extinction coefficient (σ), which is related to aerosol optical thickness (τ); single scattering albedo (ω); and the asymmetry factor (γ). These parameters vary as a function of the wavelength (λ), the relative humidity, and the horizontal and vertical distribution of the aerosols. The single scattering albedo (ω_0, Equation 1.1) is the ratio between scattering and extinction (i.e., absorption plus scattering). Aerosol that is mainly scattering has ω_0 values of near 1, while values lower than 0.8 imply that the particles could have a warming effect (Haywood and Ramaswamy, 1998).

$$\omega_0 = \frac{\sigma_s}{\sigma_e} = \frac{\sigma_s}{\sigma_s + \sigma_a} \tag{1.1}$$

Scattering aerosols (e.g., organic carbon, nitrate, and black carbon) cause a net negative radiative forcing at the top of the atmosphere (TOA), while the net effect of partially absorbing aerosols (e.g., black carbon and, to a lesser extent, organic carbon) depends on the properties of the underlying surfaces and the fraction of solar radiation that is scattered upward by the particles (Chylek and Wong, 1995). The partially absorbing aerosols reduce the amount of solar radiation that reaches the surface and warms the surrounding atmosphere. Therefore, when these aerosols are located above dark surfaces (e.g., oceans and forests) a negative radiative forcing at the TOA is expected because less solar radiation is absorbed by the ground. In contrast, when located above highly reflective surfaces (e.g., clouds, deserts, ice, and snow) aerosols cause positive radiative forcing at the TOA because less solar radiation reaches and is reflected by the surface.

Partially absorbing aerosols can modify certain processes in clouds and snow, which cause a feedback on the radiative balance of the Earth. The warming of the atmosphere around clouds (caused by the absorbing aerosols) limits its growth and favors its evaporation, thereby reducing its lifetime. The albedo of the cloud is thereby decreased, which can reverse the cooling of the scattering aerosols (direct forcing) (Ackerman et al., 2000). These changes in the cloud properties modify the precipitation, which affects the wet removal of pollutants (Ramanathan et al., 2001a). When partially absorbing aerosols are deposited on snow, the surface becomes darker (more absorbing), which

warms it and reduces its albedo to a greater extent than the loss of solar radiation caused by the aerosols in the atmosphere (Flanner et al., 2009). The warming of the reduced albedo snow causes a more rapid growth of the snow effective grain size, which consequently modifies the snow albedo because finer grains are more reflective (Flanner and Zender, 2006). However, this kind of feedback at the surface is not discussed in this thesis because the model used (ECHAM/MESSy Atmospheric Chemistry model, EMAC) does not account for them.

The optical properties of aerosols strongly depend on the mixing state of the particles. Freshly emitted smoke plumes generally contain particles in an external mixing state, while chemically aged plumes are formed by internally mixed particles. The model assumes a homogenous internal mixture, which is a good approximation for aged particles but does not explicitly represent the core-shell structure that occurs in reality. The internal homogenous mixture absorbs solar radiation to a greater extent than the external mixture; the increased cross section of the aerosols outweighs the reduction in absorption efficiency when an internal mixture is considered (Klingmüller et al., 2014). The best current estimation of BC direct forcing is 0.71 Wm^{-2} (0.08 to 1.27 Wm^{-2}). Biomass burning also releases organic carbon, nitrate and sulfate (which are mainly scattering particles), thereby resulting in a slightly negative direct forcing for BB. Bond et al. (2013) estimate this to be -0.06 Wm^{-2} (-1.45 to +1.9 Wm^{-2}). However this estimation may be modified by a redistribution of BB emissions because the role of absorbing aerosols is enhanced when located at higher altitudes — particularly over clouds— while the role of scattering species decreases because of humidity effects (Heintzenberg et al., 1997).

Injecting BB particles at higher altitudes influences their lifetime (via changes in microphysical and deposition processes) and distribution (by facilitating a larger transport). Consequently, changes in the lifetime of BC may extend its effect as a short lived warming agent, whereas transport to remote areas covered by snow or ice may also enhance its positive forcing.

The aerosol indirect effect is the mechanism by which the aerosols modify the microphysical properties and hence the radiative properties, amount, and lifetime of clouds. The efficacy of the aerosol particles to act as a CCN, which depends on their size, chemical composition, mixing state, and environment (i.e., the local supersaturation), is key in determining these processes. Biomass burning emissions act as efficient CCN

that modify cloud formation and precipitation (e.g., Asa-Awuku et al., 2008; Feingold et al., 2001; Janhäll et al., 2010; Kivekäs et al., 2008; Luderer et al., 2006; Reid et al., 2005; Reutter et al., 2009; Rissler et al., 2004; Roberts et al., 2002; Rose et al., 2010; Rosenfeld et al., 2008; Spracklen et al., 2011; Trentmann et al., 2006). Changes in the injection altitude of the BB aerosols may enhance this process by increasing the concentration of the particles at the planetary boundary layer height (PBLH), where the base of the clouds is located. The extended lifetime may allow more particles to become active.

The aerosol semi-direct effect may be enhanced by the presence of absorbing aerosols around the clouds, which could cause enough warming to evaporate them and drive the net effect of partially absorbing particles (Ackerman et al., 2000).

Properly representing the BB emissions is crucial for accurately quantifying the radiative balance because the direction of the radiative forcing is dependent on the distribution (vertical and horizontal) of the aerosols.

1.3   Fire, Energy, and Height

The altitude reached by the BB smoke plumes is determined by a complex relation between the energy released by the fire and the current local meteorological conditions. The heat released by the fire warms the surrounding air, thereby creating buoyancy and lifting the emissions up to an altitude limited by the local atmospheric conditions. The injection height is therefore directly proportional to the energy released along the flame front (Lavouè et al., 2000). This energy is determined by the heat content, which depends on fuel properties such as dryness and amount. The fuel properties change regionally, seasonally, and temporally (depending on the stages of the combustion). Consequently, the intensity of the energy released by the fire varies largely (so as the local atmospheric conditions), which results in equally variable plume heights. Observations of isolated fires have located plumes completely within the PBLH (e.g., Trentmann et al., 2002), the free troposphere (FT) (~ 2 to 7 km) (e.g., Blake et al., 1994; de Gouw et al., 2006; Wofsy et al., 1992), or even the lower stratosphere (LS) (> 10 km) (e.g., Damoah et al., 2006; Dirksen et al., 2009; Fromm and Servranckx, 2003; Fromm et al., 2000, 2005), although the latter is rare and usually involves unstable atmospheric conditions and pyroconvective events. Satellite based observations

provide a tool to locate smoke plumes at regional to global scales using Lidar observations (e.g., Labonne et al., 2007; Raffuse et al., 2012), stereo imaging (e.g., Kahn et al., 2007, 2008; Mims et al., 2010; Tosca et al., 2011; Val Martín et al., 2010), and aerosol index (AI) measurements (e.g., Guan et al., 2010).

These data provides equally variable conclusions. For example, using data from the Cloud-Aerosol Lidar with Orthogonal Polarization, (CALIOP), Labonne et al. (2007) concluded that the emissions are rarely directly injected above the PBLH. On the other hand, using observations from the Multi-angle Imaging Spetro-Radiometer (MISR) Kahn et al. (2008) show that in boreal regions, 5% to 18% of the plumes reach the free troposphere with injection heights of approx. 4.5 km. Using MISR observations, Val Martín et al. (2010) found that 4% to 12% of plumes were injected in the FT in North America in 2002 and 2004–2007. Differences between these instruments arise from the area covered by them and the local overpass time of the satellites (Kahn et al., 2008). As a result, MISR reveals more buoyant plumes closer to the source than CALIOP. However, because of the observation time (13:30), CALIOP reveals more plumes at a more intense stage.

Isolated, regional or global observations locate plumes inside the PBLH (e.g., Labonne et al., 2007; Lamarque et al., 2003; Langmann et al., 2009; Trentmann et al., 2002), in the FT (e.g., Colarco et al., 2004; Damoah et al., 2004; Guan et al., 2010; Kahn et al., 2007, 2008; Leung et al., 2007; Luderer et al., 2006; Mazzoni et al., 2007; Turquety et al., 2007; Val Martin et al., 2006; Val Martín et al., 2010) or even in the LS (e.g., Damoah et al., 2006; Dirksen et al., 2009; Fromm and Servranckx, 2003; Fromm et al., 2000, 2005; Jost et al., 2004; Trentmann et al., 2006).

These results stress the variability of the plume height and the role of local parameters (intensity of the fire and local weather conditions) in estimating the altitude of BB injection.

1.4 Scientific Questions

There is an obvious need to properly represent the injection of the emissions of BB in order to correctly quantify its role in the climate system. This gives rise to several questions, which will be discussed in this thesis.

1. INTRODUCTION

How can the plume height be determined and how should the emissions be vertically distributed?

It is not easy to accurately represent the height of BB injection in global models because explicitly calculating all of the small scale processes involved is computationally expensive. For regional models, this is achieved using cloud-resolving models (CRM) that account for the buoyancy generated by the fire as well as fine scale meteorological conditions. The widely used 1-D plume rise parameterization was originally developed by Latham (1994) (based on first law of thermodynamics and vertical motion equations of motion) and embedded in 3-D regional forecast models CATT-BRAMS (e.g., Freitas et al., 2006, 2007), CAM (e.g., Guan et al., 2008) and WRF-Chem (e.g., Grell et al., 2011; Pfister et al., 2011; Sessions et al., 2011).

Using such parameterizations in global models is computationally expensive because it requires small scale information (e.g., diameter of the plume, temperature, density, and velocity of the outgoing gasses) and the integration of differential equations for each fire.

An alternative approach for models is to release the emissions at a fixed height within the PBL (e.g., Colarco et al., 2004; Davison et al., 2004; Forster et al., 2001; Lamarque et al., 2003; Liousse et al., 1996), at an altitude based on an empirical height-fire intensity relationship (e.g., Hodzic et al., 2007; Lavouè et al., 2000; Wang et al., 2006) and to distribute them uniformly through the troposphere (e.g., Cook et al., 2007; Generoso et al., 2007; Matichuk et al., 2007; Pfister et al., 2005, 2006) or predetermined fractions for inside and outside the PBLH (e.g., Generoso et al., 2007; Hyer et al., 2007; Leung et al., 2007; Turquety et al., 2007).

None of these schemes account for the role of local atmospheric conditions at the time of the events or the strong regional and temporal variability of the fires. The emissions usually remain inside the boundary layer. Considering the wide range of observed plume heights, this behavior is not realistic.

The goal is to realistically and efficiently represent the BB injection height in a global climate model (GCM) such as EMAC. In order to achieve this, a vertical distribution function VDF (Section 2.2.2) and four schemes (FH, Section 2.2.3; HD, Section 2.2.4; VEG, Section 2.2.5; FRP based on Sofiev et al. (2012), Section 2.2.6) were developed and implemented in this thesis.

How does the injection height works inside the model?

The injection height is determined through four different methods that increase in level of complexity. Both FH and HD have heights that are regionally and temporally constant, VEG provides heights that vary regionally but that are temporally constant, and FRP generates plumes that vary both regionally and temporally. This variability plays an important role in the amount of emissions that are released above the PBLH and consequently on the mass that can be transported to remote areas. Moreover, the time resolution of the injection plays an important role in transporting the emissions, especially in equatorial Africa, where convection is an important parameter for vertical transport (Williams et al., 2010) and the concentration of species in the UT/LS. The quantification of the regional and temporal variability of the injection heights is addressed in Section 3.1.

The magnitude of the effect of BB emissions may be enhanced when they are released above the PBLH. The relationship between plume height and PBLH is therefore evaluated in Section 3.2.1. Considering the variability of the PBLH and the plume height (for VEG and FRP) different fraction of emissions are released above the PBLH. These fractions are estimated in Section 3.2.2.

What is the performance of the schemes compared to plume height observations?

The plume heights obtained by VEG and FRP schemes are compared to plumes obtained by MISR. The comparison is done with those two schemes because FH and HD schemes produce invariant altitudes. This is evaluated in Section 3.3.

Does the injection height modify the lifetime, transport, and global burden of BB aerosol emissions?

Fire plumes that are injected above the PBLH can be transported on continental (e.g., Colarco et al., 2004; Duck et al., 2007; Wotawa and Trainer, 2000), intercontinental (e.g., Honrath et al., 2004; Real et al., 2007; Val Martin et al., 2006), and even hemispheric (e.g., Damoah et al., 2004; Dirksen et al., 2009) scales. Moreover, even when the emissions are not directly injected above the PBLH, they can be transported to areas of lower PBLH, lofted by pyro-convection, or transported to high altitudes by deep convection. If the emissions are not properly injected, all of these mechanisms

can be underestimated.

The length of time that aerosol emissions remain in the atmosphere (i.e., lifetime), which is determined by the removal mechanisms (dry and wet deposition), limits their transport. Deposition is directly influenced by the height at which particles are released, while the efficiency of removal depends on the size of the particles. The different heights at which the emissions are injected determine the conditions at which the aerosols grow. Passive aerosol tracers (PAT) (Kunkel et al., 2012)) were used to follow the evolution of the BB particles (Section 4.2). Changes to the deposition processes are evaluated in Section 4.3. The lifetime extension was quantified in Section 4.4. The horizontal and vertical distribution of the aerosol emissions is assessed in Section 4.5.

Does modifying the injection height of biomass burning emissions influence the associated aerosol species?

Biomass burning contributes to a certain percent of the total emissions (Table 1.1) and this contribution varies seasonally (Figure 1.2). Biomass burning greatly contributes to the primary aerosol emissions BC and OC. Changes in the distribution of these aerosol species are assessed in Section 5.1. Fires release nitrogen oxides and —to a lesser extent— sulfur dioxide, which are aerosol precursors. Changes in the vertical distribution of these aerosol precursors may influence the conversion of gas to particles. The changes in the distribution of particulate nitrate and particulate sulfate are investigated in sections 5.2.1 and 5.2.2, respectively.

Does modifying the injection height of biomass burning emissions affect the tropospheric chemistry?

The BB emissions influence the tropospheric chemistry by changing the oxidation capacity and ozone formation as well as by enhancing VOC concentrations (Section 1.2). Injecting BB emissions at higher altitudes can intensify the magnitude of these effects, which are quantified in sections 5.3.1, 5.3.3 and 5.3.2, respectively.

Does modifying the injection height of biomass burning emissions affect the atmospheric radiative transfer?

The transfer of atmospheric radiation is directly affected by changes in radiative species and indirectly by modifying cloud properties. The role of aerosols as short lived radia-

tive agents is affected by the changes in lifetime, distribution, and burden (a product of modifying the height of the BB injection) (Section 1.2). Consequently, the aerosol optical depth (AOD) and the single scattering albedo (SSA) are immediately affected by these changes. These are assessed in sections 6.1.1 and 6.1.2, respectively.

The cloud properties may be affected by the efficient production of CCN by BB emissions, which may in turn be enhanced by the injection height. The magnitude of the CCN enhancement is evaluated in Section 6.2.1.

The variations of the clear-sky and all-sky fluxes quantify the radiative effect of the climate modifications attributable to the injection height of the BB emissions. The magnitude of these variations is assessed in Section 6.3.

1.5   Overview and Thesis Structure

This work aims at representing the complex and highly variable process of BB injection height in a computationally efficient manner suitable for a state-of-the-art atmospheric chemistry general circulation model (EMAC) without losing the relevant variability (regional and temporal) that characterize the plume heights. A vertical distribution function (VDF) and four schemes were therefore developed (FH, HD, VEG) and implemented (FRP).

This thesis also aims at quantifying the effects associated with modifying the injection height of BB emissions and evaluating the importance of the injection altitude on several processes. Two sets of simulations (described in Section 2.3) were used to evaluate the effects of modifying the BB injection heights. One set suppresses the feedback (Section 2.1.2.3) from chemistry to dynamics and facilitates the quantification of the effects on trace gasses and aerosols. The other set of simulations includes the feedback to assess the full interaction of the tracers with the environment in order to quantify the complete effect of modifying the injection height of BB on the radiation transfer.

The thesis evaluates the performance of the schemes and quantifies the effects caused by modifying the injection height of the BB.

The first part briefly describes the Atmospheric Chemistry General circulation Model EMAC (where the schemes have been implemented), the schemes and their implementation (Section 2.2), and the performance of the schemes (Chapter 3). Assessing the performance of the injection height schemes entails evaluating their variability (regional

and temporal), the relationship between plume height and PBLH, and the amount of mass that each scheme releases above the PBLH as well as comparing plume heights (determined by VEG and FRP schemes) with MISR observations.

The second part evaluates the effects produced by modifying the BB injection height. This includes quantifying the changes suffered by the BB aerosol emissions (Chapter 4) and assessing the effects on the aerosol tracers and species relevant for tropospheric chemistry (Chapter 5) as well as the radiative effects associated with the changes to the aerosols and other radiative species (Chapter 6). The final remarks, conclusions, and outlook are discussed in Chapter 7.

2

Methodology

This chapter describes the main technical tools as well as the changes made to the model in order to improve BB emissions. This section describes both the model and the method.

2.1 Model Description

This thesis utilized EMAC (ECHAM5/MESSy Atmospheric Chemistry), a numerical chemistry and climate simulation model system composed of an atmospheric core and a series of submodels that describe atmospheric processes and their interactions with oceans, land, and anthropogenic influences. ECHAM5 serves as the meteorological base model, and the Modular Earth Submodel System (MESSy) deals with the atmospheric processes by coupling with base model dynamics or expanding certain chemical processes. ECHAM version 5.03.02 was combined with the 2nd version (Jöckel et al., 2010) of the Modular Earth Submodel System (Jöckel et al., 2005). This section describes both as well as the submodels relevant to this study.

2.1.1 General circulation model: ECHAM5

ECHAM is an atmospheric general circulation model developed at the Max Planck Institute for Meteorology in Hamburg. It is based on the ECMWF (European Centre for Medium-Range Weather Forecasts) forecast model. ECHAM5 is the 5th generation (Roeckner et al., 2003). Version 5.3.02 of ECHAM5 was used in this thesis. Various horizontal and vertical resolutions are available. The horizontal resolutions available

range from T21 to T159; this study used a resolution of T42. The discretization is achieved by the horizontal representation of the truncated series of spherical harmonics for the variables vorticity, divergence, temperature, natural logarithm of the surface pressure, and geo-potential. In ECHAM5, triangular truncations are used at wave numbers corresponding to those of the horizontal resolutions available (21, 31, 42, 63, 85, 106, and 159). The standard vertical resolution has 19 or 31 levels that cover the troposphere and the lower stratosphere up to 10 hPa (30 Km). The pressure in each level depends on the surface pressure. This dependency decreases with height so that the upper levels do not follow the terrain and the lower ones do. The middle-atmosphere version (Giorgetta et al., 2006) has 39 or 90 vertical levels that can reach 0.01 hPa (80 km). For L90, 25 of those levels are located in the stratosphere. The time step length depends on the horizontal and vertical resolution, thereby satisfying the Courant-Friedrich-Levi (CFL) criterion (Courant et al., 1928), which is required for stability.

Table 2.1: ECHAM5 horizontal resolutions and corresponding time steps

Resolution	Number of longitudes	Number of latitudes	Approximate box width [degrees]	Approximate box width at equator [km]	Time step [s]
T21 L19	64	32	5.62	626	2400
T31 L31	96	48	3.75	417	1800
T42 L31	128	64	2.81	313	1200
T63 L31	192	96	1.87	209	720
T85 L31	256	128	1.41	156	480
T106 L31	320	160	1.12	125	360
T159 L31	480	240	0.75	83	180

A semi-implicit centered in time integration (leapfrog scheme) based on the work of Robert et al. (1972) was used. This affords relatively large time steps while preserving stability, which increases the efficiency of the integration. The leapfrog scheme, together with the compliance to the CFL criterion, contributes to the computational stability. However, it is also necessary to apply a time filter (Asselin, 1972) to prevent the growth of spurious computational modes. Tracer advection is treated with a semi-Lagrangian

method introduced by Lin and Rood (1996), which is mass conserving by definition. However, applying this over the vertical grid may produce some inconsistencies between the density field that is calculated through the advection scheme from the winds and the density field that is based on the hybrid sigma-pressure coordinates. A consistent grid must therefore be maintained during a time step, whereby changes in pressure levels caused by advection match the changes caused by the surface pressure at the next time step Jöckel et al. (2001). Temperature, vorticity, divergence, and logarithm of the surface pressure as well as water vapor, cloud water, and cloud ice are calculated using a set of primitive equations for moist atmosphere.

2.1.2   Modular Earth Submodel System: MESSy

The Modular Earth Submodel System (MESSy) is a structured interface composed of a set of submodels that perform the relevant processes and a base model that provides the meteorological conditions (Jöckel et al., 2005). The interface allows the submodels to use and modify meteorological variables provided by the base model, thereby facilitating the feedback the from chemical and physical processes. The submodels perform the relevant processes (e.g. chemical and transport mechanisms), remove trace gases and aerosols, and import and treat emissions. More information about the current status of the submodels is provided by Jöckel et al. (2010) and the MESSy website. The MESSy infrastructure shares information between processes and the base model, while preserving a modularized structure expressed in four layers; two for the base model (BML and BMIL) and two for the submodels (SMIL and SMCL). The base model layer (BML) contains the base model, ECHAM5, for the present study. The base model interface layer (BMIL) manages the information, collects the required data for each individual submodel, and exchanges data between submodels, and imports data. The submodel interface layer (SMIL) manages the procedures for the individual submodels and the communication between the BMIL and the SMCL. The submodel core layer (SMCL) contains the individual codes for each of the submodels and is where each submodel independently performs its main calculations. This study utilized an extended variant of the MESSy Version 2.42. As a mayor part of this work, I have developed four different schemes to inject and distribute BB emissions. This development has been included as a new subroutine in the ONEMIS submodel and allows for choosing between schemes.

2.1.2.1 MESSy Submodels

The relevant processes performed by MESSy are described below. Only certain submodels were used in this thesis (Table 2.2). The complete list of the submodels is available on MESSy website.

Emissions: ONEMIS, OFFEMIS, TNUDGE

The emissions are handled by four submodels: OFFEMIS, ONEMIS, TNUDGE (Kerkweg et al., 2006b), and LNOX (Tost et al., 2007b). The emissions are mainly divided into those that depend on the current state of the model and those that do not. The former are treated in ONEMIS (ONline EMISsions) and the latter in OFFEMIS (OFFline EMISsions). Long lived species are processed with TNUDGE. The LNOX submodel calculates the NO_x emitted during lighting.

The OFFEMIS submodel takes care of the OFFline EMISsions using pre-calculated input files, which were adjusted to the model resolution using NCREGRID (Jöckel, 2006). The resulting emissions are given as a tracer tendency or as a lower boundary condition and are only applicable for surface emission fields. The emissions are divided in three types depending on their purpose.

> **Surface emissions (2D):** For emissions located directly at the bottom of the atmosphere. Input files contain emission fluxes in molecules m^{-2} s^{-1}.

> **Multilayer emissions (Nx2D):** For emissions that occur at defined heights above the surface. The input files contain three-dimensional fields in fluxes (molecules m^{-2} s^{-1}) at the determined heights, which are defined at the import namelist. Anthropogenic emissions are released at six heights. Biomass burning gas emissions are part of this type on the original MESSy version and are directly injected at one layer located at 140 m.

> **Volume emissions (3D):** For vertically distributed emissions that are not located at a predefined height. The input files contain three-dimensional emission rates in molecules m^{-3} s^{-1}. Aircraft and volcanic emissions are part of this emission type.

The ONEMIS submodel calculates the ONline EMISsions i.e., the emissions that need to be recalculated at each time step. This applies to emissions that require further

Table 2.2: MESSy submodels used for the simulations in this thesis

Submodel	Function	Reference	Test stage
AIRSEA	Ocean-atmosphere exchange	Jöckel et al. (2006)	O
AEROPT	Aerosol optical depth	Pozzer et al. (2012)	B
CLOUD	Cloud processes and cover	Jöckel et al. (2006)	B
CONVECT	Convection processes	Tost et al. (2006b, 2010)	B
CVTRANS	Convection transport of tracers	Tost (2006)	B
DDEP	Dry deposition	Kerkweg et al. (2006a)	B
GMXe	Aerosol microphysics and gas/aerosol partitioning	Pringle et al. (2010a) Tost and Pringle (2012)	B
H2O	H2O as a tracer	Jöckel et al. (2006)	O
JVAL	Photolysis rate coefficients	Jöckel et al. (2006)	B
LNOX	NOx lighting production	Tost et al. (2007b)	B
MECCA	Tropospheric and stratospheric chemistry	Sander et al. (2005)	B
MSBM	Heterogeneous reactions	Jöckel et al. (2006)	O
OFFEMIS	Off-line emissions	Kerkweg et al. (2006b)	O
ONEMIS	On-line emissions	Kerkweg et al. (2006b)	B
RAD4ALL	Radiation	Jöckel et al. (2006)	B
SCAV	Wet deposition	Tost et al. (2006a, 2007a)	B
SEDI	Aerosol sedimentation	Kerkweg et al. (2006a)	O
TNUDGE	Tracer nudging	Kerkweg et al. (2006b)	O
TROPOP	Tropopause diagnose and boundary layer height	Jöckel et al. (2006)	O

The last column shows the development stage of each of the submodels. O: Operational; B: Beta; A: Alpha.

calculations before being released in the model i.e., those that are modified by wind speed, soil properties, radiation, and precipitation. In this thesis, BB emissions are vertically distributed up to a height determined by the selected scheme. With this on-line treatment of BB emissions, the regional and vertical distribution as well as the temporal variability can be included, thereby accounting for most of the variability in BB emissions. This submodel has a main division between gas phase and aerosol phase emissions that arise from the difference in emission methods applicable to each one. Gas phase emissions are assigned to the tracers in the same way that OFFEMIS does i.e. as a lower boundary or as a tendency. Aerosol emissions cannot be directly assigned to their corresponding tracers because the aerosol distribution is managed at another submodel (GMXe). Therefore, the aerosol channel objects created in ONEMIS are later modified there.

Submodel TNUDGE creates pseudo emissions for tracers with highly uncertain emission fluxes (e.g., CFCs), tracers with longer lifetimes (e.g.,. CH_4), or tracers relevant only in specific regions (e.g.,. stratospheric O_3). Important BB emissions are treated in this submodel because of their longer lifetime and uncertainty (CH_4 and CO_2), the restrictions inside the model for reproducing all the deposition processes, or the relevance to stratospheric chemistry (N_2O).

The LNOX submodel calculates the NO_x during lighting. Four parameterizations with different approaches are available. The scheme of Price and Rind (1994) was applied in the current study. A C-shape distribution (Pickering et al., 1998)that adjusts to the convective column depth is applied. The total production of lightning–NO_x is on the same scale as the flash frequency and the amount of produced NO_x per single flash (Jöckel et al., 2006).

Planetary boundary layer and tropopause height: TROPOP

The tropopause is determined in the submodel TROPOP using the WMO definition (WMO, 1992). Tropopause height is based on the temperature lapse rate and the potential vorticity (Jöckel et al., 2006). This submodel estimates the planetary boundary layer height, which is essential for the FRP scheme. In the model, the boundary layer is calculated based on the work of Holtslag (1993; 1990) using the bulk Richardson number approach (Seibert et al., 2000; Sørensen et al., 1996; Stull, 1988). The PBLH is set by the height at which the bulk Richardson number reaches a determined value

(critical Richardson number); for stable conditions, the considered value is 0.33 (Wetzel, 1982). For convective conditions, the value is 0.22 (Vogelezang and Holtslag, 1996). For the simulations in this study, the PBLH varies between 29 and 6590 m, with an average of 590 m.

Aerosol microphysics and gas/aerosol partitioning: GMXe

Global Modal-aerosol eXtension (GMXe) (Pozzer et al., 2012; Pringle et al., 2010a,b; Tost and Pringle, 2012) performs the aerosol processes (nucleation, coagulation, transfer of coated hydrophobic aerosols to hydrophilic aerosols, condensation and gas aerosol partitioning) in two main parts i.e., microphysics and gas/aerosol partitioning.

The first one manages the interaction of seven log-normal modes with an extended version of the M7 modal aerosol scheme (Stier et al., 2005; Vignati et al., 2004; Wilson et al., 2001). There are four sizes: nucleation, Aitken, accumulation, and coarse. Each has a fixed standard deviation (Table 2.3). Soluble modes comprise all four sizes, while insoluble only comprise three because the nucleation mode only consists of hydrophilic sulfate. Each mode i is defined by the number concentration N_i, the number mean radius $\bar{r}_i$, and the geometric standard deviation σ_i. Consequently, the distribution of aerosol size is determined by superposing the seven log-normal modes:

$$n(\ln r) = \sum_{i=1}^{7} \frac{N_i}{\sqrt{2\pi} \ln \sigma_i} \exp\left(-\frac{(\ln r - \ln \bar{r}_i)^2}{2 \ln^2 \sigma_i}\right) \quad (2.1)$$

Table 2.3: Aerosol modes names, mean sizes, and standard deviations for hydrophobic and hydrophilic modes.

	Mean size [nm]	Standard deviation	Hydrophilic mode	number	Hydrophobic mode	number
Nucleation	1	1.59	ns	1	–	–
Aitken	20	1.59	ks	2	ki	5
Accumulation	230	1.59	as	3	ai	6
Coarse	1580	2.00	cs	4	ci	7

2. METHODOLOGY

The aerosol number and mass are calculated prognostically. The species explicitly treated by GMXe are: nitrate (NO_3^-), ammonium (NH_4^+), sulfate (SO_4^{2-}), sodium (Na^+), chlorine (Cl^-), and sulfuric acid (HSO_4^-) as well as dust, black carbon (BC) and organic carbon (OC). Black carbon is emitted in the aitken insoluble mode. Organic carbon is also emitted in aitken mode, but is divided into soluble and insoluble (65% Aitken soluble and 35% Aitken insoluble). The nucleation of new particles is based on the approach of Vehkamäki et al. (2002) and calculated as a function of temperature, relative humidity, and sulfuric acid (H_2SO_4) concentration. Coagulation is performed according to Vignati et al. (2004), and the coagulation coefficients are based on Brownian motion (Fuchs, 1964). This process stipulates the rules for particles when moving from smaller to larger sizes and from hydrophobic to hydrophilic modes i.e., when two particles of different sizes coagulate, the resulting particle will have the size of the larger particle. When insoluble and soluble particles coagulate, the resulting particle will be hydrophilic if there is sufficient hydrophilic material for coating via coagulation.

The second part deals with the thermodynamic treatment. The gas/aerosol partitioning of the semi volatile inorganic species is done through ISORROPIA-II (Fountoukis and Nenes, 2007), which is an inorganic equilibrium model able to conduct the interaction of K^+, Ca^{2+}, Mg^{2+}, NH_4^+, Na^+, SO_4^{2-}, NO_3^-, Cl^-, and H_2O. The gas-aerosol-solid equilibrium state is solved by considering the chemical potential of species (Nenes et al., 1998, 1999) and by choosing specific compositional regimes that minimize the number of equations and iterations required. To reduce the computational costs, pre-calculated reference lookup tables are used to determine activity coefficients (Pozzer et al., 2012; Pringle et al., 2010b). For inorganic species and sub-saturated conditions (RH < 95%), water uptake is also calculated in ISORROPIA-II. The transfer between modes is calculated twice; once after coagulation and once after gas/aerosol partitioning. In the latter, this is done when soluble material condensates onto insoluble particles at the partition. The resulting amount of insoluble particles that are transferred to the soluble modes corresponds to the fraction able to receive five monolayers of hydrophilic material (Stier et al., 2005; Vignati et al., 2004). This aerosol ageing allows organic and BC to evolve into the hydrophilic modes. Because of aerosol processes such as coagulation and condensation, the final BB emissions are only given in four modes (ks, as, cs, ki). During fires, particle formation is a combination of condensation (NH_4^+,

SO_4^{2-}, NO_3^-) and —to a lesser extent— primary particles (BC and OC). Hence, most of the particle mass is in the accumulation mode.

Aerosol optical properties: AEROPT

The AEROPT submodel calculates the AERosol OPTical properties (e.g.,. AOD, single scattering albedo, asymmetry factor) based on pre-calculated three-dimensional lookup-tables that combine the wavelength and information about aerosol size. The scheme is based on the work of Lauer et al. (2007). Lookup-tables for the extinction coefficient σ_{sw}, single scattering albedo ω_{sw}, and asymmetry factor γ_{sw} for short wave (sw), as well as the extinction coefficient σ_{lw} for long wave (lw) are calculated using the predefined log-normal modes (mode width and mean radius). These lookup tables are created using LIBRADTRAN (Mayer and Kylling, 2005) for different aerosol types. AEROPT considers DUST, SS, BC, OC, aerosol water (H_2O) and WASO (water soluble compounds, e.g.,. NH_4^+, SO_4^{2-}, HSO_4^-, and NO_3^-). The refractive indexes for these compounds are taken from several databases e.g.,. HITRAN 2004 (Pozzer et al., 2012). The wavelength refractive index for each of these species as well as the Mie size parameter is used in a set of Mie calculations that yields a three-dimensional lookup table. For each mode of the aerosol distribution, the volume-weighted mean complex refractive index is determined during the simulation. During the model simulation, the Mie size parameter for each wavelength band is calculated based on the mean radius of the mode. Finally, the lookup tables for the extinction coefficients, single scattering albedo, and asymmetry factor are obtained using the required parameters (Mie size parameter, complex refractive index, and mode mean radius). These coefficients are determined for 16 predefined bands in the long wavelength and 16 bands in the short wave spectrum. Because these predefined wavelengths may not match the ones used to calculate the radiation of the base model (ECHAM5), a map is generated between them using weighted interpolation. This method is also applied to determine the values of diagnostic wavelengths e.g., 550 nm. The aerosol optical depth (AOD) is first calculated per mode using the extinction coefficient for a single particle. It is then multiplied by the number of particles per grid cell in each layer. The AOD per layer is the sum of all the modes in each layer. Its vertical integration provides the total atmospheric AOD per grid cell (Pozzer et al., 2012).

2. METHODOLOGY

Radiation: RAD4ALL

Radiative processes are performed in the RAD4ALL submodel, which is an implementation of the ECHAM5 radiation code in accordance with the MESSy standard (Jöckel et al., 2006). The required input parameters can come from either uniform volume mixing ratios, external climatologies, or prognostic variables. In this thesis, RAD4ALL was coupled with prognostic cloud cover, cloud water, and cloud ice as well as specific humidity. Depending on the experimental setup, trace gases were obtained as either uniform mixing ratios (e.g.,. CO_2, CH_4, N_2O, CFC11 and CFC12), external climatologies (O_3), or prognostic variables. Depending on the experimental setup, the aerosols were either obtained from internal climatology (Tanre et al., 1984) or by AEROPT.

Cloud processes: CLOUD

Cloud cover and microphysics, including precipitation, are calculated in the CLOUD submodel, which is a modularized version of the original ECHAM5 cloud scheme code (Roeckner et al., 2003). Microphysics is based on the work of Lohmann and Roeckner (1996) and assumes cloud water and cloud ice as prognostic variables. Therefore, prognostic equations are provided for all aqueous phases. The microphysics scheme considers phase changes between the water components, precipitation processes (autoconversion, accretion, aggregation), the evaporation of rain, the melting of snow, and the sedimentation of ice. The cloud cover parameterization (Tompkins, 2002) is statistically based i.e., the scheme uses a probability density function (PDF), a beta function that describes the total water content (water vapor, cloud water, and cloud ice mixing ratios). The PDF changes according to the prognostic water variables determined in the microphysics section. Other processes such as deep convection, large-scale condensation, and turbulence also contribute to the fluctuations in the total water content. Changes in the total water content therefore modify the high-order moments of the PDF. Finally, the cloud fraction can be diagnosed by integrating the supersaturated part of the PDF.

Cloud convection: CONVECT

Convection is managed by the CONVECT submodel, which allows for several convective schemes (Tost, 2006; Tost et al., 2006b). The default, which was used in this thesis, is Tiedtke (1989) with Nordeng (1994) modifications. The scheme is based on

the mass-flux approach (Arakawa and Schubert, 1974), which considers convection as an ensemble of various sized clouds (spectral cloud ensemble). It modifies the equations for the large-scale budget of the environmental dry static energy as well as the specific humidity. However, the cloud ensemble is not explicitly resolved; it is represented as a bulk (Yanai et al., 1973). The scheme includes deep convection, shallow convection, and midlevel convection, each with its corresponding entrainment and detrainment parameterization. Convection is triggered by a positive temperature difference (0.5 K) between an air parcel and the surroundings at the level of free convection (LFC). The Nordeng modification adjusts the closure under the assumption that the updraft mass flux depends on the convective available potential energy (CAPE). It uses a relaxation time during which the scheme should remove instability.

Convective tracer transport: CVTRANS

The submodel CVTRANS (Tost et al., 2010) calculates the ConVective TRANSport of tracers using a bulk approach based on that of Lawrence and Rasch (2005). The vertical transport in convective columns is calculated by considering tracer mass fluxes, updraft, and downdraft as well as the entrainment and detrainment of the tracer mass fluxes in each layer. Substantial detrainment occurs only in the upper troposphere and in the lowest model layer. The scheme is monotonic, positive definite, and mass conserving. Details about the submodel can be found in Tost (2006).

Deposition processes

Trace gases and aerosols are removed from the atmosphere by deposition processes that affect the distribution of the global burden and the lifetime of the species. Both wet and dry deposition are considered in three submodels: SCAV (Tost et al., 2006a), DDEP, and SEDI (Kerkweg et al., 2006a). Dry deposition is separated in two submodels, DDEP and SEDI, which represent different processes. DDEP considers only the deposition processes associated with surface/air exchange and is implemented in the lowest model layer, while SEDI represents the effect of gravity and acts over the whole column. It is more relevant for aerosols because they have larger mass than gases.

Dry deposition DDEP

This submodel takes into consideration the removal of gases and aerosols from the

atmosphere by uptake or by turbulent transfer onto the surface of the earth in the absence of clouds and precipitation. The sink process is based on the work of Ganzeveld and Lelieveld (1995) for gases and on the work of Stier et al. (2005) for aerosols; both use the big leaf approach (Ganzeveld et al., 1998; Hicks et al., 1987). The deposition velocity v_d for gas species (X) depends on three resistances: R_a, aerodynamic resistance (e.g., roughness length, friction velocity); R_s, surface resistance (e.g., roughness length, friction velocity); and R_{qbr}, quasi-laminar boundary layer resistance (roughness length).

$$v_d(X) = \frac{1}{R_a + R_{qbr}(X) + R_s(X)} \qquad (2.2)$$

The resistance depends on the type of surface: water, snow/ice, bare soil, vegetation, and wet skin (i.e., vegetation or wet bare soil). The deposition velocities are calculated for land or for ocean depending on which one occupies most of the cell. The deposition velocity in the whole grid cell is the composition of all the deposition velocities of the surfaces present in either the land or ocean grid cell. This velocity is calculated for O_3, NO, NO_2, HNO_3, and SO_2. For different gases, the velocity is interpolated from O_3 and SO_2 depending on their solubility and reactivity. For aerosols, the deposition velocity is calculated in a similar manner. For the surface resistance R_s only three surface types are considered: bare soil/snow, vegetation, and water. The deposition velocity for each surface type depends on the aerodynamic resistance, R_a, and a deposition velocity that contains the aerosol information (particle radius, particle density, and standard deviation of the mode radius). The overall deposition velocity is the composition of the three individual surface type deposition velocities and the fractions of snow, bare soil, water, vegetation, wet skin, and ice present in the cell. Finally, the deposition flux is determined by multiplying the concentration of the species at the surface with the deposition velocity. More information about the implementation can be found in Kerkweg et al. (2006a).

$$F_{ddep} = c(X)v_d(X) \qquad (2.3)$$

Sedimentation: SEDI

The SEDI submodel represents the particle descent caused by gravity through the whole column; it therefore only applies to aerosol particles. This is an important sink process for large aerosol particles because they have more mass than gases, which

have a negligible mass. This process therefore has a marked effect on the lifetime and burden distribution of aerosols. It is based on the aerosol sedimentation theory. The particle descent is represented by an approximation of the terminal velocity reached by the particles when falling through the atmospheric fluid. The terminal sedimentation velocity v_t is based on the Stokes velocity v_{Stokes} and modified by the Cunningham slip-flow factor f_{Csf} and the Slinn factor f_{Slinn}.

$$v_t = v_{Stokes}\, f_{Csf}\, f_{Slinn} \tag{2.4}$$

The Stokes velocity depends on the density and radius per aerosol mode. The Cunningham slip-flow factor corrects for the aerodynamic differences generated by the spherical assumption and depends on the aerosol radius per mode. The Slinn factor accounts for the use of lognormal modes; because the particle radius varies over a wide range, the sedimentation velocity of all particles of a lognormal mode is greater than the velocity for a particle with the mean radius. The Slinn factor thus uses the standard deviation of the radius per mode to correct for this difference. Further details are provided by Kerkweg et al. (2006a).

Wet deposition and aqueous phase chemistry: SCAV

Liquid phase chemistry inside clouds and precipitation as well as wet deposition of trace gases and aerosol particles is performed in the SCAV submodel. This sink process markedly affects the global distribution of aerosol particles, especially the smaller ones that are not efficiently removed by sedimentation. Two removal processes are distinguished: nucleation scavenging (NS) and impaction scavenging (IS). The former refers to the removal during nucleation and growth of cloud droplets. The latter refers to the uptake of gases and aerosols by droplets while falling. At the top layer, only NS is considered because nothing falls from the upper layer. In the layers below, the precipitation flux from the upper layer generates IS. In each layer, IS is calculated first followed by NS. In the absence of clouds, the NS in the respective layer is neglected. Only the fraction of the cell covered by clouds contributes to the scavenging.

Gas phase scavenging can be performed by either a classical approach with fixed scavenging coefficients or a system of coupled Ordinary Differential Equations (ODE) that represents the processes. In this thesis, the latter is used because of its ability to resolve feedback mechanisms between multi-phase chemistry and transport processes. Because

2. METHODOLOGY

it facilitates changes to the chemical reaction system, the scheme uses the numerical equation solver KPP (Kinetic PreProcessor: Damian et al., 2002; Sandu and Sander, 2006). The model time step must be subdivided in order to accurately represent the required chemical reactions. This is done with a Rosenbrock solver (Sandu et al., 1997) applied to the ODE system. A third order solver was used in this thesis.

The uptake and release of gases by droplets follows Henrys equilibrium law with a correction for gas phase diffusion limitation and the accommodation coefficients (Tost et al., 2006a).

The liquid phase reaction set is described in Sander et al. (2005) and Ervens et al. (2003). Temperature, pressure, and liquid water content are used to calculate the reaction rates at each model time step and in each vertical layer. The complete tropospheric column is considered at each time step because the gas uptake is limited by the amount dissolved in the precipitation.

Like the gas phase treatment, the scavenging of aerosols uses two approaches for determining the scavenging coefficients (i.e., fixed and online). Nucleation scavenging follows the Brownian motion (Seinfeld and Pandis, 2006) and an empiric function that parameterizes the nucleation and growth of cloud droplets. Brownian motion is the dominant process for particles smaller than 0.1 μm, while nucleation and the growth of cloud droplets become relevant for larger particles. A semi-empirical formula from Pruppacher and Klett (2000) is used to determine the nucleation scavenging coefficient for Brownian motion, while the empiric function only refers to the uptake of aerosols by cloud droplets.

Impaction scavenging depends on three processes i.e., Brownian motion, interception, and impaction. The first one dominates the scavenging of smaller particles, while the latter ones influence IS for larger particles. Scavenging by hydrometeors uses a function for collection efficiency Seinfeld and Pandis (2006). The impaction scavenging coefficient is determined using the effective precipitation flux, the radius of rain droplets, and the collision efficiency. Finally, NS and IS coefficients are applied to each aerosol species. After NS and IS are calculated, only the fraction of chemically active species scavenged by the rain flux from the upper layer are chemically integrated. This chemically active fraction is subtracted from the total wet deposition flux prior to chemical integration. The concentration of the resulting species is included in the flux for the layer below. The starting liquid phase concentration in each layer is determined by

the chemical composition of the rain flux falling from the upper layer; the gas phase concentration depends on the ambient values in that particular layer. The fraction of species that falls in the lower layer (i.e., the scavenged fraction) is determined from the ratio between the formation of precipitation and the total cloud water content in each time step. Finally, the chemical composition of the rain is defined by the composition of the rain flux coming from the lowest model layer. The resulting chemical composition and pH of the rain may affect the ground. This submodel is described in detail in Tost et al. (2006a).

Air-Sea exchange: AIRSEA

This submodel calculates the exchange of tracers between the atmosphere and the ocean. Because it focuses on organic compounds, it is necessary for representing a reasonable global budget of tracers such as methanol and acetone. The AIRSEA submodel uses a two-layer approach to simulate the bi-directional exchange of VOC and their oxidation products (Jöckel et al., 2006). A detailed description of the submodel can be found in Pozzer et al. (2006).

Water tracer and feedback: H2O

The feedback between the specific humidity of the base model and the tendency of the H_2O tracer is controlled in the H2O submodel, which defines gaseous H_2O as a tracer and provides its initialization in stratosphere and mesosphere from satellite data. The feedback with specific humidity of the base model is controlled via synchronization. At each time step, the value and tendency of the H_2O tracer is replaced by the value and tendency of the specific humidity in the base model. The new H_2O tracer tendency is determined in MECCA submodel as a result of online chemical processes; in the H2O submodel, as a specific climatology, or the sum of both. Finally, this H_2O tracer tendency replaces the one from the specific humidity (Deckert et al., 2011). More details can be found in Jöckel et al. (2006).

Gas phase chemistry: MECCA

The chemical mechanism is managed in the MECCA (Module Efficiently Calculating the Chemistry of the Atmosphere) submodel (Sander et al., 2005, 2011). The MECCA submodel includes the standards O_3, CH_4, HO_x, and NO as well as non-methane hy-

drocarbons (NMHC). Isoprene chemistry is calculated using the Mainz Isoprene Mechanism(MIM: Pöschl et al., 2000). For the stratosphere, chlorine (Steil et al., 1999) and bromine (Meilinger, 2000) reactions are considered. In this thesis, 129 gaseous species were considered for a total of 299 equations. At each interval, the species concentration is determined by solving the set of stiff ODE. The KPP solver (Sandu and Sander, 2006) is used to integrate this set of stiff differential equations. Appropriately representing the chemical reactions requires smaller time steps. The 3rd order Rosenbrock solver is therefore used. Heterogeneous reactions are determined with the MSBM submodel, while photolysis rates are set by the JVAL submodel. Further details of the MECCA submodel and a description of the improvements developed for MESSy version 2 can be found in Jöckel et al. (2006, 2010). Organic species reactions are evaluated in Pozzer et al. (2007).

Stratospheric heterogeneous reactions: MSBM

The heterogeneous reaction rates on polar stratospheric cloud (PSC) and on stratospheric background aerosol are calculated in the Multiphase Stratospheric Box Model (MSBM). For a better consistency in the stratosphere, the MSBM submodel combines (and replaces) the PSC (Buchholz, 2005; Kirner, 2008) and HETCHEM (Jöckel et al., 2006) submodels. Heterogeneous reaction rates on nitric acid trihydrate (NAT) and reaction on sulfate aerosol are simulated in the MSBM submodel. The gas-liquid-ice-phase partitioning of H_2O in the stratosphere is performed in MSBM submodel Jöckel et al. (2006).

Photolysis rate coefficients: JVAL

The photolysis rate coefficients (J-values) are calculated on-line according to the submodel of Landgraf and Crutzen (1998), which uses cloud water and ice content as well as cloudiness determined by the base model. For aerosol, ozone, and greenhouse gasses, the submodel can use prognostic or climatological values. More details are available in Jöckel et al. (2006).

2.1.2.2 Data Assimilation

The assimilation of observational or reanalysis data, along with prescribed sea surface temperatures (SSTs), is used to simulate realistic synoptic conditions in the model.

Reanalysis data from the ECMWF is therefore assimilated. The base model (ECHAM5) is forced towards realistic meteorological conditions by adding an artificial tendency to the model equations of the four prognostic variables: temperature, vorticity, divergence, and surface pressure. This process is called nudging and entails adding a Newtonian relaxation term $\partial X_{mod}/\partial t$ to each variable in each layer. The non-physical relaxation term is determined by a relaxation coefficient G that multiplies the difference between the observational value and the model calculated value of variable X.

$$\frac{\partial X_{mod}}{\partial t} = G \left(X_{obs} - X_{mod} \right) \tag{2.5}$$

Because the relaxation term is an artificial contribution, G has to be weak enough so as not to disturb the consistency of the model physics but strong enough to push the model towards the assimilated data. Therefore, G represents the strength of the nudging. The magnitude of G has to be comparable to the Coriolis parameter and must satisfy the numerical stability $G \leq 1/\Delta t$. The typical values are at a magnitude of 10^{-5} s^{-1}. The solution of the relaxation term provides the value of the desired model state of variable X.

$$X_{mod} = X_{obs} + \left(X_i - X_{obs} \right) e^{-Gt} \tag{2.6}$$

X_i is the initial value of the modeled variable X at the start of the nudging period. The model state approaches the observed state exponentially with and e-folding time to $T_G = 1/G$. This four-dimensional assimilation technique has been implemented in ECHAM (Jeuken et al., 1996; van Aalst et al., 2004) and widely used in EMAC (Jöckel et al., 2006; Lelieveld et al., 2007; Pozzer et al., 2012). In this thesis, three levels at the surface are left free of nudging in order to avoid inconsistencies in the boundary layer representations of the model and the ECMWF data. Stratospheric dynamics are also left free. Levels 7 to 28 were weakly nudged. This data assimilation more consistently compares the model and observations. Because the nudging is weak, the model approximates the observed meteorology but does not exactly reproduce it. However, despite the large grid boxes, the model results approximate well enough to be comparable to observations in point to point basis. The use of reanalysis data instead of real observations only becomes important when the model and the observed meteorology are compared at regional scales.

2. METHODOLOGY

2.1.2.3   Feedback Between Chemistry and Dynamics

No Feedback

For certain analyses, it is not enough to nudge the model towards real meteorology because the parameterizations and small-scale dynamical processes are unaffected by this nudging. The magnitude of some changes in the emissions can be hard to identify because of the natural variability of the system. Because one of the goals of this study was to assess the differences when a specific injection scheme is used, the noise must be reduced. A binary identical simulation is therefore required to quantify the changes generated by different simulations.

The Quasi Chemistry-Transport Mode (QCTM: Deckert et al., 2011)generates identical binary simulations for meteorological state variables by suppressing the feedback between chemistry and dynamics. Chemical perturbations will thus not affect meteorological patterns. This is achieved using offline mixing ratios of radiative species that enter the radiation scheme and nitric acid in the polar stratospheric clouds as well as by restricting the chemical updates in the H_2O tracer to the product of the offline methane oxidation. If the feedback is allowed, despite the identical initialization, the meteorological state of the two simulations will diverge after a couple of time steps as a result of the inherent chaos in the system. Spatiotemporal transport and variability are identical for two QCTM simulations if they are initialized with the same data. The QCTM setup is obtained by choosing a uniform offline volume mixing ratio of species in the namelists of the MSBM and RAD4ALL submodels. This involves using the climatological tendency for the H_2O tracer in the H2O submodel as well as the original ECHAM5 cloud parameterization scheme in the CLOUD submodel.

Feedback

The QCTM setup allows quantification of the changes caused by the transport differences emerging from the height at which emissions are injected. In contrast, to assess the effects of the differences in the injection height of the emissions, it is necessary to account for the feedback of chemistry on dynamics. Therefore, another set of simulations without nudging and with feedback were performed. The feedback of chemistry over dynamics is achieved by using prognostic values for the radiative species and chemically induced changes in the H_2O tracer tendency as well as a cloud parameterization that includes the effect of the prognostic variables. The chemical effects over the H_2O tracer

come from the MECCA submodel in which a tendency is calculated and from PSC formation in the MSBM submodel where the H_2O tracer is modified by the HNO_3 mixing ratio. The H_2O tracer affects dynamics through the feedback generated when the calculated tracer tendency modifies the water vapor determined in the ECHAM5 base model. Water vapor is an important tracer that influences radiation, cloud physics, and atmospheric chemistry as a source of hydroxyl-radical (OH·) or as a product of stratospheric CH_4 degradation. The feedback in radiation is managed at the RAD4ALL submodel namelist where the radiative species CO_2, CH_4, O_3, N_2O, CFC-11 and CFC-12 are taken from prognostic calculations instead of from offline mixing ratios. The direct aerosol effect is included by using the aerosol properties of AEROPT. Instead of the standard cloud scheme from ECHAM5, the clouds are parameterized by selecting CDNC/ICNC from Lohmann et al. (2010). This includes the indirect aerosol effect.

2.2 Description of the Method

The BB emissions must be treated on-line because of the high variability of these emissions and the need to inject and distribute them at suitable heights i.e., at heights that represent the processes involved in the injection of emissions without being too expensive to calculate in global models. The objective is to create a three-dimensional emission field that represents the unsteadiness of the emissions. This goal is achieved by introducing a new emission type to the ONEMIS submodel. This new emission type creates the three-dimensional field by vertically distributing the original two-dimensional field. I have therefore developed a vertical distribution function (VDF) and four schemes that determine the injection height under different approaches. Fixed Height (FH), Heat Disturbance (HD), Vegetation (VEG), and Fire Radiative Power (FRP) are the available plume height schemes. The implementation is allocated in the two ONEMIS model code layers and the namelist (Figure 2.1). The injection height scheme and the emissions to be distributed are selected at the namelist (ONEMIS NML). At the SMIL, the required input parameters (e.g., PBLH) and input data (i.e. frp, land cover, and emissions) are obtained by accessing their channel objects. The output channel objects for the emissions generated are created in the SMIL where the core-layer subroutine is also called, and the vertical distribution is executed using the VDF determined in the SMCL. The injection height is calculated in the SMCL according to the selected scheme. This injection height is then used to adjust the VDF.

This section explains how the injection height is determined by each scheme and how the emissions are distributed using the VDF. The emission field and the required data for the individual schemes are also described. The year 2006 was chosen because of the temporal intersection of the observations. MISR plume observations for five regions (Africa, Indonesia, North America, Siberia, South America, and Southern Asia) are available under the scope of the plume data project. The CALIPSO observations started in 2006. The MODIS observations were also available for this year. Neutral El Niño conditions prevailed from May to mid-September, when a moderate El Niño was developed from the end of one year into the next. An El Niño event contributed to the dry conditions over Indonesia (Worden et al., 2013), which led to the strong peatland fire emissions (Figures 2.3 and 2.2).
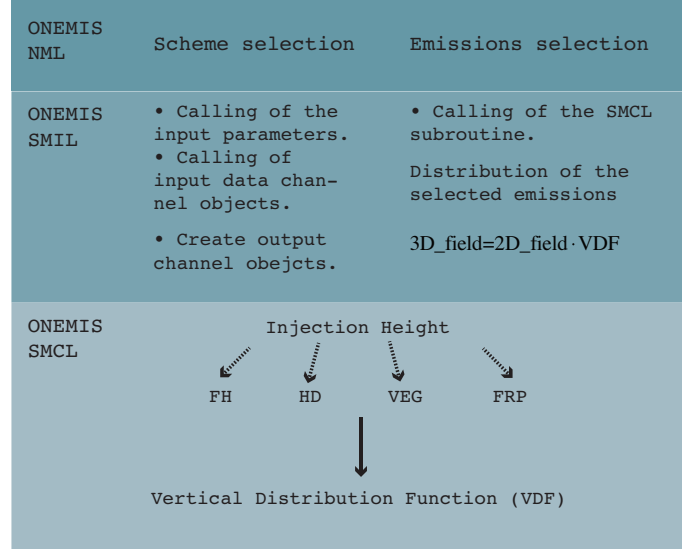
Figure 2.1: Visualization of the implemented changes, their location and function.

2.2.1 Biomass Burning Emissions Database: GFED

Biomass burning emission fields are provided by the version 3 of the Global Fire Emission Database (GFED3). The dataset consists of monthly emissions from 1997 to 2009 with a resolution of 0.5°×0.5°. For this study, only the 2006 emissions were used.

The emissions are estimated by the CASA-GFED3 model, based on the Carnegie Ames Stanford Approach (CASA) biogeochemical model (Field et al., 1995; Potter et al., 1993; Randerson et al., 1996). The CASA-GFED3 model generates monthly BB emissions and burned area in a grid of 0.5°×0.5° (van der Werf et al., 2010). The CASA model calculates the monthly net primary productivity (NPP) based on light-use efficiency ε (modified by temperature T and moisture P). The satellite-derived fraction of the available photosynthetically active radiation $fAPAR$ absorbed by plants and solar incoming radiationn PAR are used as an input.

$$NPP = fAPAR \times PAR \times \varepsilon_{(T,P)} \tag{2.7}$$

The NPP is delivered to leaves and roots for herbaceous vegetation as well as stems and roots for woody vegetation. If the mean annual precipitation is high, the NPP is delivered to the leaves or stems. In years with low mean annual precipitation, the NPP is delivered to the roots. The carbon content is determined by CASA from the carbon output of the NPP as well as carbon losses from heterotrophic respiration, fires,

herbivore consumption, and fuel wood collection (van der Werf et al., 2003), thereby yielding a value for the available fuel.

Once the amount of carbon is determined at each grid, the carbon emission flux is calculated based on burned area from MODIS (Giglio et al., 2010), tree mortality, and the combustion completeness of the available fuel.

Finally, the emissions are determined from the calculated carbon flux and the emission factors that translate the carbon loss into a particular trace gas or aerosol. The emissions from six different sources are differentiated and provided. Emission factors (EF) from Andreae and Merlet (2001) were applied to tropical forest, grasslands and savannas, extra-tropical forest, and agricultural residues (Table 2.4). The EF of woodland is an average of the EF for grasslands and savanna and the EF of deforestation. Peat fire EF is based on Christian et al. (2003).

The GFED3 provides emission fields for carbon (C), dry matter (DM), CO_2, CO, CH_4, NMHC, H_2, NO_x, N_2O, $PM_{2.5}$, total particulate matter (TPM), SO_2, OC, and BC. In this thesis the following emissions are used: CO, NO, SO_2, OC, BC and NMHC. The NMHC included are: ethene (C_2H_4), ethane (C_2H_6), propene (C_3H_6), propane (C_3H_8), n-butane (NC_4H_{10}), acetaldehyde (CH_3CHO), acetone (CH_3COCH_3), acetic acid (CH_3CO_2H), methanol (CH_3OH), formaldehyde (HCHO), formic acid (HCOOH) and methyl ethyl ketone (MEK). Some important BB emissions (CO_2, CH_4, H_2, and N_2O)are not explicitly treated in the model. These are, however, treated in the TNUDGE submodel because of the longer lifetimes, uncertainties, limitations in the emissions, and sink processes. Because the ocean is not fully coupled, an important part of the CO_2 sink process may not be captured. For CH_4, the longer lifetime and emissions uncertainty place its treatment at TNUDGE. This submodel also includes H_2 because of its sink at soils (Conrad and Seiler, 1985) as well as N_2O because of its longer lifetime and emissions from tropical soils and oceans. Because these greenhouse gases influence the radiative temperature tendencies in RAD4ALL, a consistent mixing ratio is required.

Savanna and grassland along with deforestation fires are the major contributors to BB emissions (Figure 2.2). However, the emission rate for each of the species clearly varies for the different fire types (Figure 2.3). The contribution of OC from extra-tropical forest is thus comparable to Savanna and Grassland emissions in 2006.

Table 2.4: Emission factors per fire type.

	Deforestation	Savanna and Grassland	Woodland	Forest	Agricultural waste	Peatland
CO	1626	1646	1636	1572	1452	1703
NO	2.26	2.12	2.19	3.41	2.29	2.26
SO$_2$	0.71	0.37	0.54	1.00	0.40	0.71
OC	4.30	3.21	3.76	9.14	3.71	4.30
BC	0.57	0.46	0.52	0.56	0.48	0.57
NMHC	7.00	3.41	5.21	5.69	11.19	7.00

Compounds used in this thesis in g specie per kg of dry matter burned.
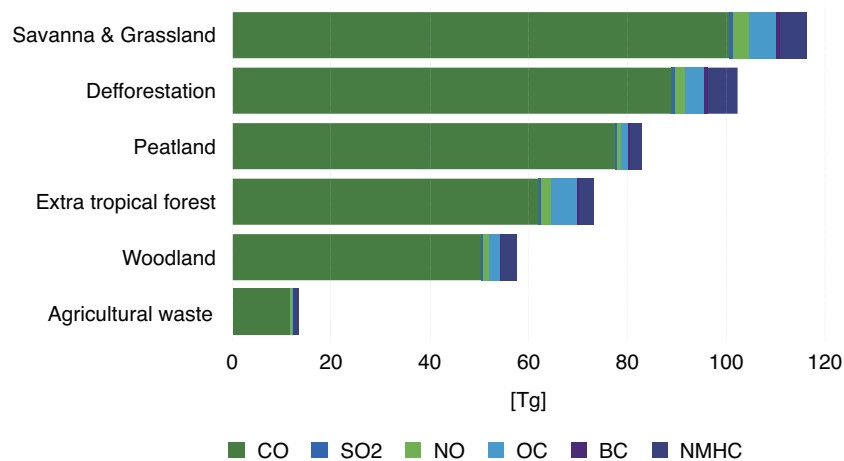
Figure 2.2: The 2006 emissions used in this thesis (in Tg per year). Emissions are separated by the six fire types distinguished on GFED3.

Deforestation fires are an important contributor of 2006 BB emissions (Figures 2.2 and 2.3) and are highly correlated to the drought driven by El Niño conditions, especially in Equatorial Asia for the moderate El Niño conditions (van der Werf et al., 2008a,b; Worden et al., 2013) from September 2006 to the following year. Because of these conditions, choosing 2006 for the simulations allows for substantially more peatland emissions than in any other year. Because the occurrence of wildfires depends on the dryness of the vegetation determined by atmospheric conditions, the BB emissions have a large inter-annual variability (Figure 2.4).
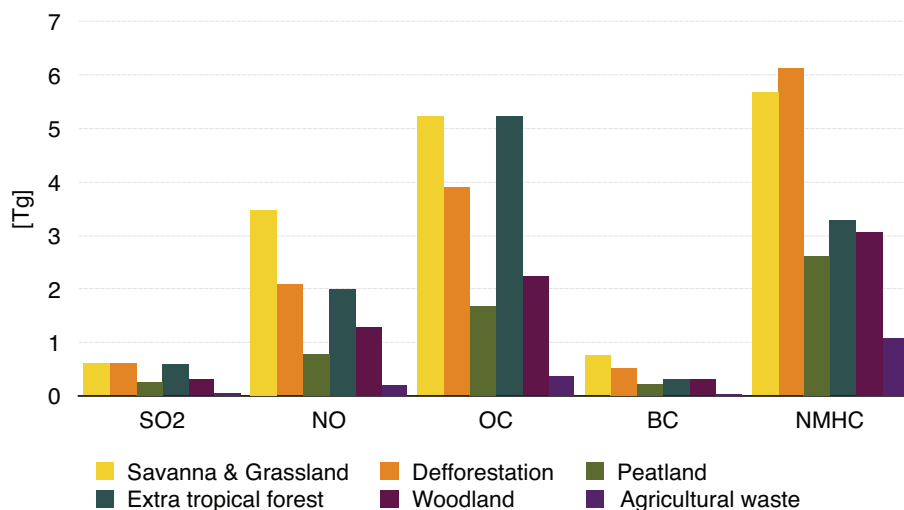
Figure 2.3: Emissions used in this thesis (without CO, in Tg per year) separated by fire type.
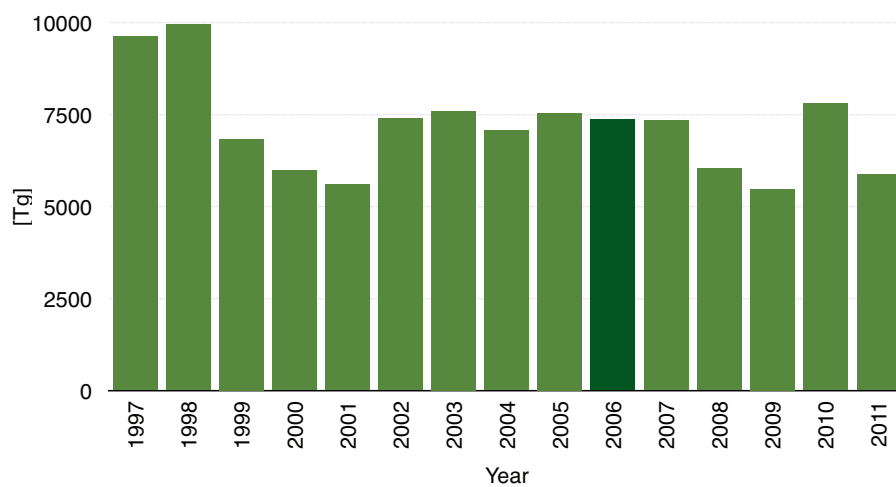
Figure 2.4: Total BB emissions in Tg per year from 1997 to 2011.

2.2.2 Vertical Distribution Function: VDF

The vertical distribution function (VDF) assigns the estimated fractions of the compound to the corresponding vertical levels. The distribution function automatically adjusts to the vertical resolution of the model and to the provided plume injection height (determined by the selected scheme). The shape generated by the function (Figure 2.5) is based on the idea that the emissions are quickly injected into the top of the

plume, while a fraction of the emissions remains at the flame front. This results in the injection of ⅓ of the total emissions near the surface (production region), ⅙ on the middle (transport region) and ½ on the top level (injection zone).
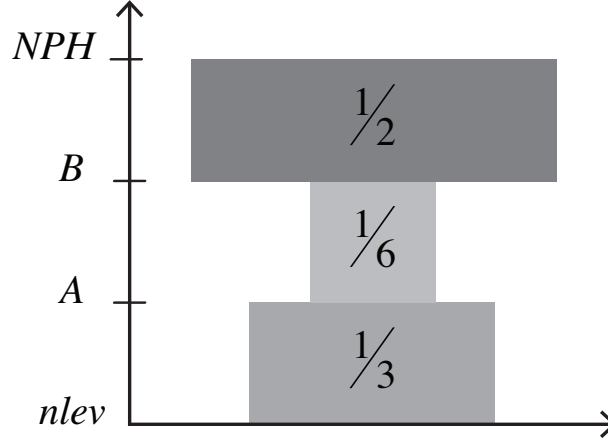
Figure 2.5: Vertical Distribution Function (VDF) shape.

In order to generate these fractions, the temporal function, F_t (Equation 2.8), has a value of 0 at all the levels above the top of the plume and three different values (3,1, and 2) for each zone. If different vertical profiles are required, the function can be easily modified. If desired, this can facilitate the representation of different vertical profiles according to stages of the fire.

$$F_t(n) = \begin{cases} 0 & 1 \leq n < NPH \\ 3 & \text{NPH} \leq n < B \\ 1 & \text{B} \leq n < A \\ 2 & \text{A} \leq n < nlev \end{cases} \tag{2.8}$$

Where n is the model level index, NPH is the plume injection height model level, $nlev$ is the surface level, B is the first inflection point and A is the second (Figure 2.6). In order to ensure the mass conservation, it is necessary to normalize the temporal vertical function (2.8). The resulting function is the final VDF (Equation 2.9).

$$F(n) = \frac{F_t(n)}{\sum_{i=1}^{nlev} F_t(i)} \tag{2.9}$$

39
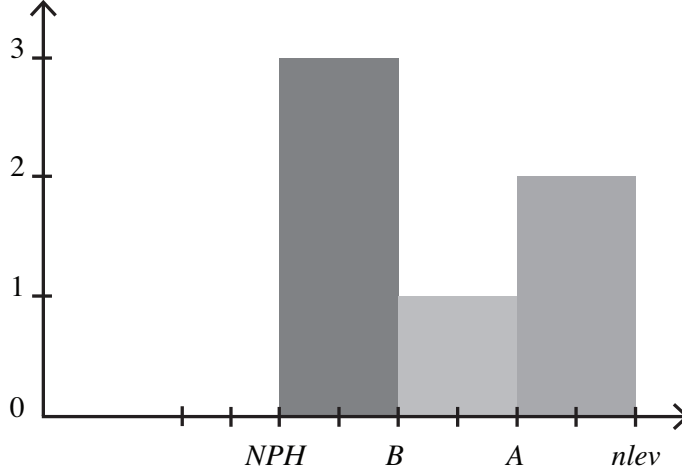
Figure 2.6: Visualization of the temporal vertical distribution function showed in equation 2.8.

Therefore the sum of the vertical levels of the final function is equal to one (Equation 2.10).

$$\sum_{j=1}^{nlev} F(j) = 1 \tag{2.10}$$

Finally the normalized function is applied to the 2D emission field to produce the 3D emission field (Equation 2.11).

$$Emission\,field\,3D(n) = Emission\,field\,2D \times F(n) \tag{2.11}$$

The process is slightly different for the Vegetation (VEG) and Fire Radiative Power (FRP) schemes because they require intermediate steps that combine all the vertical functions corresponding to the vegetation types or categories inside each grid cell.

2.2.3 Fixed Height: FH

Fixed height is the simplest scheme; it only needs a predetermined injection height. In this case, 1.5 km, similar to the altitudes suggested by Kauffman et al. (2003) (0.9–1.5 km) and used by Wang et al. (2006) (1.2 km). The unmodified version of EMAC directly injects BB gas emissions at 140 m. No vertical distribution is applied, and the aerosols remain at the lowest level. The main improvement afforded by this scheme is

therefore the vertical distribution and the injection of both gas and aerosols at a higher altitude.

Biomass burning emissions are not entirely injected at the top of the plume. However, because of turbulent mixing, they are rather unequally distributed along the vertical (Kahn et al., 2007; Labonne et al., 2007). The emissions can be distributed automatically by the model if the emissions remain inside the mixing layer. However, some other processes may be missed or underestimated.

For this scheme, the specified height does not require any calculation; it is only necessary to convert the given altitude (in meters) to the equivalent model level. A particular height may not correspond to the same model level globally. Depending on location and time, this height may instead correspond to a different level because EMAC is a hydrostatic model with a hybrid pressure coordinate system.

This particular height was chosen because it represents a wider range of fires. It may be smaller than most boreal forest fires and larger than agricultural ones. However, it is important to consider that the altitude that fire plumes reach depends on fuel properties and weather conditions, which results in a wide spectrum of heights for a single region and even for a single fire.

On the scope of the MISR Plume height project, 161 African plumes were observed with heights ranging from 350 m to 3.67 km. Another 77 smoke plumes over North America observed by MISR during the summer of 2004 show heights ranging from 700 m to 5.2 km (Mazzoni et al., 2007)). Considering these observations and the 500 m of uncertainty in MISR data, 1.5 km is a good and simple approach for representing smoke plumes. This particular altitude is also chosen because of the effects of BB when emissions are released above the boundary layer. Some studies (e.g., Langmann et al., 2009; Trentmann et al., 2002) suggest that most BB emissions remain inside the boundary layer. Direct injection into the free troposphere is uncommon. This statement is also supported by CALIOP observations made during July and August 2006 (Labonne et al., 2007) as well as MOPITT observations (Lamarque et al., 2003).

Plumes have also been detected above the boundary layer (e.g., Damoah et al., 2006; Fromm and Servranckx, 2003; Fromm et al., 2000, 2005; Lavouè et al., 2000; Luderer et al., 2006; Rosenfeld et al., 2007). Transport has been observed over continental (e.g., Colarco et al., 2004; Duck et al., 2007; Wotawa and Trainer, 2000) and intercontinental regions (e.g., Damoah et al., 2004; Dirksen et al., 2009; Honrath et al., 2004; Real et al.,

2007). The MISR observations from 2004 to 2009 show that 4–12% of the plumes were injected above the PBLH in boreal fires. This number varies from year to year and can even reach 35% if latter stages of the plume evolution are considered (Val Martín et al., 2010).

The discrepancy between MISR and CALIOP may be result from the spatial coverage and differences in instrument sensitivity. Although MISR has a greater coverage, CALIOP is more sensitive to the aerosol vertical profile but often does not detect the actual source of the fire. Instead, it captures the smoke around the fire inside the boundary layer.

Modeling studies (Generoso et al., 2007; Hyer et al., 2007; Leung et al., 2007; Pfister et al., 2011; Turquety et al., 2007) reveal that 50% of the emissions should be injected over the PBL in extratropical fires in order to match the observations. The injection of the gas emissions at 140 m in the reference simulation may underestimate some effects because approx. 67% of the total mass is released inside the boundary layer. Test simulations were performed at different injection heights (Pozzer et al., 2009), but 140 m gave the best results for the year 2000. However, it is important to consider that this height was only applied to gas emissions and not to aerosols and that all the mass was directly injected at that height without any vertical distribution. In addition, a selected height for a particular year may not represent the observations from different years because of the high seasonal and inter-annual variability of BB emissions. A realistic injection height is fundamental for modelling the atmospheric effects of BB. Because of the large variability in the plume height and the scarcity of temporal and spatial observations, it is not easy to determine a particular height for all fires. However, a good initial approach is to choose a height that could represent some of the fires and that injects a fraction of the mass above the boundary layer.

2.2.4   Heat Disturbance: HD

The second scheme is based on the idea that the energy released by the fire heats the surrounding air creating buoyancy. Together with the local weather conditions, these are the main forces responsible for the injection height. The process itself is more complex than what is represented in this scheme. However, there are some limitations, especially in the amount of energy directly converted into vertical motion. The amount of radiative energy converted into vertical motion mainly depends on the volume of air

heated i.e., the size of the fire. Moreover, processes such as the entrainment caused by wind shear also depend on the size of the fire. The temperature and velocities of the outgoing gases should also be considered as well as the release of latent heat and local meteorological conditions. Given that in global models, the horizontal resolution is a constraint, these sub-grid processes could not be explicitly resolved. This scheme is a simplified version of the process. A fixed surface temperature anomaly, ΔT, is assigned. It is assumed that the air over the fire will rise until it reaches equilibrium with the surroundings. The speed at which equilibrium is reached will determine how high the top of the plume will be. The rate at which temperature decreases is established as a certain percentage of loss for each 100 m. The temperature anomaly is set at 1000 K, which is a representative temperature of the outgoing gases during the flaming phase of a fire.

The method entails calculating the plume height in meters using Equations 2.12 and 2.13. The plume height will be set at the height at which the temperature difference is lower than or equal to ε (Equation 2.13). Finally, the plume height in meters is then converted to the corresponding model level.

$$\Delta T(100_j) = (1 - Lr)\Delta(100(j - 1)) \tag{2.12}$$

$$PH = \min\{h \mid \Delta T(h) \leq \varepsilon\} \tag{2.13}$$

Where $j \leq 1$ and $\Delta T(0){=}1000$K.

Unless the loss ratio is dynamically calculated, this method is essentially a more realistic way to select a fixed height scheme or a vegetation scheme if different temperature anomalies are to be used at different regions.

2.2.5 Vegetation: VEG

The third scheme emerges from the need to represent the regional variability in the height of the plume injection. The differences are partially a product of the fuel properties (amount, composition, and dryness). These properties lead to characteristic fires (emissions and plume height), which depend on the type of vegetation burned. For instance, dense crown fires in boreal forest are more intense. The energy available to be converted in vertical motion is thus larger, which would result in plumes reaching higher altitudes. However, the final elevation is also bound by local weather conditions.

2. METHODOLOGY

By assigning a particular injection altitude to each type of land cover, the properties of the fuel are implicitly included.

2.2.5.1   Land Cover Data

The 2006 vegetation information was obtained from MODIS Land Cover Type Climate Modeling Grid (CMG) product MCD12C1 (Friedl et al., 2010). MCD12C1 provides yearly L3 global dominant land cover types in a resolution of 0.05° as well as the sub-grid frequency distribution of the land cover types. This CMG product is generated using the same algorithm that produces the MCD12Q1 and provides yearly land cover properties derived from Terra and Aqua MODIS data in a global 500 m sinusoidal grid. The land cover type used in the VEG injection height scheme contains 17 land cover classes (Figure 2.7) defined by the International Geosphere Bio-sphere Program (IGBP), 11 natural vegetation classes, 3 mosaicked land classes, and 3 non-vegetated land covers. A height was assigned to each land cover type (Table 2.5). The heights were established according to the ones suggested at the EDGAR 3.2 Fast Track 2000 dataset (32FT2000: van Aardenne et al., 2005) as a result of a personal communication with D. Lavoué. These heights were used in the 2003/2004 ACCENT-IPCC and AEROCOM experiments, the emissions of primary aerosol and precursor gases for the years 2000, and 1750 prescribed data-sets for AEROCOM (Dentener et al., 2006). In this work, the heights remain the same, but the vertical distribution is different because the distribution is automatically determined by the VDF.

Method

Given the horizontal resolution of the model (96721 km^2), it is usual that various types of land cover fall into each grid cell. It is essential to include all of these by combining them into a single plume. By assigning a fixed altitude to each vegetation type, the approach becomes analogous to the FH scheme. Consequently, the process for each land type is similar. Once the height in meters is assigned to each of the 17 land covers, this altitude is converted into a model level using geo-potential height. A vertical distribution function $F(n, e)$, is determined for each vegetation type. The plumes for the ecosystems in each grid cell are then combined using their fraction in the grid cell $f(e)$, to generate the final vertical distribution function (Equation 2.14).

Table 2.5: Land cover types and correspondent assigned heights in meters.

Land cover type	height [m]	Land cover type	height [m]
water	0	savanna	1000
evergreen needleleaf forest	6000	grassland	1000
evergreen broadleaf forest	1000	permanent wetlands	0
deciduous needleleaf forest	3000	croplands	100
deciduous broadleaf forest	2000	urban and built-up	0
mixed forest	2000	cropland/nat veg mosaic	100
closed shrublands	2000	snow and ice	0
open shrublands	1000	barren or sparsely vegetated	0
woody savanna	3000	unclassified	–

MODIS Land Cover Type
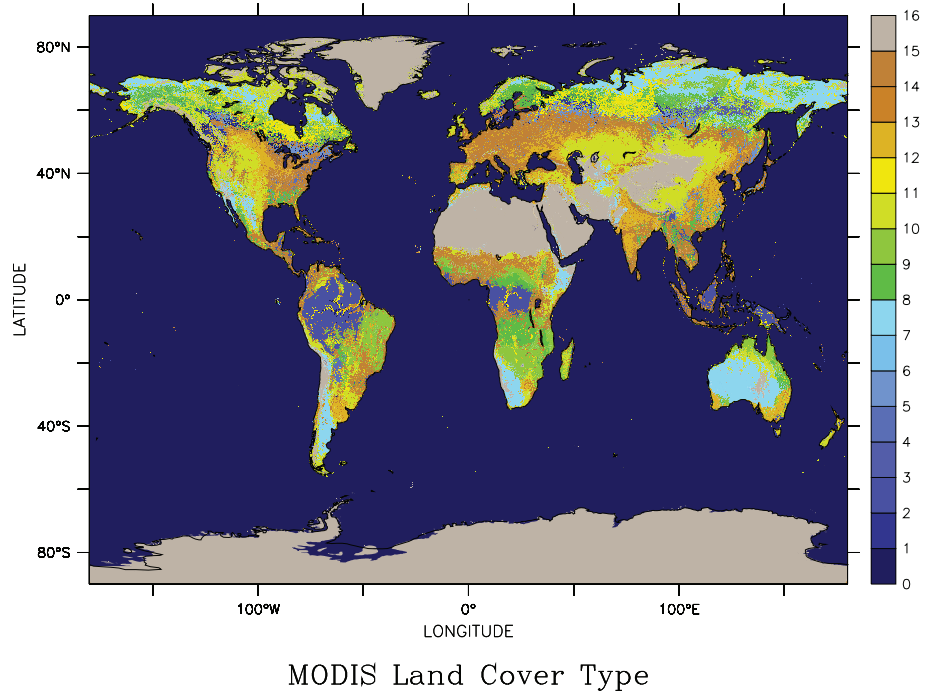
Figure 2.7: International Geosphere Biosphere Program (IGBP) land cover type for 2006.

$$F(n) = \sum_{e=1}^{17} f(e) \, F(n, e) \qquad (2.14)$$

Where $e[1:17]$ is the land cover index.

The use of vegetation data also allows for the representation of the seasonal changes in the plume injections caused by the seasonal changes in vegetation (more humid/ less humid) if monthly vegetation data is available. It is also suitable for studies of future scenarios in which future land use change can be easily assessed in contrast to attempting to estimate the future values of the highly variable fire intensity.

2.2.6   Fire Radiative Power: FRP

This scheme aims at combining the two basic processes involved in the plume injection height, the energy released by the fire and the local meteorological conditions; both quantities being highly variable. As meteorological conditions, the PBLH and the atmospheric stability play a key role in determining the injection height. The air entrainment caused by wind shear is only important for small fires (Freitas et al., 2010). The height of the boundary layer limits the upward transport of tracers, keeping most of the BB emissions inside it. The uplift generated by the fire must have enough energy to be able to break the boundary layer and directly inject the tracers into the free troposphere. Otherwise, the emissions will remain trapped inside the boundary layer. The thermal energy generated by the fire transforms into upward motion by buoyancy. This energy, together with the PBLH, will determine whether the plume can reach the free troposphere.

The frp is the fire intensity determined by the energy irradiated during combustion; hence, the intensity will depend on fuel properties such as composition, amount, and dryness. The frp represents the mass of consumed fuel given the heat from the combustion. The frp is actually the chemical energy product of the combustion of vegetation emitted as radiation. Fires should radiate as grey bodies. Therefore, it is a good approximation to assume that the frp is equivalent to the total radiative power as described by Stefan-Boltzmann law. The frp is then proportional to the temperature of the fire. The fire radiative energy (fre) can be obtained by integrating the frp over the duration of the fire. This fre is proportional to the total energy liberated during combustion. The relationship between fre and combustion was first established by Kaufman et al. (1998). Consequently, the emissions can be directly estimated from the frp (Kaiser et al., 2012) given the combustion rate (Wooster et al., 2005) and the aerosol emission rate (Ichoku and Kaufman, 2005).

The FRP scheme implements the formula developed in Sofiev et al. (2012) assuming

a CAPE. The formula was calibrated using plume height observations obtained by the MISR (Multi-angle Imaging SpectroRadiometer) Plume Height Project (Kahn et al., 2008; Mazzoni et al., 2007). The dataset comprises 2000 plume heights obtained over United States, Canada, and Siberia during 2007 and 2008. The formulation is based on the idea that the energy released by the combustion will heat the volume of air that is in contact to the fire, leading to buoyancy and upward motion until the equilibrium is reached. The release of latent heat during the uplift is an important mechanism that increases the plume height (Freitas et al., 2007). This effect is implicitly included during the calibration process.

2.2.6.1 Fire Radiative Power Data

This scheme requires the fire radiative power (frp) as an input quantity. The mean frp is obtained from the MODIS CMG collection 5 fire product (Giglio, 2013; Giglio et al., 2006). The dataset used is MYD14CMH, which was derived from the Aqua-MODIS data and provides monthly global fire information in a 0.5° spatial resolution. The frp is determined from the infrared brightness temperature using the 4 μm and 11 μm channels that are sensitive to temperatures of 450 and 400 K, respectively. The frp formulation was proposed in Kaufman et al. (1998). The frp is limited to cloud-free areas because thermal energy cannot pass through clouds. Terra and Aqua MODIS sun-synchronous satellites provide frp data. The former satellite passes over the observation points at 10:30/22:30 local equatorial time, and the latter passes over at 01:30/13:30. A combination of both products could reproduce the strong diurnal cycle of the fire intensity. However, for the sake of simplicity and consistency, only the Aqua dataset was used to assess the effects of the injection height in the model. The Aqua data was selected because it passes over most of the fires during the peaks in fire intensity and activity. It therefore captures more fires, thus reproducing the diurnal cycle better than Terra. Moreover, the magnitude of frp is 10% larger in Aqua compared with Terra (Giglio et al., 2006).

Most of the fires had low intensities. During regridding, the average per grid cell masks the contribution of high intensity fires. To properly calculate the injection height, both low and high intensity fires must be captured. The original frp data was thus converted to eighteen categories of frp intensity (Figure 2.8); for each category, a representative frp value in megawatts was assigned (Table 2.6). Using the categories affords the inclu-

sion of the complete spectrum of fire intensities. Moreover, by using an index fraction re-grid (IXF), the contribution of each fire category inside the grid cell is included in a manner similar to the fractions of vegetation obtained from the land cover type in the VEG scheme.

Table 2.6: Fire radiative power category and assigned value in MW.

Category	frp [MW]	Category	frp [MW]
1	0	10	90
2	10	11	100
3	20	12	200
4	30	13	300
5	40	14	400
6	50	15	500
7	60	16	600
8	70	17	1000
9	80	18	1500

Fire Radiative Power Categories
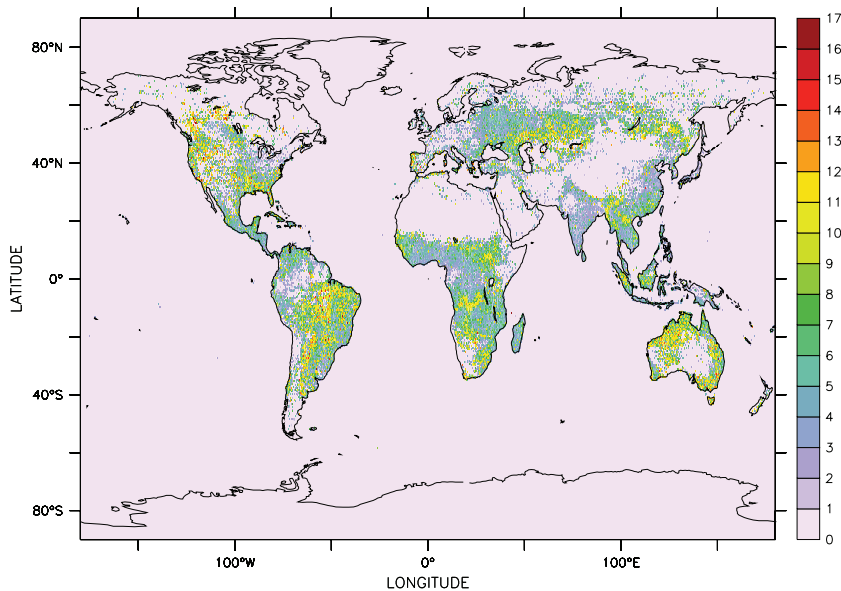
Figure 2.8: Fire radiative power categories for 2006.

48

Method

The plume height is proportional to the PBLH and to the frp. It is modified by the atmospheric stability represented by the ratio between the Brunt Väisälä frequency at the free troposphere (NFT) and a reference value (N_0) of $2.5 \times 10^{-4} \text{s}^{-2}$.

$$PH = \alpha \text{PBLH} + \beta(frp)^{\gamma} \exp\left(\frac{-\delta N_{FT}^2}{N_0^2}\right) \qquad (2.15)$$

The parameters α, β, γ and δ regulate the dependencies of the plume height at different atmospheric regions (Equation 2.15). α represents how freely the plume goes through the PBLH. β adjusts for the contribution of the fire intensity. γ controls for the power-law dependency on frp. δ determines the importance on stability at the free troposphere. Three sets of parameters are required for the plume height estimation (Table 2.7).

The plume height (Equation 2.15) is initially evaluated with the first set of parameters shown in Table 2.7. For this first estimation, the dependency on frp is the largest. Together with PBLH, it is assumed to be the main process in estimating the PH. At this point the role of atmospheric stability is neglected, therefore δ has a value of zero. Once the PH has been estimated, the PH must be compared with the PBLH. If the PH is lower or equal to PBLH, the PH is recalculated with the values of the second set of parameters (Table 2.7). These parameters tend to result in an overestimation of the lower plumes and an underestimation of the higher ones. In contrast, if PH is higher that PBLH, the formula is evaluated with the parameters of the third set (Table 2.7). The value of α represents the fraction of PBLH that is freely passed, which is nearly all in this case. The lower value of γ represents the negative effect that the stable stratification exerts on the plume rise in the free troposphere.

Table 2.7: Parameters for the estimation of plume height in the FRP scheme.

	I	II	III
α	0.15	0.24	0.93
β	102	170	298
γ	0.49	0.35	0.13
δ	0	0.6	0.7

All parameters are unitless, except for β, which is in meters.

This is performed for the eighteen values of the frp categories, thereby leading to individual estimations of the PH. Subsequently, in a process similar to the one performed for the VEG scheme, the different plumes heights contained in each grid cell are combined to produce a single plume that represents the whole grid cell. This plume has the altitude of the highest estimated plume, whereas the mass distribution is weighted according to the contribution of each fire category present in the grid cell (Equation 2.16).

$$F(n) = \sum_{c=1}^{18} f(c) \, F(n, c) \tag{2.16}$$

The success of the plume height estimation strongly depends on the quality of the PBLH parameterization and on the frp observations; the Brunt Väisälä frequency only has a minor influence, but the stability at the free troposphere should be partially reflected in the estimation of the PBLH. This also becomes clear in the model results in which the PBLH plays an essential role in limiting the height of the plume. Thus, only fires with sufficient energy will be able to break through the PBLH. Once they have crossed it, they will follow its shape. Therefore, both the estimation of the PBLH and the frp data are essential for determining the plume height. This trend has been observed in Labonne et al. (2007); Luderer et al. (2006); Trentmann et al. (2006). The advantage of this formula is the use of the key quantities (PBLH and frp) as well as the lack of complex calculations and its realistic approach, which make it suitable for global models. The formula could be improved if plumes from different regions were included in the calibration.

2.3 Set Up of the Model and Simulations

Two sets of simulations were performed for this thesis (Section 2.1.2.3): one set with suppressed feedback to quantify the changes and another with feedback to evaluate the effects of changes in the radiation transfer. Each set is composed of a control simulation and one simulation for each of the four different injection height schemes. All submodels described in Section 2.1.2 were used in both simulation sets.

The simulations are identified as follows. Fixed height: FH; heat disturbance: HD; vegetation: VEG; fire radiative power: FRP; and control: CTRL. The schemes and their required input data were described in Section 2.2.

For the set of simulations without feedback, one year plus six months of spin-up was performed. This set was weakly nudged towards 2006 meteorology, as described in Section 2.1.2.2.

For the set with feedback, ten years plus six months of spin-up were performed. Over the course of those ten years, the input data provided correspond to 2006 to generate a consistent feedback. Sea surface temperatures (SST) were taken from the AMIPII database (Taylor et al., 2000).

3

Plume Height

In this chapter, the performance of the injection height for each of the schemes is assessed. The height at which BB emissions are injected may reinforce the effects depending on the amount of mass that is injected above the boundary layer. Therefore, both the injection height and the mass above the PBLH are important for the assessment.

Because of the quick mixing and deposition occurring inside the boundary layer, the mass that is released above it may be subjected to enhanced transport and lifetime, which influence the effects. Furthermore, the mass released at higher altitudes is exposed to different temperatures and background concentrations, which could result in diverse chemical interactions and ageing paths.

This chapter is divided in three sections. The first part entails assessing the effective injection height, PH (i.e., the height of the model level that corresponds to the top of the plume, NPH) and its variability. The second involves evaluating the amount of mass injected above the boundary layer (MABLH). Although PH and MABLH are not part of the standard model output, they were created in order to evaluate the performance of each scheme.

Finally in the third part, the VEG and FRP plume heights are compared to the 2006 smoke plume heights obtained by MISR.

The set of simulations without feedback (Section 2.3) was used to assess these quantities. This assures that the diurnal cycle of the boundary layer height is similar for all schemes because of the identical binary meteorological conditions for all the simulations in this set (Section 2.1.2.3). Hence, all schemes should be subject to the same

variability in the PBLH. Consequently, the differences and variability in the height and mass injections could only originate from the choice of the scheme. Using the set of simulations without feedback facilitates the comparison between the plume heights obtained by FRP and the plume altitudes observed by MISR because this set was weakly nudged towards 2006 meteorology (Section 2.1.2.2).

3.1 Plume Height Variability

This work introduced variability in the injection height in order to reproduce the heterogeneity in the observed plumes. Such variability is present in both the VEG and FRP schemes. The diurnal variability, the regional variability, and the seasonal variability (for FRP) are addressed in this section.

For three of the four schemes, a PH invariant in time was determined. This was either a single quantity for all grid-cells (FH and HD) or a quantity that depends on the vegetation type present in the grid-cell (VEG). Only the FRP scheme calculates a PH that varies both regionally and in time (diurnal and seasonal) according to the PBLH, the atmospheric stability, and the frp (Section 2.2.6). The FRP dependency in the PBLH introduces more variability in the injection height than the other schemes. The strong variability in the PH and consequently in the mass that is injected above the boundary layer is reflected in the results of the FRP scheme (Chapters 4, 5 and 6).

3.1.1 Temporal Variability

In order to evaluate the PH temporal variability, a series of box plots showing the distribution of the 5-h PH global mean per month for each scheme was constructed. Only July is shown considering that FRP generates its highest PH in this month (Figure 3.1). The global mean of the PH was calculated to mask the inherent regional variability in the VEG and FRP plume height estimations. For the VEG scheme, the PH varies regionally according to the vegetation type. Similarly this occurs for the FRP scheme, which has regional differences that are a product of the diverse fire intensities at different grid-cells. For the simulations performed in this thesis, frp remains constant over a month. This quantity therefore only provides seasonal variability. As a result of the masked regional variability, the 6 km PH values of the VEG scheme were extracted from the distribution.
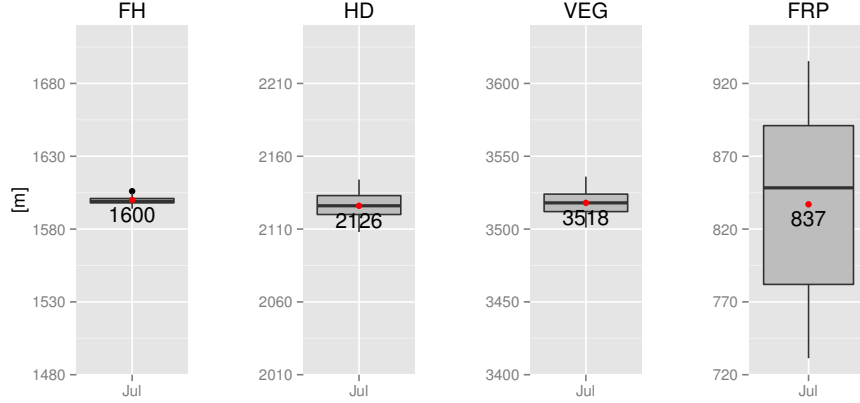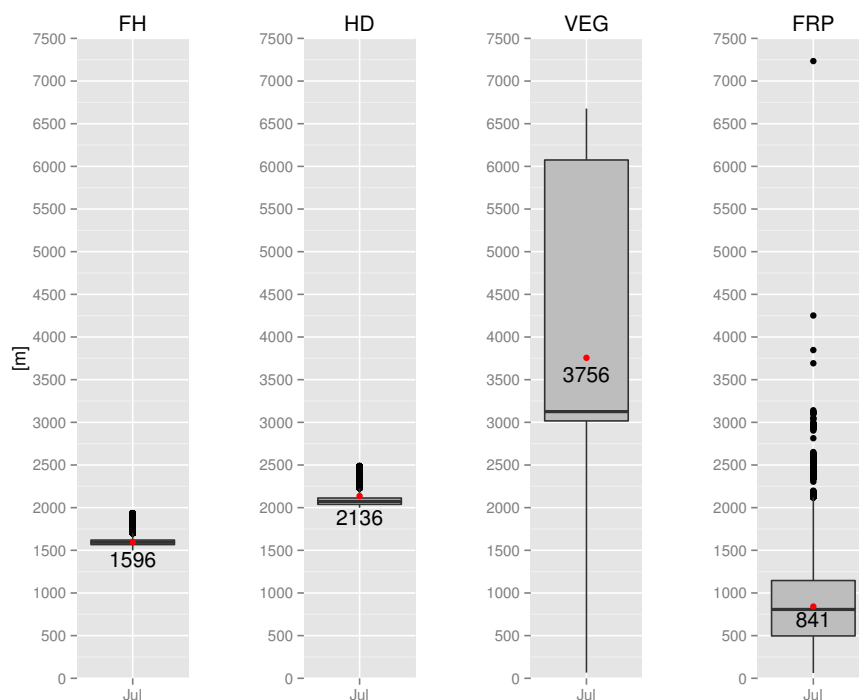
Figure 3.1: Hourly variability of the globally averaged PH for July.
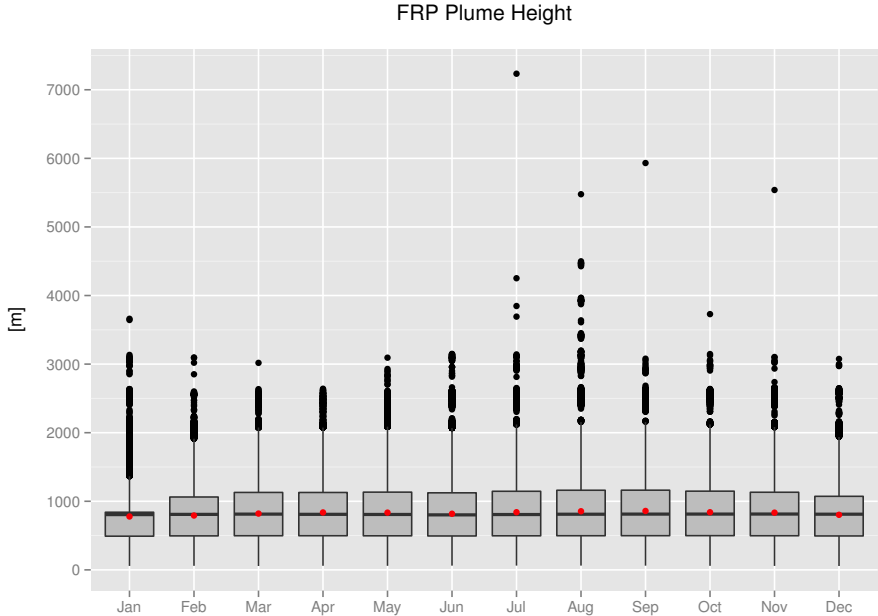The mean is represented by the red points, and its value is shown bellow.
More information about the box plot construction can be found in the appendix (Section 8.1.1).

The temporal variability can be seen in the height of the box (i.e., the Inter Quartile Range, IQR); that for the FH, HD, and VEG schemes is less than 15 m, while for FRP, it is 109 m. This small variation results in a constant injection altitude for the first three schemes and in an hourly fluctuating injection for FRP, at any given grid-cell.

For the FRP scheme at any particular region, the height at which the emissions are injected therefore varies over time according to the PBLH, which possesses a strong diurnal cycle that is passed along to the PH estimation, and to a lesser extent, the atmospheric stability. Therefore, most of the variability of this scheme will come from the model internal parameterization of the boundary layer height.

The small dispersion observed in the other schemes is a product of the changes in the height of the model level (originating from variations in the surface pressure), which are also embedded in the FRP scheme, albeit to a lesser extent. The variability in the model level plays a role because the effective injection height is defined as the altitude of the top of the plume model level (NPH); the height of this level can vary. In other words, a particular height could correspond to a different model level for particular regions or times.

3.1.2 Regional Variability

The temporal and regional variabilities are included in the distribution of the 5-h July PH output for each scheme (Figure 3.2). The large regional variability in FRP and VEG can be seen in the broad range of several kilometers for both schemes.

Figure 3.2: Plume height distributions for July.

The mean is represented by the red points, and its value is shown bellow.

More information about the box plot construction can be found in the appendix (Section 8.1.1).

For FH and HD, the PH remains around the specific height and only varies according to the model level variations. The VEG scheme shows the largest inter quartile range (IQR) product of the amplitude (100 m to 6 km) of the predetermined heights for the vegetation types. The FRP scheme has the lowest mean value as well as both the lowest (61.98 m) and highest (7234 m) PH, thereby revealing the strong effect of the diurnal variability that arises from the PBLH as well as the regional variability that arises from the frp value.

3.1.3 Seasonal Variability

For FH, HD, and VEG, the PH remains constant over the year, which makes their results more consistent; the noise generated by the variations in the input parameters is reduced, which becomes evident when looking at the annual means.

On the other hand, FRP has a more realistic seasonal cycle as observed in the outliers in Figure 3.3. The seasonal cycle becomes important because of interaction with other emissions as well as the horizontal transport patterns, which are enhanced by convective transport and sometimes limited by scavenging.

Figure 3.3: FRP Plume Height for 2006.

The mean is represented by the red points and its value is shown bellow.

More information about the box plot construction can be found in the appendix (Section 8.1.1).

The PH of 7.2 km for July corresponds to a point south of the Amazon Rainforest, which has a frp value of 90 MW.

FRP has the smallest mean PH value (Figures 3.2 and 3.1). and is also preserved in Figure 3.3. This is reflected in the differences between the schemes and the reference simulation (Chapters 4, 5, and 6). Using daily frp values could increase the number

of intense fires that are missed in the monthly values and may result in more plumes reaching higher altitudes. However, the relationship between PH and frp iis not as direct as the relationship between PBLH and PH (Figure 3.4, lower right panel). Using daily values will also introduce more variability to the PH estimation at the same time that will reproduce the most intense fires. The PH outliers inject the emissions at higher altitudes and may be the ones causing the positive differences in BB aerosol concentrations at the free troposphere, sometimes in conjunction with convective transport.

3.2 Plume and Boundary Layer Height

The boundary layer not only plays an important role in determining the plume for the FRP scheme but also in enhancing transport; the reduced deposition increases the lifetime. This section discusses the relationship between the plume injection height and the boundary layer as well as the fraction of mass that is injected above the PBLH.

3.2.1 Plume Height and Boundary Layer Relationship

The variation of the PH compared with the PBLH is addressed using the 5-h output (Figure 3.4). Only July is shown because this is the month with the highest PH for FRP and the month with more plumes injected above the PBLH.

The small variability generated by the model level for the FH and HD schemes can be seen in the upper panels. At certain times and for specific regions, the determined PH corresponds to a higher model level. This translates into a greater effective injection height, which results in plume height values from 1.5 to 2 km for FH, and 2 to 2.5 km for HD (Figure 3.2). As a consequence of the chosen height for FH and the calculated but constant injection for HD, more plumes are injected above the PBLH over Africa for HD than for FH.

The lower left panel shows the five heights assigned to the different land cover types in the VEG scheme (Table 2.5). Because the highest value of the PBLH for this month in the grid-cells with fires is 5.7 km, all the plumes above 6 km are injected constantly over the PBLH in the VEG scheme (Figure 3.4, points to the left of the identity).

The lower right panel shows the relationship between PH and PBLH, which results from including the PBLH in the PH when calculating the FRP scheme. The lines

Figure 3.4: Plume Height vs Boundary layer height July.
Africa (red), South America (black), North America (blue), rest of the world (magenta).
The identity is represented by the black line.

that characterize each altitude result from categorizing the original frp values. If all fire intensity values were used instead of the categories, the PH would have less clearly defined values. This image reveals that when the PBLH is low and the fire has enough energy, the top of the plume can be located above the boundary layer. The final injection height would then be determined by other factors such as the Brunt Väisälä frequency. This behavior becomes evident when the plumes reach 1.5 km; from this altitude, the plumes that are located above the PBLH are completely separated from the ones that are below. The outliers are clearly identified as isolated points (from 2 km height) that do not follow the linear relationship between the PBLH and PH. The outliers were seen in the box-plot distributions for all months except January, February, and December (Figure 3.3). Similar results are found by Kahn et al. (2008) at approx. 2 km height in the comparison between 2004 plumes retrieved by MISR over the Alaska and Yukon area and the PBLH obtained from the version 4 of the Goddard Earth Observing System Model (GEOS-4: Bloom et al., 2005).

3.2.2 Mass Above the Boundary Layer

A high altitude of the top of the plume does not necessarily result in more mass being injected above the PBLH because of the differences in the vertical distribution introduced by each scheme. This is especially important for VEG and FRP schemes for which the injection altitude is determined by the largest of the heights present in the grid-cell. The mass is weighted according to the fraction that the different vegetation types or frp categories occupy in the grid-cell. The amount of mass injected above the PBLH therefore fluctuates substantially; this quantity influences the effects.

categories occupy in the grid-cell. The amount of mass injected above the PBLH therefore fluctuates substantially; this quantity influences the effects. The fraction of mass injected above the boundary layer is determined by the PH, the vertical distribution function (VDF), and, of course, the boundary layer height. The minimum fraction of mass injected above the PBLH varies between schemes; this is negligible for FRP and VEG, 20% for FH, and 18% for HD. The maximum fraction of mass injected above the PBLH for any plume is a number that results from the PH and the VDF construction. For VEG and FRP, this maximum is reached when the biggest fraction of grid-cell is occupied by the most intense fire (i.e., the vegetation type with the 6 km PH or the greatest frp category value) and the PBLH is low. The mean fraction of mass injected above the PBLH (for VEG and FRP) per grid-cell varies according to the different combinations of PBLH values and fire intensities (determined by the vegetation type or frp value). The global average of the mean fraction per month (Table 3.1) has little variation over the year for FH and HD. Conversely, for VEG, the fraction ranges from 23% in March to 29% in July, while FRP ranges between 10% in June to 13% in January, February, August, and September.

Table 3.1: Average fraction of mass injected above the PBLH per grid-cell.

	Mean [%]	Max [%]
FH	56	77
HD	58	76
VEG	26	82
FRP	12	67

For the FH, HD, and VEG schemes more plumes on average are injected above PBLH than for the FRP scheme (Table 3.2). This is also seen for July (Figure 3.4). Despite the larger percentage of plumes located above the PBLH for VEG, the average fraction of mass injected over the PBLH per grid-cell in this scheme is 26%, which is lower than the values for FH and HD (Table 3.1).

The height at which the maximum fraction of mass above the PBLH is reached in the FRP scheme is the altitude of the PH mean, which is approx. 840 m (Figure 3.5).

The weighted contribution of the different fire categories and its influence on the amount of mass injected at each layer results in only a small fraction of the emissions being effectively injected above the PBLH for the FRP scheme (for plumes of higher altitudes). To test the influence of the weighted contribution of the small fire intensities on the amount of mass injected at the top of the plume, another simulation, MFRP, was performed with a modified version of the FRP scheme. This simulation calculates the PH using the maximum frp value present in the grid cell. The contribution of the smaller categories inside the grid-cell is thus neglected. This height is used to calculate the VDF. Hence, the plumes for this version have the same height as the ones for FRP scheme. However, the mass distribution does not account for the smaller fires present in the cell. Consequently, the amount of mass injected at the top of the plume is higher than the values shown for FRP (Table 3.1). The maximum annual average is 70%, the minimum is 14%, and the mean is 39% (Figure 3.5, right panel). For FRP, at a given height, the fraction varies from almost zero to the maximum according to the fires present in the grid-cell (Figure 3.5, left panel). Because the PH remains the same as in FRP, the frequency of plumes injected above the PBLH does not change. Therefore, the extra mass above the PBLH in the MFRP simulation only results in a difference of 1% compared with FRP in the global budget of species (e.g., BC and OC). A similar effect can be achieved when the resolution of the model is increased because the contribution of the different fires per grid-cell becomes larger. The fraction of mass above the PBLH consequently shifts towards the higher values.

Table 3.2: Plume height, total fire events, and percentage of plumes located above the PBLH.

	PBLH mean [m]	Total events	FH [%]	HD [%]	VEG [%]	FRP [%]
Jan	499	621	96	98	97	82
Feb	540	619	94	97	97	80
Mar	593	747	92	96	96	78
Apr	628	844	91	95	95	78
May	617	912	92	96	95	78
Jun	606	944	92	95	96	78
Jul	601	1098	92	96	96	78
Aug	622	1023	91	95	95	77
Sep	624	981	91	95	95	78
Oct	579	909	93	96	95	81
Nov	575	757	94	96	96	80
Dec	529	717	96	98	96	82
mean	548	848	93	96	96	79

Second column, global mean boundary layer height. Third column, number of monthly grid-cells with BB emissions (i.e. fire events). Four to seventh columns, average percentage of plumes located above the PBLH per month.
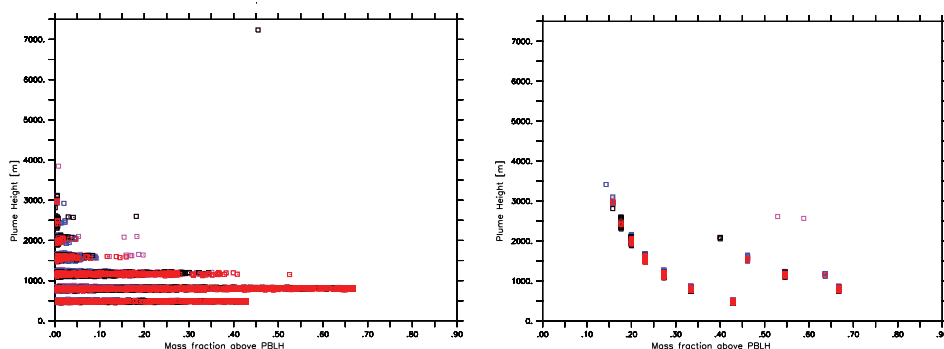
Figure 3.5: Plume Height and fraction of mass above the boundary layer FRP (left) MFRP (right). Africa: red, South America: black; North America: blue; Rest of the world: magenta.

Analyzing the CALIPSO data for summer 2006 (Labonne et al., 2007) revealed that most of the observed plumes remain inside the boundary layer and that only some plumes (detected directly over the fire) are located above the PBLH. This suggests that the emissions were directly injected at those altitudes. However, moist convection cannot be ruled out as a transport mechanism. Using data from the 2004 MISR observations over North America, Mazzoni et al. (2007) also suggest that most plumes are located inside the mixing layer.

These findings contrast the larger fraction of plumes injected above the PBLH in the injection schemes. However, the constant monthly emissions in the model, which includes night time when the PBLH is low, have to be considered. The uncertainties in the observations of the instruments (CALIPSO and MISR), their time, and geographical coverage must all be considered. The fraction of plumes directly injected above the boundary layer must also be assessed.

The sources of uncertainty in CALIPSO are introduced by the clouds at the time of the observations due to the The sources of uncertainty in CALIPSO are introduced by the clouds at the time of the observations and result from the difficulties in distinguishing them from aerosols and the noise in CALIPSO Lidar data during the day, when most fires are the product of agricultural practices. As a result of the number of MISR observations, MISR is more likely to capture the buoyant plumes than CALIOP because MISR circles the earth 3.5 times, while CALIOP circles the earth once. However, because of the observation times, CALIOP (1:30 PM) is more likely to capture the plumes at their maximum altitude than MISR, which passes over at approx. 10:30 (+1 h) local time. Because of the geographical coverage of MISR, it will also observe the plumes closer to the source, thereby minimizing the effect of independent transport. It is therefore harder for CALIOP to distinguish whether the plume has been directly injected above the PBLH or lofted to that altitude.

The performance of the injection height schemes can therefore be better assessed by comparing smoke plumes obtained in 2006 by MISR with the plumes determined by the model at the exact time and location, as described in the following section.

3.3   Plume Height Observations

The ability of the schemes to reproduce observed altitudes of the plumes is evaluated using information retrieved by the MISR on board of the NASA Terra satellite (Kahn et al., 2007, 2009).

The smoke plume data was obtained from the MISR Plume Height Project website. Plumes from seven regions over Africa, Asia, Indonesia, North America, South America, and Siberia are available for 2006 (Table 3.3).

Table 3.3: MISR plume height project smoke plumes from 2006.

Region	Longitude	Latitude	Date 2006	Median value of median PH [m]
Africa	10W - 40E	0 - 20N	Jan	1283
Indonesia	90E - 120E	10S - 10N	Jul - Oct	959
North America	160W - 40W	10N - 75N	Mar - Oct	2191
Siberia	60E - 140E	50N - 70N	Jul	1597
Amazon	60W - 45W	20S - 0	Aug - Sept	1279
Bolivia-Paraguay	75W - 45W	30S - 10S	Aug - Sept	1003
Asia	90E - 110E	15N - 30N	Feb - May	1897

Data from the 2007 and 2008 fire seasons was used to calibrate and determine the parameters in the PH estimation of FRP scheme (equation 2.15). Consequently, the comparison of FRP altitudes with 2006 MISR plume height observations is done on data independent from the observations used to determine the FRP parameters. This independency is necessary for properly evaluating the performance of the FRP scheme. In addition to FRP plume heights, the altitudes determined for the VEG scheme were also evaluated in order to assess the performance of regionally different but temporally fixed injection heights because these are also used in other global models.

The FRP and VEG plume heights at the exact location and detection time were compared to the MISR smoke plumes. Only those labeled as "good" and "fair" were used in this evaluation. The labels ("poor","fair" and "good") are a function of the number of heights successfully retrieved for a region, the percentage of the region area that is filled with successful heights, the standard deviation/mean of the successful heights, and the wind direction.

Thirteen smoke plumes located over eight grid-cells in North America were not considered by the model because of discrepancies between the emissions field, which determines the plume occurrence in the model, and the MISR data.

Several factors such as the MISR uncertainty of 500 m (Kahn et al., 2007) as well as the 10:30 local overpass time of MISR being on board of Terra satellite, which may not capture the fires at its maximum power, must be considered. The fire intensity information (frp) used to calculate plume height in the FRP scheme was obtained by Aqua satellite, which passed over the fires at 13:30 local time (Section 2.2.6.1).

Three parameters were used to determine how well the injection height schemes can reproduce the observed plume altitudes: the Pearson's correlation coefficient, the root mean squared error, and the prediction percentage within the observational accuracy (Table 3.4). For the latter, three categories of percentage prediction are considered: good, for the plumes modeled with a difference of 500 m or less from the MISR observations; high, for the altitudes modeled 500 m above the observed plumes; and low, for the plume heights modeled below 500 m of the MISR plumes.

The Pearson's correlation coefficient (r) is 0.3 for VEG and 0.2 for FRP, globally. For the VEG scheme, a better fit was achieved for North America (0.35). For the FRP scheme, a better fit was achieved for Africa (0.41). This poor correlation can be partially explained by the uncertainty of the MISR observations (500 m) and by additional error ($\pm$ 200 m) caused by the wind correction during the processing of MISR plume heights.

Therefore, when this uncertainty in the percentage of plumes predicted by the schemes is considered, their performance is improved. FRP injects 52% of its plumes in no more than 500 m distance from the observed MISR altitude, whereas VEG scheme predicts only 11% of the plumes within the MISR uncertainty range.

The VEG scheme mostly reproduces the outlier values of MISR. While FRP better reproduces most MISR plume heights, it misses the outliers (Figure 3.6, left panel). Despite the better correlation of the VEG scheme (compared with FRP), it clearly fails to predict most plume heights within the uncertainty of the MISR, thereby leading to an overestimation; 87% of the plumes are located more than 500 m above the observations. This can also be observed in Figure 3.6, where the box of VEG distributions is constantly above the third quartile of MISR; the VEG box is mainly located in the area of the MISR outliers, which is also reflected in the large RMSE (Table 3.4). However,

the peak in the intensity of the fire may be missed by MISR. The VEG may therefore not be overestimated if latter plume stages are considered. Nonetheless, the VEG scheme still fails to simulate the diurnal cycle observed in the injection height of the fire, while the FRP scheme realistically reproduces these variations in the PH.
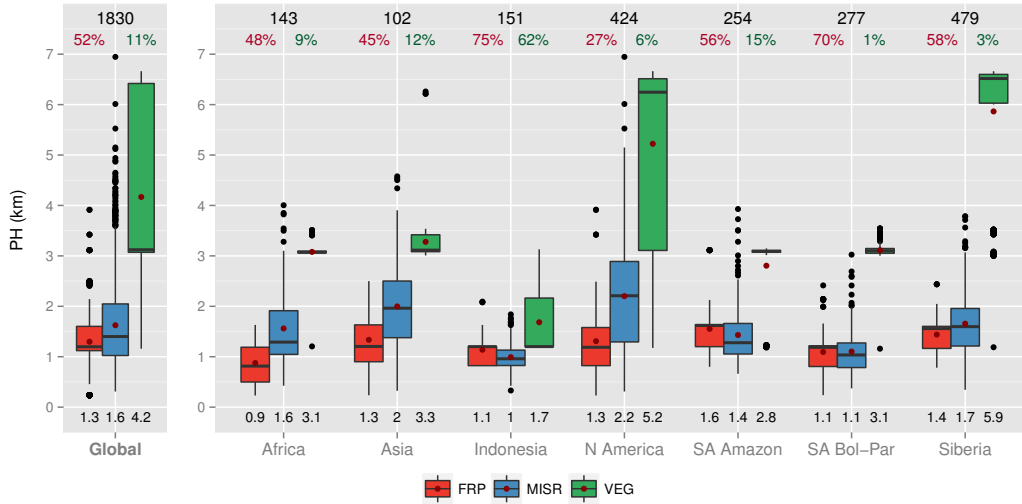
Figure 3.6: Plume height distributions for MISR (blue) VEG (green) and FRP (red). Global distributions are shown in the left panel and regional distributions in the right. The number of observations is shown in black numbers at the top of each region. The prediction percentages within the 500 m MISR uncertainty are shown at the top in red for FRP and green for VEG. The mean plume height values in kilometers are shown at the bottom and represented by the red dot.

Poorly correlated FRP reproduces more than half of the observed plumes. However, it is also evident that some of the plumes are underestimated (Table 3.4 and Figure 3.6). It is important to consider that African, South American, Asian, and Indonesian plumes where not used to estimate the original parameters. Nevertheless, for those regions, there are a high percentage of good predictions (Bolivia-Paraguay and Indonesia); in the Amazon, more than half of the plumes heights are predicted reasonably well, and in Asia and Africa, three quarters of the calculated PH are good predictions within the MISR uncertainty.

When the FRP PH parameters were determined by Sofiev et al. (2012), the evaluation done with the control subset gave 63% good, 18% high and 19% low predictions. Similar values are expected when different datasets are used for evaluation. However,

Table 3.4: FRP and VEG performance compared to MISR plume heights.

	FRP	VEG
Pearson's correlation	0.20	0.33
Prediction good [%]	52.4	10.9
Prediction hight [%]	13.4	87.4
Prediction low [%]	34.2	1.7
RMSE [m]	961	3075

two sources of discrepancy were identified between the good prediction percentage for the control subset and the one in this evaluation: The PBLH parameterization and the frp values. It is reasonable to assume that using monthly frp values to construct categories leads to underestimation because the PBLH parameterization were used extensively and because the frp values originally used to estimate the PH parameter were the ones associated with the fires at the exact time of their occurrence. The monthly frp values from Aqua are greater than the ones from Terra. However, they were not enough to compensate for the magnitude of the instant daily values retrieved by Terra at the time of the MISR observations. Although the monthly frp values used reproduce more than half of the PH observations, they do not contain the intense fires, which are responsible for the higher injections represented in the distributions by the outliers.

A comparison with the fire power associated to the MISR plumes and the frp assigned to the plumes in the model shows a poor correlation. The RMSE of the frp for the plumes within the 500 m MISR uncertainty is 453 MW, while the RMSE for the plumes outside the good prediction interval is 1139 MW. From these RMSE and the percentage predicted in the evaluation of our plume heights (52%) and in the control subset (63%), it is obvious that the model does not reproduce the higher injections because it does not include the higher frp values associated with those fires. Consequently, using lower frp values affects the determination of plume height, results in the underestimation of the higher injection altitudes, and has consequences on the frequency of injection and the fraction of mass above the PBLH. Therefore, the model should be improved by using daily frp values. This will entail an extra variability element and will still require the creation of categories in order to overcome the lower values generated by regular regridding. Nevertheless, using daily frp will be more realistic and will include

the most intense fires responsible for the larger injections. This will likely result in an increase in the percentage prediction of the FRP of MISR plumes.

In summary, the constant injection height for the FH, HD, and VEG schemes together with the higher frequency in the occurrence of plumes reaching altitudes above the PBLH and the larger fractions of mass injected above it all result in larger annual mean differences from the CTRL simulation than the ones simulated for the FRP scheme. However, FRP provides a better percentage prediction of the observed plumes as a consequence of the inclusion of important processes involved in the PH determination. Although some MISR outliers are missing, the FRP is a more realistic approach for representing the effects in a timelier manner with influences on transport and photo-chemistry. Nonetheless, the importance of injecting BB emissions —especially aerosol particles— at a certain height other than the surface is reflected in the effects on life-time, transport, and global burden.

4

Biomass burning primary aerosol emissions

This chapter focuses on the changes in the burden and transport experienced by the aerosol emissions as a consequence of selecting the injection height scheme. The set of simulations without feedback (Section 2.3) was therefore used.

The differences in the BB aerosol emissions were evaluated using PAT (Kunkel et al., 2012). These passive tracers help to identify the modifications in size distribution, transport, and deposition resulting from the selected injection height scheme. These passive tracers are a copy of the aerosol species from BB. They undergo the same processes as their original tracers, but they do not contribute to the total mass nor do they influence the chemical and microphysical properties of the total aerosol distribution. Using PAT helps to distinguish the OC and BC products of BB from the other sources, making them an ideal tool for analyzing the evolution of the BB aerosol emissions.

The passive tracers are primary implemented in the GMXe submodel (Section 2.1.2.1). The PAT undergo the same microphysical processes as real tracers e.g., coagulation and coating with condensable material, which can cause a transfer from hydrophobic to hydrophilic modes. The availability of this coating material is determined by thermodynamic conditions, which are affected by the altitude. Therefore, the microphysical processes that allow the aerosol particles to grow from the aitken size and transfer from the hydrophilic to the hydrophobic modes can be modified by the injection height. As the original tracers, the PAT experience dry and wet depositions. However, their influence on the transfer of radiation is excluded.

4. BIOMASS BURNING PRIMARY AEROSOL EMISSIONS

The number and mode in which the PAT are emitted is set in the GMXe namelist. Three aerosol tracers are created for this work: one for BC and two for OC. The emissions that these passive tracers represent are released in aitken size, which is insoluble for the former and both soluble and insoluble for the latter. New passive tracers are created for the modes in which products of the emitted tracer can be formed. In this case, the emitted tracers can be transferred to the soluble modes: aitken (ks), accumulation (as), and coarse (cs).

The distance at which the aerosol particles are transported depends on the time they remain in the atmosphere before removal. The height at which the emissions are injected influences the deposition efficiency by exposing the particles to different regimes. These regimes determine how much coating material is available as well as the necessary conditions for particle growth. The developing paths and the final sizes of the particles can therefore be different. As a result, the deposition rate, lifetime, and transport vary. Increasing the lifetime of the particles influences their global budget as well as the effects on radiation and on cloud processes and properties.

In this chapter, the microphysical and deposition processes as well as lifetime and transport are evaluated in order to obtain a complete overview of the evolution of BB aerosol emissions. The effect of the differences in the BB emissions on the total gas and aerosol tracers is evaluated in Chapter 5, and the effects on cloud and optical properties are addressed in Chapter 6.

4.1 Global Budget

The total load of the aerosol tracers is the result of several processes. This burden will be evaluated in this section in order to lay the framework for the changes addressed in the following sections. The two primary aerosol tracers, OC and BC, are emitted as BC_{ki} (PA03), OC_{ks} (PA01) and OC_{ki} (PA02). The total OC comprises 35% hydrophobic (OC_{ki}) and 65% hydrophilic (OC_{ks}). The three PAT created are treated as different tracers; the insoluble ones are therefore transferred to the soluble modes following subsequent growth, while the soluble tracers evolve into larger hydrophilic ones.

The relative differences in the global burden (compared with the CTRL simulation) of the three passive aerosol tracers are positive, indicating an increase in the global budget (Figure 4.1). There are larger differences in the PA01 tracer (compared with the CTRL
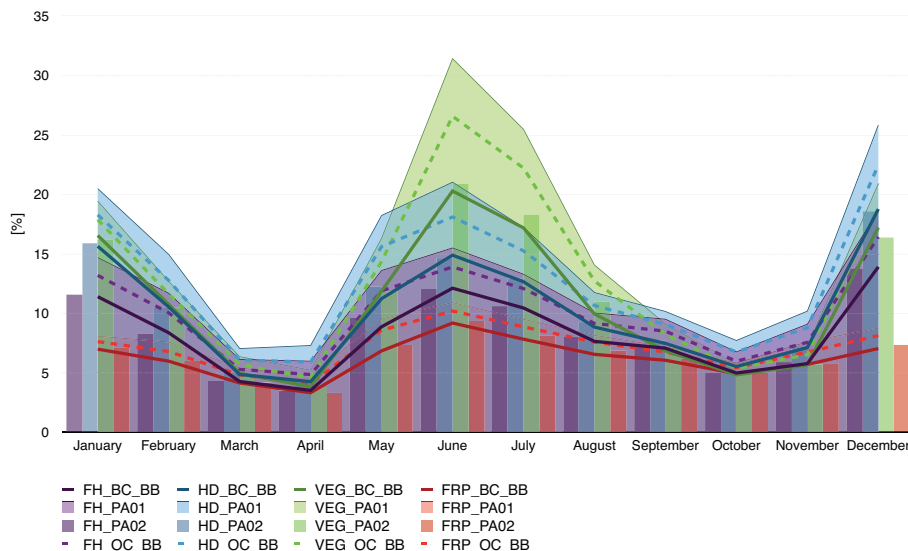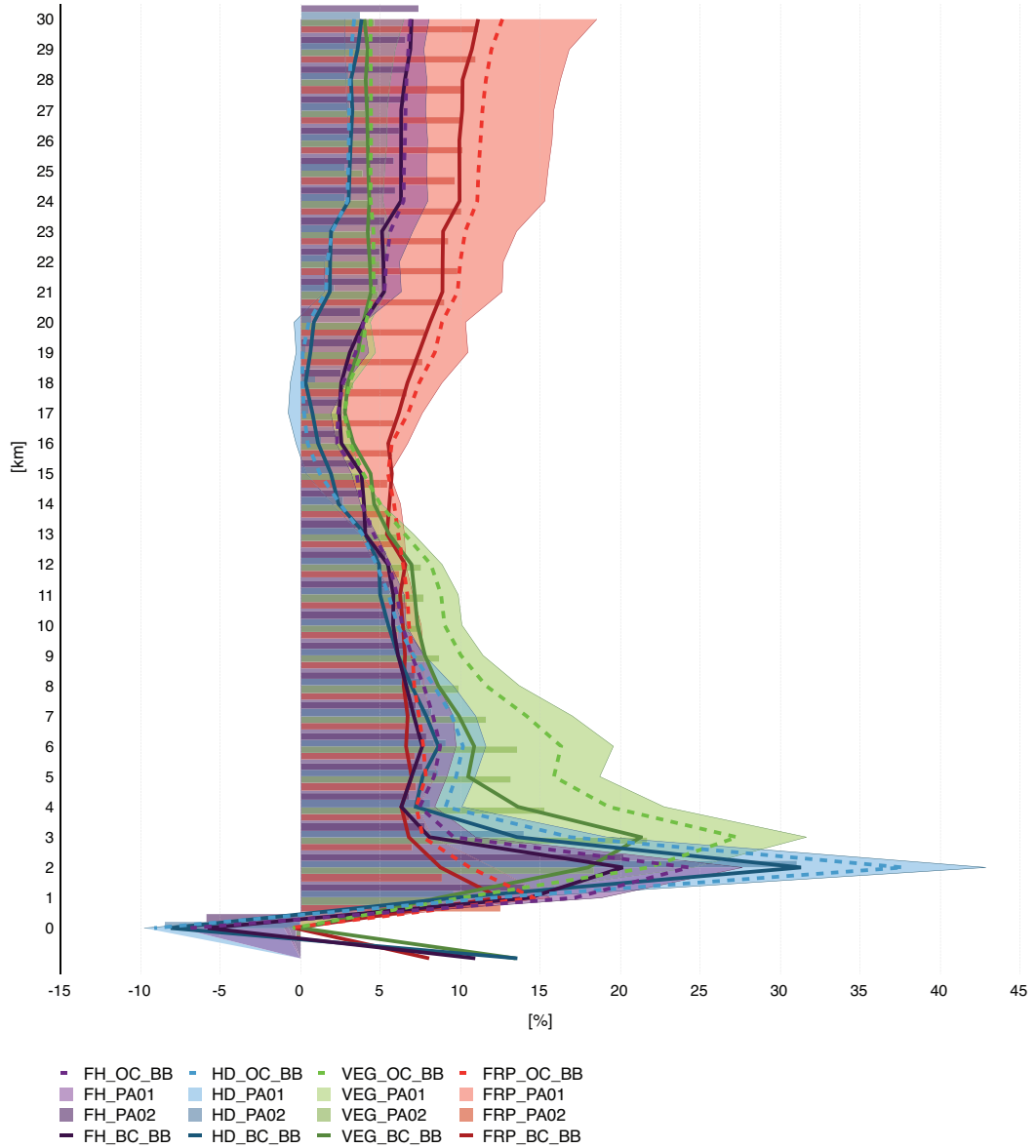
Figure 4.1: PAT global budget relative difference $\frac{\text{SCH-CTRL}}{\text{CTRL}} \times 100$.

Lines represent the relative differences of OC_{BB} (sum of PA01 and PA02, dashed lines) and BC_{BB} (PA03, continuous lines). The relative differences of the two OC passive tracers, PA01 and PA02, are represented by the bars (OC_{insol}, PA02) and by the areas (OC_{sol}, PA01).

simulation) because more than half of the OC is released in the aitken hydrophilic mode and because more OC is released than BC.

The magnitudes of the relative differences have minima in March and October, which is one month before the minima of the emissions and (as a consequence) the global burden that occurs in April and November. The larger differences arise in July and December i.e., the local summer months for the boreal and austral hemispheres.

During the boreal summer months, the largest relative changes are found in the VEG scheme. These are a result of the regional variations in the injection height in this scheme. During May to August (with a peak in July), some fires occurs for the vegetation type with injection height of 6 km. As discussed in the previous chapter, these plumes are constantly injected above the PBLH, thereby generating the largest change in the global burden (Figure 3.4). The HD scheme has major relative differences in the global burden (compared with the CTRL simulation) during the rest of the year. This is a consequence of the largest mean fraction of mass, which is injected above the PBLH in this approach (Table 3.1). The temporal and spatial variability in the FRP

scheme results in the lowest mean differences (Chapter 3). The vertical distribution of the relative difference of the three PATs (Figure 4.2) shows that the peak in the difference for each scheme is found at the average injection height: 1.5 km for FH; 2 km for HD; 3 km for VEG; and 1 km for FRP (Section 3.1). At altitudes higher than 12 km (where the aerosol concentrations are low), the FRP scheme shows the largest relative differences. This suggests that deep convection may play an important role as a vertical transport mechanism (see Section 4.5). No difference or even small negative differences (PA01) are observed in the HD scheme between 16 and 20 km (Figure 4.15). This suggests a less efficient vertical transport (see Section 4.5). VEG and FRP have small differences at altitudes lower than 1 km. This is because both schemes inject certain mass at these heights from small agricultural fires. In the VEG scheme, this has an assigned height of 100 m (Table 2.5). Aerosol emissions are released at the surface in the CTRL simulation because of the quick mixing inside the PBLH. However, this small difference suggests the importance of injecting the aerosol emissions at a height other than at the surface.

The relative differences for BC_{BB} and OC_{BB} are similar for altitudes higher than the tropopause. An exception is FRP, which shows the largest differences at the higher altitudes. Although the absolute values of the enhanced concentrations at this height are low, this behavior is common because enhanced aerosol concentrations in the UT/LS region have been associated with transport of BB emissions by deep convection (e.g., Andreae et al., 2001; Fromm and Servranckx, 2003; Jost et al., 2004; Luderer et al., 2006; Pickering et al., 1996).

For OC_{BB}, the relative differences are located between the PA02 and PA01 values. The magnitude of the changes in the OC_{BB} is usually closer to that of the PA01 values because 65% of the OC_{BB} emissions were released in this tracer. However, for the FRP scheme, at altitudes above the tropopause, the relative change in OC_{BB} is closer to the PA02. This is because soluble compounds are less likely to be transported to this height; they are more efficiently removed by wet deposition at lower altitudes. This suggest that in this region, the PA01 tracer may be transported by deep convection, thus creating a larger relative difference at this height, where it is less abundant.

The magnitude of the changes in the BC_{BB} is similar to that of the PA02 values because both represent the evolution of the Aitken hydrophobic tracers. The following sections address the increase in the global budget described in this section.

Figure 4.2: Global budget relative difference profile $\frac{\text{SCH-CTRL}}{\text{CTRL}} \times 100$.

Lines represent the relative differences of OC_{BB} (sum of PA01 and PA02, dashed lines) and BC_{BB} (PA03, continuous lines). The relative differences of the two OC passive tracers, PA01 and PA02, are represented by the bars (OC_{insol}, PA02) and by the areas (OC_{sol}, PA01).

4.2   Microphysics

As soon as the aerosol particles are released, they are subject to microphysical processes that determine their size evolution. In this section, the changes in the aerosol size distribution are addressed for the three aerosol tracers. In order to assess these differences, the ratio between the aerosol mass in a particular mode and the total mass of the aerosol tracer is compared to the same ratio in the CTRL simulation. Because of the increase in the total aerosol burden, a simple comparison of the tracers from the schemes with the ones from the CTRL simulation will be inaccurate. The particular aerosol mode must therefore be put in context with the total aerosol tracer in order to look at the changes in the mass distribution for the different aerosol sizes. The difference in these ratios indicates whether the fraction between a particular size and the total is preserved or whether the mass distribution has been modified.

The global annual mean changes in the particular ratios ^{PAT}mode/PAT with respect to the same ratios for the CTRL simulations were analyzed for the BC_{BB} and OC_{BB} (sum of PA01 and PA02) as well as the PA01 and PA02 tracers (Figure 4.3). The aitken insoluble (ki) ratio increased (compared with the ki ratio in the CTRL simulation) for all schemes and for all tracers containing the ki aerosol mode (i.e., BC_{BB}, OC_{BB}, and PA02). The ki ratio increased because of the direct emission of this mode by BC_{BB} and by the PA02 tracer (originated from the OC_{ki}). The increase is partially the result of the deposition processes, which are less efficient for aitken particles. The enhancement in the ki faction also suggests a slower transfer to the hydrophilic modes as a consequence of the vertical distribution of the available coating material and the concentrations of the released ki particles. In some regions, the available coating material increases at altitudes other than the injection height or remains unchanged (compared with the CTRL simulation), whereas the amount of ki particles is larger. This results in a smaller fraction (compared with the CTRL simulation) of the released ki particles being transferred to soluble modes for the plume height simulations. The reduced efficiency of the transfer to the hydrophilic modes is reflected in the decrease of the ratio of these soluble modes for PA03 (BC_{BB}) and PA02 (Figure 4.3). The magnitude of the increase in the ki ratio is similar for PA03 (BC_{BB}) and for PA02. Nevertheless, the amplitude of increase in the ki ratio is limited when the total OC_{BB} iis considered (dark solid color bars in Figure 4.3) because PA02 represents only 35% of the total OC_{BB}.

Analogous to the increase in the ki ratio of the PA03 and PA02, the increase in ks for the PA01 tracer (originated from the OC_{ks}) is positive and large (e.g., 20% for HD) as a consequence of the direct emission in this mode and the less efficient removal of this size. Despite the considerable enlargement shown by the PA01, the ks mode represents a small fraction of this tracer. Moreover, although PA01 represents more than half of the total OC_{BB}, considering the reduction of the ks shown by the PA02 will result in an impact of lower magnitude (e.g., $\approx 3\%$ for HD) over the total increase in the ks fraction for OC_{BB}.
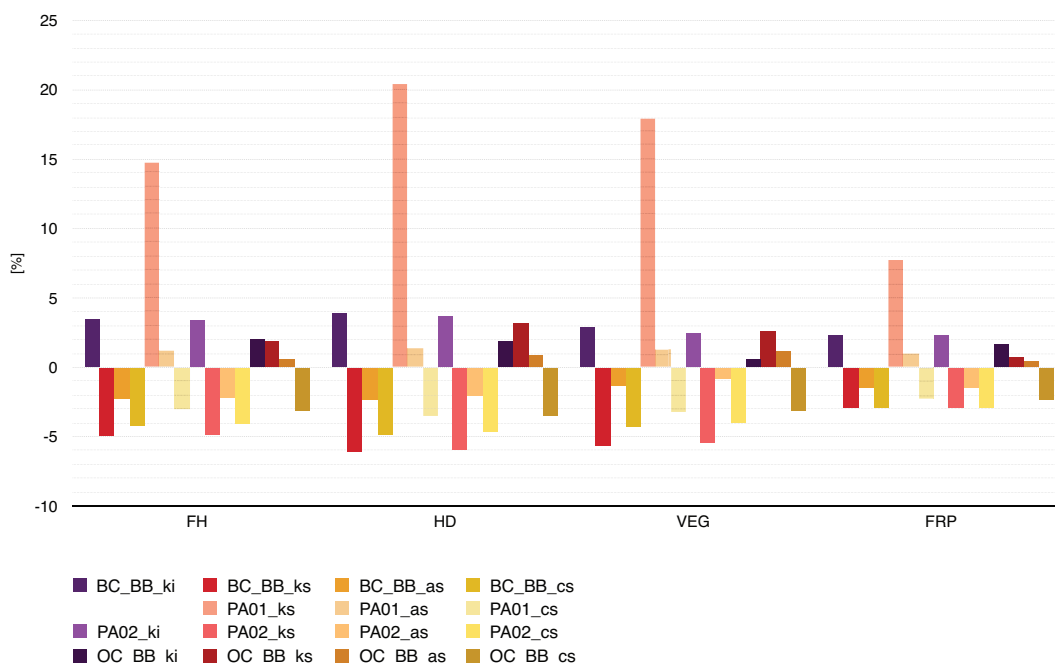
Figure 4.3: Ratio $\frac{PAT_{mode}}{PAT}$ relative difference $\frac{SCH\text{-}CTRL}{CTRL} \times 100$.

ki: aitken insoluble; ks: aitken soluble, as: accumulated soluble; cs: coarse soluble.

Each scheme set is composed by: the four BC_{BB} aerosol modes, the four OC_{BB} (sum of PA01 and PA02) aerosol modes, the three OC_{sol} aerosol modes and the four OC_{insol} aerosol modes.

The vertical profiles of the PAT_{mode}/PAT ratio for BC_{BB} (Figure 4.4) and for OC_{BB} (Figure 4.5)as well as for the individual PA01 and PA02 tracers (Figure 4.6) show patterns similar to the ones discussed for Figure 4.3.

The ki fraction for the schemes is larger than the one for CTRL for altitudes above the injection heights. At the surface, where the CTRL simulation releases the emissions,

the fraction of ki is larger for the CTRL than for the schemes; this difference in the ki ratio is smaller for VEG and FRP schemes because of their injections at lower heights in some regions. As a consequence of the lower amount of ki at the surface for the injection height simulations (compared with the CTRL), the fraction of particles that can be transferred to the hydrophilic modes is larger in the plume height simulations. Therefore, for all schemes, the fraction of the hydrophilic modes as and cs increases at the surface.

For BC_{BB}, the ks fraction at the surface is low, and the small differences appear only at altitudes above 13 km. For OC_{BB} (Figure 4.5), the ks fraction shows small differences at the altitude of the average injection heights as a result of the direct emission of the PA01 in this size, which produces the increases shown in Figure 4.6. For FRP and VEG schemes, the increases in the fraction of ks at higher altitudes suggests the immediate vertical transport of the injected emissions (Figure 4.6). At the same time, as a consequence of the emissions of ki mode by the PA02 and the subsequent transfer of this mode to the ks, differences in the ks can be seen at higher altitudes in the OC_{BB} (Figure 4.5). These are similar to the ones seen for BC_{BB} in Figure 4.4. The VEG scheme shows the most substantial change in the ks ratio at 16 km for both BC_{BB} (Figure 4.4) and OC_{BB} (Figure 4.5).

At altitudes above the tropopause (approx. 15 km), for the three aerosol passive tracers, FRP depicts a larger increase in the relative difference of the as fraction than the other schemes (Figure 4.2). Although at this height, the aerosol concentration is extremely low and the extra mass is not enough to modify the size distribution, the fact that the increase in the as mode is seen at this altitude suggests a vertical transport in addition to the direct injection occurring after the ageing of the emitted particles.

The biggest divergence from the CTRL occurs at the altitude of the average injection height of each scheme. Increasing the ks fraction only slightly affects the mass distribution because it only represents about 1.8% of the total OC mass. However, it does locally affect the lifetime of the OC because the smaller particles are less efficiently removed.

The ks mode represents a small fraction of the total OC_{BB} closer to the surface. Above 4 km, the fraction increases (Figure 4.5 for the OC_{BB}, and Figure 4.6, for the individual PA01 and PA02 tracers). The effect of the relative increase in this size is therefore limited and becomes important only at higher altitudes, where the concentration of the

tracers decay.

The geographical distribution of the differences between the ratio $^{PAT_{mode}}/_{PAT}$ for the injection height schemes and the ratio for the CTRL follows the trend in most regions. For BC_{BB}, the increase in the ki ratio can be seen in vicinity of the BB production regions as well as downwind in the transport zones that extend over the ocean for all schemes. An exception is VEG, which shows an increase in ki in less extended areas as a consequence of the constant higher injection altitudes in this scheme (Figure 4.7). Contrary to the global tendency (Figure 4.3), a decrease in the ki ratio occurs in Alaska and Canada (Figure 4.7). VEG and HD schemes show the biggest differences in this region as a consequence of the average injection of the emissions at altitudes higher than those of the FH and FRP schemes. This suggests a more efficient transfer from the hydrophobic to the hydrophilic modes for those VEG and HD because of the altitude dependency of the parameters (temperature and pressure), which determines the available coating material and regulates the transfer to the hydrophilic modes. For HD, the transport zone in the North Pacific Ocean does not show a decrease in the ki ratio as it does for the VEG scheme but rather an increase as it does for the other schemes (Figure 4.7).

The ki ratio changes are associated with the changes in the as ratio (Figure 4.8) i.e., in the areas where the ki ratio increases, the as ratio decreases. In contrast, in the regions where the ki ratio decreases, the as ratio increases. The increases in the hydrophilic modes ratio are more intense for the HD and VEG schemes; for the latter, it extends to the North Pacific Ocean and to the North Atlantic, which is consistent to the decrease in the ki ratio for VEG in those areas. This increase in the hydrophilic ratios for the VEG scheme is reflected in a 50% increase of the fraction of BC that comes from BB in the as mode and in 35% over the North Atlantic and North Pacific Ocean.

The differences for ks are closer to zero because this aerosol mode represents only a small fraction of the total species (Figure 4.4). The cs ratio decreases in most regions, which follows the global trend (Figure 4.9). However, in some areas (e.g. The South Atlantic Coast of Argentina in the VEG scheme), the particles are able to grow all the way to the cs, thereby increasing the ratio of this aerosol mode in those regions.

The increases in the ki ratio for OC_{BB} are less extended than the increases for BC_{BB} because the ki aerosol mode represents a smaller fraction of the former than it does for the latter (Figure 4.10).
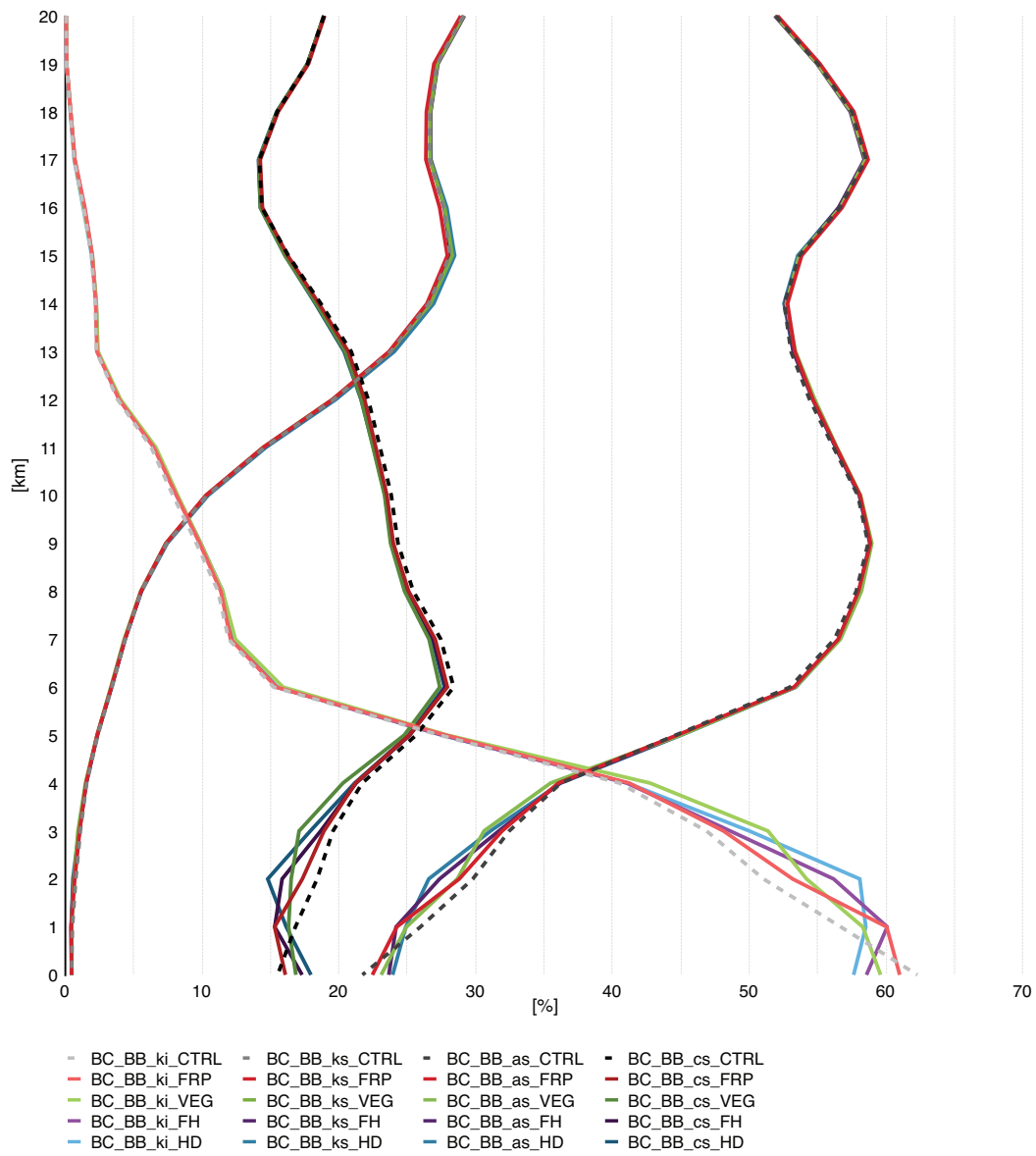
Figure 4.4: Ratio $\frac{\text{PA03}_{\text{mode}}}{\text{PA03}}$ vertical distribution.

SCH values are in continuous lines; CTRL values are in dashed lines.
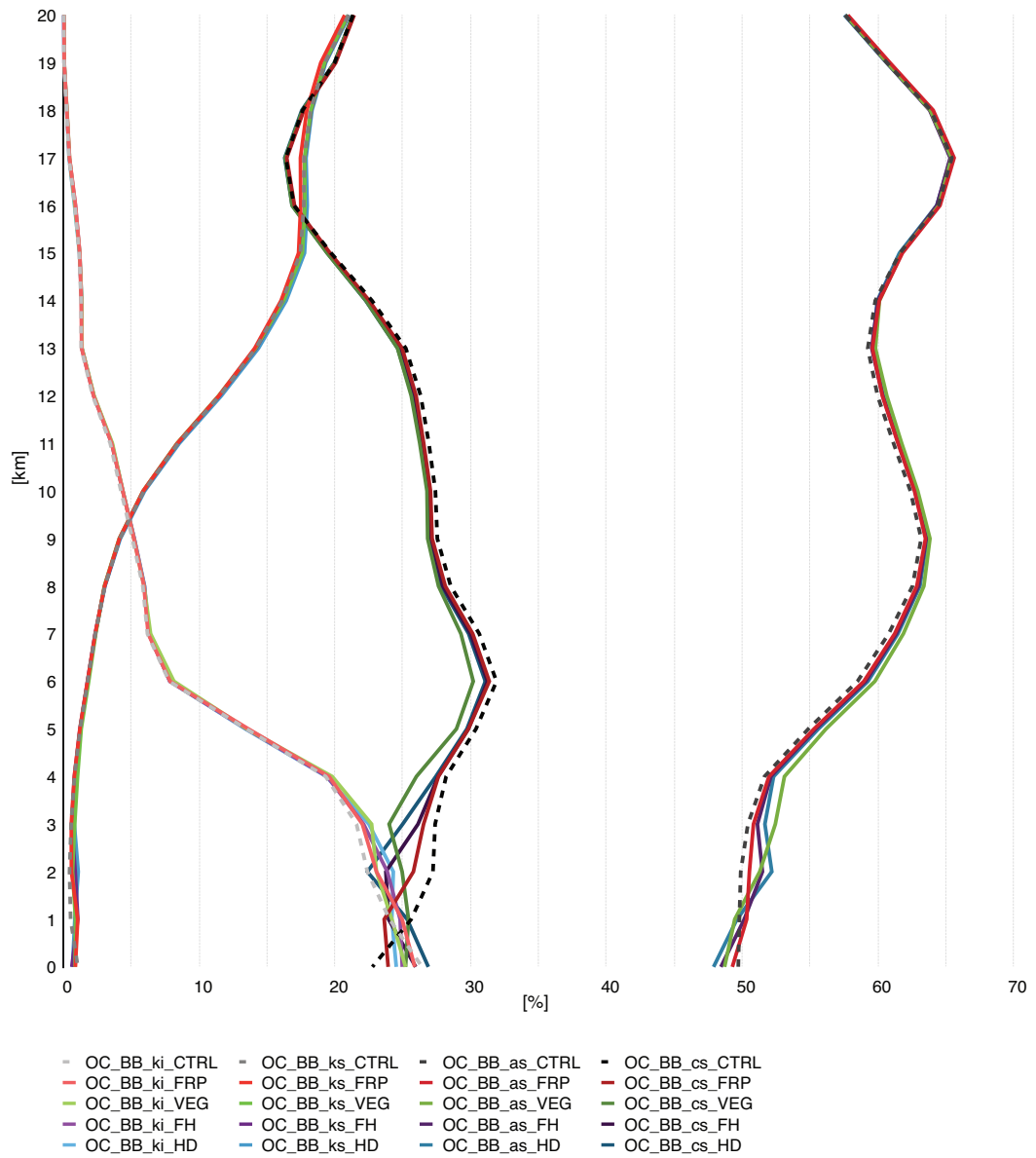
Figure 4.5: Ratio $\frac{\mathrm{PA0102_{mode}}}{\mathrm{PA0102}}$ vertical distribution.

SCH values are in continuous lines; CTRL values are in dashed lines.
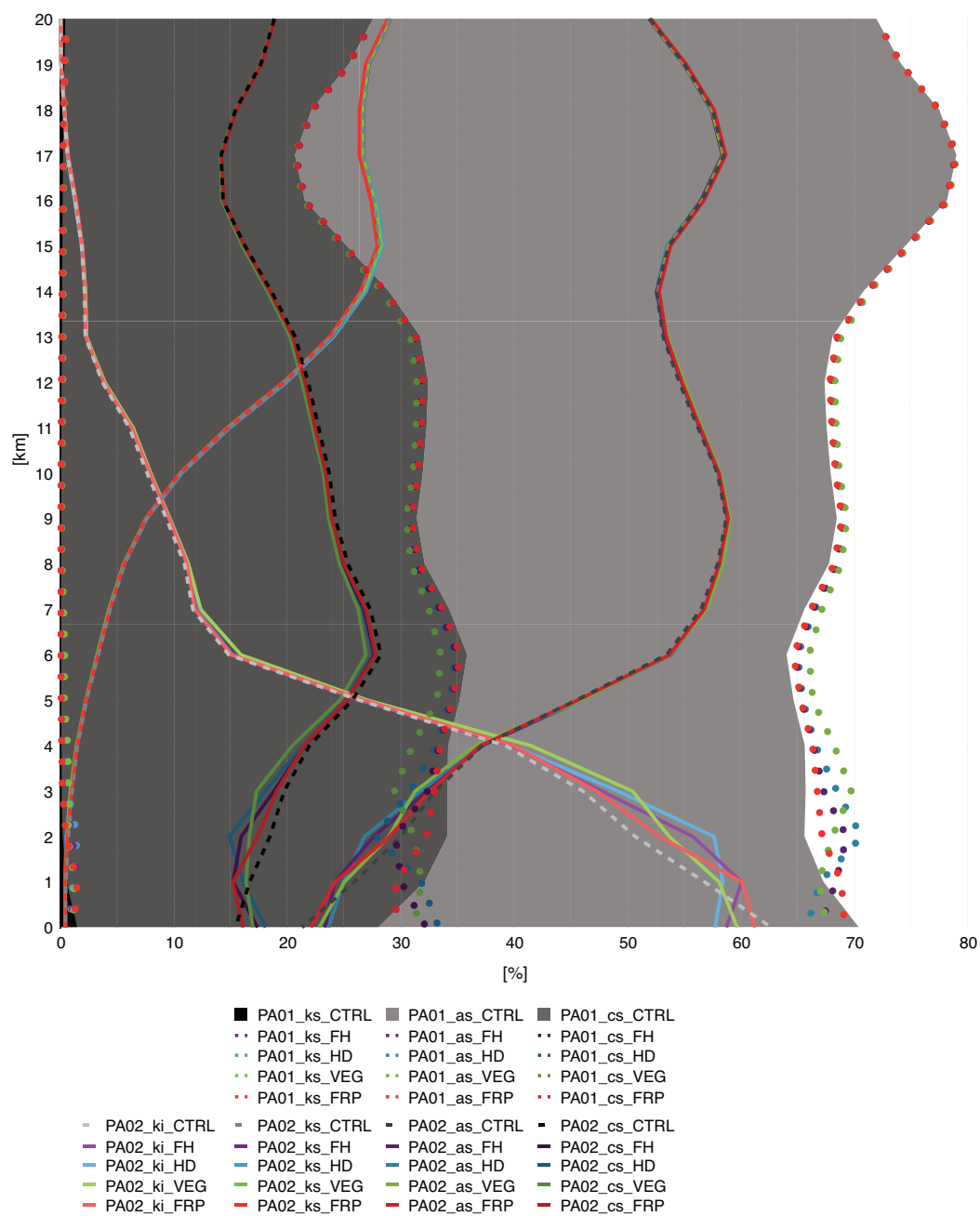
Figure 4.6: Ratio $\frac{\text{PAT}_{\text{mode}}}{\text{PAT}}$ vertical distribution.

SCH values are in continuous lines; CTRL values are in dashed lines.

The ks mass ratio increases throughout the BB production regions, especially in South America and Indonesia for all schemes as well as in Canada for the VEG scheme. Even though an increase in the as ratio is observed in the transport regions after the ageing of the particles, in most downwind regions, the aerosol is not able to grow up to cs. The VEG scheme has the biggest magnitude in the increase in the cs ratio over a wider area than the other schemes e.g., the Southern Coast of Argentina extending all the way to the Antarctic Northern Coast as well as the Sahara Desert and the Pacific Coast of North America.

The differences in the ratios seen in the VEG compared to the other schemes highlights the importance of the injection height over the availability of coating material and the thermodynamic conditions present at the different regions and injection altitudes, which results in diverse ageing paths experienced by the particles.

The transfer from the hydrophobic to the hydrophilic mode is determined by coagulation with hydrophilic particles as well as condensation. The fraction of hydrophobic particles that can be transferred is therefore limited by the amount of soluble material. The injection of the emissions at higher altitudes implies different temperature and pressure conditions. These directly affect the amount of soluble material, which also varies regionally.

Over Africa, the concentration of bisulphate (HSO_4^-) show an annual mean increase of 2 to 3% at heights ranging from 1.5 to 3 km. Sulfate (SO_4^{2-}) shows an annual mean increase from approx. 2% (VEG and FH) to 3% (HD) at approx. 2 km, whereas FRP shows increases of less than 1%. For ammonium (NH_4^+), there is an enhancement in the annual mean concentrations. This amounts to 3.3% at 2 km for VEG and 5.6% (HD) and 4.2% (FH) at 1.6 km. Nitrate (NO_3^-)has an annual mean increase of 2.7% (FRP) at the average injection height, 7.3% (VEG and FH) at 1.5 km, and up to 8.6% (HD) at 1.6 km. Over Indonesia, with respect to HSO_4^- concentration, there is an annual mean increase of 4 to 8% at 6.5 and 15 km. Over Alaska, the annual mean increase of HSO_4^- is 2.9% (HD) at 1.5 km and 5.7% (VEG) at 13 km.

The increases in HSO_4^-, SO_4^{2-}, NO_3^- and NH_4^+ affect the transfer to the hydrophilic modes through coagulation but are not reflected by a decrease in the ki mode number concentration in those areas. Conversely, there is an increase in the ki number concentration, which is also apparent in the increased mass ratio (Figure 4.7).
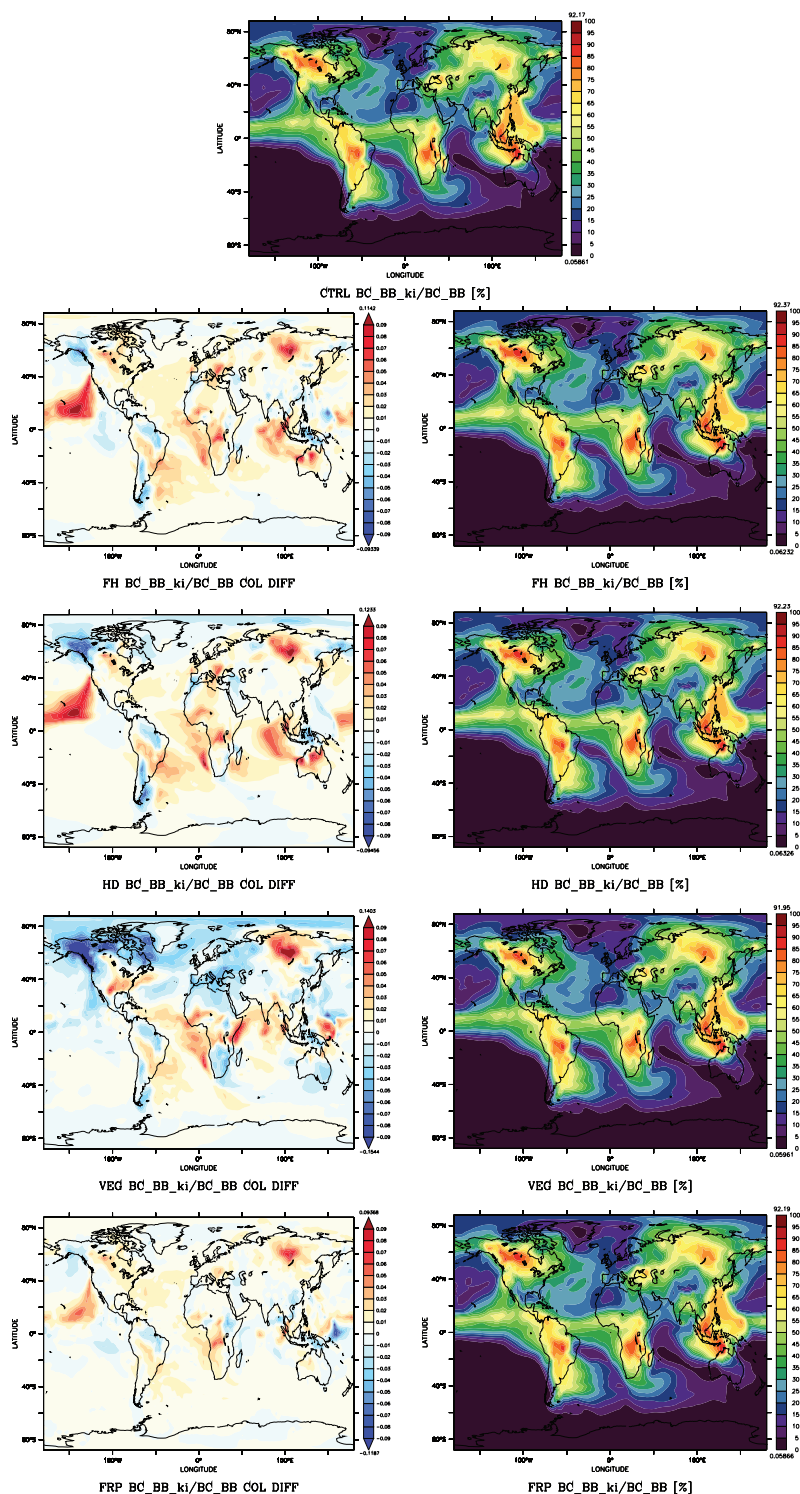
Figure 4.7: Column integrated ki ratio $\frac{\text{BC BB}_{ki}}{\text{BC BB}}$.

The central image shows the column integrated ki ratio for CTRL. The left panels show the difference between the column integrated ratio for injection height schemes and the one for the CTRL simulation. The right panels show the associated column integrated ki ratio for each injection height scheme.
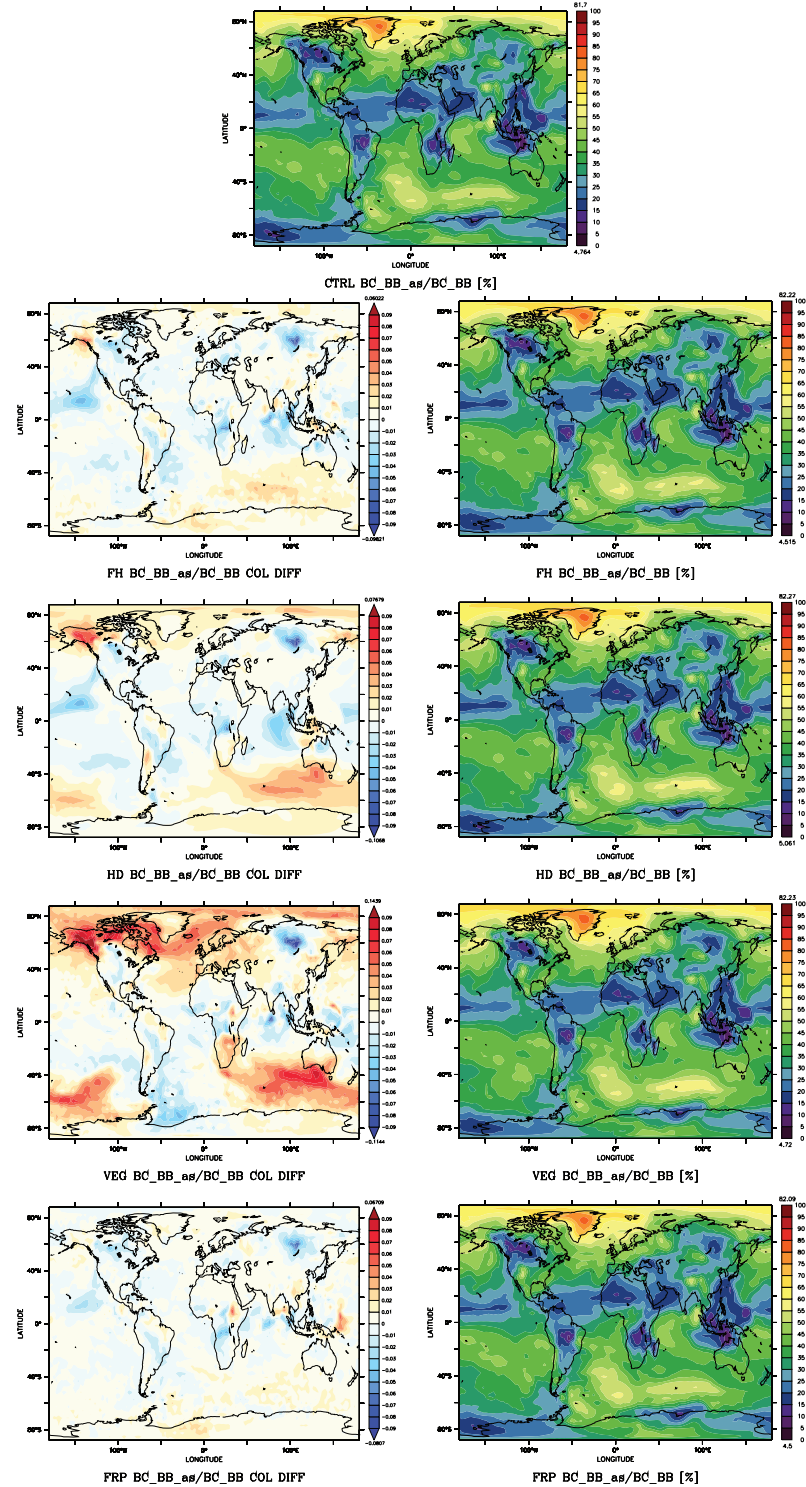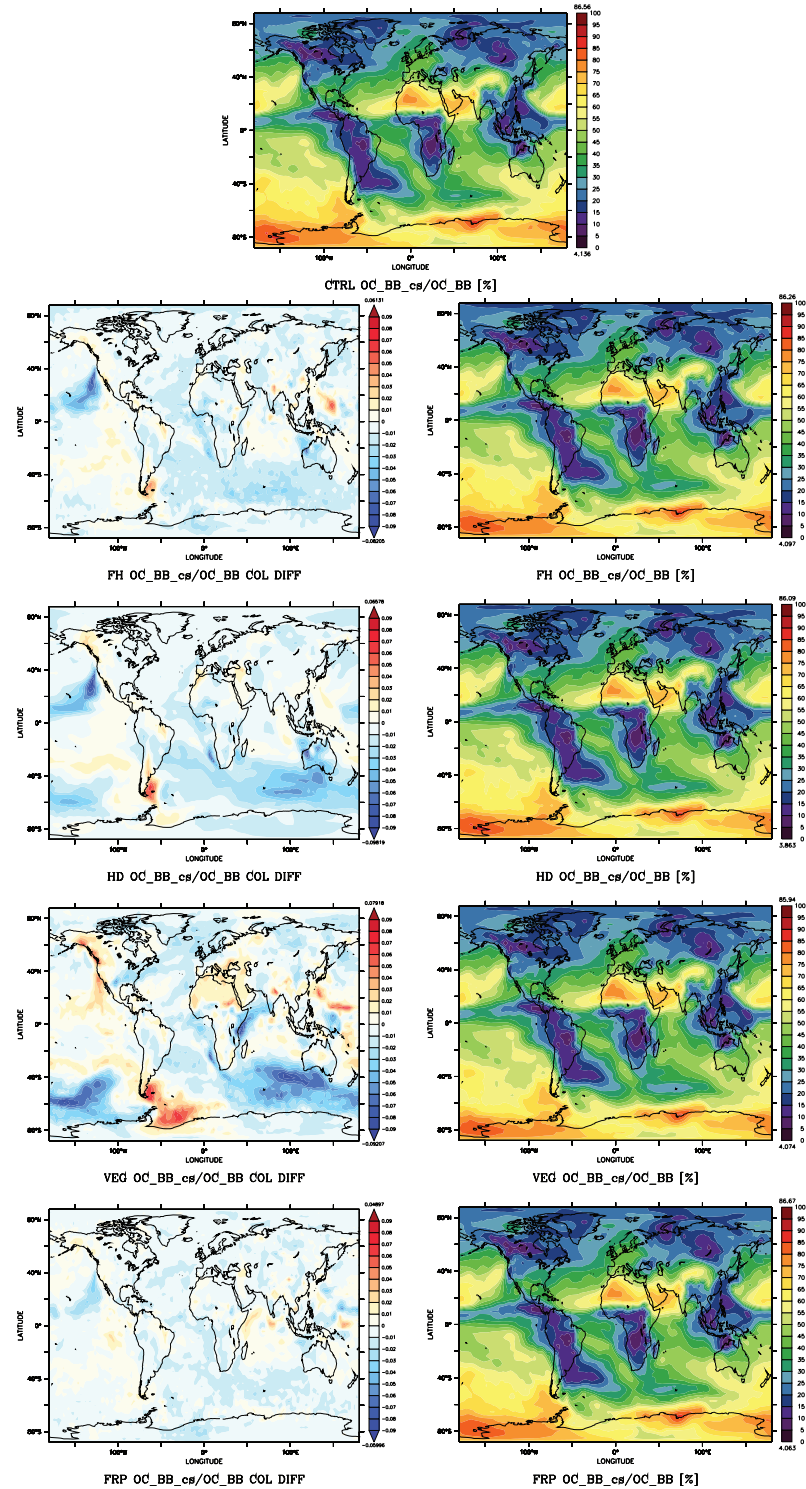
Figure 4.8: Column integrated *as* ratio $\frac{\text{BC BB}_{as}}{\text{BC BB}}$.

The central image shows the column integrated *as* ratio for CTRL. The left panels show the difference between the column integrated ratio for injection height schemes and the one for the CTRL simulation. The right panels show the associated column integrated *as* ratio for each injection height scheme.
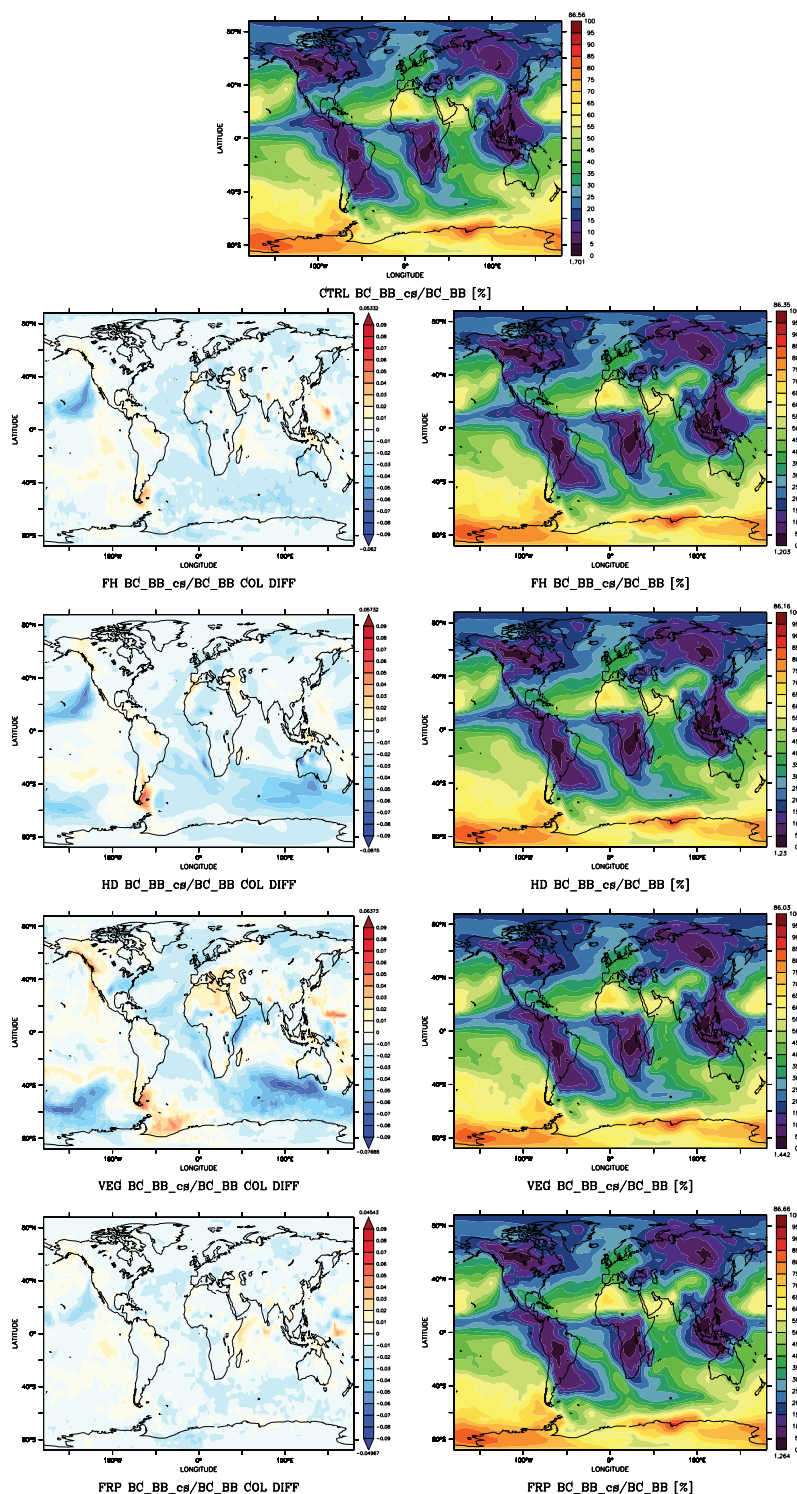
Figure 4.9: Column integrated *cs* ratio $\frac{\text{BC BB}_{cs}}{\text{BC BB}}$.

The central image shows the column integrated *cs* ratio for CTRL. The left panels show the difference between the column integrated ratio for injection height schemes and the one for the CTRL simulation. The right panels show the associated column integrated *cs* ratio for each injection height scheme.
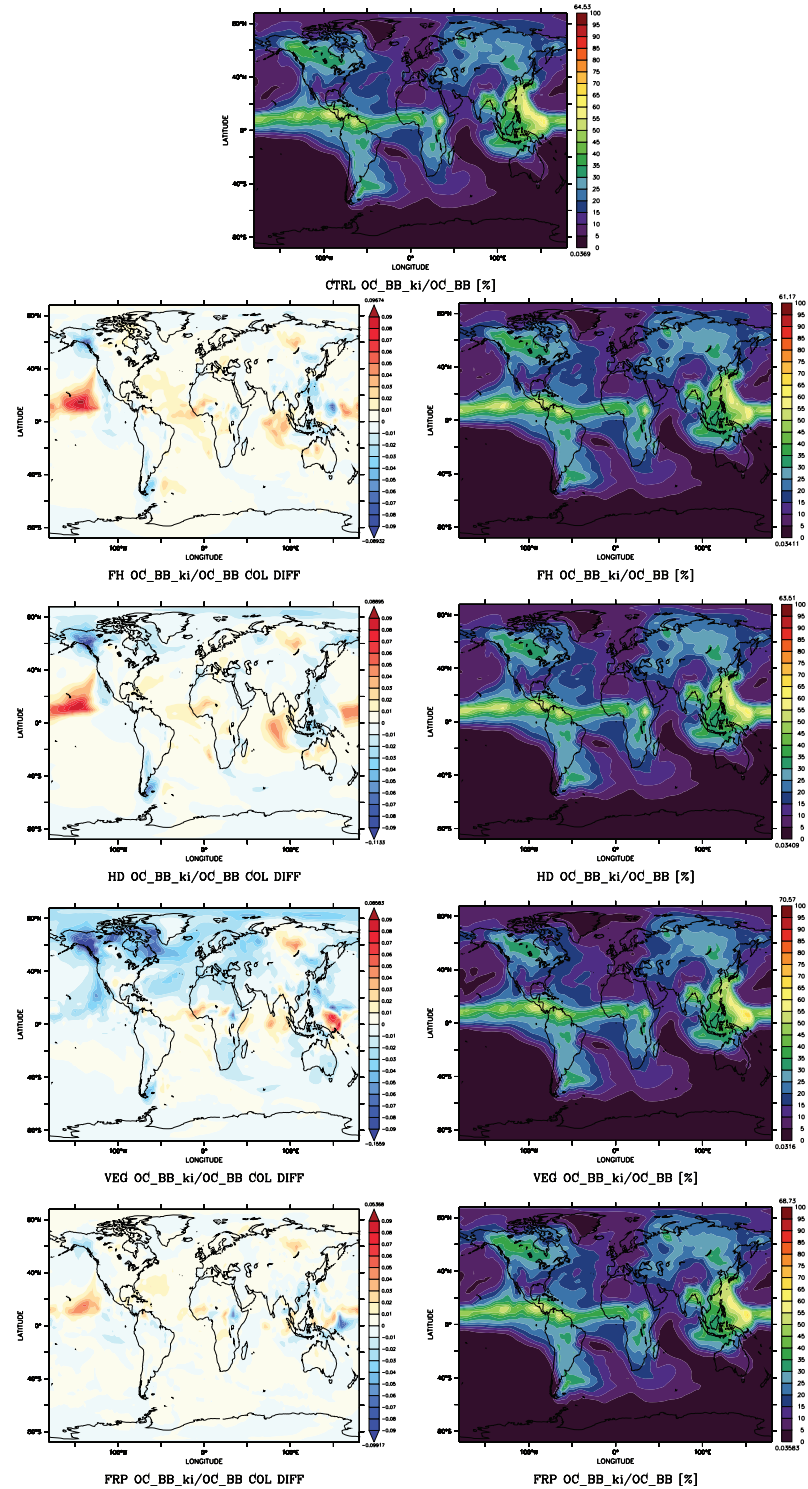
Figure 4.10: Column integrated ki ratio $\frac{\text{OC BB}_{ki}}{\text{OC BB}}$.

The central image shows the column integrated ki ratio for CTRL. The left panels show the difference between the column integrated ratio for injection height schemes and the one for the CTRL simulation. The right panels show the associated column integrated ki ratio for each injection height scheme.
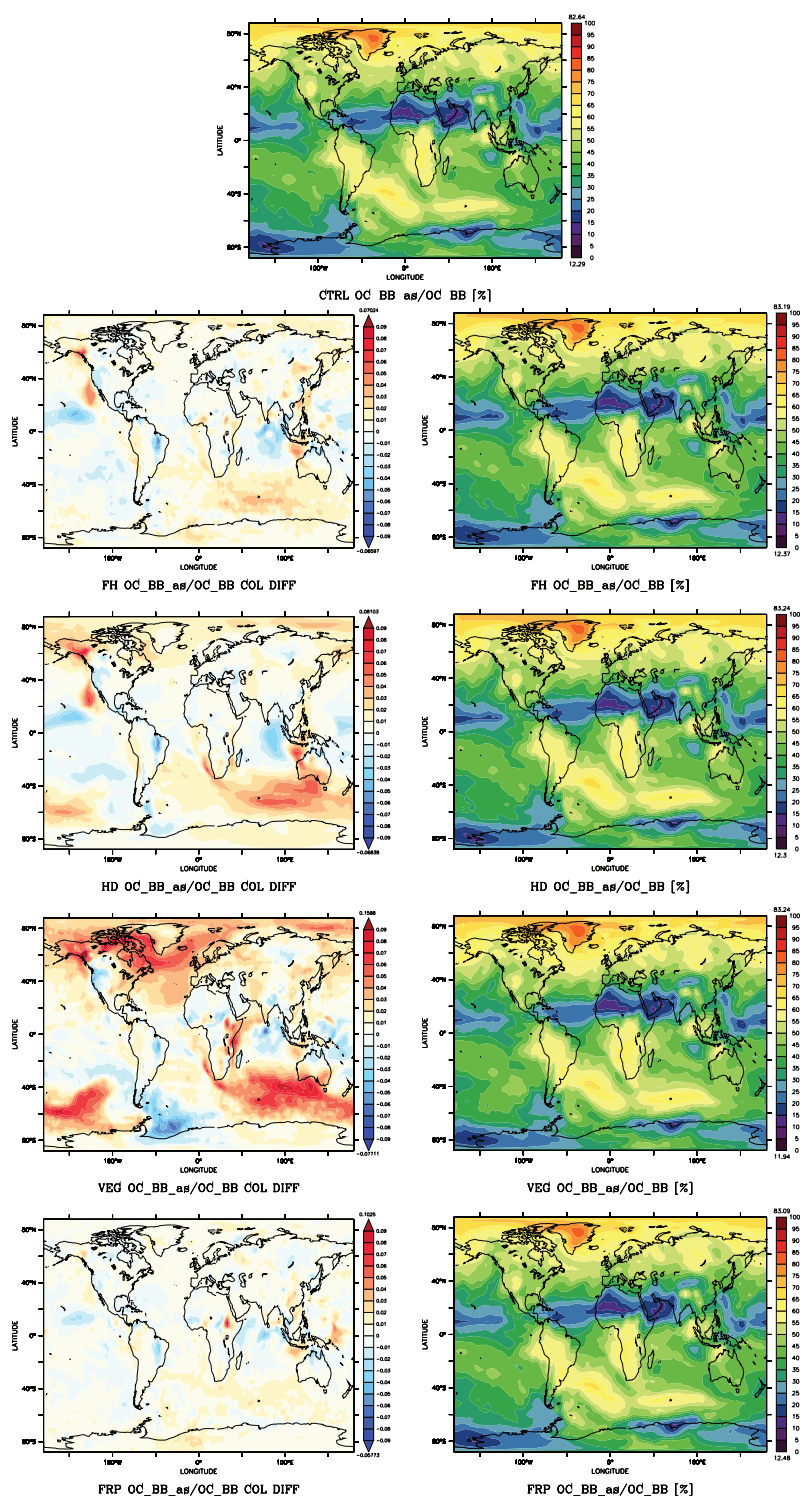
Figure 4.11: Column integrated *as* ratio $\frac{\text{OC BB}_{as}}{\text{OC BB}}$.

The central image shows the column integrated *as* ratio for CTRL. The left panels show the difference between the column integrated ratio for injection height schemes and the one for the CTRL simulation. The right panels show the associated column integrated *as* ratio for each injection height scheme.

Figure 4.12: Column integrated *cs* ratio $\frac{\text{OC BB}_{cs}}{\text{OC BB}}$.

The central image shows the column integrated *cs* ratio $\frac{\text{OC BB}_{cs}}{\text{OC BB}}$ for CTRL. The left panels show the difference between the column integrated ratio for injection height schemes and the one for the CTRL simulation. The right panels show the associated column integrated *cs* ratio for each injection height scheme.

4. BIOMASS BURNING PRIMARY AEROSOL EMISSIONS

Coagulation is determined by Brownian motion and is strongly affected by the particle concentration. The increase in the soluble aerosol responsible for coagulation does not directly translate into an efficient transfer of the hydrophobic aerosol to the hydrophilic aerosol because it is observed at altitudes that often do not match the average injection height or where the aerosol concentration is low.

Condensation is also responsible for the changes in ageing paths experienced by the particles. The amount of gas species that can kinetically condensate is determined by the Gibbs energy and influenced by thermodynamic conditions that change along the height. The fraction of gas that can kinetically condense can be estimated. However, the amount that actually condenses is influenced by the volatility of the compound as well as thermodynamic conditions.

Condensation can be influenced by increases in nitric acid (HNO_3) and sulfuric acid (H_2SO_4). Globally, the annual mean concentration of the sulfuric acid is slightly enhanced—from less than 1% (VEG and FRP) to 2.2% (FH and HD). The global and annual mean concentration of HNO_3 increases by approx. 3 to 6% at 2 km. Nitric acid is one of the major products of NO_x chemical processing, and BB emissions contain more NO than SO_2.

Over Africa, annual mean increases in HNO_3 range from 2.5% (FRP) to 20% (HD). There are also increases in H_2SO_4 ranging from 2.3% (FRP) to 13.4% (HD). The annual mean increase of both HNO_3 and H_2SO_4 is located below the average injection height, which is at 2 km for VEG and 1.5 for the other schemes. Over Alaska, an annual mean increase in HNO_3 of 2.3% is observed exactly at the average injection height of the VEG scheme, while for HD scheme, the annual mean increase is of 3% but located slightly below the average injection height at 1.5 km. Moreover, for FRP, an annual mean increase of 2.5% in HNO_3 is observed at the average injection height. However, this does not result in an efficient transfer to the hydrophilic mode.

The amount of material that can potentially condense can fluctuate (e.g. there is a larger increase in HNO_3 over Africa than in Alaska). The differences in the transfer from the hydrophobic to the hydrophilic modes suggest that the variations in temperature along the height plays the most important role in condensation because it determines the material that can actually condense.

Considering that the increase of material affecting both coagulation and condensation mainly occurs at different heights than the average injection altitudes, it is reasonable

to assume that in most regions, the hydrophilic material remains the same as for the CTRL simulation at the injection heights. Therefore, a smaller fraction of hydrophobic material can be immediately transferred to the hydrophilic modes because more insoluble particles are present. The ki particles are less efficiently removed from the atmosphere, which allows them to interact with coating material at the regions and altitudes to which they are transported. The resulting smaller fraction of ks (originated from the BC_{ki} and OC_{ki}) may therefore be the result of an immediate transfer of some of the ki particles to the as mode via coagulation. For OC_{ks}, however, the increase in the mass fraction of ks in the BB regions is directly attributed to the injection in this aerosol mode. Following transport and deposition, the passive tracer, OC_{ks}, encounters the soluble material and evolves into as, thereby increasing the mass fraction of this size.

The changes in the different aerosol mode ratios, which ultimately affect the size distribution, can be attributed to the different conditions that the particles encounter at the height at which they are injected. The modifications observed in the mass distribution of the BC_{BB} affect the total BC i.e., by increasing the ki ratio and decreasing the other aerosol modes. Although the global effect on the mass distribution is small ($\approx 1\%$), the local differences have considerable changes seasonally and on the annual mean.

The changes in both OC_{BB} passive tracers result in a change of 1% on their global size distributions following their respective trend of the modifications i.e., for the tracer originating from OC_{ks}, an increase in the ks and as and a decrease in the cs; for the tracer originating from OC_{ki}, an increase in ki and a decrease in the hydrophilic aerosol modes. The contribution of OC from BB increased for all aerosol sizes because of the increase in the global burden of OC from this source. The contribution of the OC_{ki} passive tracer to the total ki fraction of OC increased from 70% in the CTRL simulation to up to 76% in the HD simulation. Because BB contributes less to the OC than it does to the BC, the changes in the mass distribution of the total OC result in a small increase in ki and as, and a small decrease in ks and cs. As a consequence of the high regional and temporal variability of BB, for ks and ki, these effects of 1% can grow up to 40% to 60% annually and up to 80% on July; for as and cs, the differences are lower (from 6 to 12% annually and up to 40% in July). The combined effect of both organic carbon passive tracers can be seen in the changes to the contribution of BB to the total OC (Figure 4.20).

4.3 Deposition

Aerosol particles are subject to microphysical processes and are also removed from the atmosphere by deposition. The selection of the injection height scheme directly affects those processes. The changes generated by the injection height can also affect the removal mechanism itself. These effects are analyzed in this section.

The injection height does not modify the total deposition. However, it does influence the amount of mass removed by the different processes as well as the areas where the deposition occurs after the particles have been transported.

The distribution of the average deposition shows negative differences of approx. 40% in the production areas. Because of transport mechanisms, positive differences are observed in the rest of the world. An important deposition region is located over the North Atlantic. For HD, there is an annual mean increase of 70% to more than 100%. This area is also associated with an increase in the contribution of BB to the total BC and OC tracers (Figures 4.19 and 4.20).

4.3.1 Dry Deposition

The immediate effect of the injection height on the deposition processes takes place in the dry deposition (DDEP, Section 2.1.2.1), which only acts in the lowest model layer. The effect of the injection height on the dry deposition at the surface is of higher magnitude for the aerosol emissions because unlike the gas emissions injected at 140 m, they were released at the surface in the CTRL simulation.

When the aerosol emissions are injected above the surface layer, differences of -50% for VEG, and up to -68% for the HD scheme emerge in the areas of BB production. Positive differences of higher magnitude are observed over the ocean because of transport. The total fraction of mass removed by dry deposition at the surface decreased from 14% in the CTRL simulation to approx. 8 to 9% in all schemes. Because of the small injection heights at some regions in VEG and FRP, the global mass removed by dry deposition at the surface is slightly higher than the mass removed by the same mechanism in FH and HD.

The mass that is not removed by dry deposition at the surface (in the injection height schemes) is removed by sedimentation and scavenging, which influence the total fraction of mass removed by those mechanisms.

The other dry deposition mechanism, sedimentation (SEDI, Section 2.1.2.1), is both directly (by the injection of the emissions at higher altitudes) and indirectly (by modifying the size distribution) affected by the injection height; directly. Sedimentation is more important for aerosols than for gases because of the lack of mass of the gases (compared with aerosols). Moreover, the velocity at which the particles settle depends on their diameter; larger particles sediment faster than smaller ones do. Therefore, when the emissions are injected at higher altitudes, the particles travel downwards to the boxes according to their diameters and associated terminal velocities. If the size distribution of the particles remains unchanged, the effect of the injection height is direct and the particles have to travel further downwards before reaching the surface and being completely removed. On the other hand, if the injection height does change the size distribution, the terminal velocity is adjusted according to the new size distribution. The injection height thus indirectly affects sedimentation. As shown above, the injection height influences the size distributions by increasing smaller particles and decreasing larger particles, which reduces the overall sedimentation velocity.

The relative differences observed in the annual mean sedimentation of the ki size of the PA02 and PA03 tracers, originated from the OC and BC aitken insoluble, goes from -60% for VEG and up to -76% for HD, in the areas of BB production. A positive difference in the sedimentation is observed in the rest of the world because of the transport and slow removal of the particles. The sedimentation of all aerosol sizes in both PA02 and PA03 tracers has relative differences of -25% for FRP and -34% for FH. While for the tracer originated from the OC_{ks}, the observed differences in the sedimentation are of higher magnitude, they follow the same tendency; i.e., the magnitude of the differences in the sedimentation of the fine aerosol is higher than the sedimentation of the total aerosol sizes. This suggests that the changes in the distribution of aerosol size generated by the injection height have a stronger influence on the sedimentation than the direct effect produced when the emissions are released at different altitudes.

Together, the direct and indirect effects of the injection height on the sedimentation result in a slower removal of aerosols, which increase the lifetime —and therefore the transport and the average global burden— of the tracers.

The indirect effect only applies to the fine particles, and the contribution of this particle size to the total mass is negligible. It therefore influences the lifetime of the particles rather than the average global burden. In contrast, the direct effect applies to all parti-

cle sizes and more strongly influences the average global burden than the indirect effect does. Therefore, the global burden increase results from lifetime changes, which are a product of the slow removal caused by the direct and indirect effects of the injection height. Because the fraction of fine aerosol is different for BC than it is for OC, the changes in sedimentation caused by the changes in the size distribution influence the lifetime of BC more than that of OC. Moreover, because of the larger fraction of fine aerosol for BC than for OC, both the lifetime and global burden of BC are more affected than those of OC.

On the other hand, for both BC and OC tracers, the direct effect, which influences all particle sizes, contributes equally to the lifetime and thus to the global burden. When injected at certain height, the fraction not removed by dry deposition at the surface must be removed by another mechanism e.g., sedimentation. This would increase the fraction of mass removed by sedimentation. However, at the same time, the changes in the distribution of aerosol size reduce the efficiency of this removal mechanism, thereby resulting in a smaller fraction of sedimented material. For BC_{PAT}, the total fraction of mass removed by sedimentation does not change, suggesting that globally, both processes equilibrate and that wet deposition removes the extra-fine particles caused by the injection height. For OC_{PAT}, there is a small decrease in the annual mean mass removed by sedimentation.

The changes generated by the injection height do not influence the total fraction of mass removed by sedimentation for BC_{PAT}. However, for OC_{PAT}, there is a decrease of 3.3% (VEG) and 6.6% (HD) in the annual accumulated mass removed by sedimentation because of the higher fraction of soluble material present in the OC_{PAT}. This is also reflected in an increase in the total OC_{PAT} mass removed by wet deposition (8% for VEG to 10.5% for HD).

4.3.2 Wet Deposition

Mass that is not removed by dry deposition at the surface must be removed by sedimentation and scavenging. The larger particles are efficiently removed by sedimentation, while the smaller particles are removed by wet deposition. Because of the microphysical processes, the size distribution shifts towards an increase in fine aerosols. Therefore, a larger fraction of mass must be removed by scavenging. For the hydrophobic passive tracers, there is an increase in the global fraction of mass removed by this mechanism

(from 73% in the CTRL to 78% in the FH and HD schemes). For the hydrophilic tracer, the change is of similar magnitude i.e., from 66% in the CTRL to 72.8% in the VEG scheme. For the BC$_{\text{PAT}}$, the accumulated wet deposition results in an increase of 5.8% in the FH and 8.8% in the FRP. More mass is removed by wet deposition in FRP because the increase in the ki fraction of BC for this scheme is lower than that for the other schemes. There is thus more soluble BC$_{\text{PAT}}$ for FRP than for the other schemes, and more of this material is removed by scavenging. For the OC$_{\text{PAT}}$, the increase in wet deposition is larger (8% for VEG and 10.5% for FRP).

The transport effect is observed in both the yearly average and in the accumulated wet deposition. Negative differences of 1000 μg per square meter in the yearly accumulated wet deposition are observed in the BB production regions, and positive differences of the same magnitude are observed in the nearby areas, mainly over the central Atlantic Ocean.

4.4   Lifetime

The lifetime depends on the loss rate of the emissions. In this thesis, it is determined as $\tau = {}^{\text{atmospheric burden}}/_{\text{deposition rate}}$. The lifetime of the particles is thus increased because of the reduction in the loss rate generated by the decrease in the mass immediately removed by dry deposition at the surface and by the slower sedimentation as well as by the increased conversion time from the hydrophobic mode to the hydrophilic mode followed by an efficient scavenging of soluble particles.

The slow removal results from both the direct effect of the injection height and the microphysical process influenced by the altitude at which emissions are injected. The fine particles for which the mass fraction has increased as a product of the microphysical process are more efficiently removed by wet deposition than by sedimentation. Because both processes occur simultaneously and scavenging is more efficient than sedimentation, the lifetime of fine aerosol is limited by the scavenging efficiency. The geographical distribution of the lifetime of BC$_{\text{PAT}}$ displays an increase of more than twice in the lifetime over the regions close to the sources, which is exactly where the increase in the ki mass fraction occurs. This happens particularly in the border of the Sahara Desert. Conversely, in regions in central Africa, most of the mass is removed by scavenging, and the observed increase in lifetime is of lower magnitude.

Compared with the CTRL, a slight decrease in the lifetime of the BC$_{\text{PAT}}$ is simulated

over the Sahara because of the different transport patterns that the tracers experience in the injection height simulations. This suggests that more of the fine aerosol is immediately transported over the desert in CTRL. Because of the lack of scavenging there, the lifetime of BC_{PAT} is larger than the lifetime of BC_{PAT} in any of the schemes.

The fraction of fine aerosol is larger for BC_{PAT} ($\approx 50\%$) than for OC_{PAT} ($\approx 22\%$). The effect of the wet deposition limitation is therefore more important for BC_{PAT} than for OC_{PAT}. This is also apparent in the mean fraction of BC_{PAT} and OC_{PAT} that is removed by wet deposition. For BC_{PAT}, this is 73% in CTRL and 77% to 78% in the schemes. For OC_{PAT}, this is 68% in the CTRL and 73% to 74% in the schemes. In contrast to the fine aerosol, the lifetime of the larger particles mainly depends on the efficiency of the sedimentation. This process therefore plays a more important role for OC. This is observed in Table 4.1, which contains the annual mean lifetimes of the passive tracer PA01. This tracer has the smallest lifetimes of all passive tracers because the mass fraction of fine aerosol is less than the fraction for the other PATs. Consequently, more of its mass is removed by sedimentation i.e., 20% compared with 15% for the other aerosol passive tracers. Moreover, because this tracer does not contain any hydrophobic particles, it does not have to transfer from the hydrophobic mode to the hydrophilic mode. However, the global annual mean lifetime show a small decrease in its values for the FH and HD schemes. This is associated with a decrease in the burden of the PA01 ks mode in December in North America and mainly in Africa, which contradicts the global annual mean trend shown in Figure 4.3. This may be the result of an increase in the coagulation product of the lower atmospheric temperature, which promotes the condensation of the semi-volatile aerosol precursors at the injection heights. As a result, the mean radius of the ks particles increases by more than 100%. The particles are more efficiently removed, thereby increasing the sedimentation rate by up to 25% in those regions in December. This results in a decrease of up to 13.3% in the lifetime of the PA01 for HD in December. A similar effect of lower magnitude, which does not influence the annual mean, is observed in Australia during June and July. This indicates that the microphysical effects exerted by the injection height are more important than the direct effect of the injection height on the sink processes. Regionally, the effect on the annual mean lifetime is offset by the increase in the lifetime during the remaining months, especially the local summer months. However, this lifetime decrease in local winter months may also be linked to the particularly low cor-

relation of AOD with satellite observations observed in December (Section 6.1.1).

The magnitude of the lifetime of the other OC_{PAT}, which comes from the OC_{ki} (PA02, Table 4.2), is similar to the one for the BC_{PAT} (PA03, Table 4.3) because both must undergo similar microphysical processes. The lifetime of PA02 is therefore larger than that of PA01. For this aerosol passive tracer (PA02), the decrease in the December lifetime is also observed in the global mean of this month by up to 4% in HD. However, because of its magnitude, it is not reflected in the annual mean.

The global annual average lifetime of the BC_{PAT} increased slightly from 10.82 days in the CTRL to approx. 11.14 days in the HD scheme (Table 4.3). The increase in the lifetime is larger for FH and HD, although the VEG scheme has the highest average injection altitude. Because of the regional variability of the VEG scheme, the injection height at some regions is lower than the other schemes. Therefore, a larger fraction of the mass can be immediately removed by dry deposition at the surface. These numbers place the BC_{PAT} global annual mean lifetime in the upper range of the estimated BC lifetime in the industrial era (3.8 to 11.4 days, Bond et al., 2013), while the total BC lifetime remains in the mid-range (Section 5.1.1).

Regionally, the effect of the injection height on the lifetime is larger because of the local value of the injection altitude and the seasonality of the emissions. Therefore, because of the constant annual emissions, Africa is characterized by larger lifetimes and associated variations for the three aerosol passive tracers. In North America, the VEG scheme has a BC_{PAT} lifetime of 11.3 days in July, while the CTRL simulation has a lifetime of 10.4 days. The annual mean in Table 4.3 shows the same trend, but the magnitude of the lifetime increase is smaller. In August, the effect of the injection height on the global lifetime can increase by up to 6.4% for the HD. These results illustrate that the microphysical changes produced by the injection height, which affect the deposition efficiency, strongly influence the lifetime. The increase in the lifetime can enhance the effects that these particles exert on the climate system. For example, the effect of BC on the transfer of radiation and cloud processes can be influenced by the increase in its lifetime. The extended lifetime favors the mixing of BC particles with other aerosols, which may intensify light absorption and the activity of cloud condensation nuclei.

It is highly important to accurately represent the BC lifetime because of its various effects on radiative transfer and its role as a short lived radiative forcing agent.

Table 4.1: OC_{PAT} (PA01) Annual mean lifetime in days.

	CTRL	FH	HD	VEG	FRP
Global	7.84	7.82	7.77	7.89	7.94
North America	7.36	7.45	7.50	7.78	7.46
South America	5.95	6.14	6.11	6.11	6.21
Africa	10.08	10.68	10.68	10.53	10.70
Siberia	7.11	7.27	7.38	7.34	7.21
Indonesia	4.79	4.92	4.90	4.82	4.91
Australia	5.95	6.14	6.11	6.11	6.21

Table 4.2: OC_{PAT} (PA02) Annual mean lifetime in days.

	CTRL	FH	HD	VEG	FRP
Global	10.66	10.97	10.95	10.88	10.88
North America	8.99	9.23	9.27	9.42	9.18
South America	9.78	10.25	10.27	10.13	10.23
Africa	17.02	19.25	19.39	18.64	18.49
Siberia	8.65	8.90	8.99	8.92	8.82
Indonesia	7.66	8.02	8.02	7.79	7.91
Australia	13.59	14.29	14.25	13.86	14.17

Table 4.3: BC_{PAT} (PA03) Annual mean lifetime in days.

	CTRL	FH	HD	VEG	FRP
Global	10.82	11.14	11.12	11.05	11.10
North America	9.18	9.42	9.44	9.57	9.38
South America	9.94	10.41	10.44	10.30	10.39
Africa	17.12	19.37	19.52	18.76	18.60
Siberia	8.72	8.97	9.06	8.98	8.89
Indonesia	7.71	8.06	8.06	7.84	7.96
Australia	13.88	14.59	14.54	14.17	14.47

4.5 Transport

Immediately after their release, the emissions are subject to microphysical and deposition processes. The emissions simultaneously experience vertical transport by convection and horizontal transport by winds. The extended lifetime allows the particles to be transported further away from the source regions before being removed from the atmosphere.

This transport could exert health effects over wider areas by contributing to $PM_{2.5}$ in urban regions over Africa (e.g., Cairo (Abu−Allaban et al., 2002), Oalabotjha (Engelbrecht et al., 2002), Addis Ababa (Etyemezian et al., 2005)), Asia (e.g., Delhi, Mumbai, Kolkata, Chandigarh (Chowdhury et al., 2007), Hyderabad, Dhaka, Rajshahi (Johnson et al., 2011)) and North America (e.g., Mexico City (Lei et al., 2013)). When deposited over ice or snow, the positive radiative forcing could be reinforced (Bond et al., 2013). In this section, the transport is evaluated by investigating the differences in the distribution of the BB aerosol concentrations. Surface, vertical distribution, and column burden are considered in this assessment.

4.5.1 Surface Distribution

The direct effect of injection height is observed in the differences of the BC_{PAT} and OC_{PAT} concentrations at the surface (Figures 4.13 and 4.14). Negative differences are observed in the production regions as a result of the reduced emissions released in this layer and the immediate dry deposition at the surface. Positive differences are observed downwind in the deposition zones as a result of the increased lifetime and transport.

For BC_{PAT} (Figure 4.13), between 53.9% (VEG) and up to 71.5% (HD) less mass remains in the surface layer at the areas where the fires occur. For OC_{PAT} (Figure 4.14), between 53.9% (VEG) and up to 73% (HD) less OC is present at surface in the source regions.

The extent of the area with less BC_{BB} and OC_{BB} at the surface as well as the location of the minimum points varies slightly from scheme to scheme because of the differences in calculating the injection height.

The VEG scheme simulates smaller negative values because of the lower injection heights attributed to some land cover types. The weighted contribution of these cropland vegetation categories to each grid cell results in more emissions remaining at the surface layer than for the other schemes. That is the case of Russia, part of Nigeria

and Ghana, Portugal, India, South of Mexico and South-west Australia.

For FRP, the contribution of the less intense fires to the vertical distribution function for each grid cell and the temporal variation of the PBLH parameterization results in more mass released above the surface layer in this scheme than in the VEG scheme for all regions except for Canada and Alaska.

In the production region, FH and HD, which have no regional or temporal variation, continually leave the same fraction of emissions at the surface. These fractions, which are determined by the VDF for each grid cell, are smaller for FH and for HD than for the FRP and VEG schemes. This is reflected in the larger negative relative differences for FH (-69.9% for BC_{PAT} and -71.3% for OC_{PAT}) and for HD (-71.5% for BC_{PAT} and -73% for OC_{PAT}).

The effect of the transport and the subsequent deposition of the particles is observed in the positive differences in the left panel of the Figures 4.13 (BC_{PAT}) and 4.14 (OC_{PAT}). More BC_{PAT} (from 33.7% for FRP and up to 77.24% for HD) and OC_{PAT} (from 40% for FRP and up to 109% for HD) are simulated at the surface downwind from the source regions along the storm tracks and the ITCZ.

Important transport regions are found in all schemes over the ocean, especially the central and North Atlantic as well as the North Pacific, the Guinean Gulf, and the Arctic Ocean. Over land, the Sahara Desert as well as Greenland, Russia, and Alaska display the largest relative increases in the concentrations of surface BC_{PAT} and OC_{PAT} concentrations. Of special interest is the Arctic, where the deposition of BC has important radiative effects e.g., change of snow albedo.

Because the emissions of OC are larger than the emissions of BC, both the positive and the negative differences are larger for OC than for BC. This becomes evident when the surface concentration of OC from the CTRL (Figure 4.14, upper central panel) is compared with the surface distribution of OC (Figure 4.14, right column panels). The increases in the concentrations of OC_{PAT}, which are a product of transport, can be seen in the North Atlantic, the east coast of Africa, the South Pacific Ocean, and the Sahara Desert as well as both the Arctic and the Antarctic regions.

It is important to consider that Figures 4.13 and 4.14 show the annual mean of the difference and that the FRP scheme has a strong seasonal and diurnal variation (Chapter 3), which is reflected in the smallest relative differences from the CTRL simulation compared with the other schemes. A more comprehensive comparison could be done

between the monthly disturbances from the CTRL simulation.

4.5.2 Vertical Distribution

The resulting vertical distribution of the emissions is determined by its direct injection and the deposition processes as well as the convective and large-scale vertical transport that redistributes aerosol particles as soon as they are released into the atmosphere.
In this section, the vertical distribution of the passive aerosol tracers is assessed using the differences in the zonal mean distribution of the yearly average BC_{PAT} and OC_{PAT} concentrations (Figures 4.15 and 4.16).
The vertical transport of soluble compounds is limited by scavenging because competes with the convective transport. For less soluble tracers, the convective transport plays a more important role in the vertical distribution.
The convective transport mostly ends below the tropopause because of the temperature inversion. Therefore, the main influence of the injection height schemes is located between the surface and 14 km to 16 km near the tropopause altitude (Figures 4.15 and 4.16). This is true for all schemes except for FRP for which the overall positive difference is more evenly distributed and for which the maximum discrepancies (16.5% for BC_{PAT} and 23.3% for OC_{PAT}) are located at 30 km. The relative increase in the aerosol concentration at this altitude is the result of the upward motion of tropospheric air into the stratosphere over the tropics. For FRP, this occurs because of the time correlation between the occurrence of the deep convection and the injection height determined by Equation 2.15, which strongly depends on the PBLH parameterization as well as the frp value. This effect should be more intense; however, because the highest plume events in the FRP scheme are underestimated, some of the outliers observed by MISR (Section 3.3) are missing. Furthermore, the mass injected at the top of the plume is adjusted to the contribution of the most intense fire present in the grid-cell. Convective transport depends on the convection scheme selected. In this case, the transport of Tiedtke to the upper troposphere is weaker than the other convection schemes (Tost, 2006).
Direct injection and convective transport may deposit the emissions closer to the jet streams. The horizontal transport may thereby increase. This process is more relevant for BC because of the hydrophobic emissions, which require more time to be scavenged. For the VEG and FRP schemes, the convective transport in the mid latitudes is evident
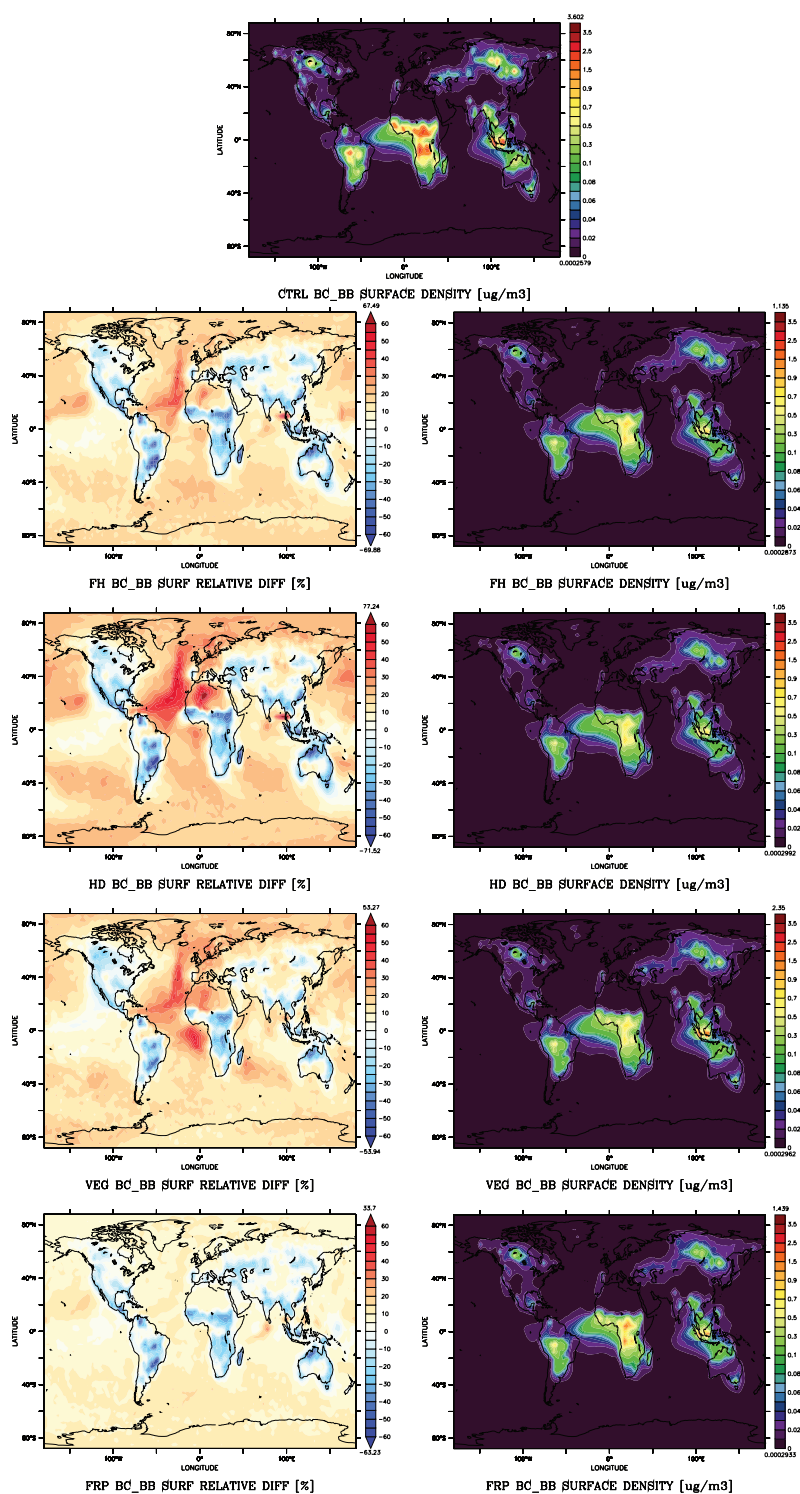
Figure 4.13: BC_{BB} surface density.

The central image shows the BC_{BB} surface density for the CTRL. The left panels show the BC_{BB} relative difference at the surface $\frac{SCH\text{-}CTRL}{CTRL} \times 100$. The right panels show the associated BC_{BB} surface density for each injection height scheme.
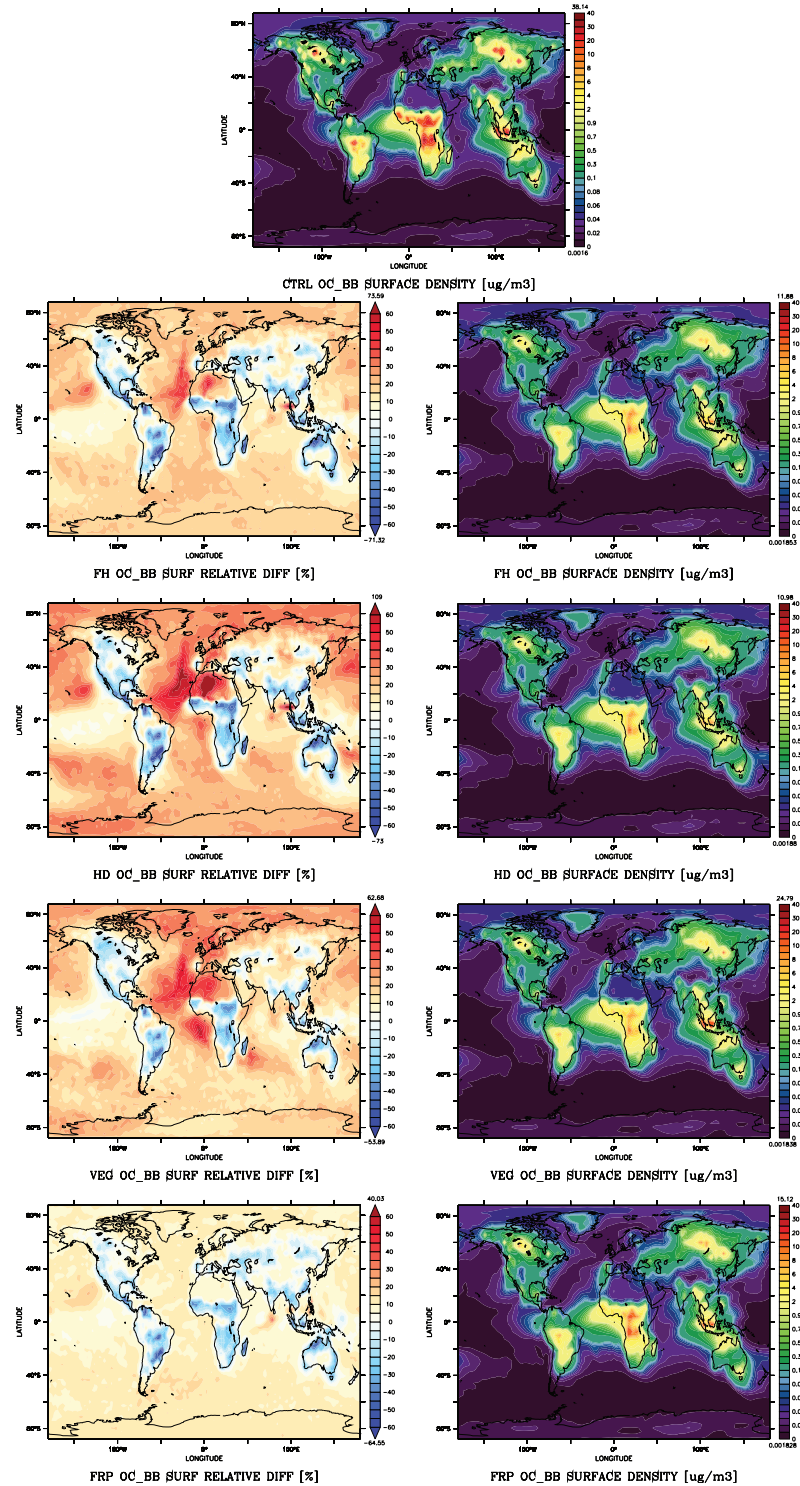
Figure 4.14: OC$_{BB}$ surface density.

The central image shows the OC$_{BB}$ surface density for CTRL. The left panels show the OC$_{BB}$ relative difference at the surface $\frac{SCH-CTRL}{CTRL} \times 100$. The right panels show the associated BC$_{BB}$ surface density for each injection height scheme.

in the differences at 40°S and 40°N along the storm tracks (Figures 4.15 and 4.16). In all schemes, the vertical transport in the ITCZ can be seen slightly north of the equator, which is the position of the ITCZ in July, when the peaks in BB emissions occur. The convective transport in this region influences the deposition rate. This consequently increases the lifetime, which results in the increased transport of emissions across the Atlantic and to the Caribbean, as seen in the column burden differences (Figures 4.17 and 4.18).

The vertical transport simulated in the storm tracks and in the ITCZ (Figures 4.15 and 4.16)is related to the horizontal transport (Figures 4.17 and 4.18) and to the differences in the surface concentrations (Figures 4.13 and 4.14) because this is where most of the wet deposition occurs.

For BC_{PAT} (Figure 4.15), the differences in FH, HD and VEG range from almost zero (FH and VEG) and slightly negative (HD) up to 35.9%, 61% and 30.6%, respectively. For FRP, the increase in the BC_{PAT} concentration is more homogeneous and positive, ranging from 3.5% to 16.5% for the zonal and annual mean. For this scheme, the temporal variability in the injection height results in the occasional release of emissions at altitudes higher than for the other approaches at the free troposphere. This allows the emissions to be transported further, which locates the maximum positive relative difference above the tropopause at 30 km. Although transport from the troposphere to the stratosphere is limited, several cases of aerosol enhancements associated with BB in the LS have been identified as a result of deep convection (e.g., Andreae et al., 2001; Cammas et al., 2009; Fromm and Servranckx, 2003; Quinn et al., 2011) or pyroconvection (e.g., Damoah et al., 2006; Fromm et al., 2008; Jost et al., 2004; Luderer et al., 2006; Trentmann et al., 2006).

The differences for the OC_{PAT} are of larger magnitude but have a similar distribution, which ranges from almost zero to 42.8%, 75.2%, and 43.37% for the FH, HD, and VEG schemes, respectively. For FRP, the relative difference in the concentration is positive (between 3.6 and 23.3%). This is similar to the BC_{PAT} but has a larger maximum value.

The small negative differences (located above the tropopause at approx. 16 km) as well as the biggest positive changes of the HD scheme at approx. 3 km height show that for this scheme, the vertical redistribution of the emissions is more confined to the troposphere and that less mass is transported further. The increases in the concentrations

of BC_{PAT} and OC_{PAT} in this scheme result from the slower deposition processes. The same pattern was observed in Figure 4.2.

For VEG in the Northern Hemisphere, the regional variations in the injection height lead to increases of 30% for BC_{PAT} and 43% for OC_{PAT} at 6 km altitude. Conversely, in Africa, the different vegetation types result in the emissions being injected at higher altitudes in the North of Central Africa (with mostly woody savannah) than in South Central Africa (which is covered by cropland and shrublands).

The South Central African region has a peak in fire activity in July and August, when the global maximum of BB emissions is reached. The resulting increase in the BC_{BB} (Figure 4.15) and OC_{BB} (Figure 4.16) concentrations in this region are observed between 3 and 5 km and are in line with the CALIPSO Lidar observations during July and August 2006 (Labonne et al., 2007), which have aerosol layers in the range of 3 to 4.5 km. These top height observations are in accordance with the ECMWF boundary layer values.

For the same region, FRP has lower maximum plume height values, which range from 2.5 to 3 km, and associated maximum boundary layer values, which range between 3.1 and 3.9 km. For North Africa, the maximum plume height values from MISR are also in good agreement with the VEG scheme, which has values ranging from 1.1 km to 3.5 km. For MISR, the values range from 0.4 to 4 km. Considering the 500 m uncertainty in MISR, these results show that the VEG scheme captures the highest plumes observed by MISR but leads to an overestimation of the small plumes. While FRP captures the average of the plumes, it results in an underestimation of the higher plumes (see Section 3.3).

In this region in January, the average of the observed plumes is 1.5 km, which is exactly the height of the FH scheme. There is no information from the MISR plume height project for this region. However, the comparisons between FRP and the North Africa plume height values show good agreement. The VEG scheme is thus a good approximation of the observed plume height. The FRP scheme, which strongly depends on the approximation of boundary layer height, leads to an underestimation of the plumes because of the uncertainty in the frp values.

The right column of Figure 4.15 shows the distribution of the annual mean BC_{PAT} concentration.

The changes to the vertical distribution are more evident for OC_{PAT} than for BC_{PAT}

(Figure 4.16, right column). The pattern of the annual and zonal mean vertical distribution of OC_{PAT} changes mainly around the equator but also in the Polar Regions. For all schemes, the maximum OC_{PAT} concentration increased.

4.5.3 Horizontal Distribution

During vertical transport, the horizontal transport by the different local wind patterns influences the air masses. The resulting transport modifications can be seen in the annual mean column burden distribution (right column panels) and relative divergences (left column panels) from the CTRL simulation for BC_{PAT} (Figure 4.17) and OC_{PAT} (Figure 4.18).

The increase in the average global burden, which is a result of the lifetime enlargement, can be seen in the overall positive relative differences for both BC_{PAT} and OC_{PAT} in all schemes. This is particularly evident along the storm tracks and the ITCZ as well as both the Arctic and the Antarctic regions. Small negative differences are observed in the production areas such as the north of Lake Victoria and Argentina as well as Central Africa and Indonesia. These range from -2.7% for BC and OC (FRP) to -12.7% for BC and -12.5% for OC (HD). The annual mean increases in the column burden vary from 15.2% (FRP) to 52.5% (HD) for BC_{PAT} and from 18% (FRP) to 66.6% (HD) for OC_{PAT}.

The emissions follow the different transport patterns produced by the wind field (overlaid in purple) at the average injection height of each scheme. Consequently, the transport pattern (i.e., the location of the maximum differences) varies slightly from scheme to scheme. However, because of the temporal variability of the injection height in FRP and its lower mean value, the increases in certain regions are mostly seen in the FH, HD, and VEG schemes.

With the help of convective transport, the westerly winds of the Northern Hemisphere jets carry the emissions from America towards the Atlantic Ocean, thereby generating a strong transport pattern that holds the maximum values in the column burden as well as in the surface relative differences (Figures 4.17 and 4.18) in the BC and OC concentrations. This particular transport is important not only because of its intensity and effectiveness in conveying emissions to the North Atlantic but also because it can contribute to the deposition of BC over the snow and ice in the Arctic as well as the arctic haze. This has led to substantial increases in this region with mean annual dif-
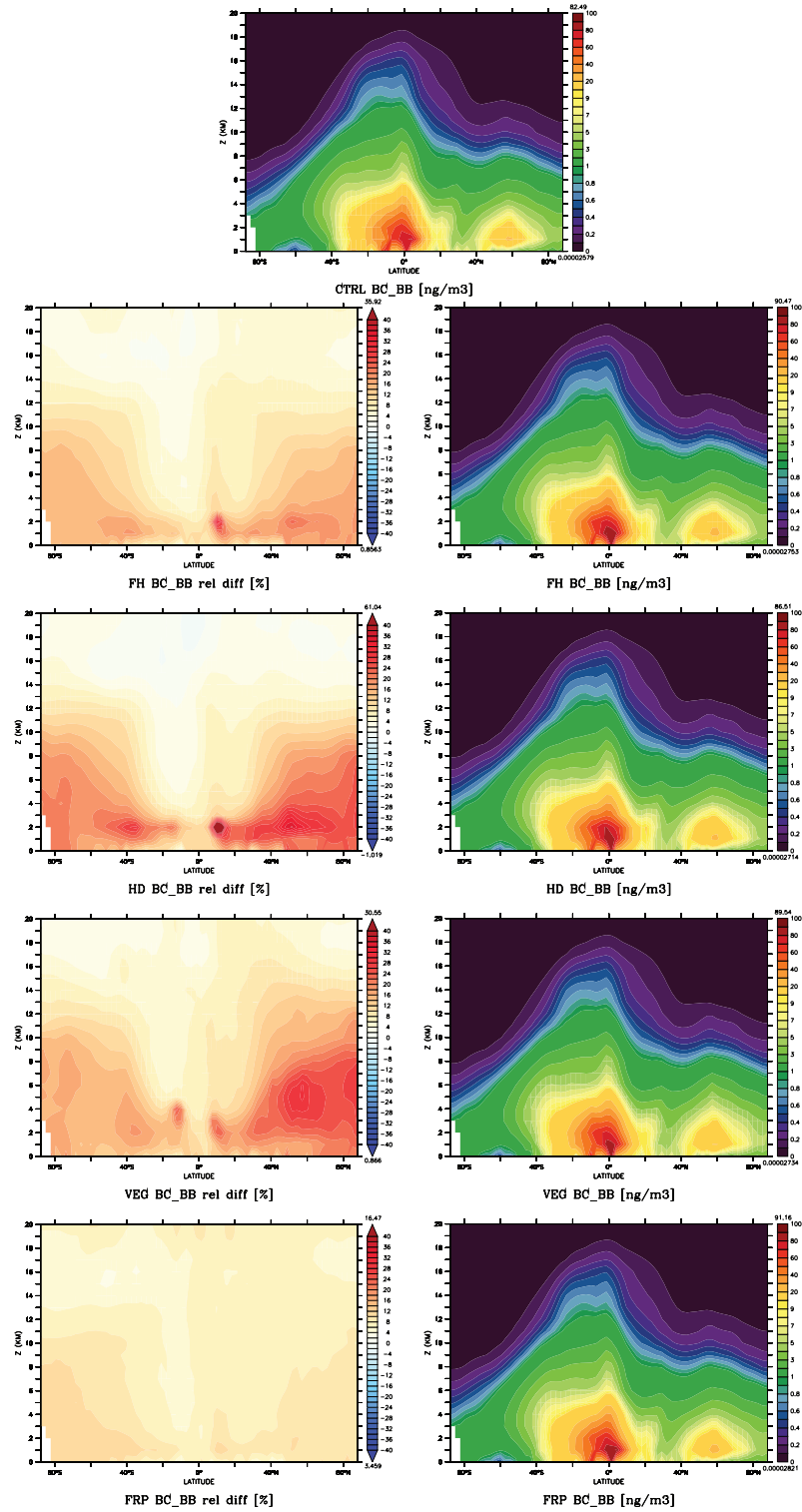
Figure 4.15: Annually and zonally averaged BC_{BB} density.

The central image shows the annually and zonally averaged BC_{BB} density for CTRL. The left panels show the BC_{BB} zonal mean relative difference $\frac{SCH-CTRL}{CTRL} \times 100$. The right panels show the associated BC_{BB} zonal mean density for each injection height scheme.
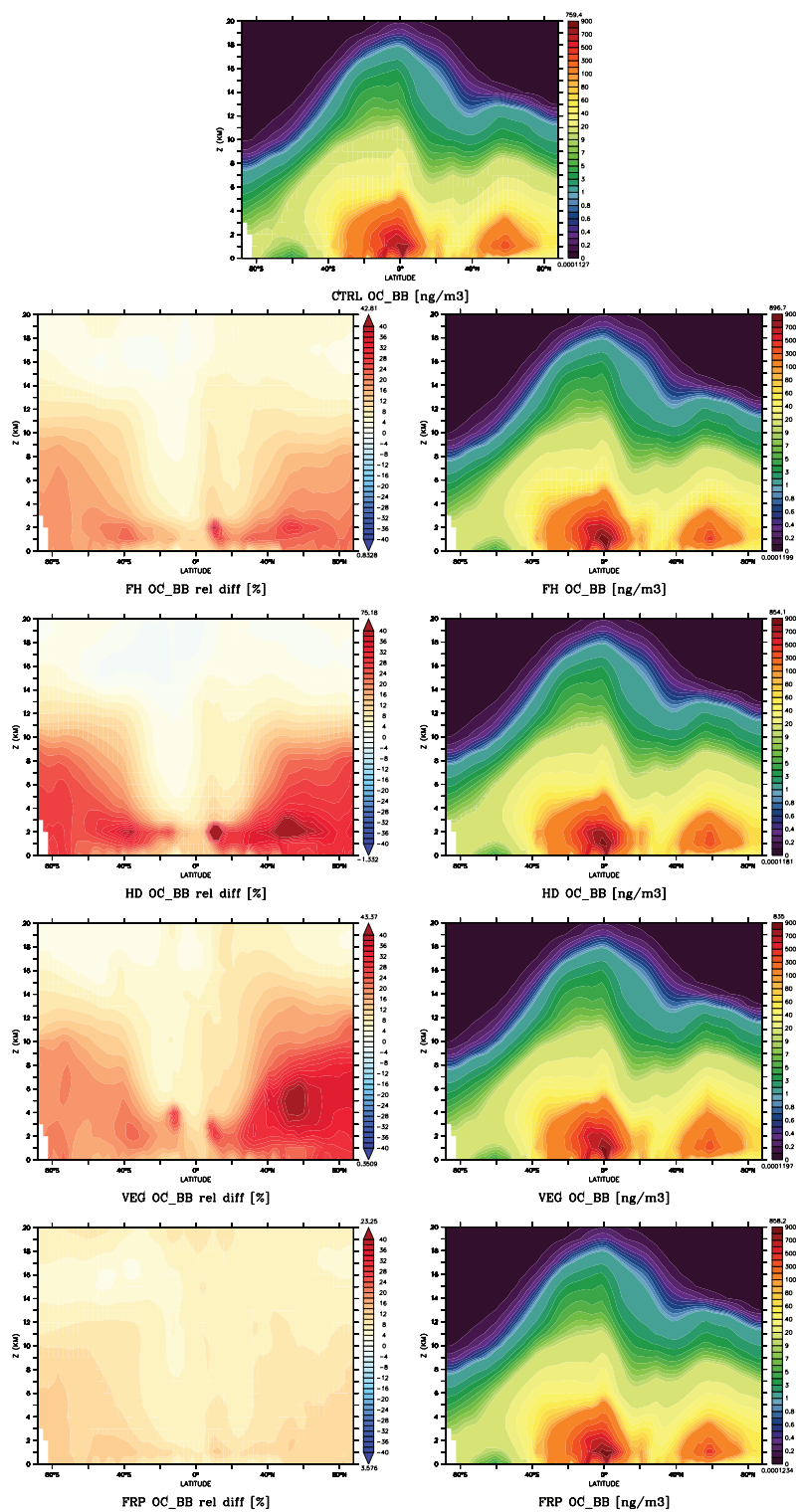
Figure 4.16: Annually and zonally averaged OC_{BB} density.

The central image shows the annually and zonally averaged OC_{BB} density for CTRL. The left panels show the OC_{PAT} zonal mean relative difference $\frac{SCH-CTRL}{CTRL} \times 100$. The right panels show the associated OC_{BB} zonal mean density for each injection height scheme.

ferences fluctuating from 15% (FRP) to 40% (HD).

The jets in the Southern Hemisphere produce positive differences along the Southern storm track, especially in Southeast Africa and in the southern coast of Australia, and can reach differences of 15% to 20%.

The easterly winds in Africa play an important role in the transport of aerosol particles to America and in the deposition of nutrients over the Atlantic Ocean. This is evident in the increase in concentration for all schemes located at the Gulf of Guinea, the Angola Coast, the Central Atlantic, and the Caribbean. The strong characteristic winds from the jet transport the emissions to the west across the Atlantic Ocean and may even reach America. The peak in the wind speed is usually located at 3 km height, although diffusion happens quickly. The particular height at which emissions are injected may not directly affect the transport by the easterly jet. The height does influence the immediate moment of the injection because the emissions are not quickly removed by dry deposition. Different height regimes also contribute to differential growth and therefore lifetime and transport.

For FRP scheme, the transport patterns are less evident because it has the lowest mean injection height; the wind pattern is more chaotic because of the disturbance created by the mountains. The effect of the mountains is also observed in the North Pacific, where the Rocky Mountains create a loop that transports the emissions from Alaska over the Pacific Ocean instead of to the continent over Canada.

Some of the observed transport patterns may be less intense when the total BC (i.e., including all sources) is considered; this is because of the seasonal variability in BB emissions and the contribution to the annual burden of BC. However, as will be discussed in Section 4.6, the contribution of the BB source to the total BC and OC has increased over the important transport regions such as the North Atlantic and the Arctic (Figures 4.19 and 4.20).

4.6 The Contribution of Biomass Burning to Total POA

Because the lifetime and consequently the global burden of BC and OC from BB has increased, the contribution of this source to the total tracers has also increased in all aerosol modes. This increase is mainly found in the ki mode in which the annual mean fraction of fine aerosol from BB has increased 6% globally because this size is primarily produced by the BB.
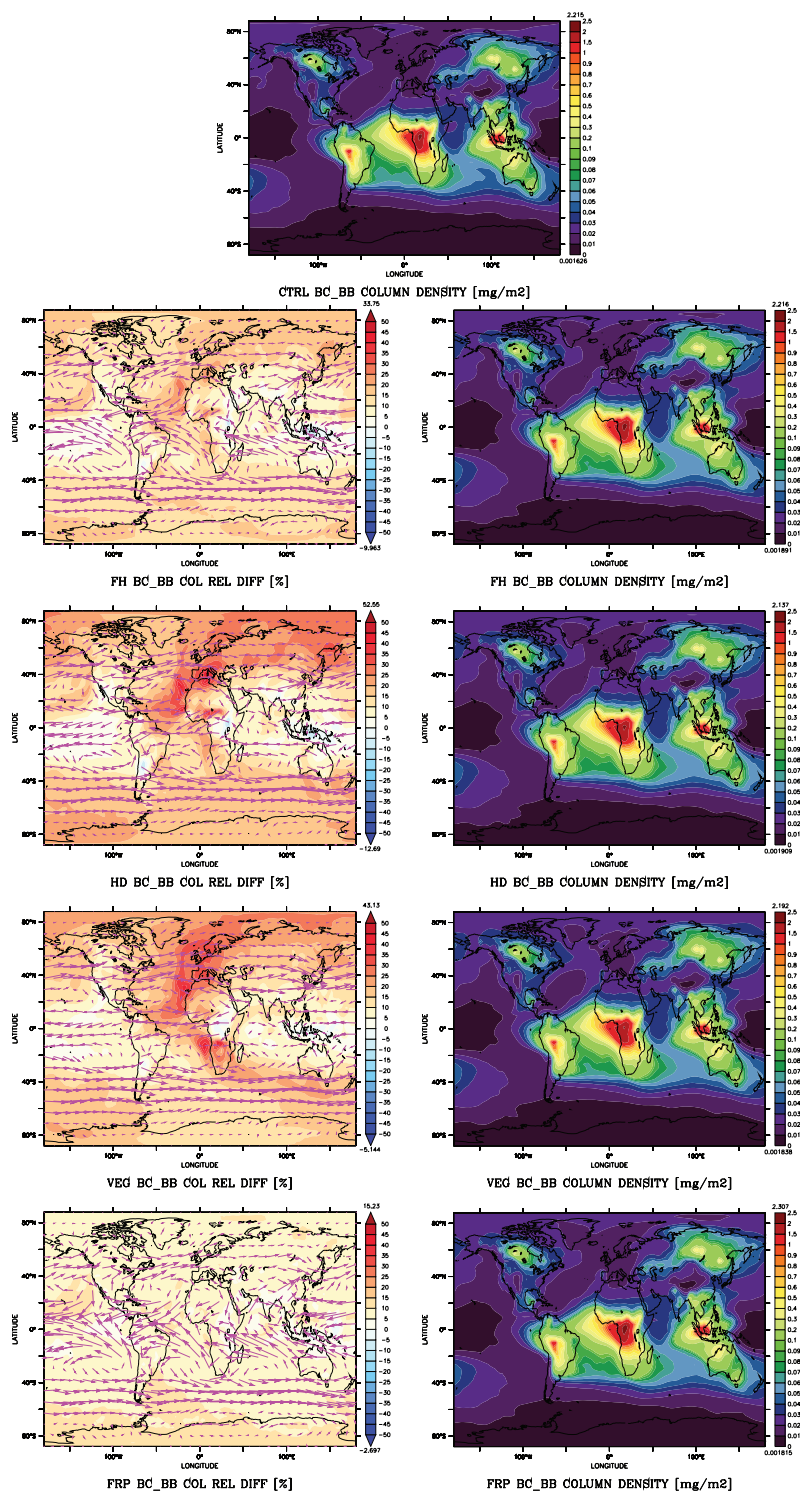
Figure 4.17: BC$_{BB}$ annual mean column burden.

The central image shows the BC$_{BB}$ annual mean column burden for CTRL. The left panels show the BC$_{BB}$ annual mean column burden relative difference $\frac{\text{SCH-CTRL}}{\text{CTRL}} \times 100$ with the wind field at the average scheme's injection height overlaid in purple. The right panels show the associated BC$_{BB}$ annual mean column burden for each injection height scheme.

Figure 4.18: OC_{BB} annual mean column burden.

The central image shows the OC_{BB} annual mean column burden for CTRL. The left panels show the OC_{BB} annual mean column burden relative difference $\frac{SCH-CTRL}{CTRL} \times 100$ with the wind field at the average scheme's injection height overlaid in purple. The right panels show the associated OC_{BB} annual mean column burden for each injection height scheme.

4. BIOMASS BURNING PRIMARY AEROSOL EMISSIONS

The contribution of BB to the total tracers on an annual mean increased between 1.5% and 2.4% for BC and between 1.7% and 2.9% for OC. In summer months the increment in the contribution is higher (e.g., 6.4% for OC and 4.8% for BC in June for VEG). Regionally, the annual mean contribution of BB has grown between 6.7% (FRP) to 12.5% (HD) and 5.8% (FRP) to 13.5% (HD). Therefore, more BC and OC from BB is part of the total burden of the tracers globally, but especially downwind from the production regions (Figures 4.19 and 4.20).

The production of BC is dominated by fossil fuel combustion in the Northern Hemisphere (except for Alaska, Canada, and Siberia) and by BB in the Southern Hemisphere (Figure 4.19). This distribution is observed in all aerosol modes. There is a less extended fossil fuel area for the ki because BB is a substantial source of this size and because fossil fuel emissions (that are also in this size range) are often associated with hydrophilic coating material.

Increases in the fraction of BB are simulated in the same locations where the transport occur i.e., along the storm tracks, the North Atlantic, the Gulf of Alaska, and the Arctic.

Because OC includes the contribution of biogenic sources as well as fossil fuel and BB, the contribution of the latter in the Southern Hemisphere is downgraded. In the industrial regions of the Northern Hemisphere (except for the obvious biomass regions over Canada and Siberia), OC is mainly the product of fossil fuel combustion and SOA formation (during summer).

The transport and deposition of light absorbing aerosols over the Arctic is particularly important because BB emissions can generate a net positive radiative forcing. The light absorbing particles reduce the albedo of the snow when deposited over it, whereas the atmospheric particles increase the absorption of the incoming solar radiation. At the same time, this reduces the amount of radiation that reaches the snow and can subsequently be reflected. The deposition on the snow is more important because its radiative forcing is of larger magnitude than the one generated by the changes to the incoming solar radiation. Moreover, the deposition modifies the granular structure of the snow. This creates feedback, which further influences the albedo and the climate forcing.

The changes in column burden contribution of BB to the total tracers influence the downwelling radiation, whereas the BB fraction at the surface and the total deposition

changes are responsible for the direct albedo effect.

Most of the light absorption is attributed to BC. However, between 30% and 50% of the light absorption is caused by non-BC particles, which are mainly OC produced from biofuel, agricultural, and boreal forest fires (Bond et al., 2013).

The contribution of BB to the Arctic varies annually and seasonally according to the fire activity in Canada and Siberia. Consequently, the estimation of the annual mean contribution can be a challenge. Additionally, the methods for measuring the light absorbing particles concentrations as well as the methods for determining the source vary because the comparison with transport models must account for the different treatment of emissions as well as the lifetime and deposition of the particles.

The annual mean contribution of BB ranges widely, and many studies focus on the concentration of BC because most of the light absorption is attributed to it. In a modelling study, Skeie et al. (2011) determined that from 2001 to 2008, the BB accounted for 15% to 36% of BC in latitudes above 65°N. However, comparisons with observations suggest a larger contribution of BB. The concentrations of BC are underestimated at the surface and overestimated at higher altitudes. Based on 2008 and 2009 data collected from 36 sites over Alaska, Canada, Greenland, Russia, and the Arctic Ocean, Hegg et al. (2009, 2010) attribute more than 90% of the BC in the Arctic to BB. For the simulations in this thesis, the annual mean fraction of BB in latitudes above 65°N is only 32% with slight increase compared with the fraction of the CTRL simulation.

Wet deposition limits both the concentration and the transport of particles. This deposition is partly responsible for the seasonal differences in the concentrations of BC over the Arctic. The scavenging reduces their abundance during summer months (when rain occurs in this region) and during the transport to high latitudes (along the storm track). Depending on the height at which emissions are injected, they may not be subject to immediate scavenging and may consequently be transported further away from the sources. The microphysical processes involved in the aging of particles affect their removal from the atmosphere and are influenced by the injection height and the atmospheric temperature.

The seasonality of the emissions and all processes involved in the transport results in a maximum of light absorbing aerosol from BB in summer and late spring. In spring, when the influence on the snow albedo is more substantial, BB is responsible for most of the light absorbing BC particles over North America, Russia, and Greenland. Fos-

sil fuel is responsible for the concentrations over the Arctic Ocean and —to a lesser extent— in Greenland (Bond et al., 2013).

In this thesis simulations, the spring contribution of BB to the total BC is 18% and 10% by the end of April. Skeie et al. (2011) report a 6 to 11% contribution of BC from BB in the snow (north of 65°N).

In summer, the measured AOD at several arctic locations (e.g., Barrow, Alaska; Alert, Canada; Summit, Greenland; Zeppelin/Ny Ålesund on Spitsbergen, Norway) revealed peaks in particle concentrations during July and August 2004 (Stohl et al., 2006).

Biomass burning has a mean annual surface contribution of between 30% and 40% over Barrow Alaska, while the column redistribution in our model improves the contribution of BB from 25% in the CTRL to 30% in the simulations. Because of the injection height, the transport has been enhanced, and the surface concentration of BC_{BB} has increased.

In winter, fossil fuel sources dominate the BC, possibly because of the increase in domestic heating requirements (Stohl et al., 2013). The contribution of BC increased by 5% (VEG) over Greenland, Alaska, and the Arctic Sea in October, November, and December as well as over Siberia and the Greenland Sea in January, February, and March.

The contribution of BB to the total OC has increased globally and decreased in the production areas. The contribution of OC increased by 6% for FRP over the Indian Ocean and up to 13.5% for HD over the Sahara Desert and Atlantic Ocean. However, the VEG scheme shows large contributions (11.32%) to the total OC over wider areas, particularly in the Arctic. This influences the transfer of radiation in the region, which has important consequences for snow and ice albedo.

The injection of BB aerosol emissions at different altitudes has modified the ageing paths, the deposition efficiency, and the lifetime, which ultimately influences the distribution, global burden, and contribution of BB to the total tracers. The effect of the tracers on which BB has an influence will be addressed in the following chapter.
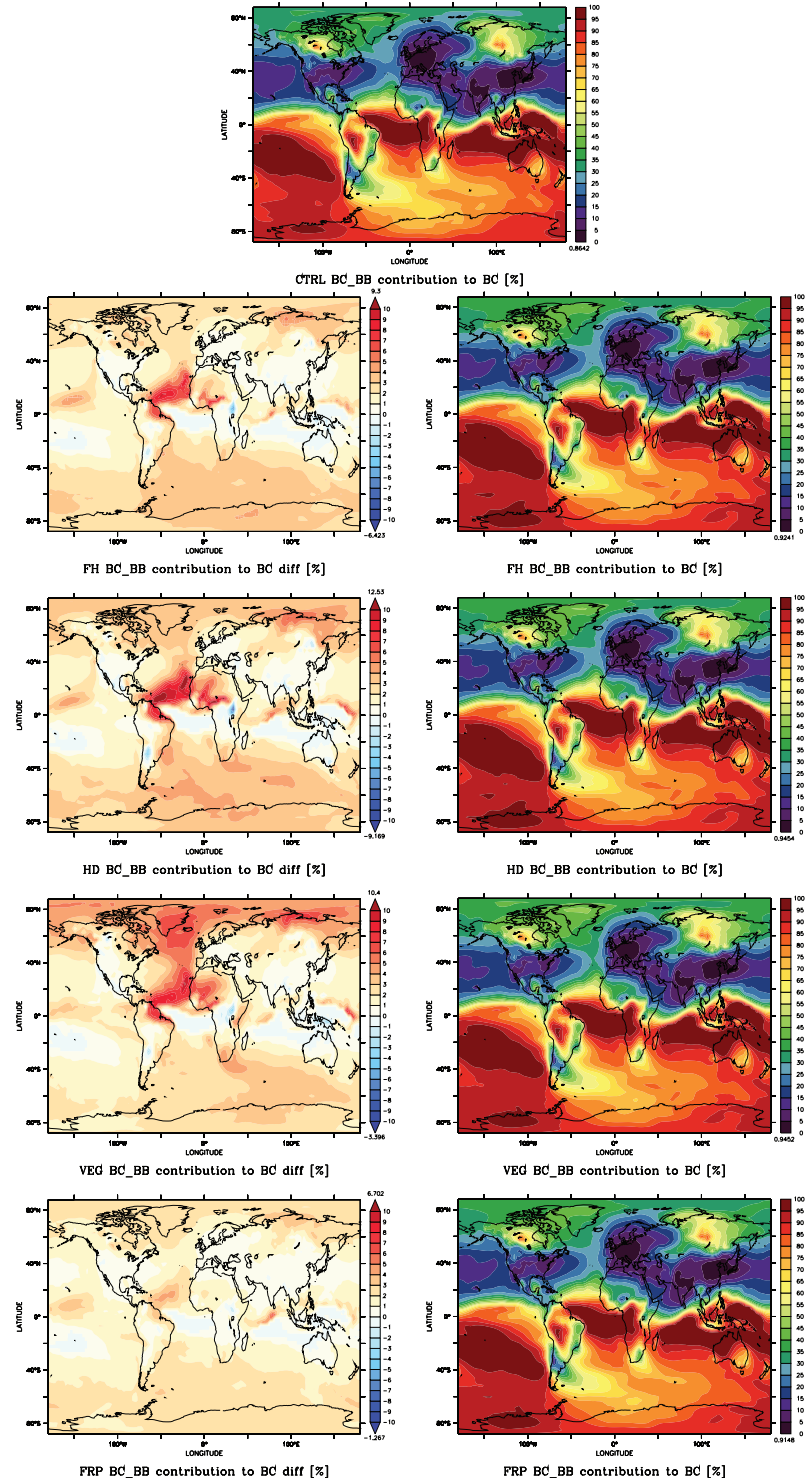
Figure 4.19: Annual mean BC_{BB} contribution to BC $\frac{BC_{BB}}{BC}$.

The central image shows the annual mean BC_{BB} contribution to BC for CTRL. The left panels show the differences between the CTRL and the SCH for the annual mean BC_{BB} contribution to BC. The right panels show the associated annual mean BC_{BB} contribution to BC for each scheme.
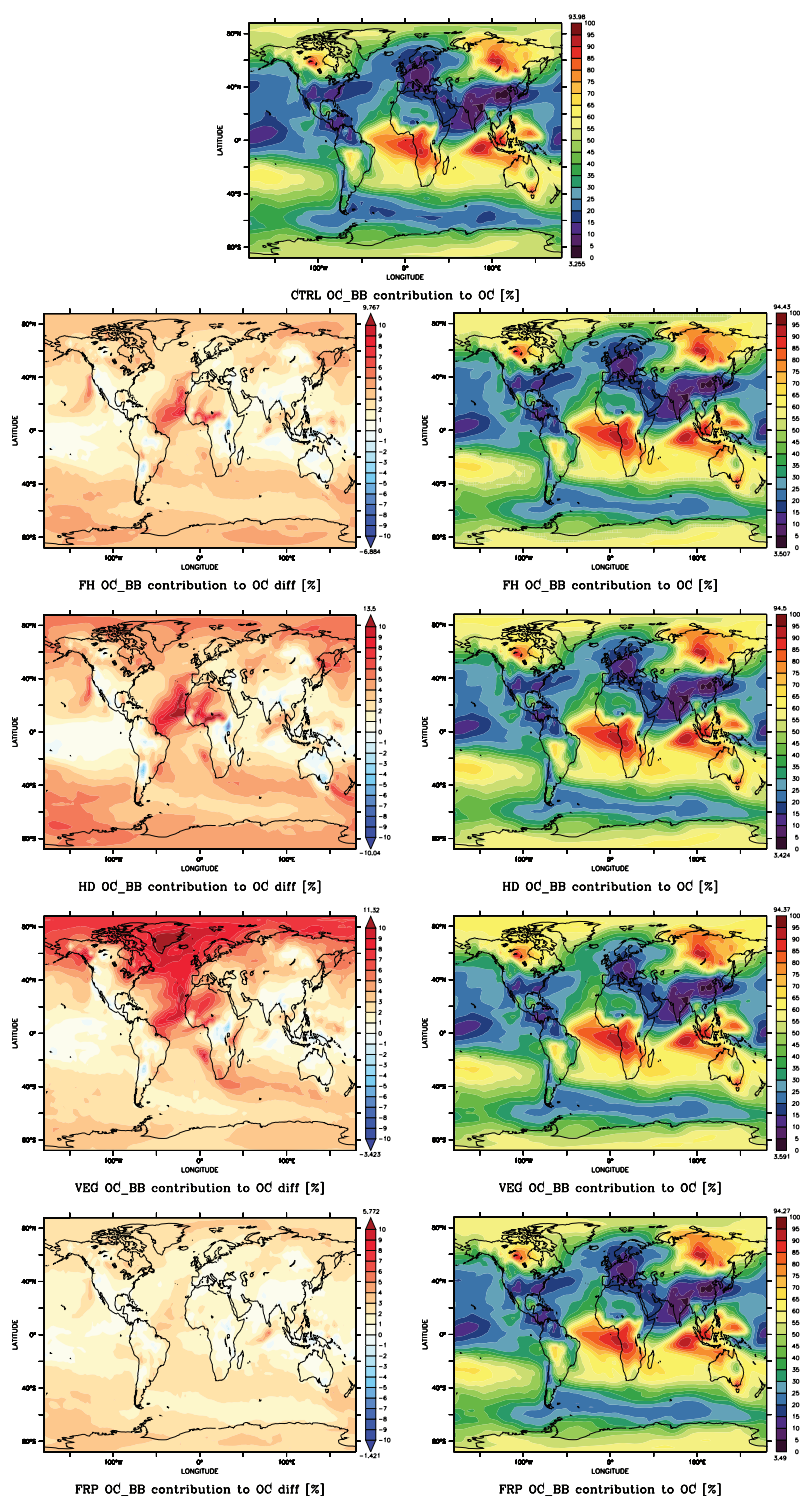
Figure 4.20: Annual mean OC$_{BB}$ contribution to OC $\frac{OC_{BB}}{OC}$.

The central image shows the annual mean OC$_{BB}$ contribution to OC for CTRL. The left panels show the differences between the CTRL and the SCH for the annual mean OC$_{BB}$ contribution to OC. The right panels show the associated annual mean OC$_{BB}$ contribution to BC for each scheme.

5

The Influence of Biomass Burning on Tracers

This chapter evaluates the influence that the injection of BB emissions has on tracers that are directly emitted by fires as well as the effects on related secondary compounds. The changes generated by the different injection heights are quantified using a set of simulations with identical binary meteorological state variables (i.e., the setup with no feedback between chemistry and dynamics, Section 2.1.2.3).

Several studies have addressed the influence of the vertical distribution of trace gas emissions on the tropospheric chemistry using EMAC. For example, in Pozzer et al. (2009), ssubstantial differences were evident close to the source of emissions. However, the overall effect on the global chemical composition was rather low. Similar results are found in this thesis. However, there are new simulated effects on tropospheric chemistry and radiation transfer, which originate from the injection of BB emissions at higher altitudes. The injection of primary aerosols is particularly important but had not been considered in the reference simulation. Releasing aerosol precursors (NO_x and sulfuric dioxide) at different temperature and relative humidity regimes is also important because this influences the formation and composition of secondary particles. The different injection height of BB aerosols immediately affects the dry deposition of species at the surface. The aging of the aerosols is also modified, thereby affecting their atmospheric removal and lifetime. This ultimately results in increases in the burden. Similarly, the production of secondary aerosols and its related reactions are influenced by the temperature and relative humidity. Both primary and secondary aerosols have an

effect on the AOD directly and indirectly by their influence over the aerosol water. The NO_x injections have effects on the ozone formation and the OH· abundance. Therefore the oxidation capacity of the atmosphere is affected, thereby influencing the carbon monoxide concentration and methane lifetime. These effects were not considered in the EMAC model reference configuration because the aerosols were released at the surface and the gas emissions at 140 m. This chapter will address these effects, and the effects on AOD will be discussed in 6.

5.1 Primary Aerosol

This section assesses the effect of varying the injection heights on the total aerosol tracers that result from the release of BB aerosol emissions at altitudes other than the surface. The previous chapter only discussed the changes experienced by the BB primary aerosol emissions. This section will address the influence of the combined changes in aerosols and their precursors on the total BC and OC tracers.

5.1.1 Black Carbon

Black carbon represents a small mass fraction ($\approx 0.5\%$) of the total BB emissions. However, it does play an important role in the climate system because it is a relevant absorbing component based on its optical attributes. The BC from BB represents about 32% of the total BC emissions (Table 1.1). However, because BC from fossil fuel is emitted at a constant rate during the year in the current model configuration, the seasonal cycle of BC is completely driven by BB emissions. Therefore, the contribution of BC_{BB} to the total BC can vary from 8.5% in May to 49.4% in August (Figure 1.2), when the maximum of BC emissions occurs. The BC_{BB} lifetime increase (Section 4.4) results in a higher BC burden in any of the simulations using an injection height scheme than in the CTRL simulation.
Because of the seasonal cycle (Figure 5.1), larger differences occur in the months in which BB emissions contribute more (Figure 5.2).
However, the peak in the relative differences of HD and VEG occurs in July. Both FRP and FH, on the other hand, have their maximum in August together with the total BC_{BB} emission maximum. This can be explained by the fraction of mass injected above the boundary layer. For FRP, the mean of this fraction is larger in August. For

the other schemes, the mean is larger in July.

When calculating the PH, FRP considers the weather conditions at the time of the fire, which results in variations in the mass injected above the PBLH (Chapter 3). In contrast, for the other schemes, the fraction of mass above the PBLH tends to be overestimated because of the constant injection height. For FH, this overestimation is lower because of its small (1.5 km) average injection height, which explains its peak in August, which is associated with the larger total BB emission fluxes.

The effect of the constant height of injection is evident in July. The maximum number of grid cells with fires occurs in this month, including the fire events at boreal regions. The VEG scheme constantly injects the maximum fraction of mass at the highest altitude (6 km) in these regions. Therefore, in July, more mass is released above the PBLH (Figure 3.4). Consequently, in this approach, July is the month with the largest relative differences.
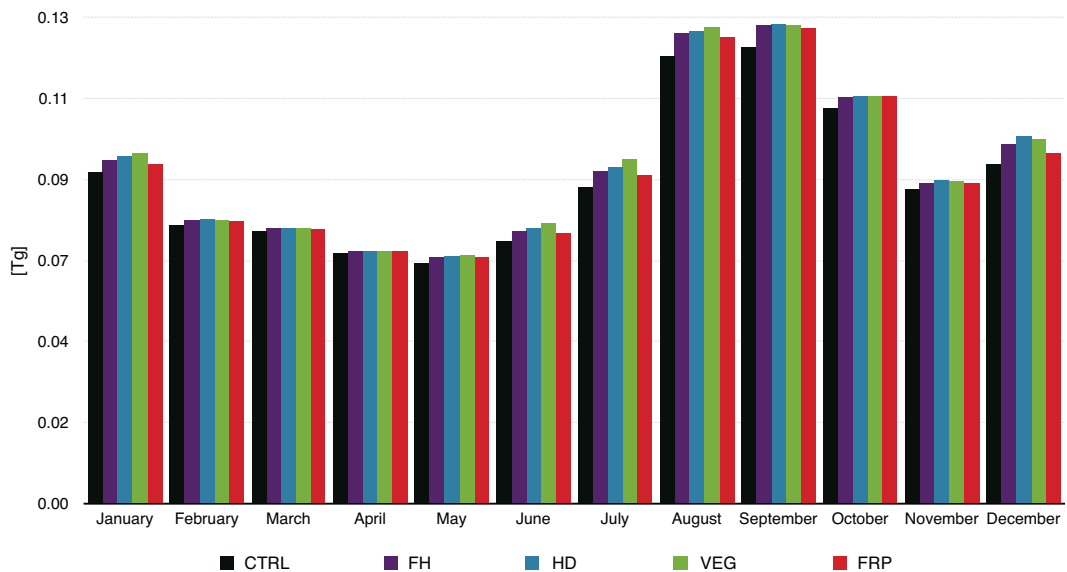
Figure 5.1: BC global burden monthly mean.

As a consequence of the injection height, there is less BC at the surface for all schemes in the regions where BB is produced (Figure 5.3). Positive differences are observed in the regions where BC is deposited after being transported downwind, especially in the equatorial Atlantic Ocean, downwind from the African production areas.

These differences vary seasonally and increase as the contribution of BC_{BB}, with the largest changes in the summer months (Figure 5.2). The differences also vary from
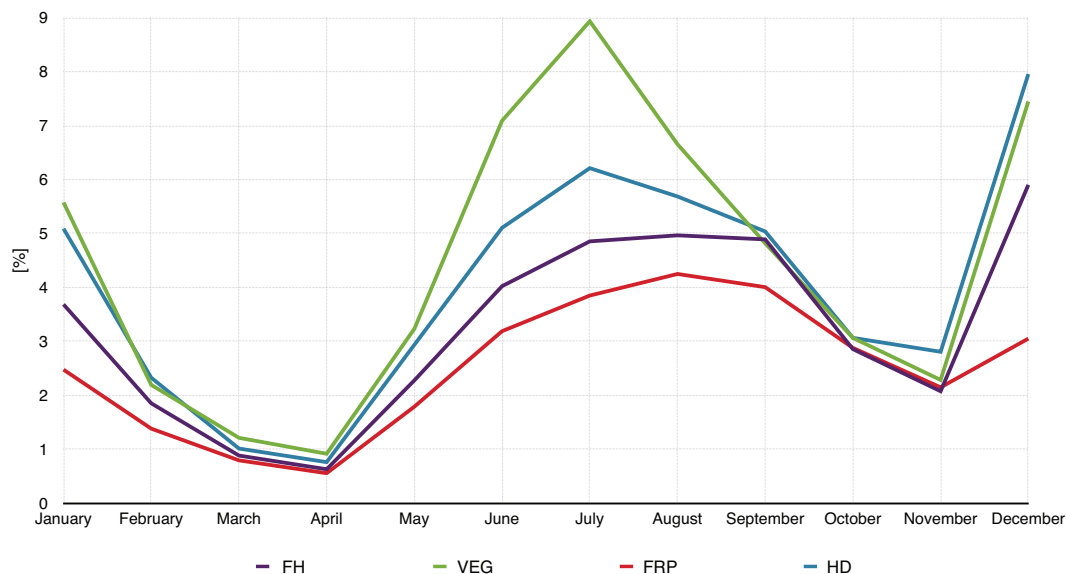
Figure 5.2: BC global burden monthly mean relative difference $\frac{\text{SCH-CTRL}}{\text{CTRL}} \times 100$.

scheme to scheme. VEG shows larger differences in summer as a consequence of the already discussed constant injection of mass above the PBLH for this scheme.

The increase of the BC global burden shown in Figure 5.2 is evident in the overall positive difference for all schemes. The magnitude of the changes in the BC tracer is lower than the changes for the particular BC_{BB} source (Section 4.5.3). However, the introduced changes in BB injection influence the annual mean BC column burden in a range from 11.4% (FRP) up to 33% (VEG).

Notably, the changes triggered by the injection height schemes slightly increase the BC column burden over the Arctic. This can be seen in Figure 5.4, where all schemes show higher concentration (light blue) compared with the CTRL (dark blue). This has important consequences over the radiative transfer in the region, as discussed in Section 4.6.

The differences shown by the VEG scheme in Africa are a product of the land cover type of the region. The area around 20°S contains mainly woody savanna vegetation (Figure 2.7) that is injected at height of 3 km, which is in contrast to the Northern African BB production region that has mixed vegetation types (woody savanna, regular savanna, grassland and cropland), which results in emissions injected at a lower height. This is also evident in the zonal mean BC relative differences on Figure 5.5.
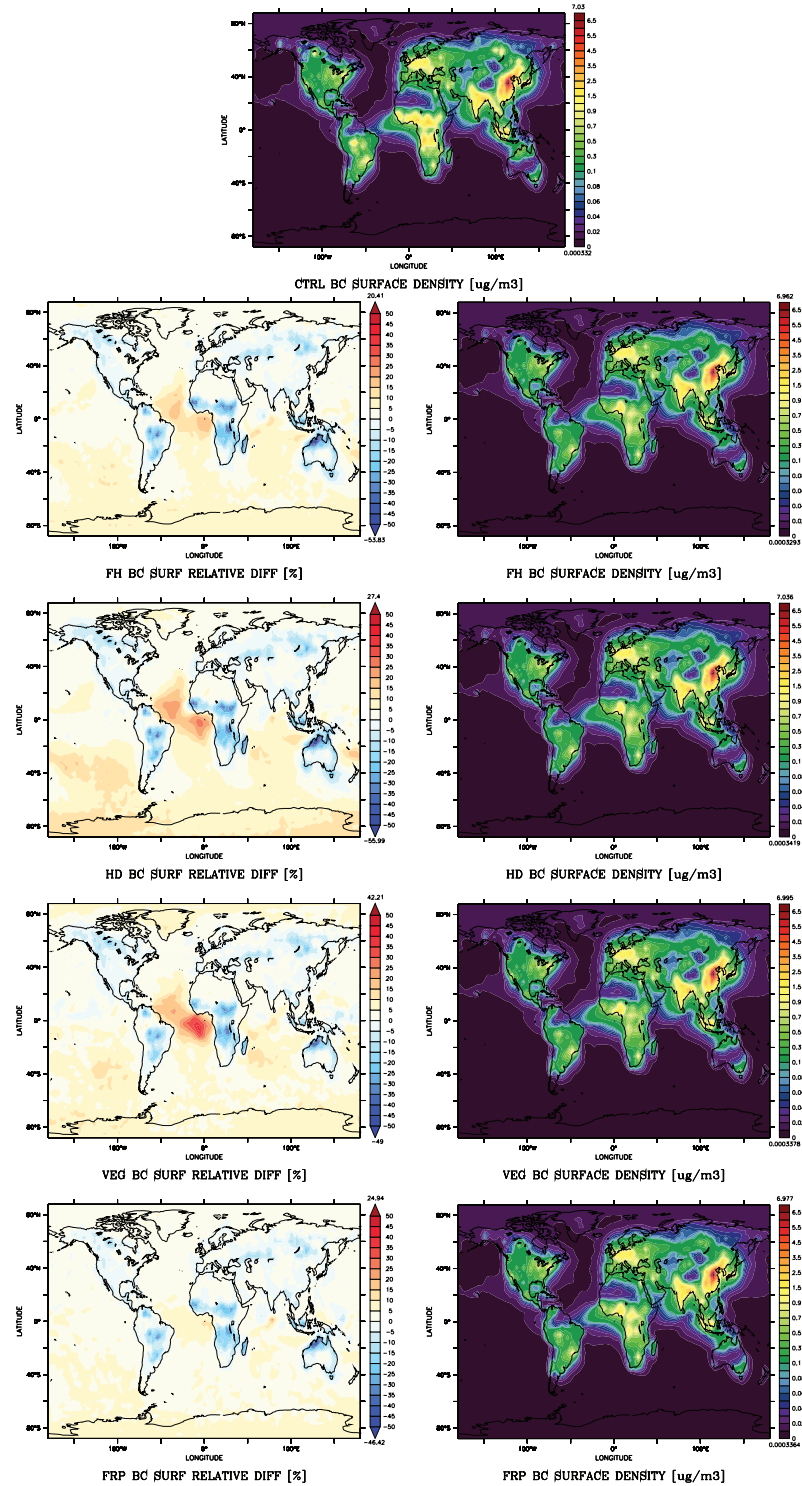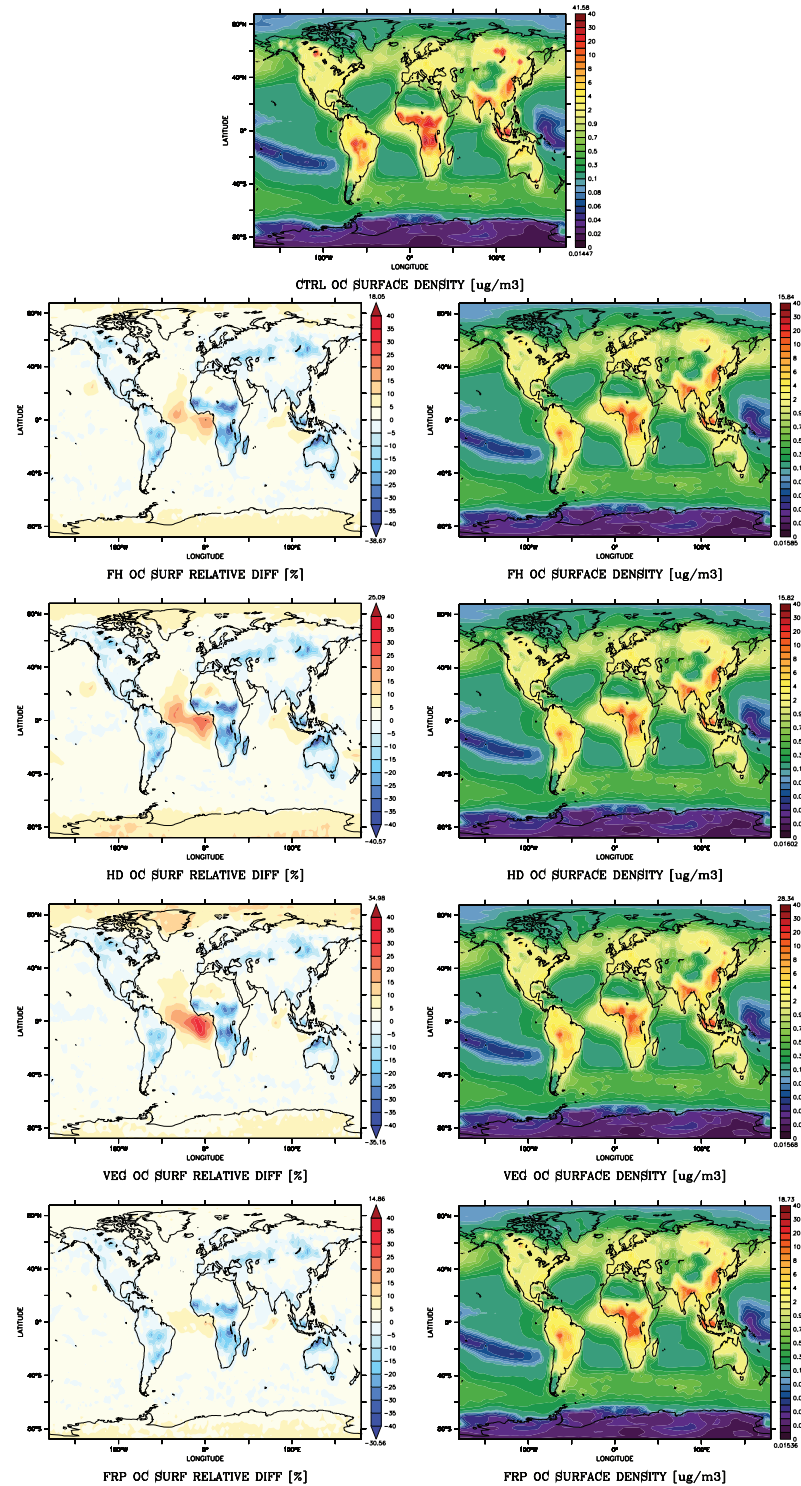
Figure 5.3: Annual mean BC surface density.

The central image shows the annual mean BC surface density for CTRL. The left panels show the BC annual mean surface relative difference $\frac{\text{SCH-CTRL}}{\text{CTRL}} \times 100$. The right panels show the associated BC surface density for each scheme.

5. THE INFLUENCE OF BIOMASS BURNING ON TRACERS

The differences in the annually and zonally averaged BC distribution (Figure 5.5) reveal the vertical transport for VEG and especially for FRP (Section 4.5.2).

In contrast, the effect of HD appears to be confined to the troposphere. Little transport is observed outside of it. As a result, even small negative differences (-1.3%) are shown above the tropopause. Despite the variations between schemes, all tend to exhibit positive differences as a result of the extended lifetime.
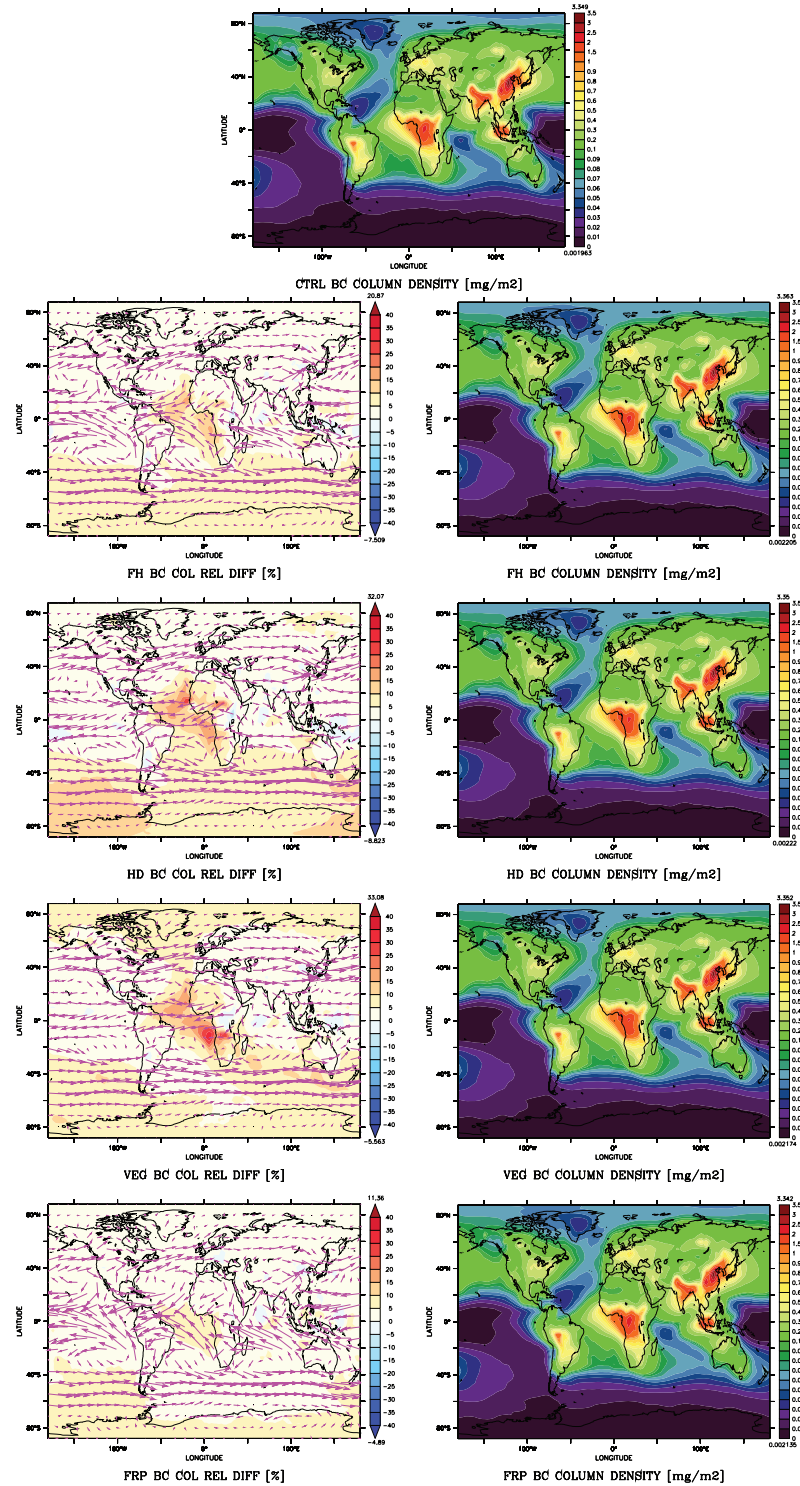
Figure 5.4: BC annual mean column burden.

The central image shows the BC annual mean column burden for CTRL. The left panels show the BC annual mean column burden relative difference $\frac{\text{SCH-CTRL}}{\text{CTRL}} \times 100$, with the wind field at the average injection height of the scheme (overlaid in purple). The right panels show the associated BC column burden for each scheme.
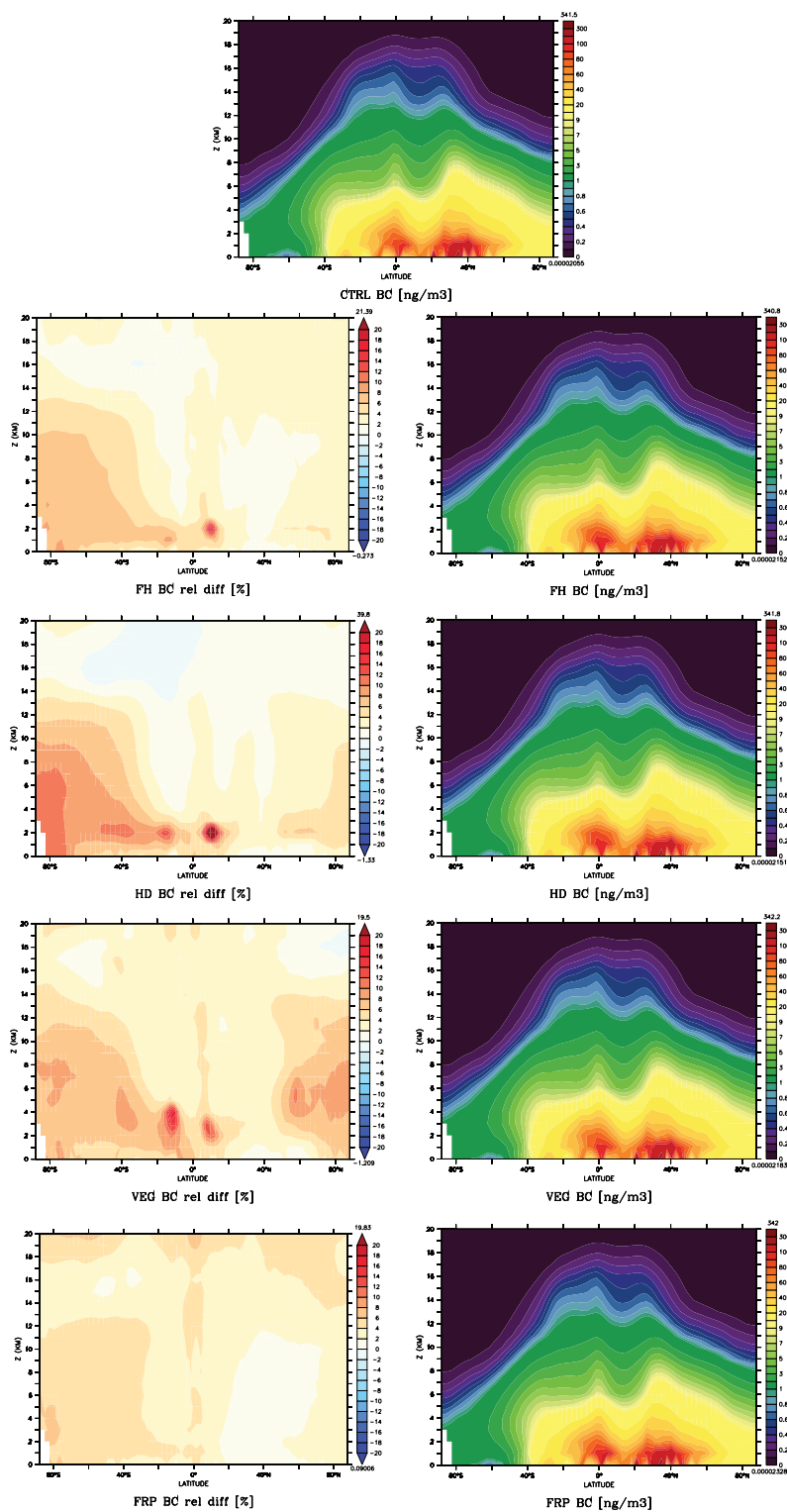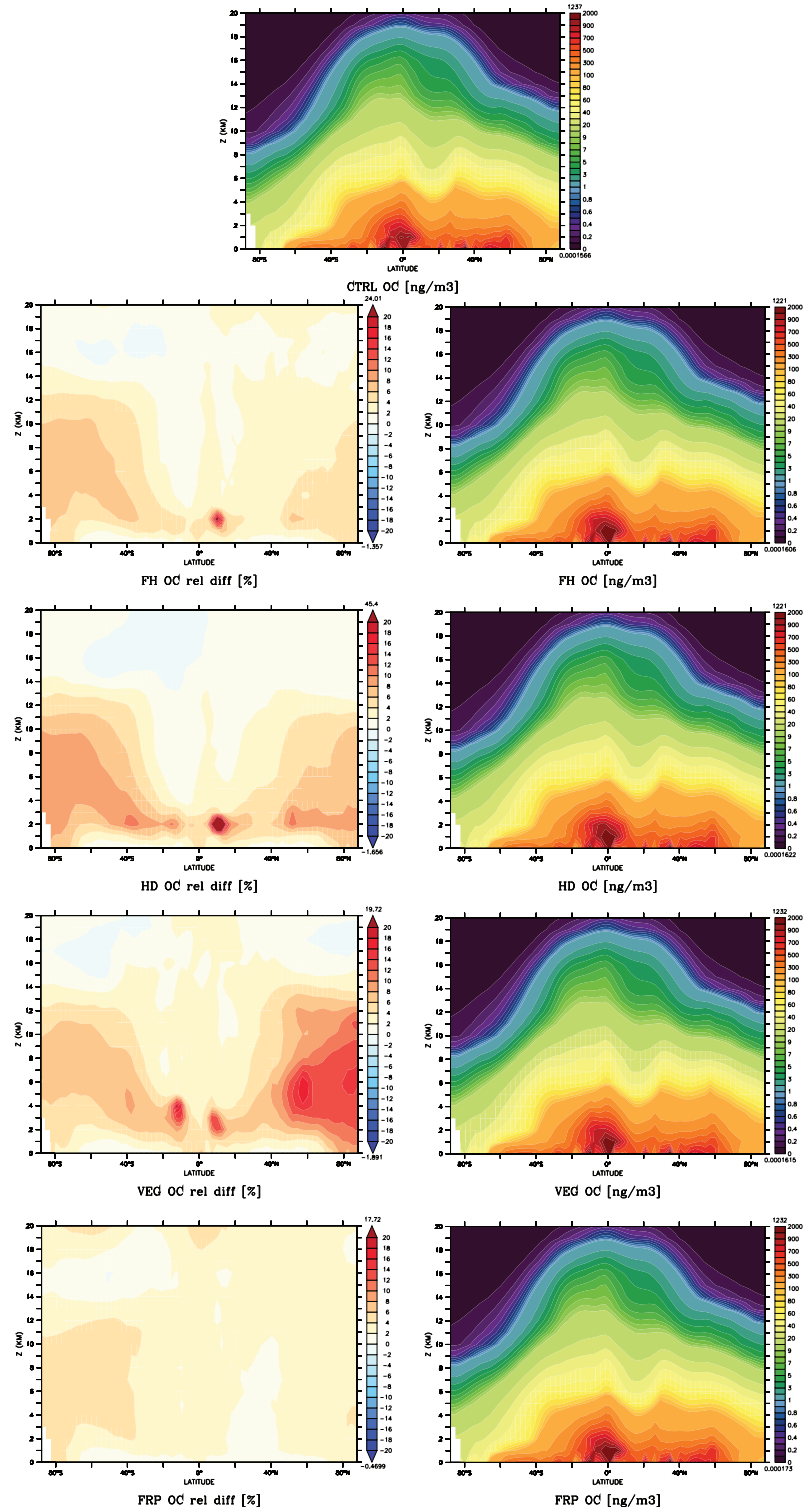
Figure 5.5: Annually and zonally averaged BC density.

The central image shows the BC annual and zonal mean density for CTRL. The left panels show the BC zonal mean relative difference $\frac{\text{SCH-CTRL}}{\text{CTRL}} \times 100$. The right panels show the associated annually and zonally averaged BC density for each scheme.

122

5.1.2 Organic Carbon

Biomass burning produces more OC ($\approx 4\%$ of the total emissions) than BC ($\approx 0.5\%$). Even though OC has more sources, BB is responsible for approx. 37% of the 2006 total OC emissions (Table 1.1). This is more than the contribution of BC_{BB} (32%) to the total BC.

As a result of the seasonal cycle in BB emissions, the OC_{BB} contribution varies from 11% in April to 49% in August (Figure 1.2), when both the maximum emissions and the largest burden occur (Figure 5.6). Analogous to BC, the peak in the relative differences occurs in July for all schemes except FRP (Figure 5.7). For the FRP scheme, the relative differences create a smooth line that follows the natural seasonal cycle of the BB emissions.

The differences between schemes are (as explained in Section 5.1.1) a product of the regional changes in the injection height, the occurrence of fire events in those areas, and the variation of the PBLH (i.e., the mass that is injected above the boundary layer).
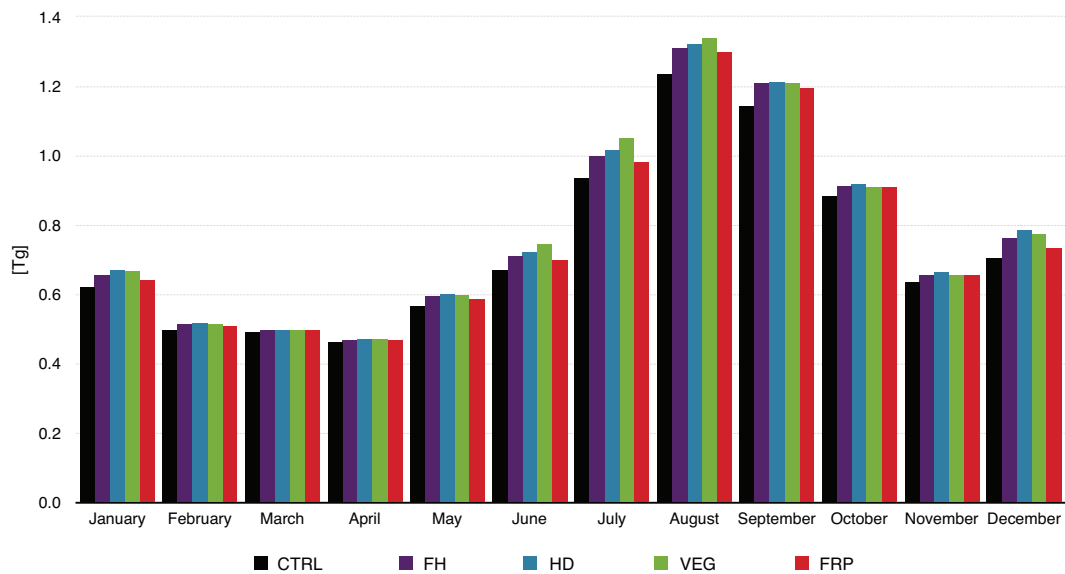
Figure 5.6: Monthly average of OC total burden.

The changes experienced by OC_{BB} are translated into the following effects on the OC annual mean.

The surface distribution (Figure 5.8) shows, as expected, negative differences of lower
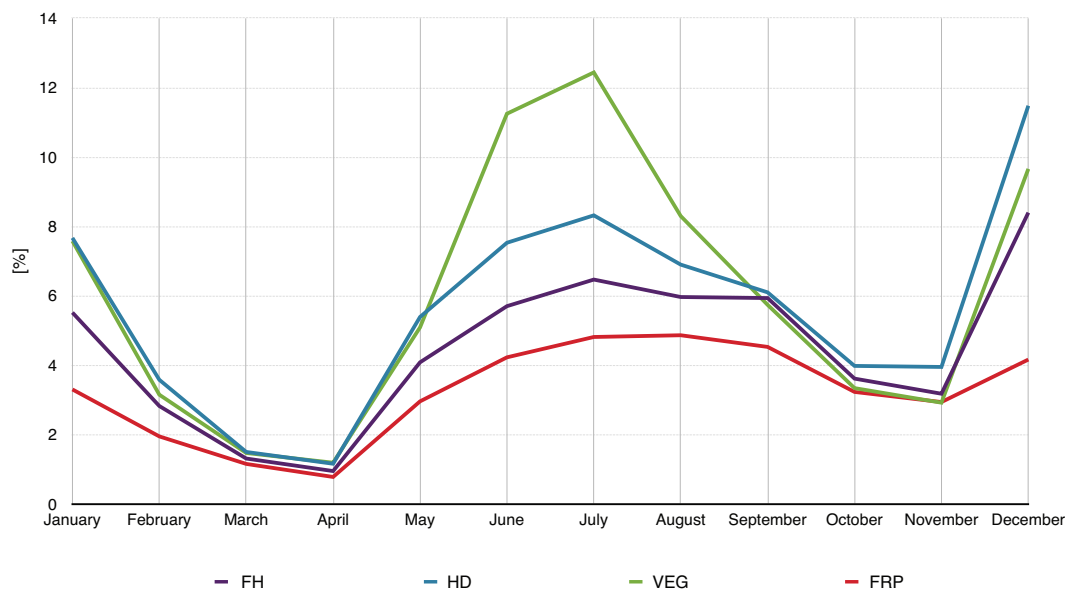
Figure 5.7: OC global burden monthly mean relative difference $\frac{\text{SCH-CTRL}}{\text{CTRL}} \times 100$.

magnitude in the biomass production regions. In contrast to the more than 50% less OC_{BB} at the surface, the total OC negative differences range from 30% to 40%. Positive differences are simulated in the subsequent transport and deposition areas, ranging from 15% for FRP to 35% for VEG.

The differences in the annual mean column burden (Figure 5.9) preserve the strong transport over the North Atlantic (Section 4.5.3). Although for the total OC, the magnitude of the positive changes has been reduced to 11% for FRP and to 40% for HD. The VEG scheme shows an increase of about 10% in the Arctic, which can influence the local transfer of radiation in addition to the enhanced BC particles.

Once again, the effect of the changes in the BB injection on the OC vertical distribution (Figure 5.10) is less intense than the effect on the OC_{BB} (Section 4.5.2). The changes in OC vertical distribution range from 17% (FRP) to 45% (HD) and are consistent with what has been found so far (Section 4.5.2). FRP shows transport above the tropopause, whereas the effects for the other schemes are confined inside the troposphere (particularly for HD).

Figure 5.8: OC annual mean surface density.

The central image shows the OC annual mean surface density for CTRL. The left panels show the OC annual mean surface relative difference $\frac{\text{SCH-CTRL}}{\text{CTRL}} \times 100$. The right panels show the associated OC annual mean surface density for each scheme.
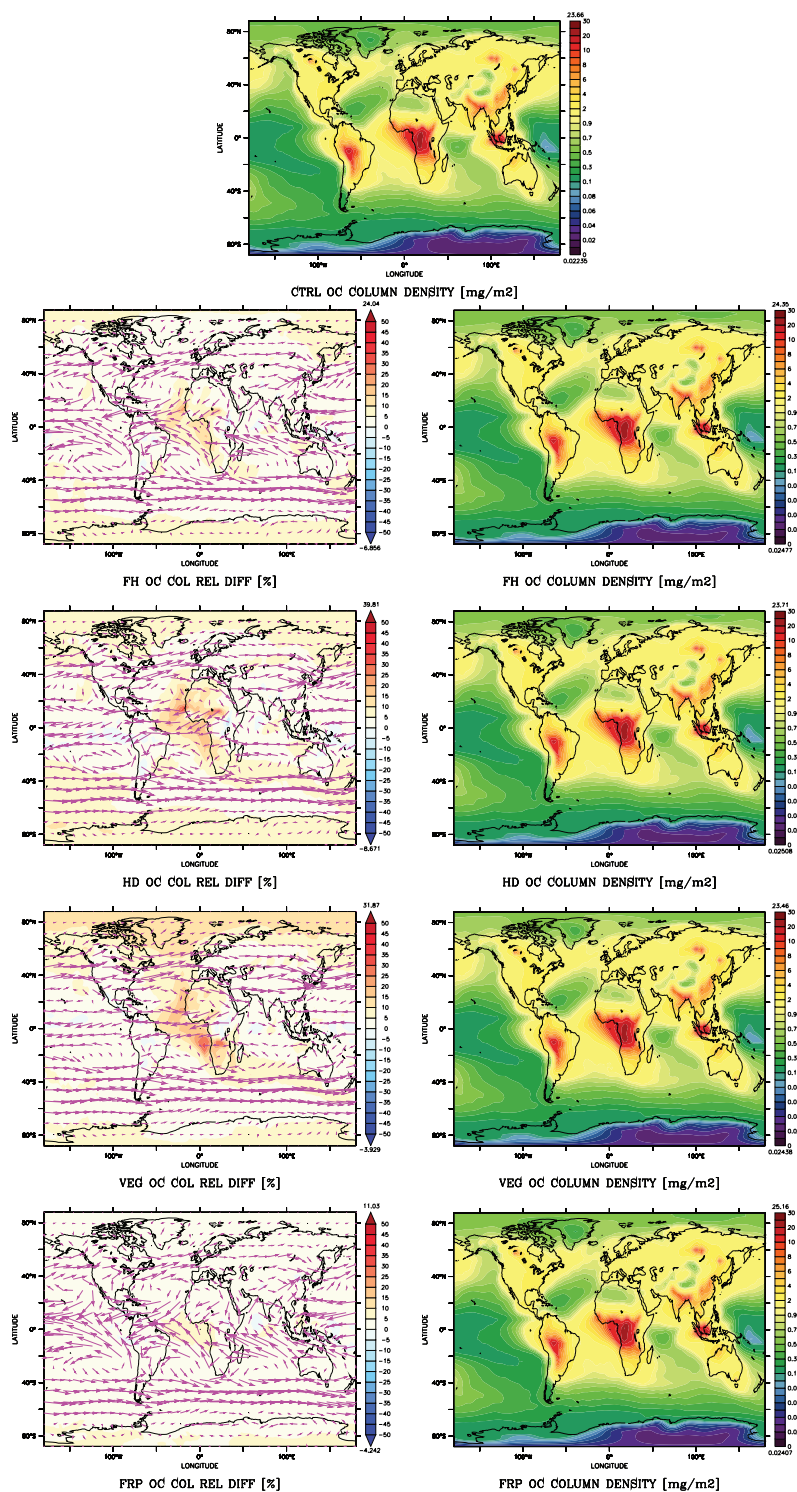
Figure 5.9: OC annual mean column burden.

The central image shows the OC annual mean column burden for CTRL. The left panels show the OC column burden relative difference $\frac{\text{SCH-CTRL}}{\text{CTRL}} \times 100$, with the wind field at the average scheme's injection height overlaid in purple. The right panels show the associated OC column burden density for each scheme.

Figure 5.10: Annually and zonally averaged OC density.

The central image shows the annually and zonally averaged OC density for CTRL. The left panels show the OC relative difference $\frac{\text{SCH-CTRL}}{\text{CTRL}} \times 100$. The right panels show the associated annually and zonally averaged OC density for each scheme.

127

5.2 Aerosol Precursor

5.2.1 Nitrogen Oxides (NO_x) and Particulate Nitrate (NO_3^-)

Biomass burning is the third most important source of nitrogen oxides (NO_x) with 19% of the total emissions, following ship emissions with 23% and fossil fuel with 51% in 2006 (Table 1.1). The seasonal cycle of NO_x is also driven by the occurrence of BB. Consequently, the larger contributions of BB occur during the summer months; in August, this accounts for 32.2% of the total monthly NO_x emissions (Figure 1.2).

Because NO_x is quickly oxidized, the changes to the NO_x injection height have almost no effect on the total burden. However, changes to NO_x injection height do affect the particulate nitrate that forms mostly from the gas phase.

The only direct source of NO_3 is the reaction of NO_2 with O_3. The other paths to nitrate formation require the previous creation of nitric acid (HNO_3). The main source of HNO_3 is the reaction of NO_2 with $OH\cdot$ which is incidentally the reaction that controls the lifetime of the NO_x lifetime. Because NO_2 decreases with altitude, the lifetime of NO_x increases with height. The other path for HNO_3 formation involves the hydrolysis of dinitrogen pentoxide (N_2O_5), which is created via an equilibrium reaction of NO_2 and NO_3. As the temperature decreases the NO_2 concentration diminish and the thermal decomposition of N_2O_5 is also reduced, shifting the equilibrium of the reaction to N_2O_5. Finally, from the N_2O_5 hydrolysis HNO_3 is created.

In the presence of ammonia (NH_3) nitric acid can form ammonium nitrate (NH_4NO_3), which dissociates in NO_3^- and ammonium (NH_4^+) in aqueous solutions (e.g., liquid aerosols and liquid droplets).

Through all of the aforementioned reactions, the balance of ions is influenced by the required equilibrium between NO_3^- anion and the cations Na^+ and NH_4^+.

The global burden of particulate nitrate (NO_3^-) increases for all schemes (Figure 5.11). The changes reach up to 3.9% in July, for VEG scheme. The peak in the relative changes occur in August for HD and in September for FH and FRP.

The simulated changes in summer months are the result of the contribution of BB emissions to the total NO_x. Additionally the variation of the maximum differences is the consequence of the temperature regimes at which emissions are injected by each scheme. The increases in NO_3^- are clearly located in the BB production areas, especially in the grassland and savanna regions, which have a larger production of NO (Figure
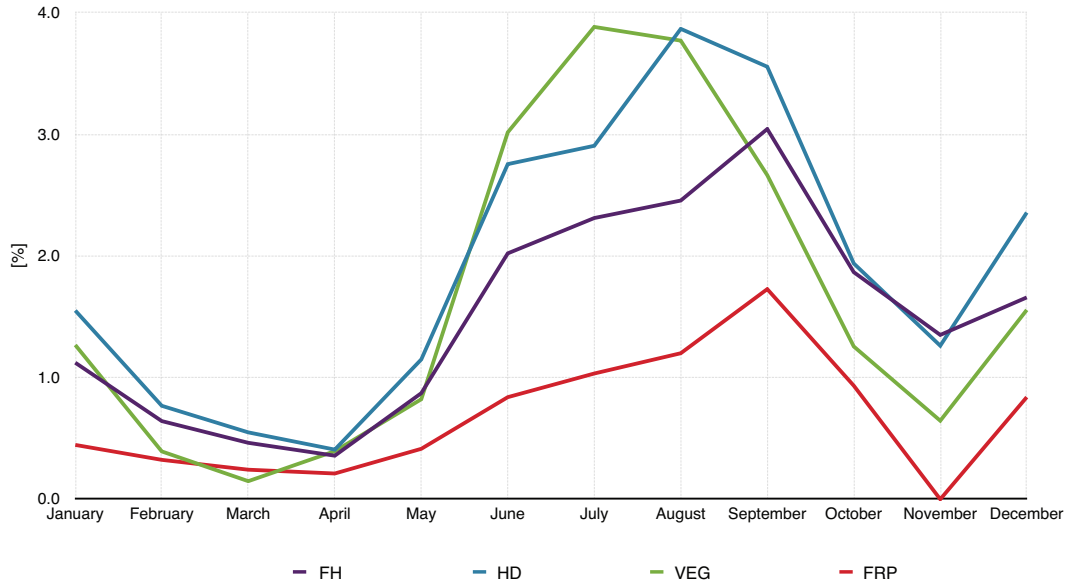
Figure 5.11: NO_3^- relative difference $\frac{SCH\text{-}CTRL}{CTRL} \times 100$.

2.3). The nitrates increases in Africa (Section 4.2) may account for the aging of BC_{BB} and OC_{BB}.

The changes in the annual mean column densities (Figure 5.12) range from 13% (FRP) to 27% (VEG). As a result of the seasonal cycle in the emissions and in the temperature regimes, the column densities differences can reach up to 82% in August over the coast of Africa.

The increases in nitrate over Africa and the adjacent ocean are associated with increases of HNO_3 ranging from 2.6% (FRP) to 14.2% (VEG). However, analogous increases in HNO_3 were not observed in South America, suggesting that paths that do not involve HNO_3 are responsible for the regional increase in NO_3^-. The hydrolysis of N_2O_5 is a possibility.

Considering that NO_3^- is part of the water soluble aerosols (WASO), its increase affects the annual mean AOD —both directly and via additional water uptake.
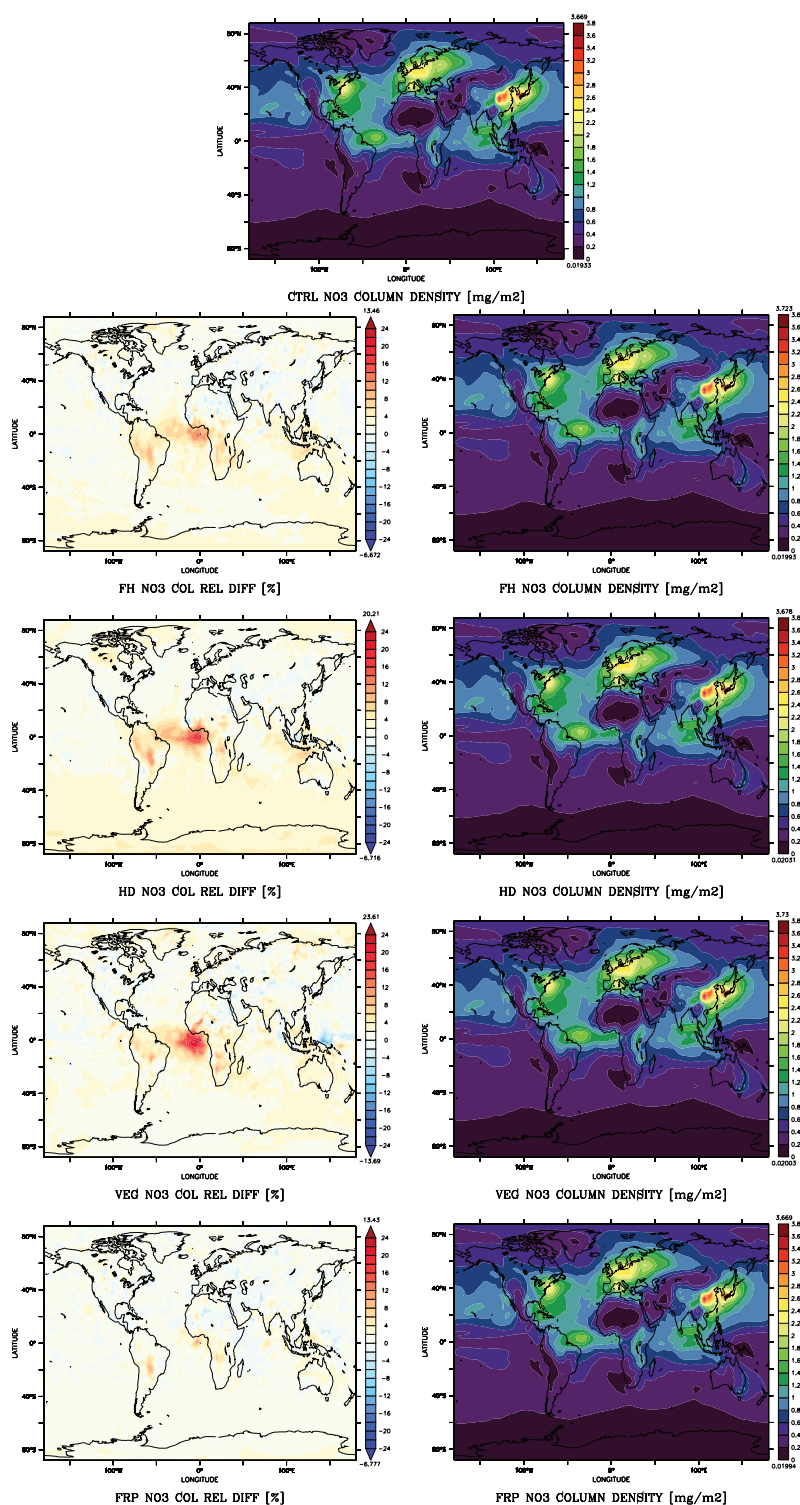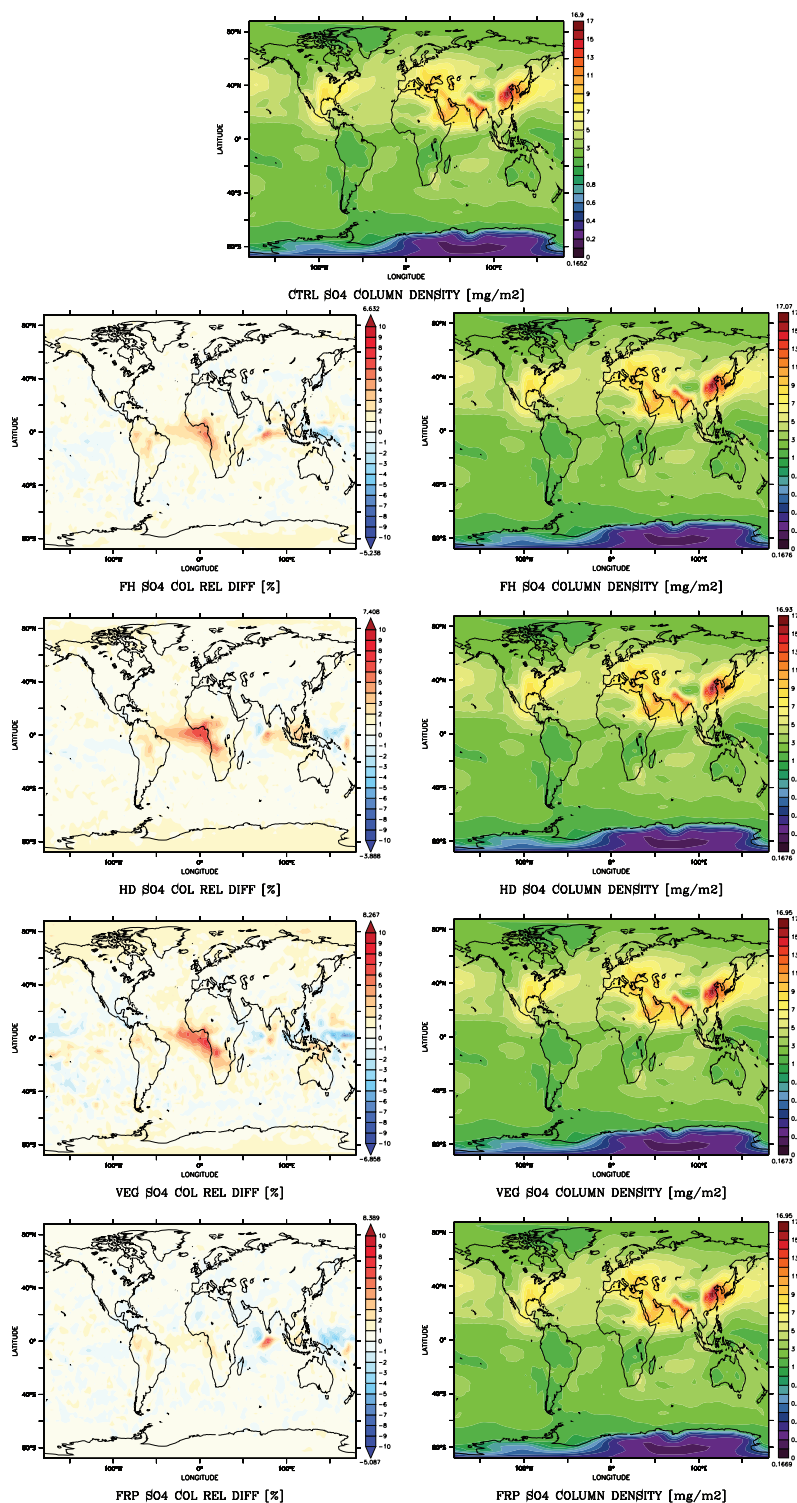
Figure 5.12: NO_3^- annual mean column density.

The central image shows the NO_3^- annual mean column density for CTRL. The left panels show the NO_3^- column density relative difference $\frac{\text{SCH-CTRL}}{\text{CTRL}} \times 100$. The right panels show the associated annual mean NO_3^- column density for each scheme.

5.2.2 Sulfur Dioxide (SO_2) and Particulate Sulfate (SO_4^{2-})

Analogously to NO_x and NO_3^-, particulate sulfate (SO_4^{2-}) is mainly created from gas phase reactions through the oxidation of sulfur dioxide (SO_2) or other sulfur containing compounds that form sulfuric acid (H_2SO_4).

Biomass burning is responsible for only 2% of the total SO_2 emissions in 2006 (Table 1.1). From the total 2006 BB emissions SO_2 constitutes a small fraction (0.5%). Therefore, the effect on the global burden of SO_4^{2-} is almost negligible (up to $\approx 1\%$ for VEG in July). However, regional effects are found on the annual mean SO_4^{2-} column density in the range of 6.6% (FH) to 8.3% (VEG) on the equatorial Atlantic Ocean and the zones around the production areas (Figure 5.13). These regional enhancements may result from variations in the local oxidation capacity (caused by the released BB emissions) or variations in the amount of SO_2 that participates on aqueous phase reactions via in-cloud oxidation to form sulfate. In contrast to the other schemes, FRP shows an increase of 8.4% over the Indian Ocean, whereas the central Atlantic Ocean shows only a small increase. The lower influence on Africa and the central Atlantic for the FRP scheme is a product of the variations in the altitudes at which emissions are released. These variable heights result in different temperature and relative humidity regimes, which influence the processes involved in the sulfate formation and lifetime.

In October, the increases in sulfate for the FRP scheme can reach up to 44% over the Indian Ocean and South America. The strong enhancement observed over the Indian Ocean in October could be the result of the transport of emissions from Indonesia that experienced dry conditions at that time. Notably, in this area FRP has a good agreement with the MISR observations over that region (Figure 3.6).

The increase of SO_4^{2-} modifies the ion balance in a similar way that NO_3^- does (see Section 5.2.3).

SO_4^{2-} is also part of the WASO, consequently, its burden increase contributes to the AOD over the affected regions. Most of the AOD comes from aerosol water. However, WASO aerosols contribute more to the total AOD than BC or OC do because water uptake plays a larger role.

Sulfate has a larger influence on the AOD because it has a greater burden than nitrate. Fires produce more NO_x than SO_2. Nevertheless, the total effect on the WASO annual mean AOD ranges from 7% (FRP) to 14% (VEG) over the BB production and adjacent areas (Section 6.1.1).

Figure 5.13: SO_4^{2-} annual mean column density.

The central image shows the SO_4^{2-} annual mean column density for CTRL. The left panels show the SO_4^{2-} column density relative difference $\frac{SCH-CTRL}{CTRL} \times 100$. The right panels show the associated annual mean SO_4^{2-} column density for each scheme.

5.2.3 Ion Balance and Associated Gas Species

The changes in the injection height of aerosol precursors directly affect the annual mean global (NO_3^-) burden of their associated aerosols. The ion balance is modified because different temperature regimes and background concentrations of other species are encountered by the emissions at various injection altitudes. SO_4^{2-} anion takes precedence over the NO_3^- anion during neutralization. However, because of the reduced effect of BB on the SO_4^{2-}, compared with the effect on the NO_3^-, the influence over the other ions is shifted towards regimes with poor sulfate concentrations.

Ammonium (NH_4^+) shows annual mean increases in the column burden ranging from 6% (FRP) to 11% (VEG) over the central Atlantic Ocean and the continental areas around the African production zones. In Indonesia and South America, there were increases of lower magnitude. The VEG scheme shows small increases over the Arctic region. FRP depict positive differences over Indonesia and the Indian Ocean. Ammonia (NH_3) shows a decrease in the annual mean column burden in the range of 4% (FRP) to 6% (VEG) over the areas where the increases in HNO_3 are located. There are also decreases over both Polar Regions. As a consequence of the changes in Nitrate and Sulfate concentrations, chloride (Cl^-) has enhancements in the range of 9.5% (FH) to 14% (FRP) over South America, Guinea coast and Indonesia (for VEG scheme). Positive chloride differences over the Indian Ocean are evident on all schemes, which is relevant because the concentration of this species over the ocean is higher than over the continents, this is the result of the transport of emissions from Indonesia. These chloride variations are partially associated with modifications of hydrogen chloride (HCl) concentrations, which shows an increase of lower magnitude (3% for FRP to 5% for VEG) over the Atlantic Ocean ITCZ region, South America and the Indian Ocean. Sodium (Na^+) annual mean increases of approx. 9% are observed over the central African coast and Atlantic Ocean, South America, Indian Ocean, Siberia, and Alaska. This is possibly the consequence of changes in coating material that result in a lower sedimentation velocity for this species.

5.3   Gas Species

As a result of the changes in the NO_x injection height OH· recycling is affected. The primary oxidizing species in the troposphere is OH·, which is formed as a result of the ozone photolysis. Consequently, NO_x presence affects the oxidation of carbon monoxide and methane.

Ozone is formed through NO_2 photolysis, the production of which depends on NO and HO_2 concentrations. Therefore, NO_x influences ozone concentrations. NO_x emissions also influence PAN formation, which is enhanced by BB emission of the acetaldehyde (necessary for PAN creation via the reaction of acetaldehyde with OH· to form peroxyacetyl radical and the subsequent reaction with NO_2, Section 1.2). PAN becomes a reservoir of NO_x because of its temperature stability dependence, enhanced by the NO_x release at higher altitudes. Moreover PAN transport to the upper troposphere is facilitated allowing the NO_x release at higher altitudes. Consequently the PAN reservoir of NO_x favors the production of ozone in remote areas. Therefore, vertical distribution of NO_x emissions has an important effect on ozone distribution, even in remote areas.

5.3.1   Oxidation Capacity (CO and CH_4)

The main removal mechanism for carbon monoxide is the oxidation reaction with OH·. As a consequence of the local increases in ozone, the concentration of OH· increases, thereby affecting the tropospheric column density of CO. This results in an annual mean decrease between 1.2% (FRP) and 6% (VEG) (Figure 5.14). An overall reduction is observed globally with the largest value located over Central Africa.

Analogous to CO, the local increases in OH· result in a reduction of CH_4 lifetime. The annual mean lifetime of methane decreases by 2.5% around the injection height altitudes (Figure 5.15). As a consequence of the variation in FRP injection height, the changes are less evident in this scheme. A small but consistent reduction in lifetime is observed worldwide.

5.3.2   Non Methane Hydrocarbons (NMHC)

Approximately 7% of the BB emissions are released in the form of NMHC. The effect on those species is not enough to influence the global burden. However, for most of those emitted species, regional changes were observed in the annual mean column density.
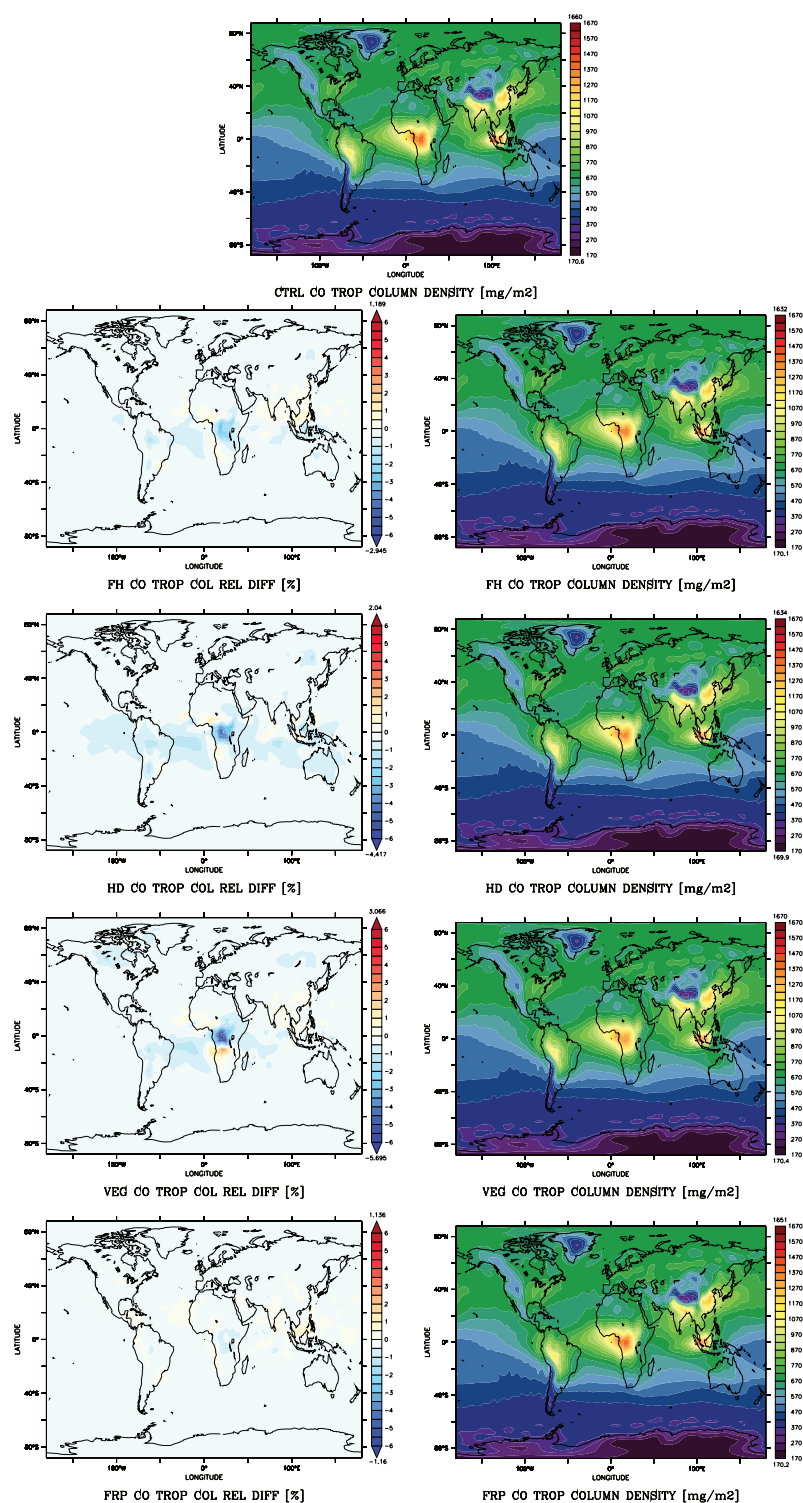
Figure 5.14: CO annual mean tropospheric column density.

The central image shows the CO annual mean tropospheric column density for CTRL. The left panels show the CO tropospheric column density relative difference $\frac{\text{SCH-CTRL}}{\text{CTRL}} \times 100$. The right panels show the associated annual mean CO tropospheric column density for each scheme.

135

5. THE INFLUENCE OF BIOMASS BURNING ON TRACERS
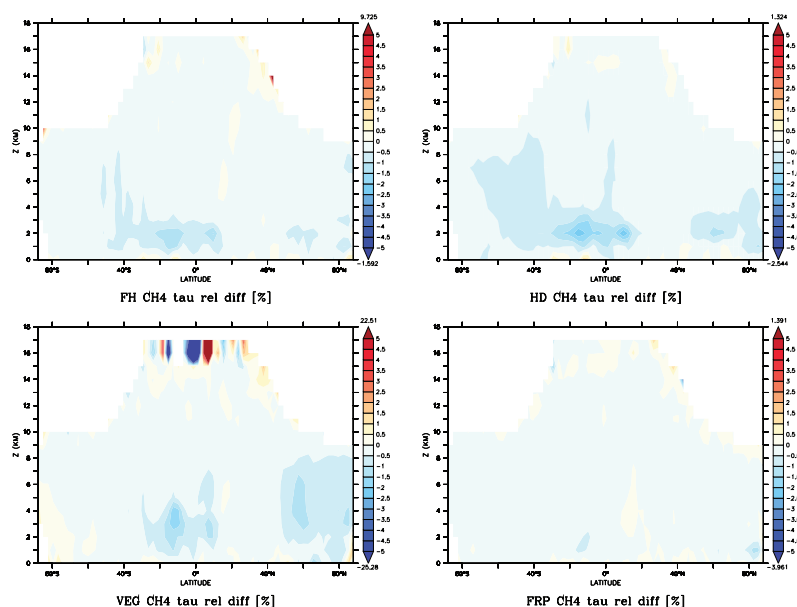
Figure 5.15: Annually and zonally averaged CH_4 lifetime relative difference $\frac{\text{SCH-CTRL}}{\text{CTRL}} \times$ 100.

For formaldehyde (HCHO), there were increases ranging from 2% (FRP) to 3.4% (HD). The changes in the injection height of this compound may influence the chemistry of the upper troposphere because it is one of the reservoir species of HO_x (key elements in the O_3 production-destruction cycle). For formic acid (HCOOH), there were increases ranging from 4.2% (FRP) to 16.9% (VEG). For acetic acid (CH_3CO_2H), there were increases ranging from 3% (FRP) to 10.6% (VEG). Decreases ranging between 2.9% (FRP) and 7.3% (VEG) were also simulated. The most substantial values were located in central Africa. For acetaldehyde (CH_3CHO), there were decreases ranging from 2.9% (FRP) to 8.9% (VEG). These decreases could be associated with the increase in the annual mean column density of PAN, which ranged between 3% (FRP) and 9% (VEG). For methanol (CH_3OH), there were decreases ranging between 1.8% (FRP) and 3.6% (VEG) with the largest differences located over Central Africa. Increases of similar magnitude (2% for FRP to 3% for VEG) were observed over South America, Indonesia, and South Africa. In the production zones, there were increases in methyl ethyl ketone (MEK) ranging from 3% (FRP) to 12% (VEG). In the adjacent regions —especially the ITCZ— there were decreases ranging from 3% (FRP) to 8.3% (VEG). For ethene (C_2H_4), there were increases ranging from 6% (FRP) and 9.6% (VEG) over

regions with minute concentrations. However, decreases of approx. 6% were seen over Siberia, Central Africa, and Alaska. For ethane (C_2H_6), there were generally decreases with peaks between 1% (FRP) and 6.5% (VEG) over Central Africa. Minor increases are seen in the adjacent regions. For propene (C_3H_6), there were increases ranging from 7% (FRP) to 15% (VEG) over the production regions in Africa, South America, and Australia. For propane (C_3H_8), there were mainly decreases; the largest values ranged between 2% for FRP and up to 7% for VEG. In this latter scheme, there was an increase of 5% directly south of equatorial Africa, the area with the largest decrease. For n-butane (NC_4H_{10}), there were decreases ranging between 2.5% (FRP) and 4% (VEG) over the Atlantic ITCZ region. Increases of approx. 3.5% were observed in South America and Indonesia. The changes in acetone (CH_3COCH_3) were limited to 2% for the VEG scheme. However, as with formaldehyde, the injection height of acetone could enhance its transport to the upper troposphere, where it can contribute to HO_x radicals by photo-oxidation. However, the evaluation of this effect is beyond the scope of this work. The images of these changes can be found in the Appendix (Section 8.2).

5.3.3 Ozone (O_3)

Injecting NO_x and NMHC together on higher altitudes has affected ozone concentrations at the surface and in the tropospheric column. The annual mean surface O_3 concentrations show an increase (compared with the CTRL simulation) that range from 2.5% (FRP) to 5% (VEG) (Figure 5.17). The largest increase is observed over the central Atlantic Ocean, followed by South Africa, South America, and Indonesia. Small increases are observed in Siberia and, in lower magnitudes, scattered over Canada. The O_3 annual mean tropospheric column density (Figure 5.18) shows enhancements in the range of 1.6% (FRP) to 2.2% (VEG) over Central Africa, South America, and in less intensity over the Arctic. Decreases in the range of 0.6% (HD) to 2.4% (VEG) are found over the Indian Ocean and Indonesia, which may be the result of changes in the transport or deposition of the ozone precursors. A modelling study (Pfister et al., 2006) for North America boreal forest fires on summer 2004 with vertically distributed BB emissions through the troposphere (up to 9 km) revealed an enhancement (compared with a simulation with emissions released at the surface) of similar magnitude (1.5%) in the O_3 tropospheric column burden. Because of the transport of O_3 and its precursors, effects from the fires are also expected downwind of remote areas. This can

be seen in the tropospheric column density enhancement on Northern Siberia, close to the Taymyr Peninsula (CTRL central panel and right column panels, Figure 5.18). Enhancements of tropospheric O_3 concentrations attributed to BB NO_x and VOC emissions over the equatorial Atlantic have been widely seen (e.g., Sauvage et al., 2007b; Thompson et al., 2000; Thouret et al., 2009). Particularly, the enhancement on the Gulf of Guinea (Sauvage et al., 2005, 2007a) and downwind over the Atlantic Ocean (Real et al., 2010), which are in agreement with the simulations of this thesis. Aircraft (Andrés-Hernández et al., 2009; Reeves et al., 2010; Williams et al., 2010) and ozonesonde measurements Thouret et al. (2009) taken as part of the African Monsoon Multidisciplinary Analysis (AMMA, www.amma-eu.org; Redelsperger et al., 2006) have shown enhancements in O_3 concentrations at around 4–5 km altitude during August 2006 near the coast of Nigeria, Benin and Ghana. This can be seen in Figure 5.16, which shows enhancements of the O_3 concentrations around the injection height in August. Enhancements at higher altitudes (10 to 12 km) can be the product of vertical transport of O_3 precursors by deep convection (Andreae et al., 2001). The zonal and annual mean ozone concentrations show small increases ($\approx 1\%$) around the injection altitudes. These increases have higher values seasonally e.g., July (1.6% for FRP to 3.6% for VEG) and December (2% for FRP to 6.8% for HD) around the injection altitudes and in the equatorial upper troposphere.
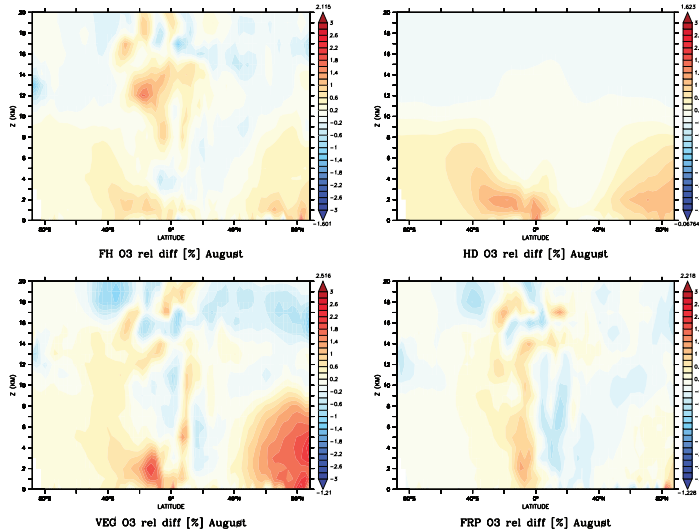
Figure 5.16: August zonal mean O_3 concentrations relative difference $\frac{\text{SCH-CTRL}}{\text{CTRL}} \times 100$.
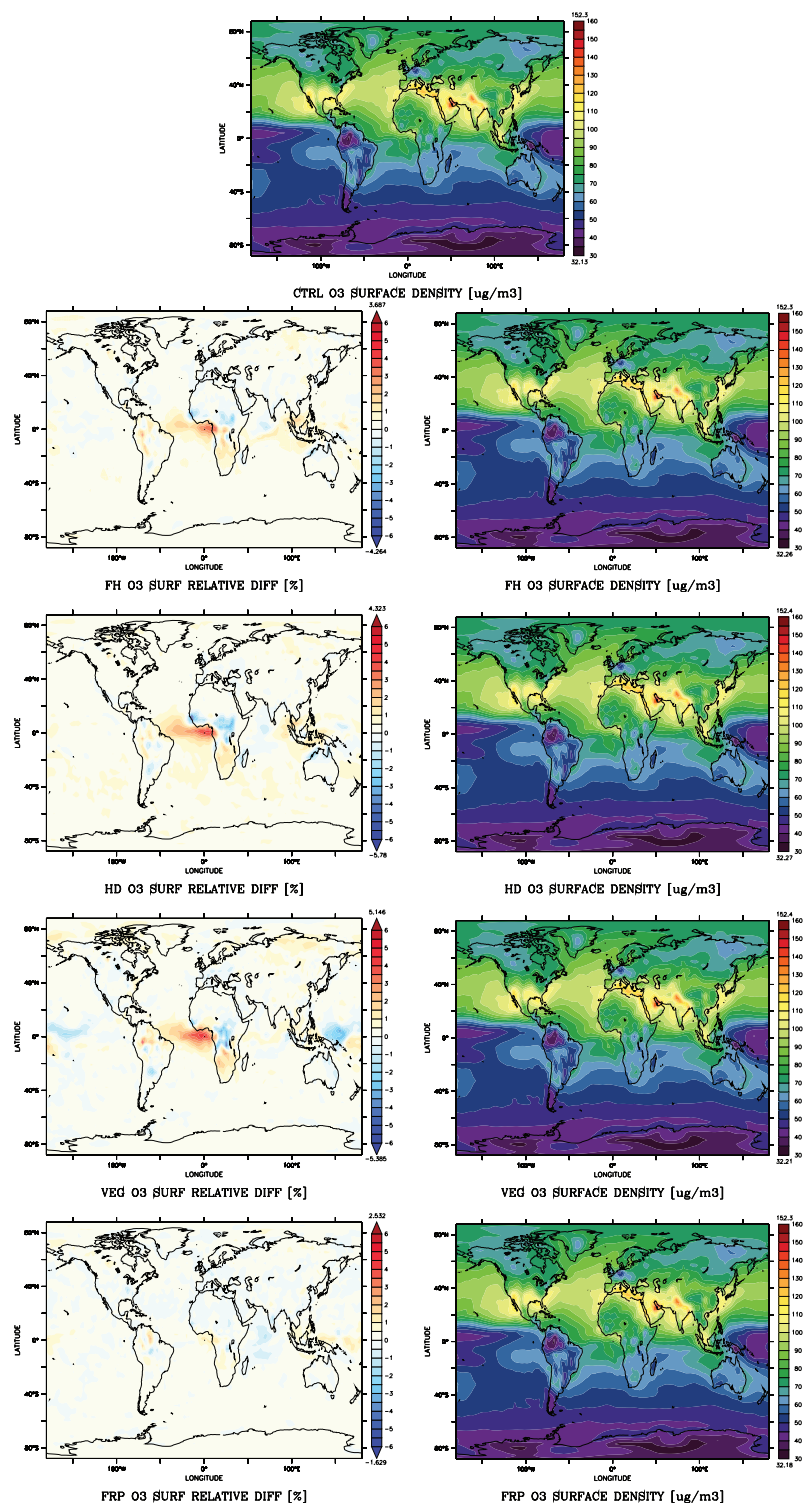
Figure 5.17: O$_3$ annual mean surface density.

The central image shows the O$_3$ annual mean surface density for CTRL. The left panels show the O$_3$ surface density relative difference $\frac{\text{SCH-CTRL}}{\text{CTRL}} \times 100$. The right panels show the associated annual mean O$_3$ surface density for each scheme.
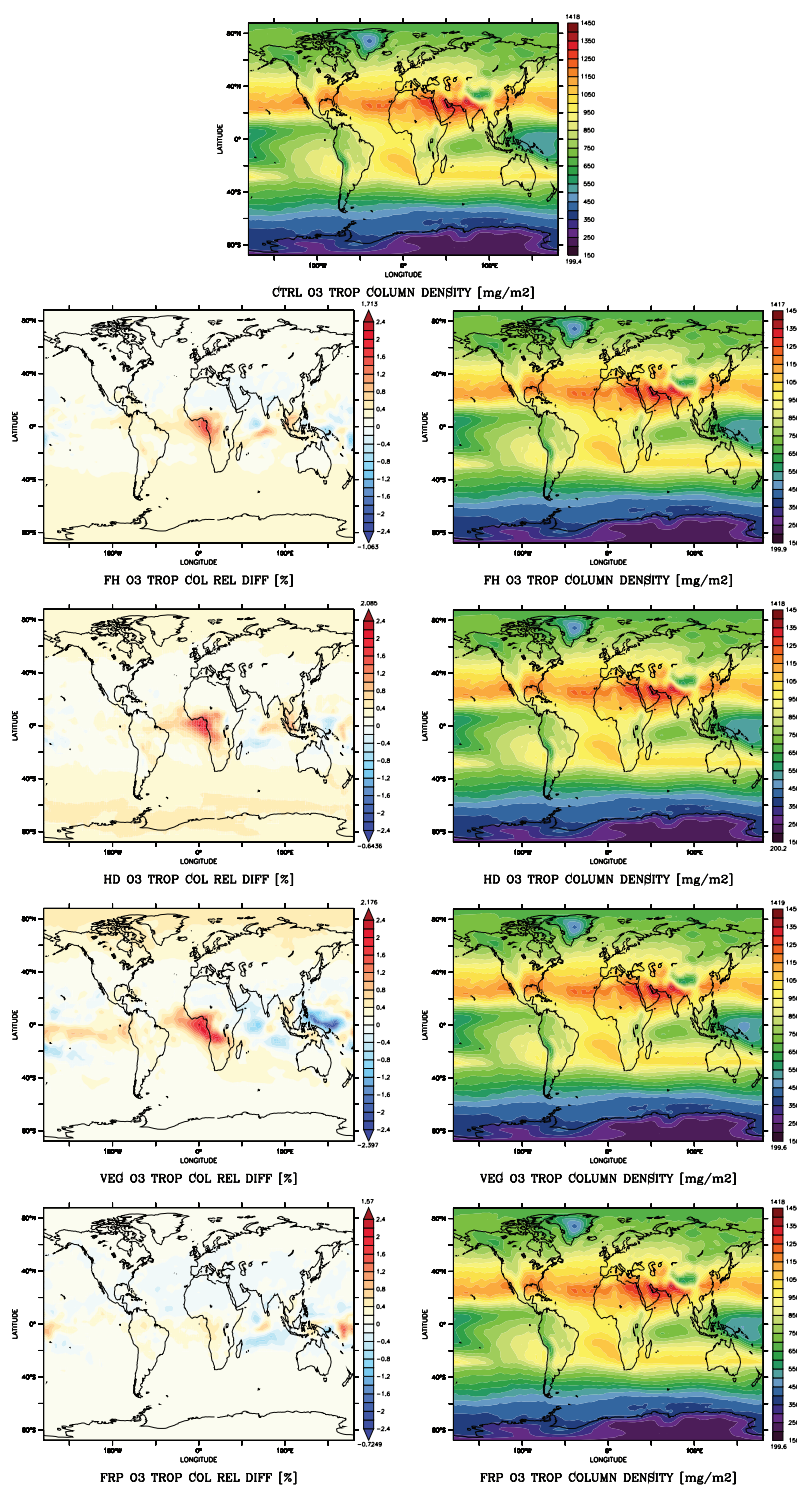
Figure 5.18: O_3 annual mean tropospheric column density.

The central image shows the O_3 annual mean tropospheric column density for CTRL. The left panels show the O_3 tropospheric column density relative difference $\frac{\text{SCH-CTRL}}{\text{CTRL}} \times 100$. The right panels show the associated annual mean O_3 tropospheric column density for each scheme.

6

The Radiative Effect of Modified BB Emissions on Climate

This chapter is dedicated to analyzing the radiative effect of height resolved BB emissions on the climate system. It focuses on making a link between the microphysical and chemical changes (e.g., secondary aerosol production) caused by the BB emissions and their effects on the cloud processes (e.g., CCN production) that influence radiative transfer.

The changes in the direct aerosol effect are driven by the optical properties of the primary and secondary aerosols and their water uptake. These are assed using the single scattering albedo ω_0 and the column integrated extinction coefficient σ (i.e., the aerosol optical depth, AOD). The AOD is chosen to evaluate the total effect of the distribution of scattering and absorbing particles along the vertical. Changes in the single scattering profile are evaluated in order to address any modifications to the radiation transfer. Variations in the ω_0 affect important processes such as cloud lifetime because of changes in heating profiles and in the albedo of highly reflecting surfaces (e.g., clouds, ice, or snow) when absorbing aerosols are located above them. Considering that BB emissions are efficient CCN, the changes in CCN concentrations are addressed as a preamble to the cloud effects in the transfer of radiation. Finally, the disturbances of the overall radiative fluxes are evaluated.

In order to assess AOD and CCN, the set of simulations without feedback between chemistry and dynamics (Section 2.1.2.3) was used to ensure identical meteorological variables when comparing simulations. To analyze changes in the transfer of radiation

(i.e., ω_0 and radiative fluxes), the set of simulations including all feedback was used.

6.1   Optical Effects

The radiative properties of both the primary and secondary aerosol product of the BB emissions as well as the changes they generated on the aerosol water contribute substantially to the AOD and therefore to the transfer of atmospheric radiation.
The optical parameters AOD (τ), single scattering albedo (ω_0), and asymmetry factor (γ) are calculated in the submodel AEROPT (Section 2.1.2.1) assuming a homogenous internal mixing. The aerosol homogenous internal mixing considered in the model represents the state of aged smoke plumes. This assumption may affect the optical properties by leading to overestimations of the absorption of solar radiation compared with the real mixing state (Klingmüller et al., 2014).

6.1.1   Aerosol Optical Depth

The aerosol optical depth (AOD), which is determined by the vertical integration of extinction coefficient (σ), is evaluated in this section. The AOD is modified by the increase in lifetime and therefore the average global aerosol burden, the microphysical evolution of the primary aerosols, the formation of secondary aerosols, and the transport of particles. The hydrophilic aerosols can additionally modify the aerosol water, which is the dominant term in extinction. Modifying the injection height influences all those processes and globally increases the AOD, particularly in the BB regions and the downwind transport zones.
The regional BC annual mean AOD at 550 nm increases from 13% (FRP) to 58% (HD) over the BB areas compared with the CTRL simulation. There are similar increases for OC, which range between 12% (FRP) and 59% (HD). The increases in the WASO annual mean AOD range from 7% (FRP) to 14% (VEG). These increases translate into an increase of the total AOD ranging from 8% (FRP) to 23% (VEG) (Figure 6.1).
Comparisons (not shown) with MODIS and MISR satellite observations show a small improvement in the AOD value ($\approx 10\%$) and in the correlation over South America, the Central and South Atlantic Ocean, the Gulf of Guinea, and the African and Indian Oceans. However, this enhancement is not enough to match the observed AOD. Therefore, the underestimation in those regions remains. It is important to consider
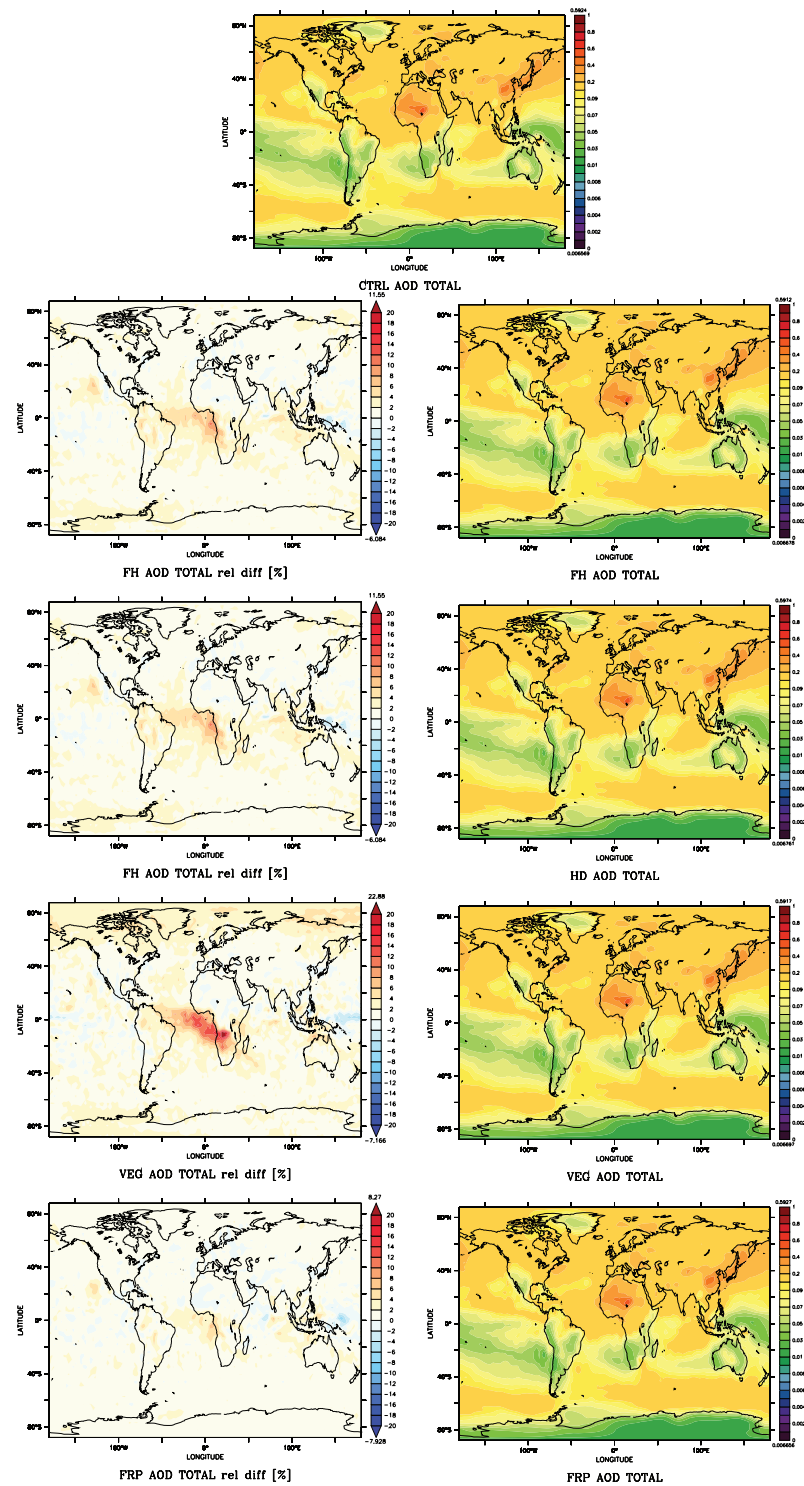
Figure 6.1: Annual mean aerosol optical depth.

The central image shows the annual mean AOD for CTRL. The left panels show the annual mean AOD relative difference $\frac{\text{SCH-CTRL}}{\text{CTRL}} \times 100$. The right panels show the associated annual mean AOD for each scheme.

the uncertainty in the satellite AOD observations, especially when the comparison is done for one year (2006).

Most models (e.g., Koch et al., 2009; Petrenko et al., 2012; Tsigaridis et al., 2014) — including EMAC (Pozzer et al., 2012)— underestimate satellite observed AOD in BB areas (e.g., Africa, Mexico and South America) by a global factor of 3.4 (Kaiser et al., 2012). Strong regional variations lead to factors of 1.5 in savannah and grasslands, factors of 2.5 for tropical forest, and factors 4.5 in extra-tropical forest (Colarco, 2011). These discrepancies can be partially attributed to uncertainties in dust modeling, which affects the AOD over Africa but not in other regions. Therefore, other reasons should be considered. Errors in the estimation of burned area and therefore fuel loads are ruled out because models have revealed little bias in CO emissions from BB in these regions (e.g., Arellano Jr. et al., 2004, 2006; Stavrakou and Müller, 2006). Consequently, lifetime (that influence the transport and ageing of particles), mass absorption cross section, and aerosol emissions may determine the AOD discrepancy.

The injection height plays an important role in some of the factors (lifetime and transport) that were improved in this study and resulted in the AOD enhancement. In Section 4.4 the magnitude of the lifetime enlargement was addressed, resulting in values for the BC_{BB} (10.82 in CTRL to 11.14 days in FH) that were in the upper range of the estimated BC lifetimes (3.8 to 11.4 days, Bond et al., 2013). It may be possible to extend the lifetime of the BC_{BB}. However, considering the magnitude of the AOD discrepancy, this will not be enough. That leads to the role of the mass absorption cross section that may be altered by the evolution of the BC mixing state. However, this is already enhanced by the homogeneous internal mixing state considered in the model. However, a core-shell treatment including multiple refractions can cause an increase in the extinction (Klingmüller et al., 2014). The remaining factor is the aerosol emissions, the underestimation of which may be a product of the uncertainty in the fuel load (which has been ruled out) and the estimation of the emission factors. The emissions of this thesis were obtained from GFED3 (Section 2.2.1), which uses the emission factors proposed by Andreae and Merlet (2001). However the values in Andreae and Merlet (2001) are based on thermal oxidation techniques, and optical absorption measurements were excluded. Further studies (Chin et al., 2002; Liley et al., 2002; Liousse et al., 1996) suggest larger emission factors when absorption measurements are used; these values had led to African emissions 2.4-fold higher than those estimated by GFED2 (Liousse

et al., 2010). Further uncertainty originates from the general estimation of emission factors on fresh plumes and comparing them with long-term regional averaged values that mostly represent aged smoke. As the emissions evolve, organic matter condenses, and no more BC is created, thereby leading to a lower BC/PM ratio. Consequently, the SSA for aged plumes is larger (more scattering than absorption) than the SSA of fresh plumes, and their comparison leads to an underestimation of either the BC emissions or the BC absorption (Bond et al., 2013). Based on the emission factors of Andreae and Merlet (2001), Bond et al. (2013) suggest that the emissions may be underestimated by a 0.6 to 4-fold.

6.1.2 Single Scattering Albedo

The single scattering albedo (ω_0) is a key parameter to determine the aerosol radiative effects because it relates the scattering and absorption components (Equation 1.1).
A net positive forcing at the top of the atmosphere (TOA) occurs when ω_0 has values below 0.85 (i.e., the absorption component becomes important). Net negative forcing at the TOA happens when ω_0 has values above 0.95 (i.e., the absorption component is negligible and the scattering component dominates). However, for the intermediate values, the net warming or cooling effect depends on the albedo of the underlying surface or clouds and the fraction of solar radiation that is scattered upward by the particles (Section 1.2). Therefore, the horizontal and vertical distribution of the absorbing and scattering aerosols influences the net radiative effect at the top of the atmosphere (TOA).
The changes in ω_0 vertical profile provide a guide for the possible radiative effects that the aerosol could directly and semi-directly exert by influencing the clouds. In this section, the changes in the single scattering albedo in the visible band (0.25–0.69 μm) are evaluated.
The global annual mean ω_0 vertical profile (Figure 6.2) shows that absorption has been enhanced in the 2 km closest to the surface and in the upper troposphere from 7 to 14 km. Because of the transport of absorbing particles to higher altitudes by the FRP scheme, a small decrease in ω_0 is shown at a height of approx. 20 km.
Regionally (Figure 6.3), reductions in ω_0 are evident for all schemes. In Africa (Figure 6.3, upper left panel), the ω_0 rapidly decays in the first 1 km. Nevertheless, the absorption enhancement is evident from the surface up to 4 km and in the most absorbing

part of the profile from 7 to 14 km. In Indonesia (Figure 6.3, lower left panel), in all schemes, increases in absorption are evident near the surface and between 7 and 13 km. The INDOEX campaign established that absorption at higher altitudes over the Indian Ocean strongly influences the hydrological cycle (Ramanathan et al., 2001b). The South American ω_0 vertical profile (Figure 6.3, lower right panel) shows an absorption enhancement in all schemes from the surface and up to 7 km. A maximum change is evident from 3 to 5 km. In the Arctic (Figure 6.3, upper right panel), for all schemes, a small absorption enhancement is found over the whole troposphere. A maximum change is located between 4 and 14 km for the VEG scheme and approx. 16 km for the FRP scheme.

The mean ω_0 in the column decreased slightly (compared with the CTRL simulation). The absorption enhancement near the surface (in the first 3 km, Figures 6.2 and 6.3) could limit the lifetime of low clouds through warming effects. In contrast, the absorption enhancement at higher altitudes could limit the growth of higher clouds and the availability of ice crystals.

6.2 Cloud Effects

6.2.1 Cloud Condensation Nuclei

The widely observed efficiency of BB particles to act as CCN has been discussed in Section 1.2. Here, changes in CCN concentration at 0.4% supersaturation are quantified. The annually and zonally averaged concentrations of CCN increased from 3.5% (FRP) to 26% (HD) (Figure 6.4). The increases are confined to the troposphere and concentrated around the injection height regions. The exception was FRP; the variability in the altitude at which emissions are released generates more evenly distributed changes. Because changes in the CCN concentrations directly affect the cloud properties, the variations in the CCN concentrations are considered at the PBLH (the typical level at which clouds form, which represents its base) (Figure 6.5). Increases from 25% (FRP) to 42% (HD) are located in the BB regions. The North Pacific area corresponds to the region in which increases in the mode mass fraction of ki were evident (Figure 4.7). This suggests that the extra ki particles, the lifetime of which has been extended after the less efficient removal (Section 4.2), are able to grow and become CCN active in the accumulation mode, thereby contributing to most of the CCN. The fraction of the
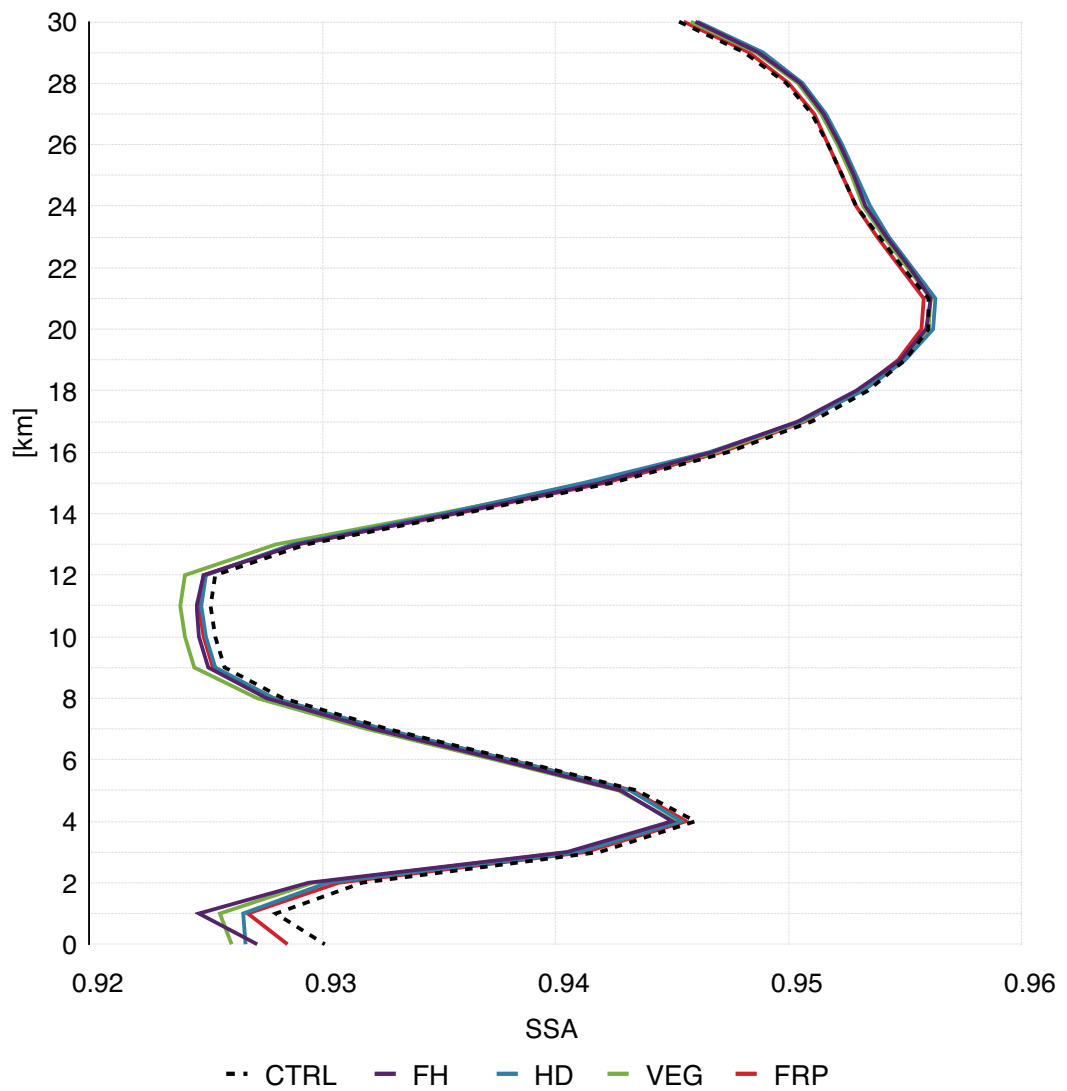
Figure 6.2: Global vertical profile of single scattering albedo.
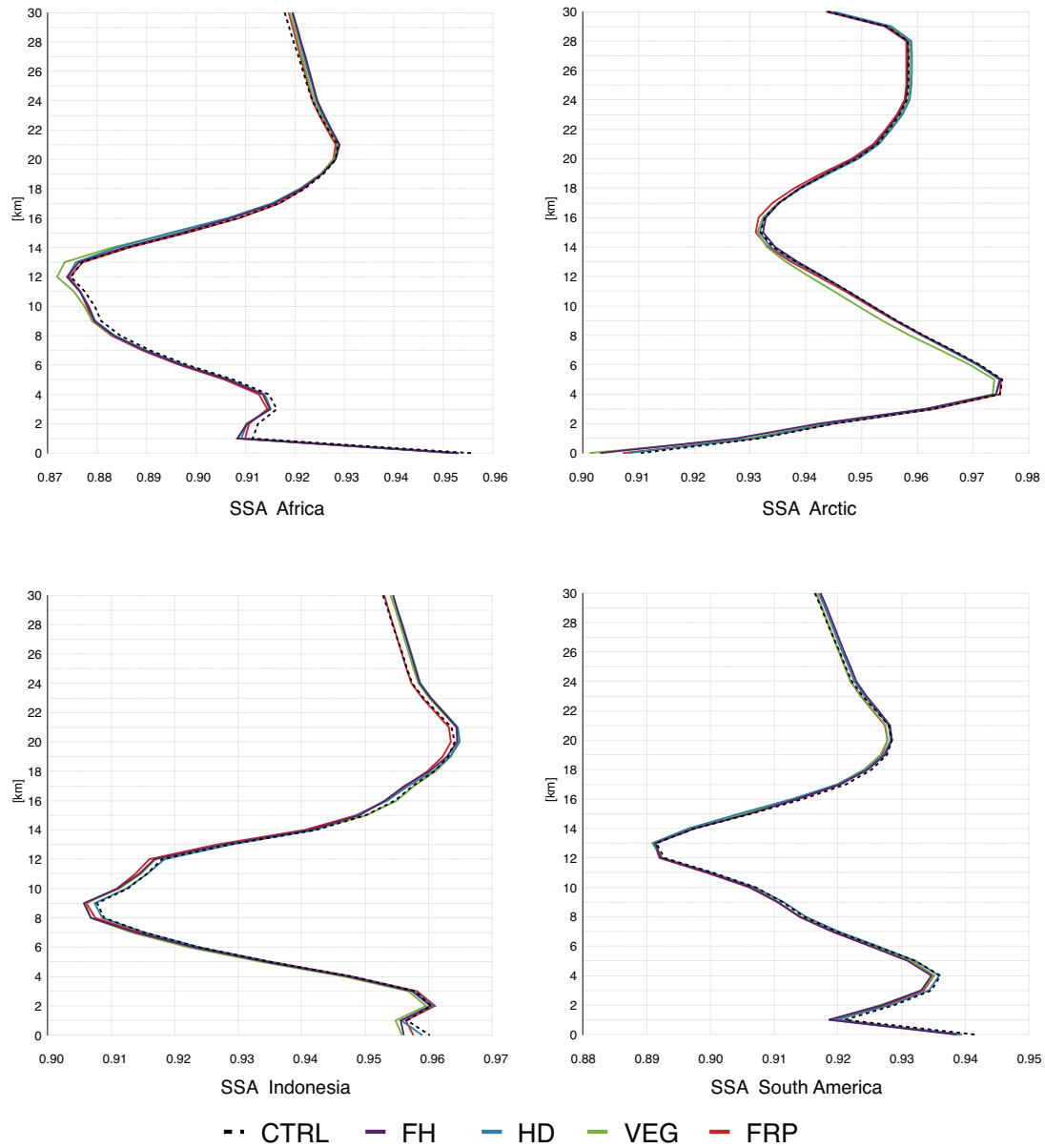
Figure 6.3: Regional Single Scattering Albedo vertical profile.

The upper left panel shows the SSA vertical profile in Africa. The lower left panel shows the SSA vertical profile in Indonesia. The upper right panel shows the SSA vertical profile in the Arctic. The lower right panel shows the SSA vertical profile in South America.

CCN in the accumulation mode has been slightly enhanced, especially in local summer months. In contrast, the fraction of the coarse and the Aitken (in larger magnitude) decreased. This supports the explanation (Section 4.2) that the ki are transferred directly to the accumulation mode (after coagulation) as a consequence of the available coating material and the lifetime enlargement.

Therefore, the enhancement of CCN concentrations results from the lifetime enlargement, which allows the particles to become activated to cloud droplets; and the burden increase, which provides more available particles for activation, particularly at the PBLH and further upwards (enhanced by the injection height).

The increase in CCN could lead to increases in cloud droplet number concentration, which leads to negative radiative forcing (cooling) by increasing the albedo effect of the clouds. Considering that the increases in the concentrations of CCN are located in areas in which the critical supersaturation is favorable for the activation of the CCN in the accumulation and coarse size (which represents most of the CCN), it is reasonable to assume that most of the CCN will develop into cloud droplets at the PBLH.

6.3   Radiative Balance

It is clear that the injection height plays an important role in several processes that either directly (by scattering and absorption) or indirectly (by the modification of cloud properties) influence atmospheric radiative transfer e.g., the evolution of the primary aerosols that increases their lifetime (Section 4.2) and distribution (Section 5.1), their capacity to become CCN (Section 6.2.1), the production of secondary aerosols (Section 5.2.1), and the local concentrations of ozone (Section 5.3.3). In this section, the effects on the radiative transfer are quantified as the difference of the TOA (net shortwave plus long-wave) radiative fluxes between the CTRL and the BB emissions scheme simulations. Clear sky and all sky flux disturbances as well as total cloud forcing are analyzed. The comparison is done using the set of simulations that allows feedback between chemistry and dynamics through radiation. The radiative forcing obtained is neither pure nor instantaneous but rather relaxed (Rotstayn and Penner, 2001) because the simulations have a fixed SST. This means that the aerosols are allowed to influence air and land temperatures as well as water vapor and cloud cover. Therefore the calculated forcing will include the feedback that emerges when the climate adjusts to the changes in land surface temperatures, lapse rate, water vapor profiles, and clouds

149
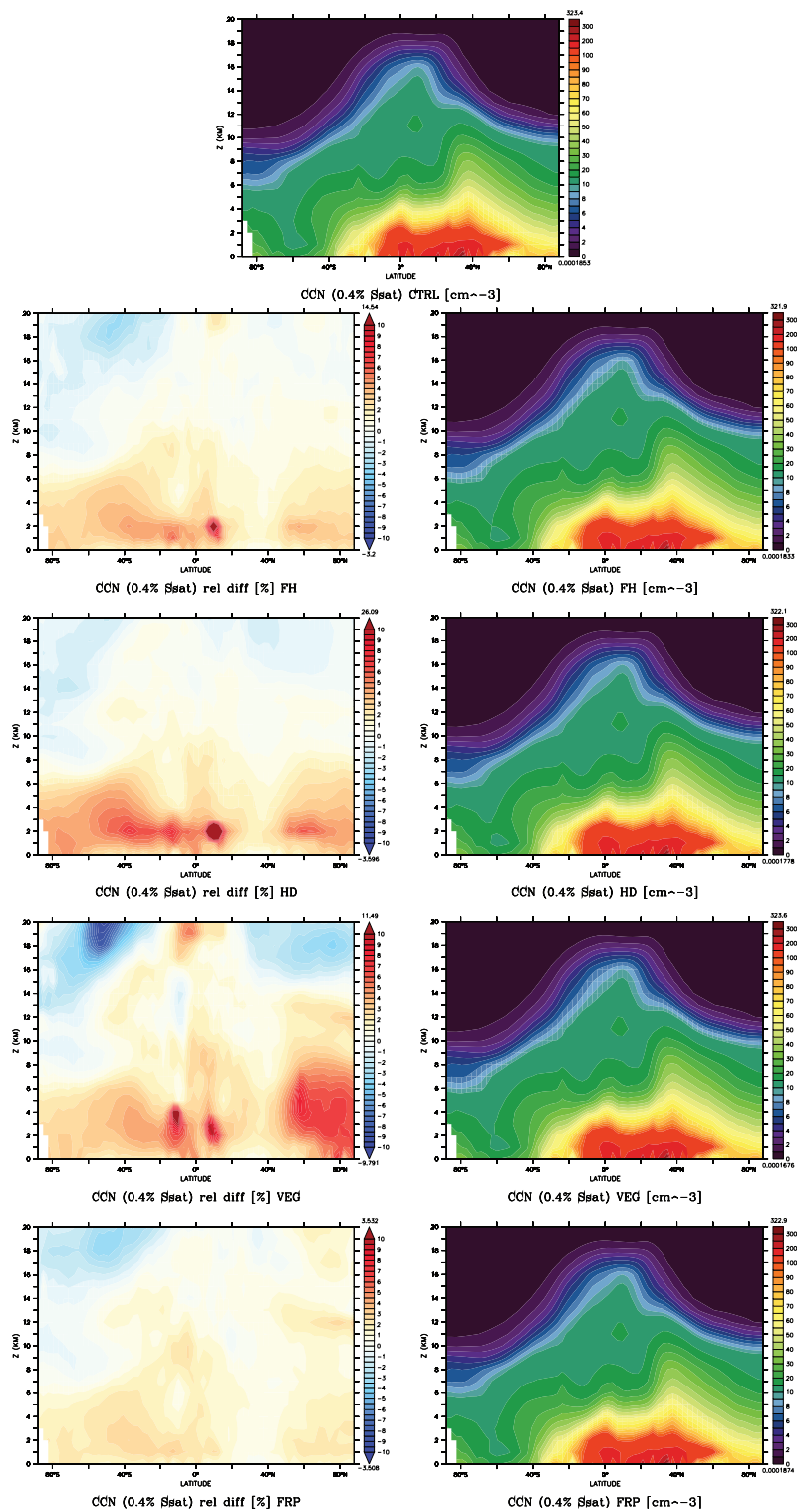
Figure 6.4: Annually and zonally averaged CCN concentration at 0.4% supersaturation. The central image shows the annually and zonally averaged CCN concentration for CTRL. The left panels show the annually and zonally averaged CCN relative difference $\frac{\text{SCH-CTRL}}{\text{CTRL}} \times 100$. The right panels show the associated annually and zonally averaged CCN concentration for each scheme.
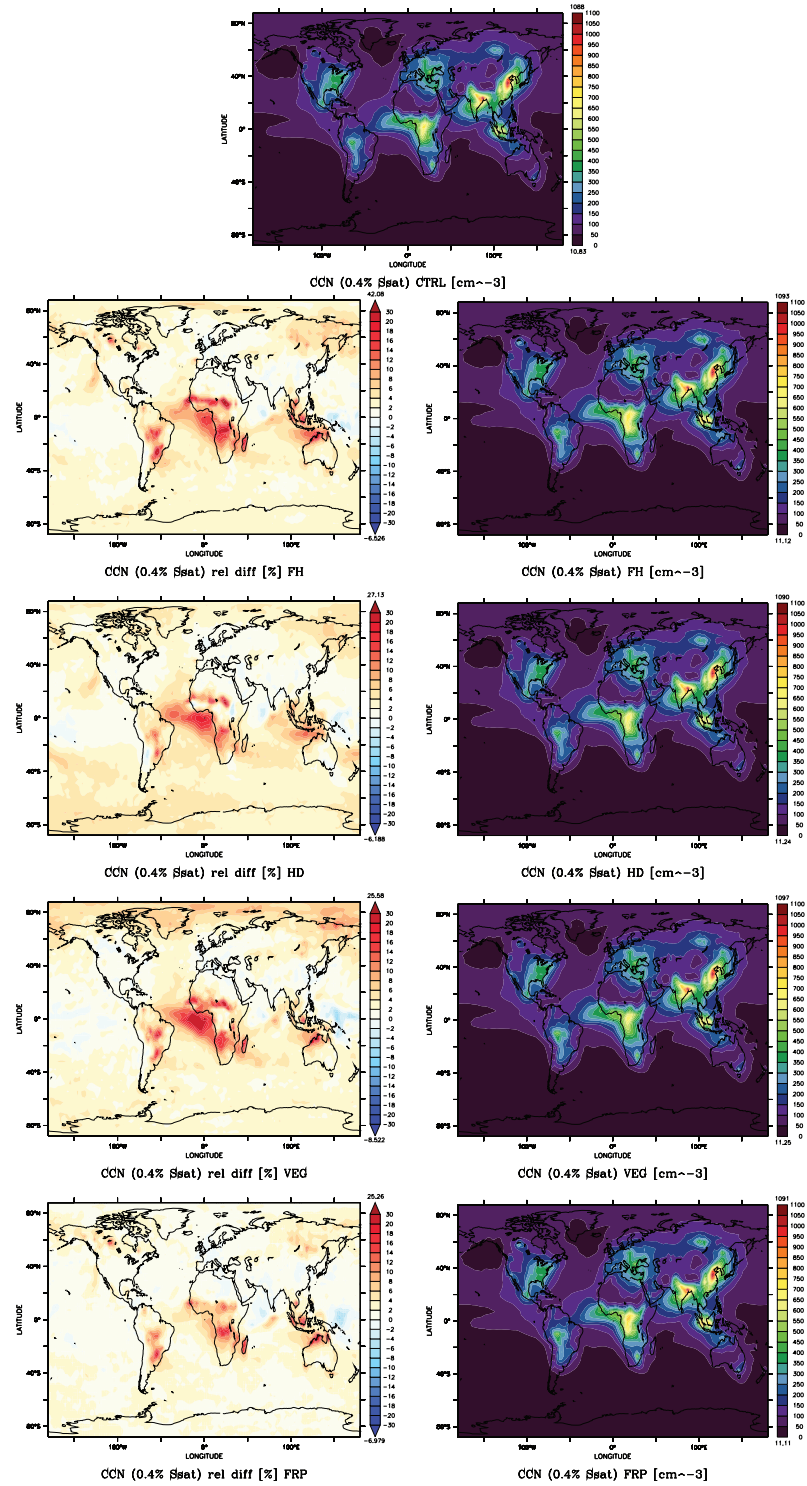
150

Figure 6.5: Annual mean CCN concentration at 0.4% supersaturation at the PBLH.

The central image shows the annual mean CCN concentration for CTRL. The left panels show the annual mean CCN relative difference $\frac{\text{SCH-CTRL}}{\text{CTRL}} \times 100$. The right panels show the associated annual mean CCN concentration for each scheme.

when the SST remains fixed and the aerosols are allowed to modify the other variables.
However, this method does provide an adequate estimation of the magnitude of the
effect that the injection of BB emissions at higher altitude exerts on the climate.

The total radiative forcing exerted by BB depends on the height at which emissions are
located, especially the distribution of absorbing particles (Bond et al., 2013) (Section
1.2). For example, the direct radiative forcing exerted by BC is a product of its life-
time and optical properties. These two factors are influenced by the injection height
through microphysical processes that affect the lifetime as a consequence of the re-
moval mechanisms and the optical properties resulting from enhanced BC mixing with
other particles. The changes in the mixing state are not considered because the optical
properties of the particle depend only on its volume concentration and do not account
for the changes in the mixing state i.e., fresh smoke has the same optical properties as
aged smoke. Considering the heterogeneous regional distribution of BB sources, not
only the radiative fluxes global mean changes are examined but also the local changes
because they can severely affect events such as precipitation.

6.3.1 Clear Sky Radiative Flux

The changes in the clear sky radiative flux reflect the direct aerosol effect (modified by
the vertical distribution of the scattering and absorbing particles) and the influence of
gaseous species.

As a consequence of the variations of both aerosols and gas, the injection height schemes
exert a global mean positive TOA forcing in the clear sky flux (compared with the
CTRL simulation) that ranges from 0.02 Wm^{-2} for HD and FRP to 0.05 Wm^{-2} for
FH and VEG (Table 6.1).

The global annual mean changes in the clear-sky shortwave are small and negative (-
0.03 Wm^{-2}), while the long-wave disturbances are larger and positive and range from
0.05 Wm^{-2} (FH and FRP) to 0.08 Wm^{-2} (VEG), suggesting that the role of scattering
species (e.g., nitrate, OC, and BC) overturns the shortwave absorbing properties of BC.
A similar value (-0.02 Wm^{-2})) can be inferred for the shortwave direct radiative forcing
by looking at the difference in the values obtained by Penner et al. (2003), analyzing
the effects of injecting BB emissions at mid-troposphere compared with at the surface.
Regionally, the positive clear-sky shortwave forcing (compared with the CTRL simula-
tion) ranges between 2.8 Wm^{-2} (FRP) and 5.8 Wm^{-2} (VEG). The positive forcing in

the shortwave clear-sky flux at TOA are located over Northern Canada, Alaska, Greenland, and Europe for FH, over Northern Canada, Europe, and Western Antarctic for HD, the North Canadian Beaufort Sea and Hudson Bay as well as Western Antarctica for VEG, and Europe, Greenland, Hudson Bay, and Western Antarctica for FRP. These values mainly show positive forcing caused by absorbing aerosols when located above reflective surfaces such as ice or snow. For all schemes, the regional negative changes in the shortwave flux at TOA, which range from 4.1 Wm^{-2} (FH) to 5.8 Wm^{-2} (FRP), are mainly located in Siberia, parts of Northern Canada and the Antarctic Peninsula. The positive changes in the long-wave flux at the TOA (compared with the CTRL simulation) range between 2.1 Wm^{-2} (FH) and 3.7 Wm^{-2} (FRP) and are located over the Indian Ocean, Australia, South Africa, the Central Atlantic Ocean, the Arabian Peninsula, and the Sahara Desert. This suggests that the increase in long-wave absorption in clear sky could be a product of modifying available coating material in contiguous dust and sea salt areas. The regional negative changes in the long-wave flux are of smaller magnitude and range from 1.7 Wm^{-2} (FH) to 2.4 Wm^{-2} (FRP) over Indonesia, South America, Mexico, the Arctic Sea, Europe, and Northern Canada.

The disturbances in the shortwave and long-wave clear sky fluxes result in the regional distribution of the net radiative forcing (compared with the CTRL simulation, Figure 6.6). The diverse sign of the regional radiative forcing indicates the dependency of the radiative effect on the vertical distribution of the emissions that, in conjunction with local weather and surface factors, results in radiative fluxes perturbations of opposite directions. The regional clear sky flux disturbances (relative to the CTRL simulation) range from 3.7 Wm^{-2} (FRP) to 5.5 Wm^{-2} (VEG) in the positive direction and from 3.6 Wm^{-2} (FH) to 4.8 Wm^{-2} (FRP) in the negative direction.

In Indonesia, FH and FRP (that on average inject the emissions at lower heights) show negative forcing that extends to Northern Australia. In contrast, VEG and HD show positive forcing. Downwind of the emission sources, the aging process becomes relevant and results in a different sign on the radiative forcing. For instance, in the Kara Sea, FH, HD, and FRP schemes have a negative forcing in contrast to the VEG scheme, which shows a positive forcing in the same region. All schemes including VEG show an increase (compared with the CTRL simulation) in the shortwave flux at the TOA, while the outgoing long-wave flux shows a decrease for VEG and HD (lower magnitude) and an increase for FH and FRP.

6. THE RADIATIVE EFFECT OF MODIFIED BB EMISSIONS ON CLIMATE

In other regions such as the Indian Ocean, the reduction (compared with the CTRL simulation) in the outgoing long-wave radiation is evident in the perturbations of the net clear sky flux (Figure 6.6). This implies that the vertical location of the absorbing agents exerts a small positive radiative forcing, even in the presence of other cooling species.
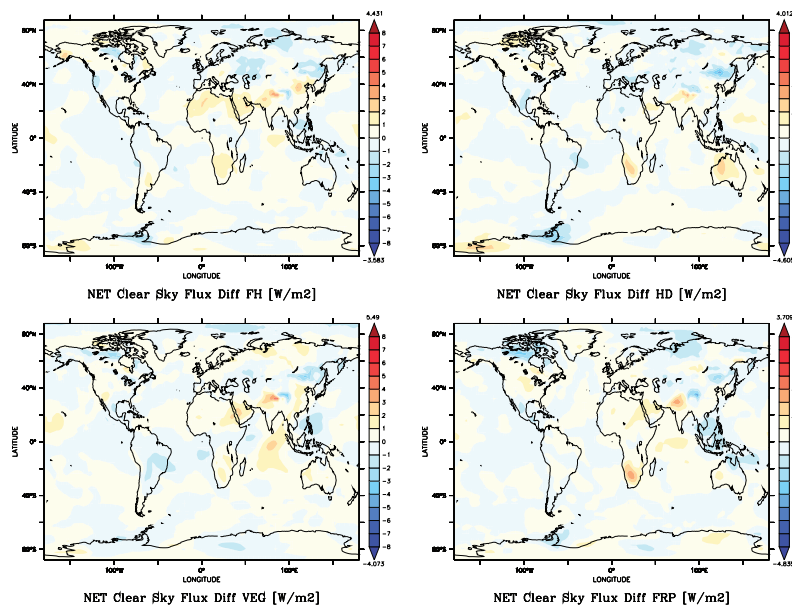

Figure 6.6: Net Clear-Sky radiative forcing relative to CTRL [Wm^{-2}]

6.3.2   All Sky Radiative Flux

The changes in the all-sky radiative fluxes reflect the response of the direct plus the indirect aerosol effects.

The global mean net flux of all sky has larger changes (compared with the changes in the clear-sky flux) that range between 0.1 Wm^{-2} (HD) and 0.25 Wm^{-2} (VEG) (Table 6.1). This suggests that the disturbance (relative to the CTRL simulation) exerted by the injection of BB emissions at higher altitudes on cloud processes is more prominent than the influence on the direct effect. The value of the global mean total radiative forcing generated by clouds ranges from 0.08 Wm^{-2} (HD) to 0.2 Wm^{-2} (VEG).

The changes in the global annual mean shortwave of all sky (compared with the CTRL simulation) range from -0.01 Wm^{-2} (HD) to 0.11 Wm^{-2} (VEG), stressing the sensitivity of the direction of the radiative forcing to the injection height of the emissions.

Regionally, the annual mean shortwave of the all-sky flux diverges from the CTRL simulation in the positive forcing in a range between 8.8 Wm^{-2} (FH) and 12.64 Wm^{-2} (FRP), while the negative forcing ranges from 8.1 Wm^{-2} (HD) to 11.4 Wm^{-2} (VEG). The positive radiative forcing in the annual mean shortwave of all sky flux is located mainly in Indonesia, Northern Canada, Baffin Bay, and the Brazilian Coast. The negative shortwave forcing (compared with the CTRL simulation) regions are located in Siberia, Alaska, and the Indian Ocean.

The variations of the all-sky global annual mean long-wave flux are larger (compared with the changes in the shortwave) and positive ranging between 0.08 Wm^{-2} (FRP) to 0.14 Wm^{-2} (VEG). Regionally, the positive changes in the long-wave flux range from 5.9 Wm^{-2} (HD) to 12.3 Wm^{-2} (VEG) over the Indian Ocean, Australia, the Central Pacific, and Alaska. The negative changes range between 7.2 Wm^{-2} (HD) and 9.8 Wm^{-2} (VEG) over Indonesia and Southern Mexico.
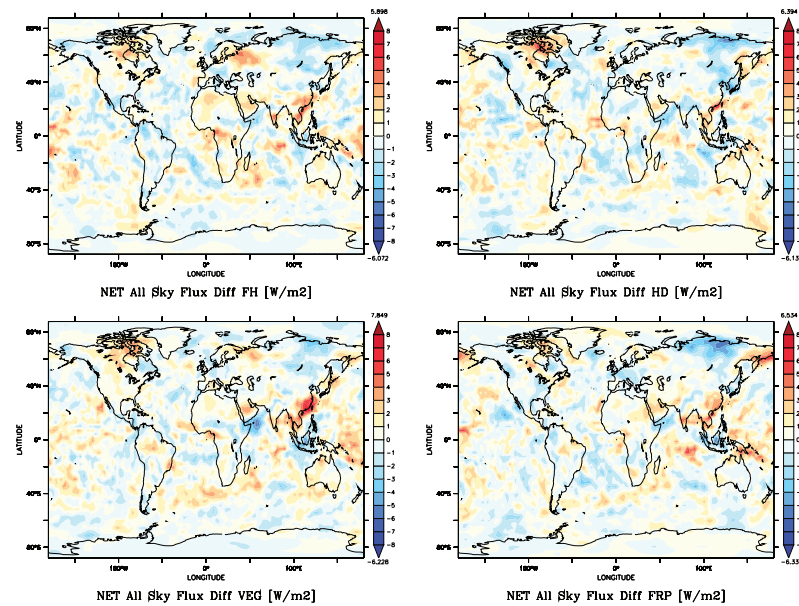
Figure 6.7: Net All-Sky radiative forcing relative to CTRL [Wm^{-2}]

The cloud albedo effect can be estimated by the changes in the shortwave cloud-sky flux (all-sky shortwave flux minus clear-sky shortwave flux) between the CTRL and the schemes simulations. As a result of the increase in the CCN concentration, the cloud albedo effect is enhanced in some regions (e.g., Siberia, Alaska, and the Indian Ocean), which manifests as negative forcing that ranges from 7.3 Wm^{-2} (HD) to 11.1

6. THE RADIATIVE EFFECT OF MODIFIED BB EMISSIONS ON CLIMATE

Wm^{-2} (VEG) (Figure 6.8). In other areas (e.g., South America, Indonesia, and Central Atlantic Ocean), the cloud albedo effect is reduced, thereby revealing a positive forcing that ranges from 9 Wm^{-2} (FH) to 12.8 Wm^{-2} (FRP) in the shortwave flux compared with the CTRL simulation. However, the value of the global annual mean shortwave cloudy-sky flux differences at the TOA indicates a positive forcing (compared with the CTRL simulation) that ranges between 0.02 Wm^{-2} (HD) and 0.15 Wm^{-2} (VEG) (Table 6.1).
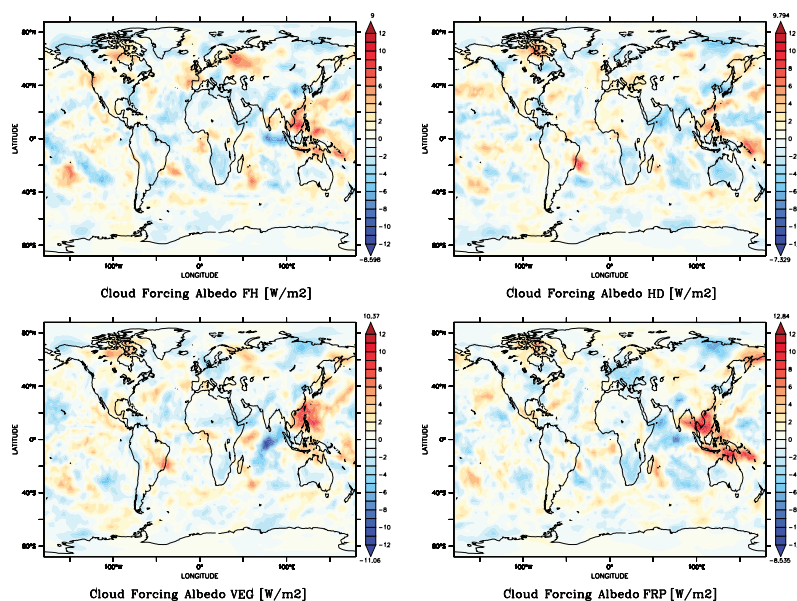
Figure 6.8: Shortwave Cloud-Sky radiative forcing relative to CTRL [Wm^{-2}]

The vertical distribution of the BB emissions could facilitate the development of high clouds that modify the long-wave radiation flux by absorption. The global mean value of the change in the long-wave flux with respect to the CTRL simulation ranges between 0.03 Wm^{-2} (FRP) and 0.06 Wm^{-2} (VEG). Regionally, positive forcing in the long-wave ranges from 4.4 Wm^{-2} (HD) to 9.9 Wm^{-2} (VEG) on the Indian Ocean (Figure 6.9). Negative forcing in the long-wave (compared with the CTRL simulation) has similar values, ranging between 6.4 Wm^{-2} (HD) to 8.2 Wm^{-2} (VEG) over Indonesia, possibly as a consequence of the evaporation of clouds associated with the absorption of shortwave (Figure 6.8).

The positive shortwave forcing seen on Indonesia (Figure 6.8) could affect the cloud properties that reduce the absorbed long-wave by those clouds, causing a negative forc-

ing in the long-wave. This ultimately results in a negative all-sky forcing in Indonesia (Figure 6.7) because the changes in the long-wave overturns the disturbances of the shortwave.

In Siberia, the net radiative forcing in all-sky is negative (Figure 6.7) because a reduction in both SW and LW cloudy sky flux and clear sky flux is evident in the region.

In the Indian Ocean, the NET all-sky flux shows a positive radiative forcing (figure 6.7), although the radiative forcing of the cloud-sky shortwave flux is negative (i.e., enhanced cloud albedo effect, Figure 6.8) and the forcing in the cloud-sky long-wave is positive (Figure 6.9). Therefore, the negative forcing exerted by the enhanced cloud albedo is outweighed by the long-wave absorption of the clouds and the absorption of aerosols in the net clear-sky (Figure 6.6). This could be generated by the combination of the effect of aerosols on top of the cloud layer, which reduces the shortwave radiation that was reflected by the clouds as well as the absorption of long-wave coming from the ocean by the cloud cover as a response of fixed SST, which do not account for the reduction in the shortwave that reach the surface.
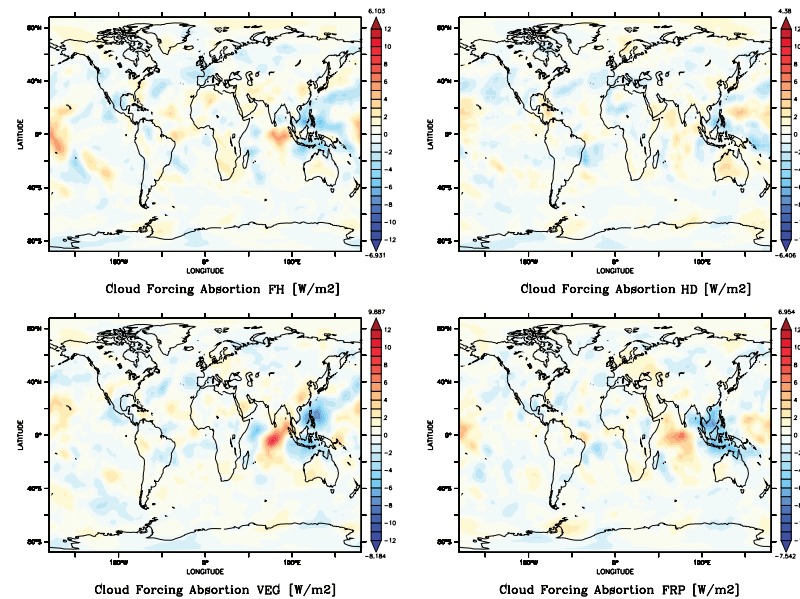
Figure 6.9: Cloudy-sky longwave radiative forcing relative to CTRL [Wm^{-2}]

All the different local effects that result in radiative forcing of opposite directions as a consequence of the interactions with cloud cover stress the importance of a proper injection height of BB emissions. Most studies that globally asses the radiative role of

6. THE RADIATIVE EFFECT OF MODIFIED BB EMISSIONS ON CLIMATE

Table 6.1: Global annual mean radiative forcing relative to CTRL [Wm^{-2}]

	FH	HD	VEG	FRP
Net All-Sky [a]	0.16	0.10	0.25	0.16
Shortwave	0.06	-0.01	0.11	0.08
Long-wave	0.10	0.11	0.14	0.08
Net Clear-Sky [a]	0.05	0.02	0.05	0.02
Shortwave	0.00	-0.03	-0.03	-0.03
Long-wave	0.05	0.06	0.08	0.05
Total Coud [b]	0.11	0.08	0.20	0.14
Cloud Shortwave [c]	0.05	0.02	0.15	0.11
Cloud Long-wave [d]	0.05	0.05	0.06	0.03

[a]Net Flux = Shortwave + Longwave

[b]Total Cloud = Net All-Sky − Net Clear-Sky

[c]Cloud Shortwave = All-Sky Shortwave − Clear-Sky Shortwave

[d]Cloud Longwave = All-Sky Longwave − Clear-Sky Longwave

BB release the emissions at the surface. When they do, they neither account for the cloud interactions nor do they include the gas phase emissions, which are important aerosol precursors that influence the abundance of tropospheric radiative species such as O_3.

The changes in the injection height of BB result in a small positive radiative forcing (compared with the CTRL simulation). These changes are mainly the result of the influence on cloud properties. Although the changes in the radiative fluxes seem rather small, it is important to consider that these disturbances emerge as a consequence of the vertical redistribution and injection of BB emissions at higher altitudes and therefore shed some light on the uncertainty and role of fires in the climate system. Because fires occur regularly, it is important to correctly represent their radiative effect on the climate system because their role in the radiative transfer sets a background for assessing the radiative balance disturbances generated by other anthropogenic emissions.

7

Conclusions

Motivated by the need to represent the injection height of BB emissions, four schemes (FH, Section 2.2.3; HD, Section 2.2.4; VEG, Section 2.2.5; FRP, Section 2.2.6) and a vertical distribution function (VDF, Section 2.2.2) were developed and implemented.

The evaluation of the changes associated with the modified injection height of the BB emissions (e.g., aerosol lifetime, global burden, and transport) and several important atmospheric effects associated with fires (e.g., gas emissions as aerosol precursors, changes in ozone concentrations, the influence on atmospheric oxidation capacity, aerosol emissions as efficient CCN, and the influence on the transfer of atmospheric radiation) are done by comparing the performance of the injection height schemes with the unmodified version of the model (CTRL, which releases the aerosol emissions at the surface and the gas emissions at 140 m).

The injection heights were predetermined (for FH, HD, and VEG) or calculated on-line (for FRP, based on Sofiev et al. (2012) formulation). As a consequence, each scheme has its own regional and temporal variability (Section 3.1) that results in diverse fractions of BB emissions (56% for FH, 58% for HD, 26% for VEG and 12% for FRP on average per grid-cell) released above the PBLH (Section 3.2.2) and at altitudes with different temperature and humidity regimes.

The FRP scheme represents the BB injection height in a more realistic way because it includes information about key parameters involved in the plume height estimation: intensity of the fire (fire radiative value frp, Section 2.2.6.1) and local weather conditions (PBLH and Brunt Väisälä frequency). As a result, 52% (globally) of the plumes calculated by FRP are located no more than 500 m (MISR uncertainty) away from the

plumes observed by MISR. However, only 11% (globally) of the plumes determined by VEG scheme are located within the MISR uncertainty. Regionally, the performance of FRP (compared with VEG) is preserved (Section 3.3) i.e., a larger number of plumes determined by FRP (compared with the plumes determined by VEG) are located within MISR uncertainty. For instance, in Indonesia, 75% of the FRP predicted plumes are located within MISR uncertainty, which is in contrast to the 62% determined by the VEG scheme. Although FRP yields a better overall representation of the plumes observed by MISR, most of the MISR outliers (represented by the VEG scheme) are underestimated. However, is important to consider that the satellite may not capture the plumes at the most intense stage because of the local overtime pass. Therefore further development of the plumes observed by MISR could reach the VEG heights later in the day.

The underestimation of the plumes generated by the FRP scheme can be improved by using daily fire information (e.g., Remy and Kaiser, 2014). Because FRP is a more realistic approach, it can represent the injection height in a timely manner (because the height varies according to the PBLH), which has consequences on the transport (vertical and horizontal) and the photochemistry.

Three passive tracers (implemented by Kunkel and Tost, Kunkel et al. (2012)) that represent the BB aerosol emissions (for OC_{BB}: one hydrophobic PA02 and one hydrophilic PA01; for BC_{BB}: one hydrophobic PA03) were used to follow their evolution (Chapter 4).

As a direct consequence of injecting the BB aerosol emissions at higher altitudes, the global annual dry deposition was reduced by between 35% (FRP) and 46% (HD) with slightly higher values (35.6% for FRP to 47% for HD) for the OC tracers (Section 4.3.1). The removal of the BB aerosols by sedimentation becomes less efficient because of the release of small size particles (aitken) at higher altitudes, thereby resulting in a small annual reduction for BC_{BB} that ranges from 0.5% (FH) to 1.47% (FRP). However, for the VEG scheme, there is a small increase (0.8%) in the mass loss trough sedimentation because of the growth of particles, which result from the increase in the available coating material at higher altitudes, where this scheme injects its emissions. For the OC_{BB} tracers, larger reduction in the annual sedimentation occurs (ranging from 3.3% for VEG to 6.6% for HD) because the fraction of smaller particles (ks, the size at which the hydrophilic part of OC_{BB} is released) has increased (compared with

the CTRL simulation) and this is more efficiently removed by wet deposition. The wet deposition of the BB aerosol emissions (Section 4.3.2) has been enhanced annually for BC_{BB} and ranges from 5.9% (FH) to 8.9% (FRP). For OC_{BB}, it ranges from 8% (VEG) to 10.5% (FRP) globally.

As a consequence of the injection of the BB emissions at higher altitudes and the microphysical evolution of the aerosol tracers, the removal efficiency has been reduced. This results in a global and annual mean lifetime enhancement for the BB aerosol emissions (Section 4.4) in the range of 2.2% (VEG) to 3% (FH) for BC_{BB} and 1.5% (HD) to 2.1% (FRP) for OC_{BB}. This enlargement locates the simulated BC_{BB} lifetimes (11.1 days) in the upper range of the currently estimated BC lifetimes (3.8 to 11.4 days, Bond et al., 2013). The largest lifetime enhancement occurs in Africa ranging from 9% (FRP) to 14.4% (HD) in the annual mean and 12% (FRP) to 20.4% (VEG) in July for BC_{BB}. Slightly smaller enhancements occur for OC_{BB} in Africa. These range from 8% (FRP) to 12% (HD) in the annual mean and from 11% (FRP) to 20% (VEG) in July.

The lifetime enlargement causes a global burden increase (Section 4.1) in the range of 6.4% (FRP) to 10.6% (VEG) in the annual mean and 9% (FRP) to 20% (VEG) in June for BC_{BB}. For OC_{BB}, the annual mean global burden enlargement ranges from 7.4% (FRP) to 13.2% (VEG) and from 10.2% (FRP) to 26.6% (VEG) in June —when the largest difference occur.

As a direct consequence of the changes in the injection altitude of the BB emissions, the annual mean aerosol surface concentration (Section 4.5.1) over the biomass burning production areas has been reduced in the range of 54% (VEG) to 71.52% (HD) for BC_{BB}. Similar values were obtained for OC_{BB} (54% for VEG to 73% for HD). As a consequence of the transport, which was facilitated by the lifetime enhancement, the annual mean surface concentration increased over the oceans (especially the Atlantic Ocean); the increases ranged from 33.4% (FRP) to 77% (HD) for BC_{BB} and from 40% (FRP) to 108% (HD) for OC_{BB}. The vertical distribution of the BB aerosol emissions (Section 4.5.2) show an enhancement mainly located inside the troposphere with peaks around the injection altitude that range from 16.5% (FRP) to 61% (HD) for BC_{BB} and from 23.3% (FRP) to 75.2% (HD) for OC_{BB}. The FRP scheme shows a more homogenous change and positive disturbances at higher altitudes (where the concentration of these aerosol tracers is low), which suggest that the variability in the injection altitude calculated by this scheme favors further vertical transport by deep convection. This

7. CONCLUSIONS

is a realistic behavior because most fires do not directly inject the emissions at higher altitudes (e.g., the upper troposphere). Instead, the emissions are lofted further as a result of local meteorological conditions (e.g., Fromm et al., 2000; Labonne et al., 2007; Mazzoni et al., 2007). The regional distribution of the annual mean column concentrations make the enhancement of the global burden evident, showing increases ranging from 15% (FRP) to 53% (HD) for BC_{BB} and from 18% (FRP) to 66.6% (HD) OC_{BB} (Section 4.5.3).

Because of the global burden increase of BB primary aerosols, the annual mean contribution of BB emissions to the BC and OC on remote areas has been enhanced in the range of 6.7% (FRP) to 12.5% (HD) for BC_{BB} and in the range of 5.7% (FRP) 13.5% (HD) for OC_{BB}. The changes at latitudes higher than 65°N (where the largest relative enhancement of the BB contributions are located both over Ocean and land) are particularly important because of the relevant role of aerosols on the radiative balance when located above highly reflecting surfaces such as snow or ice. Other regions have also shown enhancements in the BB contribution e.g., the Central Atlantic Ocean, Guinean Gulf, North Pacific Ocean, Indian Ocean, the Southern Coast of Brazil, South Africa, and the Sahara Desert (Section 4.6).

The effects of changes in the BB injection height are first and foremost reflected in the global influence on the primary aerosols (Section 5.1). The annual mean global burden shows enhancements ranging from 2.7% (FRP) to 4.6% (VEG) for BC and from 3.6% (FRP) to 6.6% (VEG) for OC. The biggest change occurs in the local summer months, especially July when most fire events take place, which cause increases in the global burden ranging from 4% (FRP) to 9% (VEG) for BC and from 5% (FRP) to 12.4% (VEG) for OC. The burden enhancement results in increases ranging from 11.4% (FRP) to 33% (VEG) for BC and from 11% (FRP) to 40% (HD) for OC over the Atlantic Ocean and to a lesser extent over the Arctic and Antarctic, where the concentration of these aerosol tracers are minor.

Although of lower magnitude, the influence of changes in the BB injection height on the secondary aerosols have a global effect on nitrate burden and regional effect on sulfate because the aerosol precursors NO_x and SO_2 are part of the BB emissions. Releasing NO_x at higher altitudes contributes to the increase of NO_3^- concentrations, for which the annual mean global burden show a small increase (0.7% for FRP to 1.8% for HD). Maximum enhancement occurs in boreal summer months; values that range

from 1% (FRP) to 4% (VEG). Regionally, this leads to annual mean increases ranging from 13% (FRP) to 24% (FRP) (Section 5.2.1). Sulfur dioxide emissions produced by fires have little influence on the global annual mean burden of the sulfate because BB is only responsible for a small percentage of the total SO_2 emissions. However, as a consequence of local changes in the oxidation capacity caused by the BB emissions, regional SO_4^{2-} concentrations have been enhanced in the range of 6.6% for FH to 8.4% for FRP (Section 5.2.2).

Substantial changes are seen for the BB emitted NMHC over areas around the production zones. The injection of NO_x and NMHC at higher altitudes is associated with regional effects on the atmospheric chemistry (e.g., oxidation capacity, OH recycling, PAN, and the production of ozone). Influence on the oxidation capacity is seen where local increases in the concentrations of OH (as a consequence of the ozone enhancement) result in a decrease in the carbon monoxide tropospheric annual mean column density (1% for FRP to 6% for VEG). Methane lifetime is affected locally by the changes in the oxidation capacity, resulting in a lifetime reduction of 2.5% around the injection altitudes (Section 5.3.1).

Local increases in the annual mean concentrations of the injected BB NMHC (formaldehyde, formic acid, acetic acid, acetaldehyde, methanol, MEK, ethene, ethane, propene, n-butane, and acetone) were identified. Some of them (e.g., acetic acid, acetaldehyde, methanol, MEK, ethene, ethane, propane, n-butane, and acetone) also decreased locally (Section 5.3.2). The role and implications of the changes in the concentration of these species is beyond the scope of this study. However, important interactions such as NO_x and acetaldehyde (involved in PAN formation) are identified. Decreases in the tropospheric annual mean column concentrations of acetaldehyde in the range of 3% (FRP) to 9% (VEG) are associated with PAN enhanced annual mean tropospheric concentrations in the same magnitude (3% for FRP to 9% for VEG). This is a consequence of the injection of BB NO_x and acetaldehyde emissions at higher altitudes, which facilitate PAN thermal stability.

The injection of NO_x and BB NMHC emissions at higher altitudes enhances the annual mean ozone concentrations locally (Section 5.3.3). At the surface, downwind from the production regions, the enhancement ranges from 3% (FRP) to 5% (VEG). In the tropospheric column, the increases range from 1.6% (FRP) to 2.2% (VEG). The mean zonal and annual concentrations of ozone increased slightly ($\approx$ 1%) around the injec-

tion altitudes. Maximum increases are observed in July (2% for FRP to 4% for VEG) and December (2% for FRP to 7% for HD) around the injection altitudes and in the equatorial upper troposphere, which is consistent with observed ozone enhancement in the BB plumes (e.g., Andreae et al., 2001; Andrés-Hernández et al., 2009; Fromm et al., 2005; Jost et al., 2004; Pfister et al., 2006; Pickering et al., 1996; Real et al., 2010).

The enhanced lifetime of primary aerosols and the burden of primary and secondary aerosols have important consequences on the radiative effects of these species. The AOD is affected directly by the presence of these aerosol tracers and indirectly by the increase of the aerosol water exerted by their enhanced water uptake (Sections 5.2.1 and 5.2.2). Consequently, the annual mean AOD (550 nm) of BC, OC and WASO has been enhanced (13% (FRP) to 58% (HD) for BC; 12% (FRP) to 59% (HD) for OC; 7% (FRP) to 14% (VEG) for the WASO). This resulted in an increase of the annual mean total AOD in the range of 8% (FRP) to 23% (VEG) compared with the CTRL simulation. Therefore, the ability of the model to reproduce observed optical thickness (MISR and MODIS observations) has been improved, resulting in a 10% enhancement (compared with the CTRL simulation). However, the AOD is still underestimated, and further improvements are limited by the uncertainty of the BC emission factors (Section 6.1.1), which are underestimated by a 0.6 to 4-fold Bond et al. (2013).

The changes in the vertical distribution of absorbing and scattering species result in enhancement of absorption, which is reflected in lower single scattering albedo values (compared with the CTRL simulation) along the whole column for FRP and up to 20 km for the other schemes. Peaks in the absorption enhancement are in the 3 km near to the surface and in the upper troposphere from 7 to 16 km, altitudes at which enhancement in extinction (caused by forest fires) has been observed (Fromm et al., 2000, 2005). In the Arctic, a small absorption enhancement is found over the whole troposphere for all schemes. Maximum changes are observed from 4 to 14 km for VEG and at approx. 16 km for FRP (Section 6.1.2).

The known efficiency of the BB particles to act as a CCN was evident in the concentrations enhancement at 0.4% supersaturation. At the PBLH, a global increase in the annual mean CCN concentrations was found with maximum values in the range of 25% (FRP) to 42% (HD) over the BB regions (Section 6.2.1).

The injection height of BB emissions plays an important role in several process that influence the atmospheric radiative transfer directly (by the redistribution of scattering

and absorbing particles) and indirectly (by the influence on cloud properties) (Section 6.3). The changes in the clear-sky radiative flux, which reflect the direct aerosol effect, show a global mean positive forcing at TOA (compared with the CTRL simulation) in the range of 0.02 Wm^{-2} (HD and FRP) to 0.05Wm^{-2} (FH and VEG). The effect of the BB injection height on the shortwave clear-sky flux is small and negative (similar to the value obtained by Penner et al., 2003), which implies that the role of scattering species (e.g., nitrate, OC, and BC) is more important than that of shortwave absorbing BC. In contrast, the changes in the long-wave clear-sky flux are positive and larger than the negative changes in the shortwave, which results in the positive forcing of the net clear-sky flux. When located above ice or snow, the effect of absorbing aerosols is seen in the positive shortwave clear-sky forcing at TOA (compared with the CTRL simulation) that increase by 2.8 Wm^{-2} (FRP) to 5.8 Wm^{-2} over Northern Canada, Alaska, Greenland, and Europe. Conversely, scattering aerosols lead to negative forcing of the shortwave clear-sky at TOA (compared with the CTRL simulation) that range from -4.1 Wm^{-2} (FH) to -5.8 Wm^{-2} (FRP) over Siberia, parts of Northern Canada and the Antarctic Peninsula. The location (e.g., the Indian Ocean, Australia, and the Sahara Desert) of the long-wave clear-sky positive forcing at TOA (compared with the CTRL simulation) in the range of 2 Wm^{-2} (FH) to 3.7 Wm^{-2} (FRP) suggests that modifying the BB injection height cause variations on the available coating material, which enhance the absorption in dust and sea salt areas adjacent to BB production regions. Negative forcing in the long-wave clear-sky flux (-1.7 Wm^{-2} for FH to -2.4 Wm^{-2} for FRP) is also simulated in some regions. The net clear-sky forcing at TOA (compared with the CTRL simulation) has regional variations in both the direction and the magnitude of the forcing, ranging from 3.7 Wm^{-2} (FRP) to 5.5 Wm^{-2} (VEG) in the positive direction (as a result of changes in the long-wave flux influenced by the variations in the available coating material in dust and sea salt areas) and from -3.6 Wm^{-2} (FH) to -4.8 Wm^{-2} (FRP) in the negative direction.

Both the direct and the indirect effect (net all-sky global mean) result in positive forcing at TOA (compared with the CTRL). This is caused by changes in the cloud properties, which result in a global mean positive forcing (0.08 Wm^{-2} for HD to 0.2 Wm^{-2} for VEG). The changes in the global annual mean shortwave all-sky flux range from slightly negative (-0.01 Wm^{-2} for HD) to positive (1.1 Wm^{-2} for VEG), stressing the importance of the BB injection height in the direction of the forcing. Regionally, the

forcing in the shortwave all-sky have values that range from 8.8 Wm^{-2} (HD) to 12.64 Wm^{-2} (FRP) in the positive direction and from -8.1 Wm^{-2} (HD) to -11.4 (VEG) in the negative direction. In contrast, the variations of the global annual mean long-wave all-sky flux are positive and larger (compared with the changes in the shortwave all-sky flux) and range from 0.08 Wm^{-2} (FRP) to 0.14 Wm^{-2} (VEG). Regionally, the forcing in the long-wave all-sky flux varies in the range of 5.9 Wm^{-2} (HD) to 12.3 Wm^{-2} (VEG) in the positive direction and from -7.2 Wm^{-2} (HD) to -9.8 Wm^{-2} (VEG) in the negative direction. The changes in the global annual mean shortwave cloud-sky flux are positive (0.02 Wm^{-2} for HD to 0.15 Wm^{-2} for VEG) and reflect the modifications to the cloud cover (including the albedo effect). Regionally, negative forcing ranges from -7.3 Wm^{-2} (HD) to -11.1 Wm^{-2} (VEG), whereas positive forcing ranges from 9 Wm^{-2} (FH) to 12.8 Wm^{-2} (FRP). The variations in the long-wave cloud-sky reflect the changes in the cloud cover, (including the development of high clouds), which results in a positive global mean forcing at TOA (compared with the CTRL simulation) in the range of 0.03 Wm^{-2} (FRP) 0.06 Wm^{-2} (VEG). Regionally, the long-wave cloud-sky forcing ranges from 4.4 Wm^{-2} (HD) to 9.9 Wm^{-2} (VEG) in the positive direction and from -6.4 Wm^{-2} (HD) to -8.2 Wm^{-2} (VEG) in the negative direction.

Outlook

This work represents the complex and highly variable process of BB injection height in a computationally efficient way (for GCMs like EMAC) and contains some of the most important characteristics of fires (regional and temporal variability, which are determined by the fuel properties and the weather conditions).

When determining the best scheme to use, it is important to consider the requirements on the simulation and the availability of the input data. Although FRP is the most realistic scheme, it relies on fire radiative power (frp) satellite observations bounded by the MODIS-era years. For studies with limited availability of frp data (e.g., future scenarios and land use change), the VEG scheme becomes an excellent tool, which provides the necessary regional differences. Moreover, the VEG scheme is comparable to other studies because it uses the heights suggested in the EDGAR 3.2 Fast Track 2000 dataset (32FT2000: van Aardenne et al., 2005), which was used in the 2003/2004 ACCENT-IPCC and AEROCOM experiments, and in the prescribed data-sets for AeroCom (Dentener et al., 2006).

The time variability and the height of the plumes in FRP scheme can be improved by using daily fire intensity information (Remy and Kaiser, 2014). Furthermore, FRP scheme combined with appropriate emissions data set can represent small fires, the effect of which has been underestimated (Randerson et al., 2012).

Comparison of the simulations with chemical trace gases observations can help to upgrade the schemes by the adjustment of the vertical distribution function (VDF) if necessary.

The improvements in the representation of the fires done in this work allow for a better estimation of the role of BB on human health in the downwind areas as well as in global warming.

7. CONCLUSIONS

8

Appendix

8.1 Statistical Methods

8.1.1 Box Plots

The upper and lower limits of the box (hinges) correspond to the first and third quartiles (the 25th and 75th percentiles). Therefore, the height of the box is determined by the Inter-Quartile Range (IQR), i.e., the distance between the first and third quartiles. The upper whisker extends from the hinge to the highest value that is within $1.5\times$ IQR of the hinge. The lower whisker extends from the hinge to the lowest value within $1.5\times$ IQR of the hinge. Data beyond the end of the whiskers are outliers and plotted as black points. The median is represented by a line inside the box. The mean is represented by a red point inside the box. The characteristics of the box plots are shown in figure 8.1.
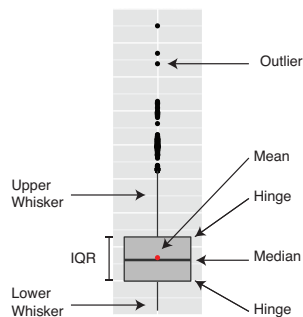
Figure 8.1: Box plot example.

8.2 Non Methane Hydro Carbons Changes
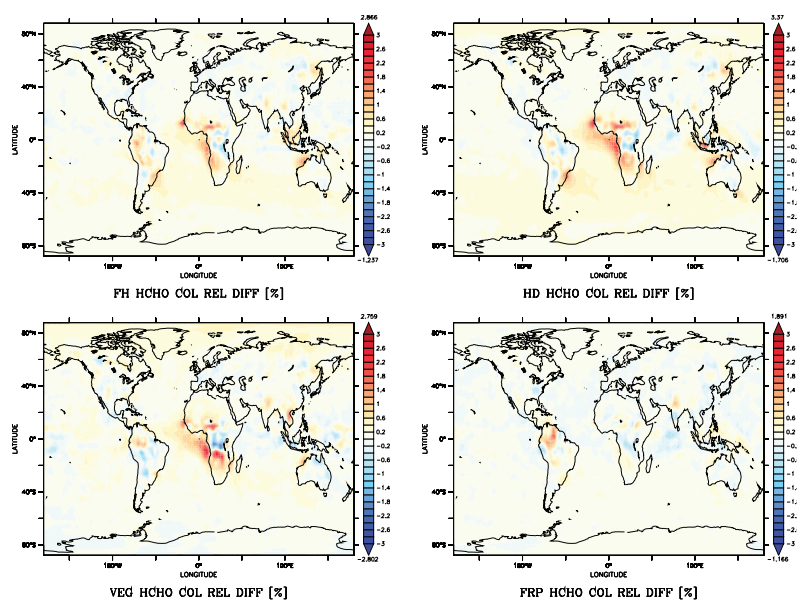
Figure 8.2: Formaldehyde (HCHO) annual mean relative difference $\frac{\text{SCH-CTRL}}{\text{CTRL}} \times 100$.
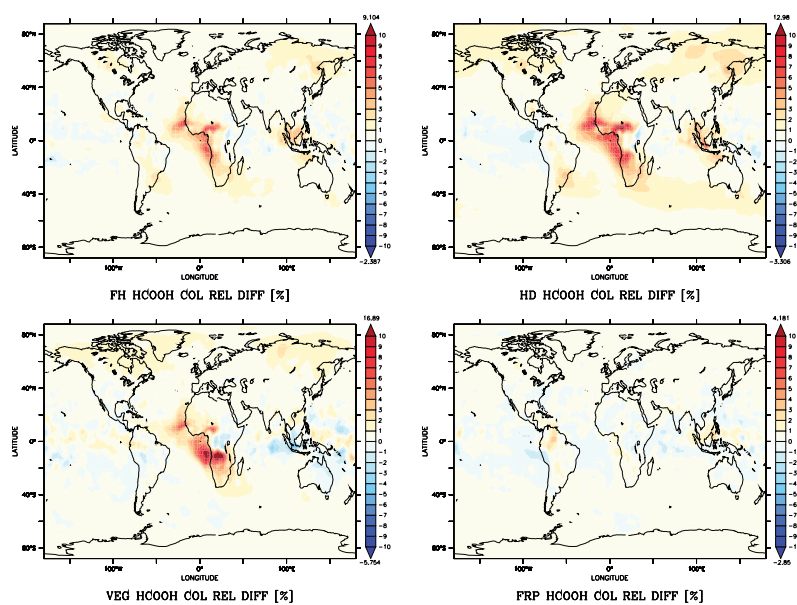
Figure 8.3: Formic Acid (HCOOH) annual mean relative difference $\frac{\text{SCH-CTRL}}{\text{CTRL}} \times 100$.
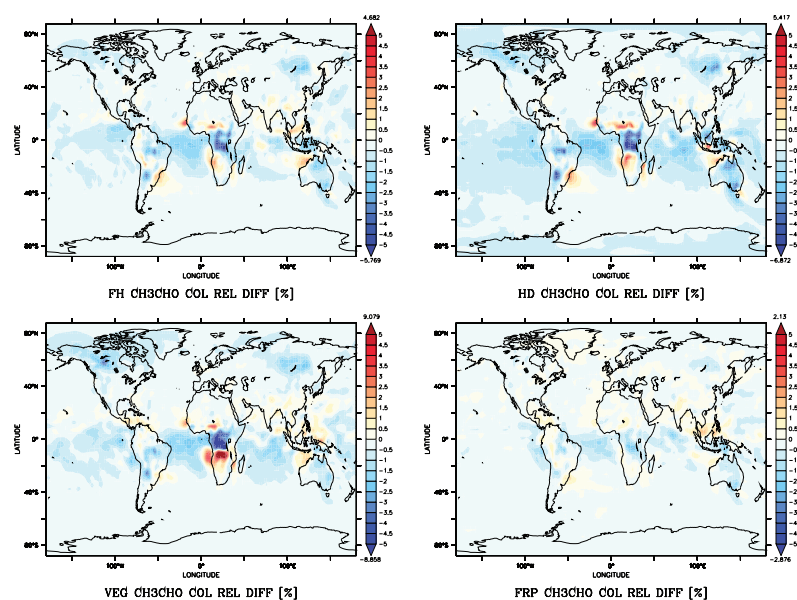
Figure 8.4: Acetaldehyde (CH_3CHO) annual mean relative difference $\frac{\text{SCH-CTRL}}{\text{CTRL}} \times 100$.
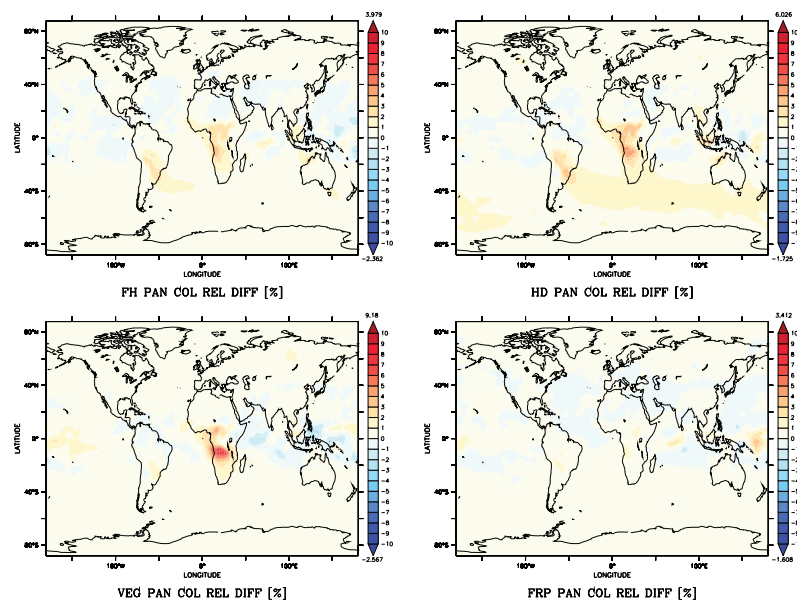
Figure 8.5: Peroxacetil Nitrate (PAN) annual mean relative difference $\frac{\text{SCH-CTRL}}{\text{CTRL}} \times 100$.

171
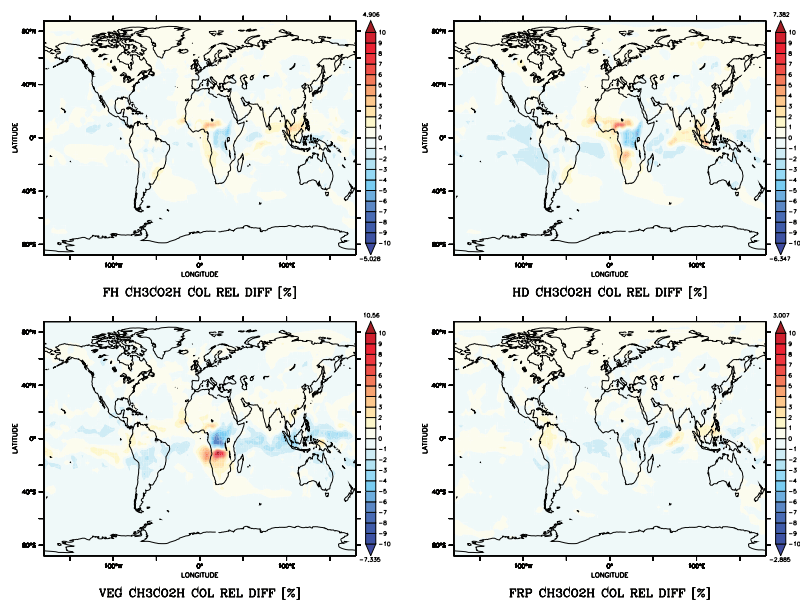
Figure 8.6: Acetic Acid (CH$_3$CO$_2$H) annual mean relative difference $\frac{\text{SCH-CTRL}}{\text{CTRL}} \times 100$.
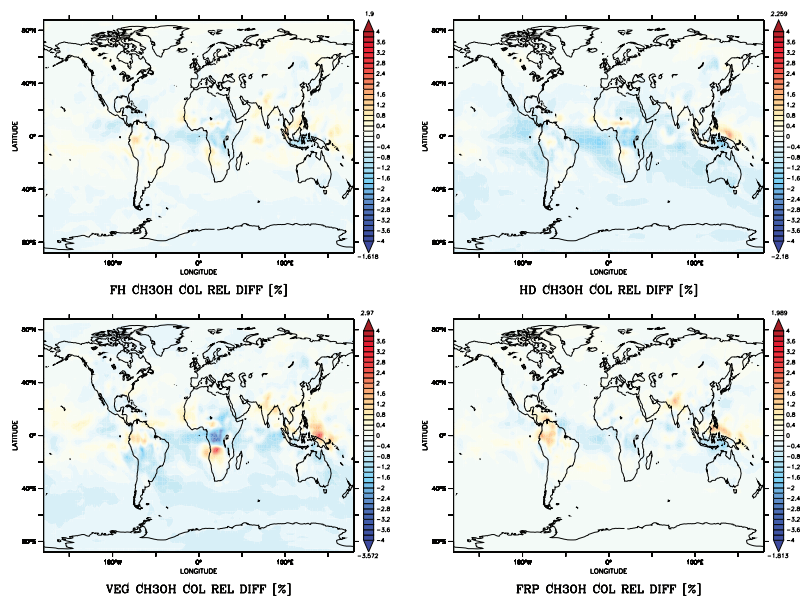
Figure 8.7: Methanol (CH$_3$OH) annual mean relative difference $\frac{\text{SCH-CTRL}}{\text{CTRL}} \times 100$.

Figure 8.8: Metyl Ethyl Ketane (MEK) annual mean relative difference $\frac{\text{SCH-CTRL}}{\text{CTRL}} \times 100$.
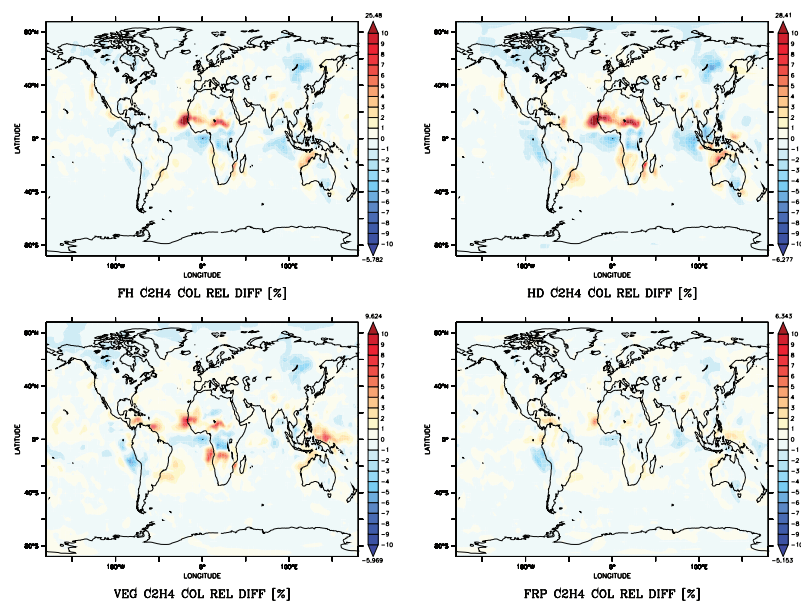
Figure 8.9: Ethene (C_2H_4) annual mean relative difference $\frac{\text{SCH-CTRL}}{\text{CTRL}} \times 100$.
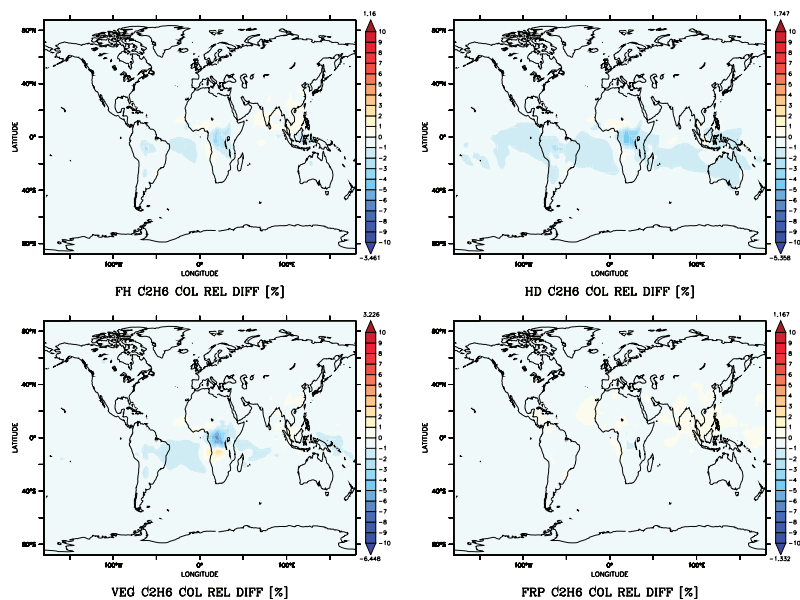
Figure 8.10: Ethane (CH$_2$H$_6$) annual mean relative difference $\frac{\text{SCH-CTRL}}{\text{CTRL}} \times 100$.
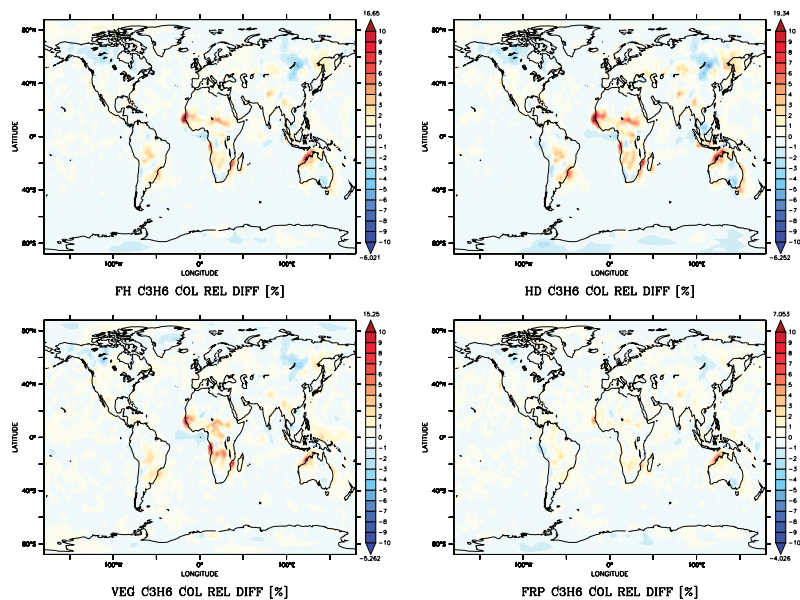
Figure 8.11: Propene (CH$_3$H$_6$) annual mean relative difference $\frac{\text{SCH-CTRL}}{\text{CTRL}} \times 100$.

Figure 8.12: Propane (CH$_3$H$_8$) annual mean relative difference $\frac{\text{SCH-CTRL}}{\text{CTRL}} \times 100$.
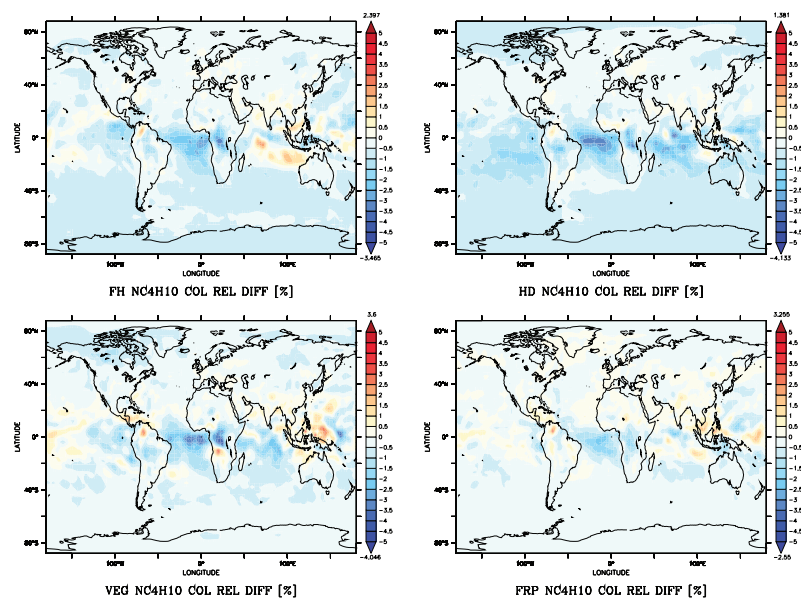
Figure 8.13: N-butane (NC$_4$H$_{10}$) annual mean relative difference $\frac{\text{SCH-CTRL}}{\text{CTRL}} \times 100$.

175

Figure 8.14: Acetone (CH$_3$COCH$_3$) annual mean relative difference $\frac{\text{SCH-CTRL}}{\text{CTRL}} \times 100$.

List of Figures

List of Tables

Nomenclature

List of Abbreviations

ai	Accumulation insoluble mode
as	Accumulation soluble mode
ci	Coarse insoluble mode
cs	Coarse soluble mode
frp	fire radiative power value
ki	Aitken insoluble mode
ks	Aitken soluble mode
ns	Nucleation soluble mode
ACCENT	Atmospheric Composition Change the European Network
AEROCOM	Aerosol Comparisons between Observations and Models
AEROPT	Aerosol optical depth calculation in EMAC
AMMA	African Monsoon Multidisciplinary Analyses
AOD	Aerosol Optical Depth
BB	Biomass Burning
BC$_{PAT}$	Black Carbon Passive Aerosol Tracer
CALIOP	Cloud-Aerosol Lidar with Orthogonal Polarisation
CAM	NCAR Community Atmosphere Model
CAPE	Convective available potential energy
CATT-BRAMS	Coupled Aerosol and Tracer Transport model to the Brazilian developments on the Regional Atmospheric Modeling System
CCN	Cloud Condensation Nuclei

NOMENCLATURE

CFCs		Chloro-Fluoro-Carbons
CLOUD		Large-scale condensation in EMAC
CMG		Climate Modelling Grid
CONVECT		Convective cloud parameterization in EMAC
CRM		Cloud-Resolving Model
CVTRANS		Convective tracer transport in EMAC
DLR		Deutsches Zentrum für Luft- und Raumfahrt
DRYDEP		Dry deposition in EMAC
ECHAM5		5th generation European Centre Hamburg general circulation model
ECMWF		European Centre for Medium-Range Weather Forecasts
EDGAR3.2FT	**2000**	Emission Database for Global Research, version 3.2, fast track
EMAC		ECHAM5/MESSy Atmospheric Chemistry Model
EMAC		ECHAM5/MESSy Atmospheric Chemistry Model
ENSO		El-Niño-Southern Oscillation
FH		Fixed Height injection height scheme
FRP		Fire Radiative Power injection height scheme
FT		Free Troposphere
GCM		General Circulation Model
GEOS		Goddard Earth Observing System Model
GMXe		Global Modal-aerosol eXtention, aerosol scheme in EMAC
HD		Heat Disturbance injection height scheme
IGBP		International Geosphere Biosphere Program
IPCC		Intergubernamental Pannel for Climate Change
IQR		Inter-Quartile Range
ISORROPIA-II		Thermodynamic equilibrium model in GMXe/EMAC
ITCZ		InterTropical Convergence Zone
IXF		Index Fraction
JVAL		Photolysis rate coecients calculation in EMAC
LNOX		NO_x production from lightning in EMAC

LS	Lower Stratosphere
LW	Long-wave
M7	Modal-aerosol scheme of Vignati et al. (2004)
MABLH	Mass Above the Boundary Layer Height
MCD12C1	MODIS Land Cover Type Yearly L3 Global
MECCA	Module Eciently Calculating the Chemistry of the Atmosphere, chemistry module in EMAC
MESSy	Modular Earth Submodel System
MFRP	Maximum Fire radiative Power
MISR	Multi-angle Imaging SpectroRadiometer
MODIS	MODerate resolution Imaging Spectroradiometer
NASA	National Space Agency
NMHCs	Non-Methane HydroCarbons
NPH	Top plume height level
OC$_{PAT}$	Organic Carbon Passive Aerosol Tracer
OFFEMIS	Off-line emissions in EMAC
OLR	Outgoing Long-wave Radiation
ONEMIS	On-line emissions in EMAC
PA01	OC$_{ks}$ aerosol passive tracer
PA02	OC$_{ki}$ aerosol passive tracer
PA03	BC$_{ki}$ aerosol passive tracer
PAT	Passive Aerosol Tracers
PBLH	Planetary Boundary Layer Height
PH	Plume Height
QCTM	Quasi Chemistry-Transport Mode
RAD4ALL	Radiation scheme of EMAC
RF	Radiative Forcing
SCAV	Wet deposition in EMAC
SEDI	Sedimentation in EMAC

NOMENCLATURE

SIN	Sinusoidal Grid
SSA	Single Scattering Albedo
SST	Sea Surface Temperature
SW	Shortwave
TNUDGE	Tracer nudging in EMAC
TOA	Top of the Atmosphere
TROPOP	Diagnostic determination of the tropopause and boundary layer height in EMAC
UT	Upper Troposphere
VDF	Vertical Distribution Function
VEG	Vegetation injection height scheme
WASO	WAter SOluble compounds
WMO	World Meteorological Organization
WRF-Chem	Weather Research and Forecasting model with chemistry

List of Species

BC	Black Carbon
$\mathbf{C_2H_4}$	Ethene
$\mathbf{C_2H_6}$	Ethane
$\mathbf{C_3H_6}$	Propene
$\mathbf{C_3H_8}$	Propane
$\mathbf{CH_3CHO}$	Acetaldehyde
$\mathbf{CH_3CO_2H}$	Acetic acid
$\mathbf{CH_3COCH_3}$	Acetone
$\mathbf{CH_3OH}$	Methanol
$\mathbf{CH_4}$	Methane
$\mathbf{Cl^-}$	Chloride
CO	Carbon monoxide
$\mathbf{H_2SO_4}$	sulfuric acid
HCHO	Formaldehyde

HCl	Hydrogen chloride
HCOOH	Formic acid
MEK	Metyl Ethyl Ketane
Na$^+$	Sodium
NC$_4$H$_{10}$	N-butane
NH$_3$	Ammonia
NH$_4^+$	Ammonium
NO$_3^-$	Particulate nitrate
NO$_x$	Nitrogen oxides
O$_3$	Ozone
OC	Organic Carbon
PAN	Peroxyacetyl nitrate
SO$_2$	Sulfur dioxide
SO$_4^{2-}$	particulate sulfate

List of Symbols

$\bar{r}_i$	Aerosol number mean radius
ω_0	Single scattering albedo
σ	Extinction coefficient
σ_i	Geometric standard deviation
τ	Aerosol optical thickness
v_d	Deposition velocity
v_{Stokes}	Stokes velocity
v_t	Sedimentation velocity
f_{Csf}	Cunningham slip-flow factor
f_{Slinn}	Slinn factor
N_i	Aerosol number concentration
R_a	Aerodynamic resistance
R_s	Surface resistance
R_{qbr}	Quasi-laminar boundary layer resistance

References

M. Abu−Allaban, A. W. Gertler, and D. H. Lowenthal. A preliminary apportionment of the sources of ambient PM10, PM2.5, and VOCs in Cairo. *Atmospheric Environment*, 36(35):5549–5557, 2002. ISSN 1352-2310. doi: http://dx.doi.org/10.1016/S1352-2310(02) 00662-3. URL `http://www.sciencedirect.com/science/article/pii/S1352231002006623`. 97

A. S. Ackerman, O. B. Toon, D. E. Stevens, A. J. Heymsfield, V. Ramanathan, and E. J. Welton. Reduction of Tropical Cloudiness by Soot. *Science*, 288(5468):1042–1047, 2000. doi: 10.1126/science.288.5468.1042. URL `http://www.sciencemag.org/content/288/5468/1042.abstract`. 6, 8

B. E. Anderson, W. B. Grant, G. L. Gregory, E. V. Browell, J. E. Collins, G. W. Sachse, D. R. Bagwell, C. H. Hudgins, D. R. Blake, and N. J. Blake. Aerosols from biomass burning over the tropical South Atlantic region: Distributions and impacts. *Journal of Geophysical Research: Atmospheres*, 101(D19):24117–24137, 1996. ISSN 2156-2202. doi: 10.1029/96jd00717. URL `http://dx.doi.org/10.1029/96JD00717`. 5

M. O. Andreae and P. Merlet. Emission of trace gases and aerosols from biomass burning. *Global Biogeochemical Cycles*, 15(4):955–966, 2001. ISSN 1944-9224. doi: 10.1029/2000GB001382. URL `http://dx.doi.org/10.1029/2000GB001382`. 2, 4, 36, 144, 145

M. O. Andreae, P. Artaxo, H. Fischer, S. R. Freitas, J. M Grègoire, A. Hansel, P. Hoor, R. Kormann, R. Krejci, L. Lange, J. Lelieveld, W. Lindinger, K. Longo, W. Peters, M. de Reus, B. Scheeren, M. A. F. Silva Dias, J. Ström, P. F. J. van Velthoven, and J. Williams. Transport of biomass burning smoke to the upper troposphere by deep convection in the equatorial region. *Geophys. Res. Lett.*, 28(6):951–954, 2001. ISSN 0094-8276. doi: 10.1029/2000gl012391. URL `http://dx.doi.org/10.1029/2000GL012391`. 72, 102, 138, 164

M. O. Andreae, D. Rosenfeld, P. Artaxo, A. A. Costa, G. P. Frank, K. M. Longo, and M. A. F. Silva-Dias. Smoking Rain Clouds over the Amazon. *Science*, 303(5662):1337–1342, 2004. doi: 10.1126/science.1092779. URL `http://www.sciencemag.org/content/303/5662/1337.full.pdf`. 2

M. D. Andrés-Hernández, D. Kartal, L. Reichert, J. P. Burrows, J. Meyer Arnek, M. Lichtenstern, P. Stock, and H. Schlager. Peroxy radical observations over West Africa during AMMA 2006: photochemical activity in the outflow of convective systems. *Atmos. Chem. Phys.*, 9 (11):3681–3695, 2009. ISSN 1680-7324. doi: 10.5194/ acp-9-3681-2009. URL `http://www.atmos-chem-phys.net/9/3681/2009/`. 4, 138, 164

A. Arakawa and W. H. Schubert. Interaction of a Cumulus Cloud Ensemble with the Large-Scale Environment, Part I. *Journal of the Atmospheric Sciences*, 31(3):674–701, 1974. ISSN 0022-4928. doi: 10.1175/1520-0469(1974) 031⟨0674:ioacce⟩2.0.co;2. URL `http://dx.doi.org/10.1175/1520-0469(1974)031<0674:IOACCE>2.0.CO;2`. 25

A. F. Arellano Jr., P. S. Kasibhatla, L. Giglio, G. R. van der Werf, and J. T. Randerson. Top-down estimates of global CO sources using MOPITT measurements. *Geophys. Res. Lett.*, 31(1):L01104, 2004. ISSN 0094-8276. doi: 10.1029/2003gl018609. URL `http://dx.doi.org/10.1029/2003GL018609`. 144

A. F. Arellano Jr., P. S. Kasibhatla, L. Giglio, G. R. van der Werf, J. T. Randerson, and G. J. Collatz. Time-dependent inversion estimates of global biomass-burning CO emissions using Measurement of Pollution in the Troposphere (MOPITT) measurements. *Journal of Geophysical Research: Atmospheres*, 111(D9):D09303, 2006. ISSN 2156-2202. doi: 10.1029/2005JD006613. URL `http://dx.doi.org/10.1029/2005JD006613`. 144

A. Asa-Awuku, A. P. Sullivan, C. J. Hennigan, R. J. Weber, and A. Nenes. Investigation of molar volume and surfactant characteristics of water-soluble organic compounds in biomass burning aerosol. *Atmos. Chem. Phys.*, 8(4):799–812, 2008. ISSN 1680-7324. doi: 10.5194/acp-8-799-2008. URL `http://www.atmos-chem-phys.net/8/799/2008/`. 8

R. Asselin. Frequency Filter for Time Integrations. *Monthly Weather Review*, 100(6):487–490, 1972. ISSN 0027-0644. doi: 10.1175/1520-0493(1972)100⟨0487:fffti⟩2.3.co; 2. URL `http://dx.doi.org/10.1175/1520-0493(1972)100<0487:FFFTI>2.3.CO;2`. 16

T. K. Berntsen, I. S. A. Isaksen, G. Myhre, J. S. Fuglestvedt, F. Stordal, T. Alsvik Larsen, R. S. Freckleton, and K. P. Shine. Effects of anthropogenic emissions on tropospheric ozone and its radiative forcing. *Journal of Geophysical Research: Atmospheres*, 102(D23):28101–28126, 1997. ISSN 2156-2202. doi: 10.1029/97JD02226. URL `http://dx.doi.org/10.1029/97JD02226`. 5

D. R. Blake, T. W. Smith, T. Y. Chen, W. J. Whipple, and F. S. Rowland. Effects of biomass burning on summertime nonmethane hydrocarbon concentrations in the Canadian wetlands. *Journal of Geophysical Research: Atmospheres*, 99(D1):1699–1719, 1994. ISSN 2156-2202. doi: 10.1029/ 93jd02598. URL `http://dx.doi.org/10.1029/93JD02598`. 5, 8

S. Bloom, A. da Silva, and D. Dee. Documentation and Validation of the Goddard Earth Observing System (GEOS) Data Assimilation System − Version 4. Tech. Rep. Ser. Global Modeling Data Assimilation NASA/TM 2005-104606, NASA, 2005. URL `http://gmao.gsfc.nasa.gov/systems/geos4/Bloom.pdf`. 59

REFERENCES

T. C. Bond, S. J. Doherty, D. W. Fahey, P. M. Forster, T. Berntsen, B. J. DeAngelo, M. G. Flanner, S. Ghan, B. Kärcher, D. Koch, S. Kinne, Y. Kondo, P. K. Quinn, M. C. Sarofim, M. G. Schultz, M. Schulz, C. Venkataraman, H. Zhang, S. Zhang, N. Bellouin, S. K. Guttikunda, P. K. Hopke, M. Z. Jacobson, J. W. Kaiser, Z. Klimont, U. Lohmann, J. P. Schwarz, D. Shindell, T. Storelvmo, S. G. Warren, and C. S. Zender. Bounding the role of black carbon in the climate system: A scientific assessment. *Journal of Geophysical Research: Atmospheres*, pages n/a–n/a, 2013. ISSN 2169-8996. doi: 10.1002/jgrd.50171. URL http://dx.doi.org/10.1002/jgrd.50171. 7, 95, 97, 111, 112, 144, 145, 152, 161, 164

K. W. Bowman, D. T. Shindell, H. M. Worden, J. F. Lamarque, P. J. Young, D. S. Stevenson, Z. Qu, M. de la Torre, D. Bergmann, P. J. Cameron-Smith, W. J. Collins, R. Doherty, S. B. Dalsøren, G. Faluvegi, G. Folberth, L. W. Horowitz, B. M. Josse, Y. H. Lee, I. A. MacKenzie, G. Myhre, T. Nagashima, V. Naik, D. A. Plummer, S. T. Rumbold, R. B. Skeie, S. A. Strode, K. Sudo, S. Szopa, A. Voulgarakis, G. Zeng, S. S. Kulawik, A. M. Aghedo, and J. R. Worden. Evaluation of ACCMIP outgoing longwave radiation from tropospheric ozone using TES satellite observations. *Atmos. Chem. Phys.*, 13(8):4057–4072, 2013. ISSN 1680-7324. doi: 10.5194/acp-13-4057-2013. URL http://www.atmos-chem-phys.net/13/4057/2013/. ACP. 5

J. Buchholz. *Simulations of physics and chemistry of polar stratospheric clouds with a general circulation model.* Thesis, Johannes Gutenberg-Universität, 2005. URL http://ubm.opus.hbz-nrw.de/volltexte/2005/818. 30

J.-P. Cammas, J. Brioude, J.-P. Chaboureau, J. Duron, C. Mari, P. Mascart, P. Nédélec, H. Smit, H.-W. Pätz, A. Volz-Thomas, A. Stohl, and M. Fromm. Injection in the lower stratosphere of biomass fire emissions followed by long-range transport: a MOZAIC case study. *Atmos. Chem. Phys.*, 9(15):5829–5846, 2009. doi: 10.5194/acp-9-5829-2009. URL http://www.atmos-chem-phys.net/9/5829/2009/acp-9-5829-2009.pdf. 102

C. A. Cantrell, L. Mauldin, M. Zondlo, F. Eisele, E. Kosciuch, R. Shetter, B. Lefer, S. Hall, T. Campos, B. Ridley, J. Walega, A. Fried, B. Wert, F. Flocke, A. Weinheimer, J. Hannigan, M. Coffey, E. Atlas, S. Stephens, B. Heikes, J. Snow, D. Blake, N. Blake, A. Katzenstein, J. Lopez, E. V. Browell, J. Dibb, E. Scheuer, G. Seid, and R. Talbot. Steady state free radical budgets and ozone photochemistry during TOPSE. *Journal of Geophysical Research: Atmospheres*, 108(D4):8361, 2003. ISSN 2156-2202. doi: 10.1029/2002JD002198. URL http://dx.doi.org/10.1029/2002JD002198. 5

R. B. Chatfield, J. A. Vastano, H. B. Singh, and G. Sachse. A general model of how fire emissions and chemistry produce African/oceanic plumes (O3, CO, PAN, smoke) in TRACE A. *Journal of Geophysical Research: Atmospheres*, 101 (D19):24279–24306, 1996. ISSN 2156-2202. doi: 10.1029/ 96JD01871. URL http://dx.doi.org/10.1029/96JD01871. 5

M. Chin, P. Ginoux, S. Kinne, O. Torres, B. N. Holben, B. N. Duncan, R. V. Martin, J. A. Logan, A. Higurashi, and T. Nakajima. Tropospheric Aerosol Optical Thickness from the GOCART Model and Comparisons with Satellite and Sun Photometer Measurements. *Journal of the Atmospheric Sciences*, 59(3):461–483, 2002. ISSN 0022-4928. doi: 10.1175/1520-0469(2002)059⟨0461:TAOTFT⟩2.0.CO; 2. URL http://dx.doi.org/10.1175/1520-0469(2002)059<0461: TAOTFT>2.0.CO;2. 144

Z. Chowdhury, M. Zheng, J. J. Schauer, R. J. Sheesley, L. G. Salmon, G. R. Cass, and A. G. Russell. Speciation of ambient fine organic carbon particles and source apportionment of PM2.5 in Indian cities. *Journal of Geophysical Research: Atmospheres*, 112(D15):D15303, 2007. ISSN 2156-2202. doi: 10.1029/2007JD008386. URL http://dx.doi.org/10.1029/2007JD008386. 97

T. J. Christian, B. Kleiss, R. J. Yokelson, R. Holzinger, P. J. Crutzen, W. M. Hao, B. H. Saharjo, and D. E. Ward. Comprehensive laboratory measurements of biomass-burning emissions: 1. Emissions from Indonesian, African, and other fuels. *Journal of Geophysical Research: Atmospheres*, 108(D23):4719, 2003. ISSN 2156-2202. doi: 10.1029/2003jd003704. URL http://dx.doi.org/10.1029/2003JD003704. 2, 5, 36

P. Chylek and J. Wong. Effect of absorbing aerosols on global radiation budget. *Geophysical Research Letters*, 22(8):929–931, 1995. ISSN 1944-8007. doi: 10.1029/95GL00800. URL http://dx.doi.org/10.1029/95GL00800. 6

P. R. Colarco. The NASA GEOS-5 Aerosol Forecasting System. In *MACC Conference*, 2011. 144

P. R. Colarco, M. R. Schoeberl, B. G. Doddridge, L. T. Marufu, O. Torres, and E. J. Welton. Transport of smoke from Canadian forest fires to the surface near Washington, D.C.: Injection height, entrainment, and optical properties. *Journal of Geophysical Research: Atmospheres*, 109(D6):D06203, 2004. ISSN 2156-2202. doi: 10.1029/2003jd004248. URL http://dx.doi.org/10.1029/2003JD004248. 9, 10, 11, 41

R. Conrad and W. Seiler. Influence of temperature, moisture, and organic carbon on the flux of H2 and CO between soil and atmosphere: Field studies in subtropical regions. *Journal of Geophysical Research: Atmospheres*, 90(D3):5699–5709, 1985. ISSN 2156-2202. doi: 10.1029/JD090iD03p05699. URL http://dx.doi.org/10.1029/JD090iD03p05699. 36

P. A. Cook, N. H. Savage, S. Turquety, G. D. Carver, F. M. O'Connor, A. Heckel, D. Stewart, L. K. Whalley, A. E. Parker, H. Schlager, H. B. Singh, M. A. Avery, G. W. Sachse, W. Brune, A. Richter, J. P. Burrows, R. Purvis, A. C. Lewis, C. E. Reeves, P. S. Monks, J. G. Levine, and J. A. Pyle. Forest fire plumes over the North Atlantic: p-TOMCAT model simulations with aircraft and satellite measurements from the ITOP/ICARTT campaign. *Journal of Geophysical Research: Atmospheres*, 112(D10):D10S43, 2007. ISSN 2156-2202. doi: 10.1029/2006JD007563. URL http://dx.doi.org/10.1029/2006JD007563. 10

R. Courant, K. Friedrichs, and H. Lewy. Über die partiellen Differenzialgleichungen der mathematischen Physik. *Mathematische Annalen*, 100:32–74, 1928. 16

P. J. Crutzen and M. O. Andreae. Biomass Burning in the Tropics: Impact on Atmospheric Chemistry and Biogeochemical Cycles. *Science*, 250(4988):1669–1678, 1990. doi: 10.1126/science.250.4988.1669. URL http://www.sciencemag.org/content/250/4988/1669.abstract. 2, 4

P. J. Crutzen, L. E. Heidt, J. P. Krasnec, W. H. Pollock, and W. Seiler. Biomass burning as a source of atmospheric gases CO, H_2, N_2O, NO, CH_3Cl and COS. *Nature*, 282(5736):253–256, 1979. doi: 10.1038/282253a0. URL http://dx.doi.org/10.1038/282253a0. 4

P. J. Crutzen, A. C. Delany, J. Greenberg, P. Haagenson, L. Heidt, R. Lueb, W. Pollock, W. Seiler, A. Wartburg, and P. Zimmerman. Tropospheric chemical composition measurements in Brazil during the dry season. *Journal of Atmospheric Chemistry*, 2(3):233–256, 1985. ISSN 0167-7764. doi: 10.1007/BF00051075. URL http://dx.doi.org/10.1007/BF00051075. 4

V. Damian, A. Sandu, M. Damian, F. Potra, and G. R. Carmichael. The kinetic preprocessor KPP-a software environment for solving chemical kinetics. *Computers & Chemical Engineering*, 26(11):1567–1579, 2002. ISSN 0098-1354. doi: http://dx.doi.org/10.1016/S0098-1354(02)00128-X. URL http://www.sciencedirect.com/science/article/pii/S009813540200128X. 28

R. Damoah, N. Spichtinger, C. Forster, P. James, I. Mattis, U. Wandinger, S. Beirle, T. Wagner, and A. Stohl. Around the world in 17 days - hemispheric-scale transport of forest fire smoke from Russia in May 2003. *Atmos. Chem. Phys.*, 4(5):1311–1321, 2004. ISSN 1680-7324. doi: 10.5194/acp-4-1311-2004. URL http://www.atmos-chem-phys.net/4/1311/2004/acp-4-1311-2004.pdf. 9, 11, 41

R. Damoah, N. Spichtinger, R. Servranckx, M. Fromm, E. W. Eloranta, I. A. Razenkov, P. James, M. Shulski, C. Forster, and A. Stohl. A case study of pyro-convection using transport model and remote sensing data. *Atmos. Chem. Phys.*, 6(1):173–185, 2006. ISSN 1680-7324. doi: 10.5194/acp-6-173-2006. URL http://www.atmos-chem-phys.net/6/173/2006/acp-6-173-2006.pdf. 8, 9, 41, 102

P. S. Davison, D. L. Roberts, R. T. Arnold, and R. N. Colvile. Estimating the direct radiative forcing due to haze from the 1997 forest fires in Indonesia. *J. Geophys. Res.*, 109(D10):D10207, 2004. ISSN 0148-0227. doi: 10.1029/2003jd004264. URL http://dx.doi.org/10.1029/2003JD004264. 10

J. A. de Gouw, C. Warneke, A. Stohl, A. G. Wollny, C. A. Brock, O. R. Cooper, J. S. Holloway, M. Trainer, F. C. Fehsenfeld, E. L. Atlas, S. G. Donnelly, V. Stroud, and A. Lueb. Volatile organic compounds composition of merged and aged forest fire plumes from Alaska and western Canada. *Journal of Geophysical Research: Atmospheres*, 111(D10):D10303, 2006. ISSN 2156-2202. doi: 10.1029/2005JD006175. URL http://dx.doi.org/10.1029/2005JD006175. 8

R. Deckert, P. Jöckel, V. Grewe, K. D. Gottschaldt, and P. Hoor. A quasi chemistry-transport model mode for EMAC. *Geosci. Model Dev.*, 4(1):195–206, 2011. ISSN 1991-9603. doi: 10.5194/gmd-4-195-2011. URL http://www.geosci-model-dev.net/4/195/2011/gmd-4-195-2011.pdf. 29, 32

A. C. Delany, P. Haagensen, S. Walters, A. F. Wartburg, and P. J. Crutzen. Photochemically produced ozone in the emission from large-scale tropical vegetation fires. *Journal of Geophysical Research: Atmospheres*, 90(D1):2425–2429, 1985. ISSN 2156-2202. doi: 10.1029/JD090iD01p02425. URL http://dx.doi.org/10.1029/JD090iD01p02425. 5

F. Dentener, S. Kinne, T. Bond, O. Boucher, J. Cofala, S. Generoso, P. Ginoux, S. Gong, J. J. Hoelzemann, A. Ito, L. Marelli, J. E. Penner, J. P. Putaud, C. Textor, M. Schulz, G. R. van der Werf, and J. Wilson. Emissions of primary aerosol and precursor gases in the years 2000 and 1750 prescribed data-sets for AeroCom. *Atmos. Chem. Phys.*, 6(12):4321–4344, 2006. ISSN 1680-7324. doi: 10.5194/acp-6-4321-2006. URL http://www.atmos-chem-phys.net/6/4321/2006/acp-6-4321-2006.pdf. 44, 166

R. J. Dirksen, K. Folkert Boersma, J. de Laat, P. Stammes, G. R. van der Werf, M. Val Martín, and H. M. Kelder. An aerosol boomerang: Rapid around-the-world transport of smoke from the December 2006 Australian forest fires observed from space. *J. Geophys. Res.*, 114(D21):D21201, 2009. ISSN 0148-0227. doi: 10.1029/2009jd012360. URL http://dx.doi.org/10.1029/2009JD012360. 8, 9, 11, 41

T. J. Duck, B. J. Firanski, D. B. Millet, A. H. Goldstein, J. Allan, R. Holzinger, D. R. Worsnop, A. B. White, A. Stohl, C. S. Dickinson, and A. van Donkelaar. Transport of forest fire emissions from Alaska and the Yukon Territory to Nova Scotia during summer 2004. *Journal of Geophysical Research: Atmospheres*, 112(D10):D10S44, 2007. ISSN 2156-2202. doi: 10.1029/2006jd007716. URL http://dx.doi.org/10.1029/2006JD007716. 11, 41

J. P. Engelbrecht, L. Swanepoel, J. C. Chow, J. G. Watson, and R. T. Egami. The comparison of source contributions from residential coal and low−smoke fuels, using CMB modeling, in South Africa. *Environmental Science Policy*, 5(2):157–167, 2002. ISSN 1462-9011. doi: http://dx.doi.org/10.1016/S1462-9011(02)00029-1. URL http://www.sciencedirect.com/science/article/pii/S1462901102000291. 97

B. Ervens, C. George, J. E. Williams, G. V. Buxton, G. A. Salmon, M. Bydder, F. Wilkinson, F. Dentener, P. Mirabel, R. Wolke, and H. Herrmann. CAPRAM 2.4 (MODAC mechanism): An extended and condensed tropospheric aqueous phase mechanism and its application. *Journal of Geophysical Research: Atmospheres*, 108(D14):4426, 2003. ISSN 2156-2202. doi: 10.1029/2002jd002202. URL http://dx.doi.org/10.1029/2002JD002202. 28

V. Etyemezian, M. Tesfaye, A. Yimer, J. C. Chow, D. Mesfin, T. Nega, G. Nikolich, J. G. Watson, and M. Wondmagegn. Results from a pilot−scale air quality study in Addis Ababa, Ethiopia. *Atmospheric Environment*, 39(40):7849–7860, 2005. ISSN 1352-2310. doi: http://dx.doi.org/10.1016/j.atmosenv.2005.08.033. URL http://www.sciencedirect.com/science/article/pii/S1352231005008344. 97

191

REFERENCES

G. Feingold, L. A. Remer, J. Ramaprasad, and Y. J. Kaufman. Analysis of smoke impact on clouds in Brazilian biomass burning regions: An extension of Twomey's approach. *Journal of Geophysical Research: Atmospheres*, 106(D19):22907–22922, 2001. ISSN 2156-2202. doi: 10.1029/2001JD000732. URL http://dx.doi.org/10.1029/2001JD000732. 8

C. B. Field, J. T. Randerson, and C. M. Malmström. Global net primary production: Combining ecology and remote sensing. *Remote Sensing of Environment*, 51(1):74–88, 1995. ISSN 0034-4257. doi: http://dx.doi.org/10.1016/0034-4257(94)00066-V. URL http://www.sciencedirect.com/science/article/pii/003442579400066V. 35

M. G. Flanner and C. S. Zender. Linking snowpack microphysics and albedo evolution. *Journal of Geophysical Research: Atmospheres*, 111(D12):D12208, 2006. ISSN 2156-2202. doi: 10.1029/2005JD006834. URL http://dx.doi.org/10.1029/2005JD006834. 7

M. G. Flanner, C. S. Zender, P. G. Hess, N. M. Mahowald, T. H. Painter, V. Ramanathan, and P. J. Rasch. Springtime warming and reduced snow cover from carbonaceous particles. *Atmos. Chem. Phys.*, 9(7):2481–2497, 2009. ISSN 1680-7324. doi: 10.5194/acp-9-2481-2009. URL http://www.atmos-chem-phys.net/9/2481/2009/. 7

C. Forster, U. Wandinger, G. Wotawa, P. James, I. Mattis, D. Althausen, P. Simmonds, S. O'Doherty, S. G. Jennings, C. Kleefeld, J. Schneider, T. Trickl, S. Kreipl, H. Jäger, and A. Stohl. Transport of boreal forest fire emissions from Canada to Europe. *J. Geophys. Res.*, 106(D19):22887–22906, 2001. ISSN 0148-0227. doi: 10.1029/2001jd900115. URL http://dx.doi.org/10.1029/2001JD900115. 10

C. Fountoukis and A. Nenes. ISORROPIA II: a computationally efficient thermodynamic equilibrium model for K+ -Ca2+ -Mg2+ -NH4+ -Na+ -SO42- -NO3- -Cl- -H2O aerosols. *Atmos. Chem. Phys.*, 7(17):4639–4659, 2007. ISSN 1680-7324. doi: 10.5194/acp-7-4639-2007. URL http://www.atmos-chem-phys.net/7/4639/2007/acp-7-4639-2007.pdf. 22

S. R. Freitas, K. M. Longo, and M. O. Andreae. Impact of including the plume rise of vegetation fires in numerical simulations of associated atmospheric pollutants. *Geophys. Res. Lett.*, 33(L17808):1–5, 2006. doi: 10.1029/2006GL026608. URL http://www.agu.org/pubs/crossref/2006/2006GL026608.shtml. 10

S. R. Freitas, K. M. Longo, R. Chatfield, D. Latham, M. A. F. Silva Dias, M. O. Andreae, E. Prins, J. C. Santos, R. Gielow, and J. A. Carvalho Jr. Including the sub-grid scale plume rise of vegetation fires in low resolution atmospheric transport models. *Atmos. Chem. Phys.*, 7(13):3385–3398, 2007. doi: 10.5194/acp-7-3385-2007. URL http://www.atmos-chem-phys.net/7/3385/2007/. 10, 47

S. R. Freitas, K. M. Longo, J. Trentmann, and D. Latham. Technical Note: Sensitivity of 1-D smoke plume rise models to the inclusion of environmental wind drag. *Atmos. Chem. Phys.*, 10(2):585–594, 2010. ISSN 1680-7324. doi: 10.5194/acp-10-585-2010. URL http://www.atmos-chem-phys.net/10/585/2010/acp-10-585-2010.pdf. 46

M. A. Friedl, D. Sulla-Menashe, B. Tan, A. Schneider, N. Ramankutty, A. Sibley, and X. Huang. MODIS Collection 5 global land cover: Algorithm refinements and characterization of new datasets. *Remote Sensing of Environment*, 114(1):168–182, 2010. ISSN 0034-4257. doi: 10.1016/j.rse.2009.08.016. URL http://www.sciencedirect.com/science/article/pii/S0034425709002673. 44

M. Fromm and R. Servranckx. Transport of forest fire smoke above the tropopause by supercell convection. *Geophysical Research Letters*, 30(10):1542, 2003. ISSN 1944-8007. doi: 10.1029/2002gl016820. URL http://dx.doi.org/10.1029/2002GL016820. 8, 9, 41, 72, 102

M. Fromm, J. Alfred, K. Hoppel, J. Hornstein, R. Bevilacqua, E. Shettle, R. Servranckx, Z. Li, and B. Stocks. Observations of boreal forest fire smoke in the stratosphere by POAM III, SAGE II, and lidar in 1998. *Geophys. Res. Lett.*, 27(9):1407–1410, 2000. doi: 10.1029/1999GL011200. URL http://www.agu.org/pubs/crossref/2000/1999GL011200.shtml. 8, 9, 41, 162, 164

M. Fromm, R. Bevilacqua, R. Servranckx, J. Rosen, J. P. Thayer, J. Herman, and D. Larko. Pyro-cumulonimbus injection of smoke to the stratosphere: Observations and impact of a super blowup in northwestern Canada on 3–4 August 1998. *J. Geophys. Res.*, 110(D08205):1–16, 2005. doi: 10.1029/2004JD005350. URL http://www.agu.org/pubs/crossref/2005/2004JD005350.shtml. 8, 9, 41, 164

M. Fromm, E. P. Shettle, K. H. Fricke, C. Ritter, T. Trickl, H. Giehl, M. Gerding, J. E. Barnes, M. O'Neill, S. T. Massie, U. Blum, I. S. McDermid, T. Leblanc, and T. Deshler. Stratospheric impact of the Chisholm pyrocumulonimbus eruption: 2. Vertical profile perspective. *J. Geophys. Res.*, 113(D8):D08203, 2008. ISSN 0148-0227. doi: 10.1029/2007jd009147. URL http://dx.doi.org/10.1029/2007JD009147. 102

N. A. Fuchs. *The Mechanics of aerosols*. Pergamon Press, 1964. 22

L. Ganzeveld and J. Lelieveld. Dry deposition parameterization in a chemistry general circulation model and its influence on the distribution of reactive trace gases. *Journal of Geophysical Research: Atmospheres*, 100(D10):20999–21012, 1995. ISSN 2156-2202. doi: 10.1029/95jd02266. URL http://dx.doi.org/10.1029/95JD02266. 26

L. Ganzeveld, J. Lelieveld, and G.-J. Roelofs. A dry deposition parameterization for sulfur oxides in a chemistry and general circulation model. *Journal of Geophysical Research: Atmospheres*, 103(D5):5679–5694, 1998. ISSN 2156-2202. doi: 10.1029/97jd03077. URL http://dx.doi.org/10.1029/97JD03077. 26

S. Generoso, I. Bey, J.-L. Attié, and F.-M. Bréon. A satellite- and model-based assessment of the 2003 Russian fires: Impact on the Arctic region. *J. Geophys. Res.*, 112(D15):D15302, 2007. ISSN 0148-0227. doi: 10.1029/2006jd008344. URL http://dx.doi.org/10.1029/2006JD008344. 10, 42

L. Giglio. Modis collection 5 active fire product user's guide version 2.5. Report, University of Maryland, 31 March 2013 2013. URL https://earthdata.nasa.gov/sites/default/files/field/document/MODIS_Fire_Users_Guide_2.5.pdf. 47

L. Giglio, I. Csiszar, and C. O. Justice. Global distribution and seasonality of active fires as observed with the Terra and Aqua Moderate Resolution Imaging Spectroradiometer (MODIS) sensors. *J. Geophys. Res.*, 111(G2):G02016, 2006. ISSN 0148-0227. doi: 10.1029/2005jg000142. URL http://dx.doi.org/10.1029/2005JG000142. 47

L. Giglio, J. T. Randerson, G. R. van der Werf, P. S. Kasibhatla, G. J. Collatz, D. C. Morton, and R. S. DeFries. Assessing variability and long-term trends in burned area by merging multiple satellite fire products. *Biogeosciences*, 7(3):1171–1186, 2010. ISSN 1726-4189. doi: 10.5194/bg-7-1171-2010. URL http://www.biogeosciences.net/7/1171/2010/bg-7-1171-2010.pdf. 36

M. A. Giorgetta, E. Manzini, E. Roeckner, M. Esch, and L. Bengtsson. Climatology and Forcing of the Quasi-Biennial Oscillation in the MAECHAM5 Model. *Journal of Climate*, 19(16):3882–3901, 2006. ISSN 0894-8755. doi: 10.1175/jcli3830.1. URL http://dx.doi.org/10.1175/JCLI3830.1. 16

J. P. Greenberg, P. R. Zimmerman, L. Heidt, and W. Pollock. Hydrocarbon and carbon monoxide emissions from biomass burning in Brazil. *Journal of Geophysical Research: Atmospheres*, 89(D1):1350–1354, 1984. ISSN 2156-2202. doi: 10.1029/JD089iD01p01350. URL http://dx.doi.org/10.1029/JD089iD01p01350. 4

G. Grell, S. R. Freitas, M. Stuefer, and J. Fast. Inclusion of biomass burning in WRF-Chem: impact of wildfires on weather forecasts. *Atmos. Chem. Phys.*, 11(11):5289–5303, 2011. ISSN 1680-7324. doi: 10.5194/acp-11-5289-2011. URL http://www.atmos-chem-phys.net/11/5289/2011/. 10

H. Guan, R. B. Chatfield, S. R. Freitas, R. W. Bergstrom, and K. M. Longo. Modeling the effect of plume-rise on the transport of carbon monoxide over Africa with NCAR CAM. *Atmos. Chem. Phys.*, 8(22):6801–6812, 2008. ISSN 1680-7324. doi: 10.5194/acp-8-6801-2008. URL http://www.atmos-chem-phys.net/8/6801/2008/. 10

H. Guan, R. Esswein, J. Lopez, R. Bergstrom, A. Warnock, M. Follette-Cook, M. Fromm, and L. T. Iraci. A multi−decadal history of biomass burning plume heights identified using aerosol index measurements. *Atmos. Chem. Phys.*, 10(14):6461–6469, 2010. doi: 10.5194/acp-10-6461-2010. URL http://www.atmos-chem-phys.net/10/6461/2010/. 9

J. M. Haywood and V. Ramaswamy. Global sensitivity studies of the direct radiative forcing due to anthropogenic sulfate and black carbon aerosols. *Journal of Geophysical Research: Atmospheres*, 103(D6):6043–6058, 1998. ISSN 2156-2202. doi: 10.1029/97JD03426. URL http://dx.doi.org/10.1029/97JD03426. 6

D. A. Hegg, S. G. Warren, T. C. Grenfell, S. J. Doherty, T. V. Larson, and A. D. Clarke. Source Attribution of Black Carbon in Arctic Snow. *Environmental Science Technology*, 43(11):4016–4021, 2009. ISSN 0013-936X. doi: 10.1021/es803623f. URL http://dx.doi.org/10.1021/es803623f. 111

D. A. Hegg, S. G. Warren, T. C. Grenfell, J. D. Sarah, and A. D. Clarke. Sources of light-absorbing aerosol in arctic snow and their seasonal variation. *Atmos. Chem. Phys.*, 10(22):10923–10938, 2010. ISSN 1680-7324. doi: 10.5194/acp-10-10923-2010. URL http://www.atmos-chem-phys.net/10/10923/2010/. 111

J. Heintzenberg, R. J. Charlson, A. D. Clarke, C. Liousse, V. Ramaswamy, K. P. Shine, M. Wendish, and G. Helas. Measurements and modelling of aerosol single-scattering albedo: Progress, problems and prospects. *Beitr. Phys. Atmos.*, 70:249–263, 1997. 7

B. B. Hicks, D. D. Baldocchi, T. P. Meyers, Jr. Hosker, R. P., and D. R. Matt. A preliminary multiple resistance routine for deriving dry deposition velocities from measured quantities. *Water, Air, and Soil Pollution*, 36(3-4):311–330, 1987. ISSN 0049-6979. doi: 10.1007/bf00229675. URL http://dx.doi.org/10.1007/BF00229675. 26

P. V. Hobbs, J. S. Reid, R. A. Kotchenruther, R. J. Ferek, and R. Weiss. Direct Radiative Forcing by Smoke from Biomass Burning. *Science*, 275(5307):1777–1778, 1997. doi: 10.1126/science.275.5307.1777. URL http://www.sciencemag.org/content/275/5307/1777.abstract. 2

A. Hodzic, S. Madronich, B. Bohn, S. Massie, L. Menut, and C. Wiedinmyer. Wildfire particulate matter in Europe during summer 2003: meso-scale modeling of smoke emissions, transport and radiative effects. *Atmos. Chem. Phys.*, 7(15):4043–4064, 2007. ISSN 1680-7324. doi: 10.5194/acp-7-4043-2007. URL http://www.atmos-chem-phys.net/7/4043/2007/. 10

A. A. M. Holtslag and B. A. Boville. Local Versus Nonlocal Boundary-Layer Diffusion in a Global Climate Model. *Journal of Climate*, 6(10):1825–1842, 1993. ISSN 0894-8755. doi: 10.1175/1520-0442(1993)006⟨1825:lvnbld⟩2.0.co;2. URL http://dx.doi.org/10.1175/1520-0442(1993)006<1825:LVNBLD>2.0.CO;2. 20

A. A. M. Holtslag, E. I. F. De Bruijn, and H. L. Pan. A High Resolution Air Mass Transformation Model for Short-Range Weather Forecasting. *Monthly Weather Review*, 118(8):1561–1575, 1990. ISSN 0027-0644. doi: 10.1175/1520-0493(1990)118⟨1561:ahramt⟩2.0.co;2. URL http://dx.doi.org/10.1175/1520-0493(1990)118<1561:AHRAMT>2.0.CO;2. 20

R. E. Honrath, R. C. Owen, M. Val Martín, J. S. Reid, K. Lapina, P. Fialho, M. P. Dziobak, J. Kleissl, and D. L. Westphal. Regional and hemispheric impacts of anthropogenic and biomass burning emissions on summertime CO and O3 in the North Atlantic lower free troposphere. *Journal of Geophysical Research: Atmospheres*, 109(D24):D24310, 2004. ISSN 2156-2202. doi: 10.1029/2004jd005147. URL http://dx.doi.org/10.1029/2004JD005147. 5, 11, 41

E. J. Hyer, D. J. Allen, and E. S. Kasischke. Examining injection properties of boreal forest fires using surface and satellite measurements of CO transport. *J. Geophys. Res.*, 112(D18):D18307, 2007. ISSN 0148-0227. doi: 10.1029/2006jd008232. URL http://dx.doi.org/10.1029/2006JD008232. 10, 42

REFERENCES

C. Ichoku and Y. J. Kaufman. A method to derive smoke emission rates from MODIS fire radiative energy measurements. *Geoscience and Remote Sensing, IEEE Transactions on*, 43(11):2636–2649, 2005. ISSN 0196-2892. doi: 10.1109/tgrs.2005.857328. 46

S. Janhäll, M. O. Andreae, and U. Pöschl. Biomass burning aerosol emissions from vegetation fires: particle number and mass emission factors and size distributions. *Atmos. Chem. Phys.*, 10(3):1427–1439, 2010. ISSN 1680-7324. doi: 10.5194/acp-10-1427-2010. URL http://www.atmos-chem-phys.net/10/1427/2010/. 8

A. B. M. Jeuken, P. C. Siegmund, L. C. Heijboer, J. Feichter, and L. Bengtsson. On the potential of assimilating meteorological analyses in a global climate model for the purpose of model validation. *Journal of Geophysical Research: Atmospheres*, 101(D12):16939–16950, 1996. ISSN 2156-2202. doi: 10.1029/96jd01218. URL http://dx.doi.org/10.1029/96JD01218. 31

P. Jöckel. Technical note: Recursive rediscretisation of geo—scientific data in the Modular Earth Submodel System (MESSy). *Atmos. Chem. Phys.*, 6(11):3557–3562, 2006. ISSN 1680-7324. doi: 10.5194/acp-6-3557-2006. URL http://www.atmos-chem-phys.net/6/3557/2006/acp-6-3557-2006.pdf. 18

P. Jöckel, R. von Kuhlmann, M. G. Lawrence, B. Steil, C. A. M. Brenninkmeijer, P. J. Crutzen, P. J. Rasch, and B. Eaton. On a fundamental problem in implementing flux-form advection schemes for tracer transport in 3-dimensional general circulation and chemistry transport models. *Quarterly Journal of the Royal Meteorological Society*, 127(573):1035–1052, 2001. ISSN 1477-870X. doi: 10.1002/qj.49712757318. URL http://dx.doi.org/10.1002/qj.49712757318. 17

P. Jöckel, R. Sander, A. Kerkweg, H. Tost, and J. Lelieveld. Technical Note: The Modular Earth Submodel System (MESSy) - a new approach towards Earth System Modeling. *Atmos. Chem. Phys.*, 5(2):433–444, 2005. ISSN 1680-7324. doi: 10.5194/acp-5-433-2005. URL http://www.atmos-chem-phys.net/5/433/2005/acp-5-433-2005.pdf. 15, 17

P. Jöckel, H. Tost, A. Pozzer, C. Brühl, J. Buchholz, L. Ganzeveld, P. Hoor, A. Kerkweg, M. Lawrence, R. Sander, B. Steil, G. Stiller, M. Tanarhte, D. Taraborrelli, J. van Aardenne, and J. Lelieveld. The atmospheric chemistry general circulation model ECHAM5/MESSy1: consistent simulation of ozone from the surface to the mesosphere. *Atmos. Chem. Phys.*, 6(12):5067–5104, 2006. ISSN 1680-7324. doi: 10.5194/acp-6-5067-2006. URL http://www.atmos-chem-phys.net/6/5067/2006/acp-6-5067-2006.pdf. 19, 20, 24, 29, 30, 31

P. Jöckel, A. Kerkweg, A. Pozzer, R. Sander, H. Tost, H. Riede, A. Baumgaertner, S. Gromov, and B. Kern. Development cycle 2 of the Modular Earth Submodel System (MESSy2). *Geosci. Model Dev.*, 3(2):717–752, 2010. ISSN 1991-9603. doi: 10.5194/gmd-3-717-2010. URL http://www.geosci-model-dev.net/3/717/2010/gmd-3-717-2010.pdf. 15, 17, 30

T. M. Johnson, S. Guttikunda, G. J. Wells, P. Artaxo, T. C. Bond, A. G. Russell, J. G. Watson, and J. West. Tools for Improving Air Quality Management: A Review of Top-Down Source Apportionment Techniques and Their Application in Developing Countries. Report, The World Bank, 2011. URL http://www.esmap.org/node/1159. 97

I. Jonquières, A. Marenco, A. Maalej, and F. Rohrer. Study of ozone formation and transatlantic transport from biomass burning emissions over West Africa during the airborne Tropospheric Ozone Campaigns TROPOZ I and TROPOZ II. *Journal of Geophysical Research: Atmospheres*, 103 (D15):19059–19073, 1998. ISSN 2156-2202. doi: 10.1029/98jd00819. URL http://dx.doi.org/10.1029/98JD00819. 5

H.-J. Jost, K. Drdla, A. Stohl, L. Pfister, M. Lowenstein, J. P. Lopez, P. K. Hudson, D. M. Murphy, D. J. Cziczo, M. Fromm, T. Paul Bui, J. Dean-Day, C. Gerbig, M. J. Mahoney, E. C. Richard, N. Spichtinger, J. V. Pittman, E. M. Weinstock, J. C. Wilson, and I. Xueref. In-situ observations of mid-latitude forest fire plumes deep in the stratosphere. *Geophys. Res. Lett.*, 31(L11101):1–5, 2004. doi: 10.1029/2003GL019253. URL http://www.agu.org/pubs/crossref/2004/2003GL019253.shtml. 5, 9, 72, 102, 164

R. A. Kahn, W. H. Li, C. Moroney, D. J. Diner, J. V. Martonchik, and E. Fishbein. Aerosol source plume physical characteristics from space-based multiangle imaging. *J. Geophys. Res.*, 112(D11):D11205, 2007. ISSN 0148-0227. doi: 10.1029/2006jd007647. URL http://dx.doi.org/10.1029/2006JD007647. 9, 41, 64, 65

R. A. Kahn, Y. Chen, D. L. Nelson, F.-Y. Leung, Q. Li, D. J. Diner, and J. A. Logan. Wildfire smoke injection heights: Two perspectives from space. *Geophys. Res. Lett.*, 35(4):L04809, 2008. ISSN 0094-8276. doi: 10.1029/2007gl032165. URL http://dx.doi.org/10.1029/2007GL032165. 9, 47, 59

R. A. Kahn, D. L. Nelson, M. J. Garay, R. C. Levy, M. A. Bull, D. J. Diner, J. V. Martonchik, S. R. Paradise, E. G. Hansen, and L. A. Remer. MISR Aerosol Product Attributes and Statistical Comparisons With MODIS. *Geoscience and Remote Sensing, IEEE Transactions on*, 47(12): 4095–4114, 2009. ISSN 0196-2892. doi: 10.1109/TGRS.2009.2023115. 64

J. W. Kaiser, A. Heil, M. O. Andreae, A. Benedetti, N. Chubarova, L. Jones, J. J. Morcrette, M. Razinger, M. G. Schultz, M. Suttie, and G. R. van der Werf. Biomass burning emissions estimated with a global fire assimilation system based on observed fire radiative power. *Biogeosciences*, 9(1):527–554, 2012. ISSN 1726-4189. doi: 10.5194/bg-9-527-2012. URL http://www.biogeosciences.net/9/527/2012/bg-9-527-2012.pdf. 46, 144

J. B. Kauffman, M. D. Steele, D. L. Cummings, and V. J. Jaramillo. Biomass dynamics associated with deforestation, fire, and, conversion to cattle pasture in a Mexican tropical dry forest. *Forest Ecology and Management*, 176(1-3):1–12, 2003. ISSN 0378-1127. doi: 10.1016/s0378-1127(02)00227-x. URL http://www.sciencedirect.com/science/article/pii/S037811270200227X. 40

Y. J. Kaufman, C. O. Justice, L. P. Flynn, J. D. Kendall, E. M. Prins, L. Giglio, D. E. Ward, W. P. Menzel, and A. W. Setzer. Potential global fire monitoring from EOS-MODIS. *J. Geophys. Res.*, 103(D24):32215–32238, 1998. ISSN 0148-0227. doi: 10.1029/98jd01644. URL http://dx.doi.org/10.1029/98JD01644. 46, 47

A. Kerkweg, J. Buchholz, L. Ganzeveld, A. Pozzer, H. Tost, and P. Jöckel. Technical Note: An implementation of the dry removal processes DRY DEPosition and SEDImentation in the Modular Earth Submodel System (MESSy). *Atmos. Chem. Phys.*, 6(12):4617–4632, 2006a. ISSN 1680-7324. doi: 10.5194/acp-6-4617-2006. URL http://www.atmos-chem-phys.net/6/4617/2006/acp-6-4617-2006.pdf. 19, 25, 26, 27

A. Kerkweg, R. Sander, H. Tost, and P. Jöckel. Technical note: Implementation of prescribed (OFFLEM), calculated (ONLEM), and pseudo-emissions (TNUDGE) of chemical species in the Modular Earth Submodel System (MESSy). *Atmos. Chem. Phys.*, 6(11):3603–3609, 2006b. ISSN 1680-7324. doi: 10.5194/acp-6-3603-2006. URL http://www.atmos-chem-phys.net/6/3603/2006/acp-6-3603-2006.pdf. 18, 19

O. Kirner. *Prozessstudien der stratosphärischen Chemie und Dynamik mit Hilfe des Chemie-Klima-Modells ECHAM5/MESSy1*. Thesis, Karlsruher Institut für Technologie, 2008. URL http://digbib.ubka.uni-karlsruhe.de/volltexte/1000010199. 30

N. Kivekäs, V.-M. Kerminen, T. Anttila, H. Korhonen, H.i Lihavainen, M. Komppula, and M. Kulmala. Parameterization of cloud droplet activation using a simplified treatment of the aerosol number size distribution. *Journal of Geophysical Research: Atmospheres*, 113(D15):D15207, 2008. ISSN 2156-2202. doi: 10.1029/2007JD009485. URL http://dx.doi.org/10.1029/2007JD009485. 8

K. Klingmüller, B. Steil, C. Brühl, H. Tost, and J. Lelieveld. Sensitivity of aerosol extinction to new mixing rules in the AEROPT submodel of the ECHAM5/MESSy1.9 atmospheric chemistry (EMAC) model. *Geosci. Model Dev. Discuss.*, 7(3):3367–3402, 2014. ISSN 1991-962X. doi: 10.5194/gmdd-7-3367-2014. URL http://www.geosci-model-dev-discuss.net/7/3367/2014/. 7, 142, 144

D. Koch, M. Schulz, S. Kinne, C. McNaughton, J. R. Spackman, Y. Balkanski, S. Bauer, T. Berntsen, T. C. Bond, O. Boucher, M. Chin, A. Clarke, N. De Luca, F. Dentener, T. Diehl, O. Dubovik, R. Easter, D. W. Fahey, J. Feichter, D. Fillmore, S. Freitag, S. Ghan, P. Ginoux, S. Gong, L. Horowitz, T. Iversen, A. Kirkevåg, Z. Klimont, Y. Kondo, M. Krol, X. Liu, R. Miller, V. Montanaro, N. Moteki, G. Myhre, J. E. Penner, J. Perlwitz, G. Pitari, S. Reddy, L. Sahu, H. Sakamoto, G. Schuster, J. P. Schwarz, Ø. Seland, P. Stier, N. Takegawa, T. Takemura, C. Textor, J. A. van Aardenne, and Y. Zhao. Evaluation of black carbon estimations in global aerosol models. *Atmos. Chem. Phys.*, 9(22):9001–9026, 2009. ISSN 1680-7324. doi: 10.5194/acp-9-9001-2009. URL http://www.atmos-chem-phys.net/9/9001/2009/http://www.atmos-chem-phys.net/9/9001/2009/acp-9-9001-2009.pdf. 144

D. Kunkel, M. G. Lawrence, H. Tost, A. Kerkweg, P. Jöckel, and S. Borrmann. Urban emission hot spots as sources for remote aerosol deposition. *Geophysical Research Letters*, 39(1):L01808, 2012. ISSN 1944-8007. doi: 10.1029/2011gl049634. URL http://dx.doi.org/10.1029/2011GL049634. 12, 69, 160

M. Labonne, F.-M. Bréon, and F. Chevallier. Injection height of biomass burning aerosols as seen from a spaceborne lidar. *Geophys. Res. Lett.*, 34(11):L11806, 2007. ISSN 0094-8276. doi: 10.1029/2007gl029311. URL http://dx.doi.org/10.1029/2007GL029311. 9, 41, 50, 63, 103, 162

A. A. Lacis, D. J. Wuebbles, and J. A. Logan. Radiative forcing of climate by changes in the vertical distribution of ozone. *Journal of Geophysical Research: Atmospheres*, 95(D7):9971–9981, 1990. ISSN 2156-2202. doi: 10.1029/JD095iD07p09971. URL http://dx.doi.org/10.1029/JD095iD07p09971. 5

J. F. Lamarque, D. P. Edwards, L. K. Emmons, J. C. Gille, O. Wilhelmi, C. Gerbig, D. Prevedel, M. N. Deeter, J. Warner, D. C. Ziskin, B. Khattatov, G. L. Francis, V. Yudin, S. Ho, D. Mao, J. Chen, and J. R. Drummond. Identification of CO plumes from MOPITT data: Application to the August 2000 Idaho-Montana forest fires. *Geophys. Res. Lett.*, 30(13):1688, 2003. ISSN 0094-8276. doi: 10.1029/2003gl017503. URL http://dx.doi.org/10.1029/2003GL017503. 9, 10, 41

J. Landgraf and P. J. Crutzen. An Efficient Method for Online Calculations of Photolysis and Heating Rates. *Journal of the Atmospheric Sciences*, 55(5):863–878, 1998. ISSN 0022-4928. doi: 10.1175/1520-0469(1998)055⟨0863:aemfoc⟩2.0.co;2. URL http://dx.doi.org/10.1175/1520-0469(1998)055<0863:AEMFOC>2.0.CO;2. 30

B. Langmann, B. Duncan, C. Textor, J. Trentmann, and G. R. van der Werf. Vegetation fire emissions and their impact on air pollution and climate. *Atmospheric Environment*, 43(1):107–116, 2009. ISSN 1352-2310. doi: http://dx.doi.org/10.1016/j.atmosenv.2008.09.047. URL http://www.sciencedirect.com/science/article/pii/S135223100800900X. 9, 41

D. Latham. PLUMP: A one-dimensional plume predictor and cloud model for fire and smoke managers. Report INT-GTR-314, Intermountain Research Station, USDA Forest Service, Nov. 1994. 10

A. Lauer, V. Eyring, J. Hendricks, P. Jöckel, and U. Lohmann. Global model simulations of the impact of ocean-going ships on aerosols, clouds, and the radiation budget. *Atmos. Chem. Phys.*, 7(19):5061–5079, 2007. ISSN 1680-7324. doi: 10.5194/acp-7-5061-2007. URL http://www.atmos-chem-phys.net/7/5061/2007/acp-7-5061-2007.pdf. 23

D. Lavouè, C. Liousse, H. Cachier, B. J. Stocks, and J. G. Goldammer. Modeling of carbonaceous particles emitted by boreal and temperate wildfires at northern latitudes. *J. Geophys. Res.*, 105(D22):26871–26890, 2000. ISSN 0148-0227. doi: 10.1029/2000jd900180. URL http://dx.doi.org/10.1029/2000JD900180. 8, 10, 41

M. G. Lawrence and P. J. Rasch. Tracer Transport in Deep Convective Updrafts: Plume Ensemble versus Bulk Formulations. *Journal of the Atmospheric Sciences*, 62(8): 2880–2894, 2005. ISSN 0022-4928. doi: 10.1175/jas3505.1. URL http://dx.doi.org/10.1175/JAS3505.1. 25

W. Lei, G. Li, and L. T. Molina. Modeling the impacts of biomass burning on air quality in and around Mexico City. *Atmos. Chem. Phys.*, 13(5):2299–2319, 2013. ISSN 1680-7324. doi: 10.5194/acp-13-2299-2013. URL http://www.atmos-chem-phys.net/13/2299/2013/. 2, 97

J. Lelieveld and P. J. Crutzen. Role of Deep Cloud Convection in the Ozone Budget of the Troposphere. *Science*, 264(5166):1759–1761, 1994. URL http://www.sciencemag.org/content/264/5166/1759.abstract. 10.1126/science.264.5166.1759. 5

J. Lelieveld, C. Brühl, P. Jöckel, B. Steil, P. J. Crutzen, H. Fischer, M. A. Giorgetta, P. Hoor, M. G. Lawrence, R. Sausen, and H. Tost. Stratospheric dryness: model simulations and satellite observations. *Atmos. Chem. Phys.*, 7(5):1313–1332, 2007. ISSN 1680-7324. doi: 10.5194/acp-7-1313-2007. URL http://www.atmos-chem-phys.net/7/1313/2007/acp-7-1313-2007.pdf. 31

J. Lelieveld, T. M. Butler, J. N. Crowley, T. J. Dillon, H. Fischer, L. Ganzeveld, H. Harder, M. G. Lawrence, M. Martinez, D. Taraborrelli, and J. Williams. Atmospheric oxidation capacity sustained by a tropical forest. *Nature*, 452(7188):737–740, 2008. ISSN 0028-0836. doi: 10.1038/nature06870. URL http://dx.doi.org/10.1038/nature06870. 4

F.-Y. T. Leung, J. A. Logan, R. Park, E. Hyer, E. Kasischke, D. Streets, and L. Yurganov. Impacts of enhanced biomass burning in the boreal forests in 1998 on tropospheric chemistry and the sensitivity of model results to the injection height of emissions. *J. Geophys. Res.*, 112(D10):D10313, 2007. ISSN 0148-0227. doi: 10.1029/2006jd008132. URL http://dx.doi.org/10.1029/2006JD008132. 9, 10, 42

H. Levy. Normal Atmosphere: Large Radical and Formaldehyde Concentrations Predicted. *Science*, 173(3992):141–143, 1971. URL http://www.sciencemag.org/content/173/3992/141.abstract. 10.1126/science.173.3992.141. 4

J. B. Liley, D. Baumgardner, Y. Kondo, K. Kita, D. R. Blake, M. Koike, T. Machida, N. Takegawa, S. Kawakami, T. Shirai, and T. Ogawa. Black carbon in aerosol during BIBLE B. *Journal of Geophysical Research: Atmospheres*, 107(D3): 8399, 2002. ISSN 2156-2202. doi: 10.1029/2001JD000845. URL http://dx.doi.org/10.1029/2001JD000845. 144

S.-J. Lin and R. B. Rood. Multidimensional Flux-Form Semi-Lagrangian Transport Schemes. *Monthly Weather Review*, 124(9):2046–2070, 1996. ISSN 0027-0644. doi: 10.1175/1520-0493(1996)124⟨2046:mffslt⟩2.0.co;2. URL http://dx.doi.org/10.1175/1520-0493(1996)124<2046:MFFSLT>2.0.CO;2. 17

C. Liousse, J. E. Penner, C. Chuang, J. J. Walton, H. Eddleman, and H. Cachier. A global three-dimensional model study of carbonaceous aerosols. *J. Geophys. Res.*, 101 (D14):19411–19432, 1996. ISSN 0148-0227. doi: 10.1029/95jd03426. URL http://dx.doi.org/10.1029/95JD03426. 10, 144

C. Liousse, B. Guillaume, J. M. Grégoire, M. Mallet, C. Galy, V. Pont, A. Akpo, M. Bedou, P. Castéra, L. Dungall, E. Gardrat, C. Granier, A. Konaré, F. Malavelle, A. Mariscal, A. Mieville, R. Rosset, D. Serça, F. Solmon, F. Tummon, E. Assamoi, V. Yoboué, and P. Van Velthoven. Updated African biomass burning emission inventories in the framework of the AMMA-IDAF program, with an evaluation of combustion aerosols. *Atmos. Chem. Phys.*, 10(19):9631–9646, 2010. ISSN 1680-7324. doi: 10.5194/acp-10-9631-2010. URL http://www.atmos-chem-phys.net/10/9631/2010/. 144

J. M. Lobert and J. Wamatz. *Emissions from the combustion process in vegetation.* Fire in the Environment: The Ecological, Atmospheric, and Climatic Importance of Vegetation Fires. John Wiley, New York, 1993. 2

J. A. Logan, M. J. Prather, S. C. Wofsy, and M. B. McElroy. Tropospheric chemistry: A global perspective. *Journal of Geophysical Research: Oceans*, 86(C8):7210–7254, 1981. ISSN 2156-2202. doi: 10.1029/JC086iC08p07210. URL http://dx.doi.org/10.1029/JC086iC08p07210. 4

U. Lohmann and E. Roeckner. Design and performance of a new cloud microphysics scheme developed for the ECHAM general circulation model. *Climate Dynamics*, 12(8):557–572, 1996. ISSN 0930-7575. doi: 10.1007/bf00207939. URL http://dx.doi.org/10.1007/BF00207939. 24

U. Lohmann, L. Rotstayn, T. Storelvmo, A. Jones, S. Menon, J. Quaas, A. M. L. Ekman, D. Koch, and R. Ruedy. Total aerosol effect: radiative forcing or radiative flux perturbation? *Atmos. Chem. Phys.*, 10 (7):3235–3246, 2010. ISSN 1680-7324. doi: 10.5194/acp-10-3235-2010. URL http://www.atmos-chem-phys.net/10/3235/2010/acp-10-3235-2010.pdf. 33

G. Luderer, J. Trentmann, T. Winterrath, C. Textor, M. Herzog, H-F. Graf, and M. O. Andreae. Modeling of biomass smoke injection into the lower stratosphere by a large forest fire (Part II): sensitivity studies. *Atmos. Chem. Phys.*, 6(12):5261–5277, 2006. doi: 10.5194/acp-6-5261-2006. URL http://www.atmos-chem-phys.net/6/5261/2006/acp-6-5261-2006.pdf. 8, 9, 41, 50, 72, 102

R. I. Matichuk, P. R. Colarco, J. A. Smith, and O. B. Toon. Modeling the transport and optical properties of smoke aerosols from African savanna fires during the Southern African Regional Science Initiative campaign (SAFARI 2000). *Journal of Geophysical Research: Atmospheres*, 112(D8):D08203, 2007. ISSN 2156-2202. doi: 10.1029/2006JD007528. URL http://dx.doi.org/10.1029/2006JD007528http://onlinelibrary.wiley.com/store/10.1029/2006JD007528/asset/jgrd13210.pdf?v=1&t=i2eusnxm&s=9938155e0f99e67731bc681bcc9c7a977fe34b87. 10

B. Mayer and A. Kylling. Technical note: The libRadtran software package for radiative transfer calculations - description and examples of use. *Atmos. Chem. Phys.*, 5 (7):1855–1877, 2005. ISSN 1680-7324. doi: 10.5194/acp-5-1855-2005. URL http://www.atmos-chem-phys.net/5/1855/2005/acp-5-1855-2005.pdf. 23

D. Mazzoni, J. A. Logan, D. Diner, R. Kahn, L. Tong, and Q. Li. A data-mining approach to associating MISR smoke plume heights with MODIS fire measurements. *Remote Sensing of Environment*, 107(1-2):138–148, 2007. ISSN 0034-4257. doi: 10.1016/j.rse.2006.08.014. URL http://www.sciencedirect.com/science/article/pii/S0034425706004354. 9, 41, 47, 63, 162

S. K. Meilinger. *Heterogeneous chemistry in the tropopause region*. Thesis, ETH, 2000. 30

S. R. Mims, R. A. Kahn, C. M. Moroney, B. J. Gaitley, D. L. Nelson, and M. J. Garay. MISR Stereo Heights of Grassland Fire Smoke Plumes in Australia. *Geoscience and Remote Sensing, IEEE Transactions on*, 48(1):25–35, 2010. ISSN 0196-2892. doi: 10.1109/TGRS.2009.2027114. 9

A. Nenes, S. Pandis, and C. Pilinis. ISORROPIA: A New Thermodynamic Equilibrium Model for Multiphase Multicomponent Inorganic Aerosols. *Aquatic Geochemistry*, 4(1):123–152, 1998. ISSN 1380-6165. doi: 10.1023/a:1009604003981. URL http://dx.doi.org/10.1023/A%3A1009604003981. 22

A. Nenes, S. N. Pandis, and C. Pilinis. Continued development and testing of a new thermodynamic aerosol module for urban and regional air quality models. *Atmospheric Environment*, 33(10):1553–1560, 1999. ISSN 1352-2310. doi: http://dx.doi.org/10.1016/S1352-2310(98)00352-5. URL http://www.sciencedirect.com/science/article/pii/S1352231098003525. 22

T Nordeng. Extended versions of the convective parametrization scheme at ECMWF and their impact on the mean and transient activity of the model in the tropics. Report, European Centre for Medium-Range Weather Forecasts, 1994. 24

J. E. Penner, S. Y. Zhang, and C. C. Chuang. Soot and smoke aerosol may not warm climate. *Journal of Geophysical Research: Atmospheres*, 108(D21):4657, 2003. doi: 10.1029/2003JD003409. URL http://dx.doi.org/10.1029/2003JD003409. 152, 165

M. Petrenko, R. Kahn, M. Chin, A. Soja, T. Kucsera, and Harshvardhan. The use of satellite-measured aerosol optical depth to constrain biomass burning emissions source strength in the global model GOCART. *Journal of Geophysical Research: Atmospheres*, 117(D18):D18212, 2012. ISSN 2156-2202. doi: 10.1029/2012jd017870. URL http://dx.doi.org/10.1029/2012JD017870. 144

G. G. Pfister, P. G. Hess, L. K. Emmons, J. F. Lamarque, C. Wiedinmyer, D. P. Edwards, G. Pétron, J. C. Gille, and G. W. Sachse. Quantifying CO emissions from the 2004 Alaskan wildfires using MOPITT CO data. *Geophysical Research Letters*, 32(11):L11809, 2005. ISSN 1944-8007. doi: 10.1029/2005GL022995. URL http://dx.doi.org/10.1029/2005GL022995. 10

G. G. Pfister, L. K. Emmons, P. G. Hess, R. Honrath, J. F. Lamarque, M. Val Martin, R. C. Owen, M. A. Avery, E. V. Browell, J. S. Holloway, P. Nedelec, R. Purvis, T. B. Ryerson, G. W. Sachse, and H. Schlager. Ozone production from the 2004 North American boreal fires. *Journal*

of Geophysical Research: Atmospheres, 111(D24):D24S07, 2006. ISSN 2156-2202. doi: 10.1029/2006JD007695. URL http://dx.doi.org/10.1029/2006JD007695. 10, 137, 164

G. G. Pfister, J. Avise, C. Wiedinmyer, D. P. Edwards, L. K. Emmons, G. D. Diskin, J. Podolske, and A. Wisthaler. CO source contribution analysis for California during ARCTAS-CARB. *Atmos. Chem. Phys.*, 11(15):7515–7532, 2011. ISSN 1680-7324. doi: 10.5194/acp-11-7515-2011. URL http://www.atmos-chem-phys.net/11/7515/2011/acp-11-7515-2011.pdf. 10, 42

K. E. Pickering, A. M. Thompson, Y. Wang, W.-K. Tao, D. P. McNamara, V. W. J. H. Kirchhoff, B. G. Heikes, G. W. Sachse, J. D. Bradshaw, G. L. Gregory, and D. R. Blake. Convective transport of biomass burning emissions over Brazil during TRACE A. *Journal of Geophysical Research: Atmospheres*, 101(D19):23993–24012, 1996. ISSN 2156-2202. doi: 10.1029/96JD00346. URL http://dx.doi.org/10.1029/96JD00346. 5, 72, 164

K. E. Pickering, Y. Wang, W. Tao, C. Price, and J.-F. Müller. Vertical distributions of lightning NOx for use in regional and global chemical transport models. *Journal of Geophysical Research: Atmospheres*, 103(D23):31203–31216, 1998. ISSN 2156-2202. doi: 10.1029/98jd02651. URL http://dx.doi.org/10.1029/98JD02651. 20

U. Pöschl, R. von Kuhlmann, N. Poisson, and P. J. Crutzen. Development and Intercomparison of Condensed Isoprene Oxidation Mechanisms for Global Atmospheric Modeling. *Journal of Atmospheric Chemistry*, 37(1):29–52, 2000. ISSN 0167-7764. doi: 10.1023/a:1006391009798. URL http://dx.doi.org/10.1023/A%3A1006391009798. 30

C. S. Potter, J. T. Randerson, C. B. Field, P. A. Matson, P. M. Vitousek, H. A. Mooney, and S. A. Klooster. Terrestrial ecosystem production: A process model based on global satellite and surface data. *Global Biogeochemical Cycles*, 7(4):811–841, 1993. ISSN 1944-9224. doi: 10.1029/93gb02725. URL http://dx.doi.org/10.1029/93GB02725. 35

A. Pozzer, P. Jöckel, R. Sander, J. Williams, L. Ganzeveld, and J. Lelieveld. Technical Note: The MESSy-submodel AIRSEA calculating the air-sea exchange of chemical species. *Atmos. Chem. Phys.*, 6(12):5435–5444, 2006. ISSN 1680-7324. doi: 10.5194/acp-6-5435-2006. URL http://www.atmos-chem-phys.net/6/5435/2006/acp-6-5435-2006.pdf. 29

A. Pozzer, P. Jöckel, H. Tost, R. Sander, L. Ganzeveld, A. Kerkweg, and J. Lelieveld. Simulating organic species with the global atmospheric chemistry general circulation model ECHAM5/MESSy1: a comparison of model results with observations. *Atmos. Chem. Phys.*, 7(10):2527–2550, 2007. ISSN 1680-7324. doi: 10.5194/acp-7-2527-2007. URL http://www.atmos-chem-phys.net/7/2527/2007/acp-7-2527-2007.pdf. 30

A. Pozzer, P. Jöckel, and J. Van Aardenne. The influence of the vertical distribution of emissions on tropospheric chemistry. *Atmos. Chem. Phys.*, 9(24):9417–9432, 2009. doi: 10.5194/acp-9-9417-2009. URL http://www.atmos-chem-phys.net/9/9417/2009/acp-9-9417-2009.pdf. 42, 115

197

REFERENCES

A. Pozzer, A. de Meij, K. J. Pringle, H. Tost, U. M. Doering, J. van Aardenne, and J. Lelieveld. Distributions and regional budgets of aerosols and their precursors simulated with the EMAC chemistry−climate model. *Atmos. Chem. Phys.*, 12(2):961–987, 2012. ISSN 1680-7324. doi: 10.5194/ acp-12-961-2012. URL http://www.atmos-chem-phys.net/12/ 961/2012/acp-12-961-2012.pdf. 19, 21, 22, 23, 31, 144

C. Price and D. Rind. Modeling Global Lightning Distributions in a General Circulation Model. *Monthly Weather Review*, 122(8):1930–1939, 1994. ISSN 0027-0644. doi: 10.1175/1520-0493(1994)122⟨1930:mgldia⟩ 2.0.co;2. URL http://dx.doi.org/10.1175/1520-0493(1994) 122<1930:MGLDIA>2.0.CO;2. 20

K. J. Pringle, H. Tost, S. Message, B. Steil, D. Giannadaki, A. Nenes, C. Fountoukis, P. Stier, E. Vignati, and J. Lelieveld. Description and evaluation of GMXe: a new aerosol submodel for global simulations (v1). *Geosci. Model Dev.*, 3(2):391–412, 2010a. ISSN 1991-9603. doi: 10. 5194/gmd-3-391-2010. URL http://www.geosci-model-dev. net/3/391/2010/gmd-3-391-2010.pdf. 19, 21

K. J. Pringle, H. Tost, A. Pozzer, U. Pöschl, and J. Lelieveld. Global distribution of the effective aerosol hygroscopicity parameter for CCN activation. *Atmos. Chem. Phys.*, 10 (12):5241–5255, 2010b. ISSN 1680-7324. doi: 10.5194/ acp-10-5241-2010. URL http://www.atmos-chem-phys.net/ 10/5241/2010/acp-10-5241-2010.pdf. 21, 22

H. R. Pruppacher and J. D. Klett. *Microphysics of Clouds and Precipitation*, volume 18 of *Atmospheric Oceanographic Series*. Kluwer Academic Publishers, 2000. 28

P.K. Quinn, A. Stohl, A. Arneth, T. Berntsen, J. F. Burkhart, J. Christensen, M. Flanner, K. Kupiainen, H. Lihavainen, M. Shepherd, V. Shevchenko, H. Skov, and V. Vestreng. *The Impact of Black Carbon on Arctic Climate*, volume 4 of *Technical Report*. Arctic Monitoring and Assessment Programme (AMAP), Oslo, 2011. ISBN 978-82-7971-069-1. URL http://www.amap.no/documents/doc/ the-impact-of-black-carbon-on-arctic-climate/746. 102

S. M. Raffuse, K. J. Craig, N. K. Larkin, T. T. Strand, D. Coe Sullivan, N. J. M. Wheeler, and R. Solomon. An Evaluation of Modeled Plume Injection Height with Satellite-Derived Observed Plume Height. *Atmosphere*, 3(1):103–123, 2012. ISSN 2073-4433. URL http://www.mdpi.com/ 2073-4433/3/1/103. 9

V. Ramanathan, P. J. Crutzen, J. T. Kiehl, and D. Rosenfeld. Aerosols, Climate, and the Hydrological Cycle. *Science*, 294(5549):2119–2124, 2001a. doi: 10.1126/science. 1064034. URL http://www.sciencemag.org/content/294/5549/ 2119.abstract. 2, 6

V. Ramanathan, P. J. Crutzen, J. Lelieveld, A. P. Mitra, D. Althausen, J. Anderson, M. O. Andreae, W. Cantrell, G. R. Cass, C. E. Chung, A. D. Clarke, J. A. Coakley, W. D. Collins, W. C. Conant, F. Dulac, J. Heintzenberg, A. J. Heymsfield, B. Holben, S. Howell, J. Hudson, A. Jayaraman, J. T. Kiehl, T. N. Krishnamurti, D. Lubin, G. McFarquhar, T. Novakov, J. A. Ogren, I. A. Podgorny, K. Prather, K. Priestley, J. M. Prospero, P. K. Quinn, K. Rajeev, P. Rasch, S. Rupert, R. Sadourny, S. K. Satheesh, G. E. Shaw, P. Sheridan, and F. P. J. Valero. Indian Ocean Experiment: An integrated analysis of the climate forcing and effects of the great Indo−Asian haze. *Journal of Geophysical Research: Atmospheres*, 106(D22):28371–28398, 2001b. ISSN 2156-2202. doi: 10.1029/2001JD900133. URL http://dx.doi. org/10.1029/2001JD900133. 146

J. T. Randerson, M. V. Thompson, C. M. Malmstrom, C. B. Field, and I. Y. Fung. Substrate limitations for heterotrophs: Implications for models that estimate the seasonal cycle of atmospheric CO_2. *Global Biogeochemical Cycles*, 10(4):585–602, 1996. ISSN 1944-9224. doi: 10.1029/ 96gb01981. URL http://dx.doi.org/10.1029/96GB01981. 35

J. T. Randerson, Y. Chen, G. R. van der Werf, B. M. Rogers, and D. C. Morton. Global burned area and biomass burning emissions from small fires. *Journal of Geophysical Research: Biogeosciences*, 117(G4):G04012, 2012. ISSN 2156-2202. doi: 10.1029/2012jg002128. URL http://dx.doi.org/ 10.1029/2012JG002128. 167

E. Real, K. S. Law, B. Weinzierl, M. Fiebig, A. Petzold, O. Wild, J. Methven, S. Arnold, A. Stohl, H. Huntrieser, A. Roiger, H. Schlager, D. Stewart, M. Avery, G. Sachse, E. Browell, R. Ferrare, and D. Blake. Processes influencing ozone levels in Alaskan forest fire plumes during long-range transport over the North Atlantic. *Journal of Geophysical Research: Atmospheres*, 112(D10):D10S41, 2007. ISSN 2156-2202. doi: 10.1029/2006jd007576. URL http://dx.doi.org/10.1029/2006JD007576. 11, 41

E. Real, E. Orlandi, K. S. Law, F. Fierli, D. Josset, F. Cairo, H. Schlager, S. Borrmann, D. Kunkel, C. M. Volk, J. B. McQuaid, D. J. Stewart, J. Lee, A. C. Lewis, J. R. Hopkins, F. Ravegnani, A. Ulanovski, and C. Liousse. Cross-hemispheric transport of central African biomass burning pollutants: implications for downwind ozone production. *Atmos. Chem. Phys.*, 10(6):3027–3046, 2010. ISSN 1680-7324. doi: 10.5194/acp-10-3027-2010. URL http: //www.atmos-chem-phys.net/10/3027/2010/. 138, 164

J.-L. Redelsperger, C. D. Thorncroft, A. Diedhiou, T. Lebel, D. J. Parker, and J. Polcher. African Monsoon Multidisciplinary Analysis: An International Research Project and Field Campaign. *Bulletin of the American Meteorological Society*, 87(12):1739–1746, 2006. ISSN 0003-0007. doi: 10.1175/BAMS-87-12-1739. URL http://dx.doi.org/ 10.1175/BAMS-87-12-1739. 138

C. E. Reeves, P. Formenti, C. Afif, G. Ancellet, J. L. Attié, J. Bechara, A. Borbon, F. Cairo, H. Coe, S. Crumeyrolle, F. Fierli, C. Flamant, L. Gomes, T. Hamburger, C. Jambert, K. S. Law, C. Mari, R. L. Jones, A. Matsuki, M. I. Mead, J. Methven, G. P. Mills, A. Minikin, J. G. Murphy, J. K. Nielsen, D. E. Oram, D. J. Parker, A. Richter, H. Schlager, A. Schwarzenboeck, and V. Thouret. Chemical and aerosol characterisation of the troposphere over West Africa during the monsoon period as part of AMMA. *Atmos. Chem. Phys.*, 10(16):7575–7601, 2010. ISSN 1680-7324. doi: 10.5194/acp-10-7575-2010. URL http://www. atmos-chem-phys.net/10/7575/2010/. 138

J. S. Reid, P. V. Hobbs, R. J. Ferek, D. R. Blake, J. V. Martins, M. R. Dunlap, and C. Liousse. Physical, chemical, and optical properties of regional hazes dominated by

smoke in Brazil. *J. Geophys. Res.*, 103(D24):32059–32080, 1998. ISSN 0148-0227. doi: 10.1029/98jd00458. URL `http://dx.doi.org/10.1029/98JD00458`. 5

J. S. Reid, T. F. Eck, S. A. Christopher, R. Koppmann, O. Dubovik, D. P. Eleuterio, B. N. Holben, E. A. Reid, and J. Zhang. A review of biomass burning emissions part III: intensive optical properties of biomass burning particles. *Atmos. Chem. Phys.*, 5(3):827–849, 2005. ISSN 1680-7324. doi: 10.5194/acp-5-827-2005. URL `http://www.atmos-chem-phys.net/5/827/2005/acp-5-827-2005.pdf`. 8

S. Remy and J. W. Kaiser. Daily global fire radiative power fields estimation from one or two MODIS instruments. *Atmos. Chem. Phys. Discuss.*, 14(14):20805–20844, 2014. ISSN 1680-7375. doi: 10.5194/acpd-14-20805-2014. URL `http://www.atmos-chem-phys-discuss.net/14/20805/2014/`. 160, 167

P. Reutter, H. Su, J. Trentmann, M. Simmel, D. Rose, S. S. Gunthe, H. Wernli, M. O. Andreae, and U. Pöschl. Aerosol- and updraft-limited regimes of cloud droplet formation: influence of particle number, size and hygroscopicity on the activation of cloud condensation nuclei (CCN). *Atmos. Chem. Phys.*, 9(18):7067–7080, 2009. ISSN 1680-7324. doi: 10.5194/acp-9-7067-2009. URL `http://www.atmos-chem-phys.net/9/7067/2009/`. 8

J. Rissler, E. Swietlicki, J. Zhou, G. Roberts, M. O. Andreae, L. V. Gatti, and P. Artaxo. Physical properties of the sub-micrometer aerosol over the Amazon rain forest during the wet-to-dry season transition - comparison of modeled and measured CCN concentrations. *Atmos. Chem. Phys.*, 4(8):2119–2143, 2004. ISSN 1680-7324. doi: 10.5194/acp-4-2119-2004. URL `http://www.atmos-chem-phys.net/4/2119/2004/`. 8

A. Robert, J. Henderson, and C. Turnbull. An Implicit Time Integration Scheme for Baroclinic Models of the Atmosphere. *Monthly Weather Review*, 100(5):329–335, 1972. ISSN 0027-0644. doi: 10.1175/1520-0493(1972)100⟨0329:aitisf⟩2.3.co;2. URL `http://dx.doi.org/10.1175/1520-0493(1972)100<0329:AITISF>2.3.CO;2`. 16

G. C. Roberts, P. Artaxo, J. Zhou, E. Swietlicki, and M. O. Andreae. Sensitivity of CCN spectra on chemical and physical properties of aerosol: A case study from the Amazon Basin. *Journal of Geophysical Research: Atmospheres*, 107(D20):8070, 2002. ISSN 2156-2202. doi: 10.1029/2001JD000583. URL `http://dx.doi.org/10.1029/2001JD000583`. 8

E. Roeckner, G. Bäuml, L. Bonaventura, R. Brokopf, M. Esch, M. Giorgetta, S. Hagemann, I. Kirchner, L. Kornblueh, E. Manzini, A. Rhodin, U. Schlese, Schulzweida U., and A. Tomkins. The atmospheric general circulation model ECHAM 5. PART I: Model description. Report 349, Max Planck Institute for Meteorology, 2003. URL `http://www.mpimet.mpg.de/fileadmin/publikationen/Reports/max_scirep_349.pdf`. 15, 24

D. Rose, A. Nowak, P. Achtert, A. Wiedensohler, M. Hu, M. Shao, Y. Zhang, M. O. Andreae, and U. Pöschl. Cloud condensation nuclei in polluted air and biomass burning smoke near the mega-city Guangzhou, China - Part 1:

Size-resolved measurements and implications for the modeling of aerosol particle hygroscopicity and CCN activity. *Atmos. Chem. Phys.*, 10(7):3365–3383, 2010. ISSN 1680-7324. doi: 10.5194/acp-10-3365-2010. URL `http://www.atmos-chem-phys.net/10/3365/2010/`. 8

D. Rosenfeld, M. Fromm, J. Trentmann, G. Luderer, M. O. Andreae, and R. Servranckx. The Chisholm firestorm: observed microstructure, precipitation and lightning activity of a pyro-cumulonimbus. *Atmos. Chem. Phys.*, 7(3):645–659, 2007. ISSN 1680-7324. doi: 10.5194/acp-7-645-2007. URL `http://www.atmos-chem-phys.net/7/645/2007/acp-7-645-2007.pdf`. 41

D. Rosenfeld, U. Lohmann, G. Raga B., Colin D. O'Dowd, M. Kulmala, S. Fuzzi, A. Reissell, and M. O. Andreae. Flood or Drought: How Do Aerosols Affect Precipitation? *Science*, 321(5894):1309–1313, 2008. doi: 10.1126/science.1160606. URL `http://www.sciencemag.org/cgi/content/full/321/5894/1309`. 8

L. D. Rotstayn and J. E. Penner. Indirect Aerosol Forcing, Quasi Forcing, and Climate Response. *Journal of Climate*, 14(13):2960–2975, 2001. ISSN 0894-8755. doi: 10.1175/1520-0442(2001)014⟨2960:IAFQFA⟩2.0.CO;2. URL `http://dx.doi.org/10.1175/1520-0442(2001)014<2960:IAFQFA>2.0.CO;2`. 149

R. Sander, A. Kerkweg, P. Jöckel, and J. Lelieveld. Technical note: The new comprehensive atmospheric chemistry module MECCA. *Atmos. Chem. Phys.*, 5(2):445–450, 2005. ISSN 1680-7324. doi: 10.5194/acp-5-445-2005. URL `http://www.atmos-chem-phys.net/5/445/2005/acp-5-445-2005.pdf`. 19, 28, 29

R. Sander, A. Baumgaertner, S. Gromov, H. Harder, P. Jöckel, A. Kerkweg, D. Kubistin, E. Regelin, H. Riede, A. Sandu, D. Taraborrelli, H. Tost, and Z. Q. Xie. The atmospheric chemistry box model CAABA/MECCA-3.0. *Geosci. Model Dev.*, 4(2):373–380, 2011. ISSN 1991-9603. doi: 10.5194/gmd-4-373-2011. URL `http://www.geosci-model-dev.net/4/373/2011/gmd-4-373-2011.pdf`. 29

A. Sandu and R. Sander. Technical note: Simulating chemical systems in Fortran90 and Matlab with the Kinetic PreProcessor KPP-2.1. *Atmos. Chem. Phys.*, 6(1):187–195, 2006. ISSN 1680-7324. doi: 10.5194/acp-6-187-2006. URL `http://www.atmos-chem-phys.net/6/187/2006/acp-6-187-2006.pdf`. 28, 30

A. Sandu, J. G. Verwer, J. G. Blom, E. J. Spee, G. R. Carmichael, and F. A. Potra. Benchmarking stiff ode solvers for atmospheric chemistry problems II: Rosenbrock solvers. *Atmospheric Environment*, 31(20):3459–3472, 1997. ISSN 1352-2310. doi: http://dx.doi.org/10.1016/S1352-2310(97)83212-8. URL `http://www.sciencedirect.com/science/article/pii/S1352231097832128`. 28

B. Sauvage, V. Thouret, J. P. Cammas, F. Gheusi, G. Athier, and P. Nédélec. Tropospheric ozone over Equatorial Africa: regional aspects from the MOZAIC data. *Atmos. Chem. Phys.*, 5(2):311–335, 2005. ISSN 1680-7324. doi: 10.5194/acp-5-311-2005. URL `http://www.atmos-chem-phys.net/5/311/2005/`. 138

REFERENCES

B. Sauvage, F. Gheusi, V. Thouret, J. P. Cammas, J. Duron, J. Escobar, C. Mari, P. Mascart, and V. Pont. Medium-range mid-tropospheric transport of ozone and precursors over Africa: two numerical case studies in dry and wet seasons. *Atmos. Chem. Phys.*, 7(20):5357–5370, 2007a. ISSN 1680-7324. doi: 10.5194/acp-7-5357-2007. URL http://www.atmos-chem-phys.net/7/5357/2007/. 138

B. Sauvage, Randall V. Martin, A. van Donkelaar, and J. R. Ziemke. Quantification of the factors controlling tropical tropospheric ozone and the South Atlantic maximum. *Journal of Geophysical Research: Atmospheres*, 112(D11):D11309, 2007b. ISSN 2156-2202. doi: 10.1029/2006JD008008. URL http://dx.doi.org/10.1029/2006JD008008. 138

P. Seibert, F. Beyrich, S.-E. Gryning, S. Joffre, A. Rasmussen, and P. Tercier. Review and intercomparison of operational methods for the determination of the mixing height. *Atmospheric Environment*, 34(7):1001–1027, 2000. ISSN 1352-2310. doi: http://dx.doi.org/10.1016/S1352-2310(99)00349-0. URL http://www.sciencedirect.com/science/article/pii/S1352231099003490. 20

J. H. Seinfeld and S. N Pandis. *Atmospheric Chemistry and Physics - From Air Pollution to Climate Change*. John Wiley & Sons, 2006. 4, 5, 28

W. R. Sessions, H. E. Fuelberg, R. A. Kahn, and D. M. Winker. An investigation of methods for injecting emissions from boreal wildfires using WRF−Chem during ARCTAS. *Atmos. Chem. Phys.*, 11(12):5719–5744, 2011. ISSN 1680-7324. doi: 10.5194/acp-11-5719-2011. URL http://www.atmos-chem-phys.net/11/5719/2011/. 10

R. B. Skeie, T. Berntsen, G. Myhre, C. A. Pedersen, J. Ström, S. Gerland, and J. A. Ogren. Black carbon in the atmosphere and snow, from pre-industrial times until present. *Atmos. Chem. Phys.*, 11(14):6809–6836, 2011. ISSN 1680-7324. doi: 10.5194/acp-11-6809-2011. URL http://www.atmos-chem-phys.net/11/6809/2011/. 111, 112

M. Sofiev, T. Ermakova, and R. Vankevich. Evaluation of the smoke-injection height from wild-land fires using remote-sensing data. *Atmos. Chem. Phys.*, 12(4):1995–2006, 2012. doi: 10.5194/acp-12-1995-2012. URL http://www.atmos-chem-phys.net/12/1995/2012/. 10, 46, 66, 159

J. H. Sørensen, A. Rasmussen, and H. Svensmark. Forecast of atmospheric boundary-layer height utilised for ETEX real-time dispersion modelling. *Physics and Chemistry of the Earth*, 21(5-6):435–439, 1996. ISSN 0079-1946. doi: http://dx.doi.org/10.1016/S0079-1946(97)81138-X. URL http://www.sciencedirect.com/science/article/pii/S007919469781138X. 20

D. V. Spracklen, K. S. Carslaw, U. Pöschl, A. Rap, and P. M. Forster. Global cloud condensation nuclei influenced by carbonaceous combustion aerosol. *Atmos. Chem. Phys.*, 11(17):9067–9087, 2011. ISSN 1680-7324. doi: 10.5194/acp-11-9067-2011. URL http://www.atmos-chem-phys.net/11/9067/2011/. 8

T. Stavrakou and J. F. Müller. Grid-based versus big region approach for inverting CO emissions using Measurement of Pollution in the Troposphere (MOPITT) data. *Journal of Geophysical Research: Atmospheres*, 111(D15):D15304, 2006. ISSN 2156-2202. doi: 10.1029/2005JD006896. URL http://dx.doi.org/10.1029/2005JD006896. 144

B. Steil, M. Dameris, C. Brühl, P. J. Crutzen, V. Grewe, M. Ponater, and R. Sausen. Development of a chemistry module for GCMs: first results of a multiannual integration. *Ann. Geophys.*, 16(2):205–228, 1999. ISSN 1432-0576. doi: 10.1007/s00585-998-0205-8. URL http://www.ann-geophys.net/16/205/1998/angeo-16-205-1998.pdf. 30

P. Stier, J. Feichter, S. Kinne, S. Kloster, E. Vignati, J. Wilson, L. Ganzeveld, I. Tegen, M. Werner, Y. Balkanski, M. Schulz, O. Boucher, A. Minikin, and A. Petzold. The Aerosol-climate model ECHAM5-HAM. *Atmos. Chem. Phys.*, 5(4):1125–1156, 2005. ISSN 1680-7316. URL http://www.atmos-chem-phys.net/5/1125/2005. 21, 22, 26

A. Stohl, E. Andrews, J. F. Burkhart, C. Forster, A. Herber, S. W. Hoch, D. Kowal, C. Lunder, T. Mefford, J. A. Ogren, S. Sharma, N. Spichtinger, K. Stebel, R. Stone, J. Ström, K. Tørseth, C. Wehrli, and K. E. Yttri. Pan-Arctic enhancements of light absorbing aerosol concentrations due to North American boreal forest fires during summer 2004. *Journal of Geophysical Research: Atmospheres*, 111(D22):D22214, 2006. ISSN 2156-2202. doi: 10.1029/2006JD007216. URL http://dx.doi.org/10.1029/2006JD007216. 112

A. Stohl, Z. Klimont, S. Eckhardt, K. Kupiainen, V. P. Shevchenko, V. M. Kopeikin, and A. N. Novigatsky. Black carbon in the Arctic: the underestimated role of gas flaring and residential combustion emissions. *Atmos. Chem. Phys.*, 13(17):8833–8855, 2013. ISSN 1680-7324. doi: 10.5194/acp-13-8833-2013. URL http://www.atmos-chem-phys.net/13/8833/2013/. 112

R. B. Stull. *An Introduction to Boundary Layer Meteorology*. Atmospheric and Oceanographic Sciences Library. Springer Netherlands, 1988. ISBN 978-94-009-3027-8. doi: 10.1007/978-94-009-3027-8. 20

D Tanre, J.-F. Geleyn, and J. M. Slingo. *First results of the introduction of an advanced aerosol-radiation interaction in the ECMWF low resolution global model, in: Aerosols and their climatic effects*. A. Deepak Publ., Hampton, VA, 1984. 24

D. Taraborrelli, M. G. Lawrence, J. N. Crowley, T. J. Dillon, S. Gromov, C. B. M. Grosz, L. Vereecken, and J. Lelieveld. Hydroxyl radical buffered by isoprene oxidation over tropical forests. *Nature Geosci*, 5(3):190–193, 2012. ISSN 1752-0894. doi: 10.1038/ngeo1405. URL http://dx.doi.org/10.1038/ngeo1405. 4

K. Taylor, D. Williamson, and F. Zwiers. The sea surface temperature and sea ice concentration boundary conditions for AMIP II simulations. Report, PCMDI, 2000. 51

A. M. Thompson, K. E. Pickering, D. P. McNamara, M. R. Schoeberl, R. D. Hudson, J. H. Kim, E. V. Browell, V. W. J. H. Kirchhoff, and D. Nganga. Where did tropospheric ozone over southern africa and the tropical atlantic come from in october 1992? insights from toms, gte trace a,

and safari 1992. *Journal of Geophysical Research: Atmospheres*, 101(D19):24251–24278, 1996. ISSN 2156-2202. doi: 10.1029/96JD01463. URL http://dx.doi.org/10.1029/96JD01463. 5

A. M. Thompson, B. G. Doddridge, J. C. Witte, R. D. Hudson, W. T. Luke, J. E. Johnson, B. J. Johnson, S. J. Oltmans, and R. Weller. A tropical Atlantic Paradox: Shipboard and satellite views of a tropospheric ozone maximum and wave-one in January–February 1999. *Geophysical Research Letters*, 27(20):3317–3320, 2000. ISSN 1944-8007. doi: 10.1029/1999GL011273. URL http://dx.doi.org/10.1029/1999GL011273. 138

V. Thouret, M. Saunois, A. Minga, A. Mariscal, B. Sauvage, A. Solete, D. Agbangla, P. Nédélec, C. Mari, C. E. Reeves, and H. Schlager. An overview of two years of ozone radio soundings over Cotonou as part of AMMA. *Atmos. Chem. Phys.*, 9(16):6157–6174, 2009. ISSN 1680-7324. doi: 10.5194/acp-9-6157-2009. URL http://www.atmos-chem-phys.net/9/6157/2009/. 138

M. Tiedtke. A Comprehensive Mass Flux Scheme for Cumulus Parameterization in Large-Scale Models. *Monthly Weather Review*, 117(8):1779–1800, 1989. ISSN 0027-0644. doi: 10.1175/1520-0493(1989)117⟨1779:acmfsf⟩2.0.co;2. URL http://dx.doi.org/10.1175/1520-0493(1989)117<1779:ACMFSF>2.0.CO;2. 24

A. M. Tompkins. A Prognostic Parameterization for the Subgrid-Scale Variability of Water Vapor and Clouds in Large-Scale Models and Its Use to Diagnose Cloud Cover. *Journal of the Atmospheric Sciences*, 59(12):1917–1942, 2002. ISSN 0022-4928. doi: 10.1175/1520-0469(2002)059⟨1917:appfts⟩2.0.co;2. URL http://dx.doi.org/10.1175/1520-0469(2002)059<1917:APPFTS>2.0.CO;2. 24

M. G. Tosca, J. T. Randerson, C. S. Zender, D. L. Nelson, D. J. Diner, and J. A. Logan. Dynamics of fire plumes and smoke clouds associated with peat and deforestation fires in Indonesia. *Journal of Geophysical Research: Atmospheres*, 116(D8):D08207, 2011. ISSN 2156-2202. doi: 10.1029/2010JD015148. URL http://dx.doi.org/10.1029/2010JD015148. 9

H. Tost. *Global Modelling of Cloud, Convection and Precipitation Influences on Trace Gases and Aerosols*. Thesis, Rheinischen Friedrich Wilhelms Universität, 2006. URL http://hss.ulb.uni-bonn.de/2006/0731/0731.htm. 19, 24, 25, 99

H. Tost and K. J. Pringle. Improvements of organic aerosol representations and their effects in large-scale atmospheric models. *Atmos. Chem. Phys.*, 12(18):8687–8709, 2012. ISSN 1680-7324. doi: 10.5194/acp-12-8687-2012. URL http://www.atmos-chem-phys.net/12/8687/2012/acp-12-8687-2012.pdf. 19, 21

H. Tost, P. Jöckel, A. Kerkweg, R. Sander, and J. Lelieveld. Technical note: A new comprehensive SCAVenging submodel for global atmospheric chemistry modelling. *Atmos. Chem. Phys.*, 6(3):565–574, 2006a. ISSN 1680-7324. doi: 10.5194/acp-6-565-2006. URL http://www.atmos-chem-phys.net/6/565/2006/acp-6-565-2006.pdf. 19, 25, 28, 29

H. Tost, P. Jöckel, and J. Lelieveld. Influence of different convection parameterisations in a GCM. *Atmos. Chem. Phys.*, 6(12):5475–5493, 2006b. ISSN 1680-7324. doi: 10.5194/acp-6-5475-2006. URL http://www.atmos-chem-phys.net/6/5475/2006/acp-6-5475-2006.pdf. 19, 24

H. Tost, P. Jöckel, A. Kerkweg, A. Pozzer, R. Sander, and J. Lelieveld. Global cloud and precipitation chemistry and wet deposition: tropospheric model simulations with ECHAM5/MESSy1. *Atmos. Chem. Phys.*, 7(10):2733–2757, 2007a. ISSN 1680-7324. doi: 10.5194/acp-7-2733-2007. URL http://www.atmos-chem-phys.net/7/2733/2007/acp-7-2733-2007.pdf. 19

H. Tost, P. Jöckel, and J. Lelieveld. Lightning and convection parameterisations - uncertainties in global modelling. *Atmos. Chem. Phys.*, 7(17):4553–4568, 2007b. ISSN 1680-7324. doi: 10.5194/acp-7-4553-2007. URL http://www.atmos-chem-phys.net/7/4553/2007/acp-7-4553-2007.pdf. 18, 19

H. Tost, M. G. Lawrence, C. Brühl, P. Jöckel, GABRIEL Team The, and SCOUT-O3-DARWIN/Active Team The. Uncertainties in atmospheric chemistry modelling due to convection parameterisations and subsequent scavenging. *Atmos. Chem. Phys.*, 10(4):1931–1951, 2010. ISSN 1680-7324. doi: 10.5194/acp-10-1931-2010. URL http://www.atmos-chem-phys.net/10/1931/2010/acp-10-1931-2010.pdf. 19, 25

J. Trentmann, M. O. Andreae, H. F. Graf, P. V. Hobbs, R. D. Ottmar, and T. Trautmann. Simulation of a biomass-burning plume: Comparison of model results with observations. *J. Geophys. Res.*, 107(D2):4013, 2002. ISSN 0148-0227. doi: 10.1029/2001jd000410. URL http://dx.doi.org/10.1029/2001JD000410. 8, 9, 41

J. Trentmann, G. Luderer, T. Winterrath, M. Fromm, R. Servranckx, C. Textor, M. Herzog, H.-F. Graf, and M. O. Andreae. Modeling of biomass smoke injection into the lower stratosphere by a large forest fire (Part I): reference simulation. *Atmos. Chem. Phys.*, 6(12):5247–5260, 2006. ISSN 1680-7324. doi: 10.5194/acp-6-5247-2006. URL http://www.atmos-chem-phys.net/6/5247/2006/. 8, 9, 50, 102

K. Tsigaridis, N. Daskalakis, M. Kanakidou, P. J. Adams, P. Artaxo, R. Bahadur, Y. Balkanski, S. E. Bauer, N. Bellouin, A. Benedetti, T. Bergman, T. K. Berntsen, J. P. Beukes, H. Bian, K. S. Carslaw, M. Chin, G. Curci, T. Diehl, R. C. Easter, S. J. Ghan, S. L. Gong, A. Hodzic, C. R. Hoyle, T. Iversen, S. Jathar, J. L. Jimenez, J. W. Kaiser, A. Kirkevåg, D. Koch, H. Kokkola, Y. H. Lee, G. Lin, X. Liu, G. Luo, X. Ma, G. W. Mann, N. Mihalopoulos, J. J. Morcrette, J. F. Müller, G. Myhre, S. Myriokefalitakis, N. L. Ng, D. O'Donnell, J. E. Penner, L. Pozzoli, K. J. Pringle, L. M. Russell, M. Schulz, J. Sciare, Ø Seland, D. T. Shindell, S. Sillman, R. B. Skeie, D. Spracklen, T. Stavrakou, S. D. Steenrod, T. Takemura, P. Tiitta, S. Tilmes, H. Tost, T. van Noije, P. G. van Zyl, K. von Salzen, F. Yu, Z. Wang, Z. Wang, R. A. Zaveri, H. Zhang, K. Zhang, Q. Zhang, and X. Zhang. The AeroCom evaluation and intercomparison of organic aerosol in global models. *Atmos. Chem. Phys.*, 14(19):10845–10895,

REFERENCES

2014. ISSN 1680-7324. doi: 10.5194/acp-14-10845-2014. URL http://www.atmos-chem-phys.net/14/10845/2014/. 144

S. Turquety, J. A. Logan, D. J. Jacob, R. C. Hudman, F. Y. Leung, C. L. Heald, R. M. Yantosca, S. Wu, L. K. Emmons, D. P. Edwards, and G. W. Sachse. Inventory of boreal fire emissions for North America in 2004: Importance of peat burning and pyroconvective injection. *J. Geophys. Res.*, 112(D12):D12S03, 2007. ISSN 0148-0227. doi: 10.1029/2006jd007281. URL http://dx.doi.org/10.1029/2006JD007281. 9, 10, 42

M. Val Martin, R. E. Honrath, R. C. Owen, G. G. Pfister, P. Fialho, and F. Barata. Significant enhancements of nitrogen oxides, black carbon, and ozone in the North Atlantic lower free troposphere resulting from North American boreal wildfires. *Journal of Geophysical Research: Atmospheres*, 111(D23):D23S60, 2006. ISSN 2156-2202. doi: 10.1029/2006jd007530. URL http://dx.doi.org/10.1029/2006JD007530. 9, 11

M. Val Martín, J. A. Logan, R. A. Kahn, F.-Y. Leung, D. L. Nelson, and D. J. Diner. Smoke injection heights from fires in North America: analysis of 5 years of satellite observations. *Atmos. Chem. Phys.*, 10(4):1491–1510, 2010. ISSN 1680-7324. doi: 10.5194/acp-10-1491-2010. URL www.atmos-chem-phys.net/10/1491/2010/. 9, 42

M. K. van Aalst, M. M. P. van den Broek, A. Bregman, C. Brühl, B. Steil, G. C. Toon, S. Garcelon, G. M. Hansford, R. L. Jones, T. D. Gardiner, G. J. Roelofs, J. Lelieveld, and P. J. Crutzen. Trace gas transport in the 1999/2000 Arctic winter: comparison of nudged GCM runs with observations. *Atmos. Chem. Phys.*, 4(1):81–93, 2004. ISSN 1680-7324. doi: 10.5194/acp-4-81-2004. URL http://www.atmos-chem-phys.net/4/81/2004/acp-4-81-2004.pdf. 31

J. van Aardenne, F. Dentener, J. Olivier, J. Peters, and L. Ganzeveld. The EDGAR 3.2 Fast Track 2000 dataset (32FT2000). 2005. URL http://themasites.pbl.nl/tridion/en/themasites/edgar/emission_data/edgar_32ft2000/index-2.html. 44, 166

G. R. van der Werf, J. T. Randerson, G. J. Collatz, and L. Giglio. Carbon emissions from fires in tropical and subtropical ecosystems. *Global Change Biology*, 9(4):547–562, 2003. ISSN 1365-2486. URL http://dx.doi.org/10.1046/j.1365-2486.2003.00604.x. 36

G. R. van der Werf, J. Dempewolf, S. N. Trigg, J. T. Randerson, P. S. Kasibhatla, L. Giglio, D. Murdiyarso, W. Peters, D. C. Morton, G. J. Collatz, A. J. Dolman, and R. S. DeFries. Climate regulation of fire emissions and deforestation in equatorial Asia. *Proceedings of the National Academy of Sciences*, 2008a. doi: 10.1073/pnas.0803375105. URL http://www.pnas.org/content/early/2008/12/15/0803375105.abstract. 37

G. R. van der Werf, J. T. Randerson, L. Giglio, N. Gobron, and A. J. Dolman. Climate controls on the variability of fires in the tropics and subtropics. *Global Biogeochemical Cycles*, 22(3):GB3028, 2008b. ISSN 1944-9224. doi: 10.1029/2007gb003122. URL http://dx.doi.org/10.1029/2007GB003122. 37

G. R. van der Werf, J. T. Randerson, L. Giglio, G. J. Collatz, M. Mu, P. S. Kasibhatla, D. C. Morton, R. S. DeFries, Y. Jin, and T. T. van Leeuwen. Global fire emissions and the contribution of deforestation, savanna, forest, agricultural, and peat fires (1997-2009). *Atmos. Chem. Phys.*, 10 (23):11707–11735, 2010. ISSN 1680-7324. doi: 10.5194/acp-10-11707-2010. URL http://www.atmos-chem-phys.net/10/11707/2010/acp-10-11707-2010.pdf. 35

H. Vehkamäki, M. Kulmala, I. Napari, K. E. J. Lehtinen, C. Timmreck, M. Noppel, and A. Laaksonen. An improved parameterization for sulfuric acidwater nucleation rates for tropospheric and stratospheric conditions. *Journal of Geophysical Research: Atmospheres*, 107(D22):4622, 2002. ISSN 2156-2202. doi: 10.1029/2002jd002184. URL http://dx.doi.org/10.1029/2002JD002184. 22

E. Vignati, J. Wilson, and P. Stier. M7: An efficient size-resolved aerosol microphysics module for large-scale aerosol transport models. *Journal of Geophysical Research: Atmospheres*, 109(D22):D22202, 2004. ISSN 2156-2202. doi: 10.1029/2003jd004485. URL http://dx.doi.org/10.1029/2003JD004485. 21, 22, 185

D. H. P. Vogelezang and A. A. M. Holtslag. Evaluation and model impacts of alternative boundary-layer height formulations. *Boundary-Layer Meteorology*, 81(3-4):245–269, 1996. ISSN 0006-8314. doi: 10.1007/bf02430331. URL http://dx.doi.org/10.1007/BF02430331. 21

J. Wang, S. A. Christopher, U. S. Nair, J. S. Reid, E. M. Prins, J. Szykman, and J. L. Hand. Mesoscale modeling of Central American smoke transport to the United States: 1. ”Top-down”; assessment of emission strength and diurnal variation impacts. *J. Geophys. Res.*, 111(D5):D05S17, 2006. ISSN 0148-0227. doi: 10.1029/2005jd006416. URL http://dx.doi.org/10.1029/2005JD006416. 10, 40

P. J. Wetzel. Toward Parameterization of the Stable Boundary Layer. *Journal of Applied Meteorology*, 21(1):7–13, 1982. ISSN 0021-8952. doi: 10.1175/1520-0450(1982) 021⟨0007:tpotsb⟩2.0.co;2. URL http://dx.doi.org/10.1175/1520-0450(1982)021<0007:TPOTSB>2.0.CO;2. 21

J. E. Williams, M. P. Scheele, P. F. J. van Velthoven, V. Thouret, M. Saunois, C. E. Reeves, and J.-P. Cammas. The influence of biomass burning and transport on tropospheric composition over the tropical Atlantic Ocean and Equatorial Africa during the West African monsoon in 2006. *Atmos. Chem. Phys.*, 10(20):9797–9817, 2010. doi: 10.5194/acp-10-9797-2010. URL http://www.atmos-chem-phys.net/10/9797/2010/. 11, 138

J. Wilson, C. Cuvelier, and F. Raes. A modeling study of global mixed aerosol fields. *Journal of Geophysical Research: Atmospheres*, 106(D24):34081–34108, 2001. ISSN 2156-2202. doi: 10.1029/2000jd000198. URL http://dx.doi.org/10.1029/2000JD000198. 21

WMO. International meteorological vocabulary, 1992. 20

S. C. Wofsy, G. W. Sachse, G. L. Gregory, D. R. Blake, J. D. Bradshaw, S. T. Sandholm, H. B. Singh, J. A. Barrick, R. C. Harriss, R. W. Talbot, M. A. Shipham, E. V. Browell, D. J. Jacob, and J. A. Logan. Atmospheric chemistry

in the Arctic and subarctic: Influence of natural fires, industrial emissions, and stratospheric inputs. *Journal of Geophysical Research: Atmospheres*, 97(D15):16731–16746, 1992. ISSN 2156-2202. doi: 10.1029/92JD00622. URL http://dx.doi.org/10.1029/92JD00622. 5, 8

M. J. Wooster, G. Roberts, G. L. W. Perry, and Y. J. Kaufman. Retrieval of biomass combustion rates and totals from fire radiative power observations: FRP derivation and calibration relationships between biomass consumption and fire radiative energy release. *J. Geophys. Res.*, 110(D24):D24311, 2005. ISSN 0148-0227. doi: 10.1029/2005jd006318. URL http://dx.doi.org/10.1029/2005JD006318. 46

H. M. Worden, K. W. Bowman, J. R. Worden, A. Eldering, and R. Beer. Satellite measurements of the clear-sky greenhouse effect from tropospheric ozone. *Nature Geosci*, 1(5):305–308, 2008. ISSN 1752-0894. doi: http://www.nature.com/ngeo/journal/v1/n5/suppinfo/ngeo182_S1.html. URL http://dx.doi.org/10.1038/ngeo182. 10.1038/ngeo182. 5

H. M. Worden, K. W. Bowman, S. S. Kulawik, and A. M. Aghedo. Sensitivity of outgoing longwave radiative flux to the global vertical distribution of ozone characterized by instantaneous radiative kernels from Aura-TES. *Journal of Geophysical Research: Atmospheres*, 116(D14):D14115, 2011. ISSN 2156-2202. doi: 10.1029/2010JD015101. URL http://dx.doi.org/10.1029/2010JD015101. 5

J. Worden, Z. Jiang, D. B. A. Jones, M. Alvarado, K. Bowman, C. Frankenberg, E. A. Kort, S. S. Kulawik, M. Lee, J. Liu, V. Payne, K. Wecht, and H. Worden. El Niño,

the 2006 Indonesian peat fires, and the distribution of atmospheric methane. *Geophysical Research Letters*, 40(18): 4938–4943, 2013. ISSN 1944-8007. doi: 10.1002/grl.50937. URL http://dx.doi.org/10.1002/grl.50937. 34, 37

G. Wotawa and M. Trainer. The Influence of Canadian Forest Fires on Pollutant Concentrations in the United States. *Science*, 288(5464):324–328, 2000. doi: 10.1126/science.288.5464.324. URL http://www.sciencemag.org/content/288/5464/324.abstract. 11, 41

M. Yanai, S. Esbensen, and J.-H. Chu. Determination of Bulk Properties of Tropical Cloud Clusters from Large-Scale Heat and Moisture Budgets. *Journal of the Atmospheric Sciences*, 30(4):611–627, 1973. ISSN 0022-4928. doi: 10.1175/1520-0469(1973)030⟨0611:dobpot⟩2.0.co;2. URL http://dx.doi.org/10.1175/1520-0469(1973)030<0611:DOBPOT>2.0.CO;2. 25

R. J. Yokelson, D. W. T. Griffith, and D. E. Ward. Open-path Fourier transform infrared studies of large-scale laboratory biomass fires. *Journal of Geophysical Research: Atmospheres*, 101(D15):21067–21080, 1996. ISSN 2156-2202. doi: 10.1029/96JD01800. URL http://dx.doi.org/10.1029/96JD01800. 2

R. J. Yokelson, R. Susott, D. E. Ward, J. Reardon, and D. W. T. Griffith. Emissions from smoldering combustion of biomass measured by open-path Fourier transform infrared spectroscopy. *Journal of Geophysical Research: Atmospheres*, 102(D15):18865–18877, 1997. ISSN 2156-2202. doi: 10.1029/97JD00852. URL http://dx.doi.org/10.1029/97JD00852. 2, 5

Curriculum Vitae

Personal

Name	Mónica Adriana Lozano Juárez
Date of birth	05 March 1981
Place of birth	Mexico City, Mexico
Citizenship	Mexican
Current address	Albert-Schwitzer-Str. 6, 55128 Mainz
Email	monica.a.lozano.j@gmail.com

Positions

01.2010 - present	Scientific employee at Max Planck Institute for Chemistry, Mainz, Germany.
01.2007 - 11.2008	Teaching assistant of Electronics Laboratory at Faculty of Sciences UNAM, Mexico City, Mexico.
02.2007 - 06.2007	Teaching assistant of Robotics at Faculty of Sciences UNAM, Mexico City, Mexico.
09.2003 - 11.2003	Student assistant at Materials Research Institute UNAM, Mexico City, Mexico.
12.2001 - 02.2002	Student assistant at Materials Research Institute UNAM, Mexico City, Mexico.

Education

09.2011	NCAS, Climate Modelling Summer School, Cambridge, UK.
01.2010 - present	PhD Student at Johannes Gutenberg-University Mainz, Germany.
06.2006 - 11.2009	MSc Atmospheric, Space and Planetary Sciences. Thesis: "Extreme Precipitation Events: The case of Apizaco Tlaxcala". Center of Atmospheric Sciences UNAM, Mexico City, Mexico.
03.2000 - 12.2005	BSc in Physics, specialized in atmospheric physics, materials sciences and astronomy.